Understanding future changes in tropical rainfall and its variability

Submitted by Alexander Drew Todd, to the University of Exeter as a thesis for the degree of Doctor of Philosophy in Mathematics, October 2018.

I certify that all material in this thesis which is not my own work has been identified and that no material has previously been submitted and approved for the award of a degree by this or any other University.

(Signature) .....

Abstract

Tropical precipitation naturally exhibits considerable spatial and interannual variability. The dominant mode of temporal variability is the El Niño-Southern Oscillation (ENSO), where sea surface temperature (SST) fluctuations in the eastern equatorial Pacific cause global weather effects. Meanwhile, changes to tropical precipitation are beginning to emerge from natural variability, caused by anthropogenic global warming. Future projections using state-of-the-art coupled climate models indicate substantial mean state and variability changes in response to increasing greenhouse gas emissions over the twenty first century. A large scale wet-get-wetter and dry-get-drier response is expected, mainly due to increased moisture in a warmer atmosphere. However, at policy-relevant regional scales this paradigm is inadequate, and the pattern of tropical precipitation changes remains uncertain, despite decades of modelling developments. Hence, the aim of this thesis is to improve our understanding of the mechanisms which control tropical precipitation, its variability, and future changes.

Three major results are presented in this thesis. Firstly, a common mechanism is found which bridges present day tropical precipitation interannual variability with simulated future mean state changes. Generally, the heaviest precipitation remains situated above the relatively warmest and most humid regions of the tropics, even as these regions shift geographically. Secondly, in an ensemble of HadGEM2-A simulations, there is evidence of a strong link between tropical land minus ocean temperature and relative humidity contrasts and the overlying atmospheric circulation, in response to idealised global warming perturbations. Since circulation and precipitation changes are strongly related in the tropics, this implies changes over tropical land are likely to be linked to regional patterns of future precipitation change. This extends results in the literature describing the important role that SST pattern and circulation changes play in tropical precipitation changes. Finally, significant changes in ENSO anomalous precipitation are simulated in the atmospheric response to either uniform or patterned SST warming, or increased CO_2 forcing. Hence, in coupled projections and reality, changes to ENSO-related precipitation are likely to result from a careful balance of several interacting process.

Acknowledgements

I would like to take this opportunity to acknowledge my supervisors: Mat Collins, Hugo Lambert and Rob Chadwick, for their generous guidance, support, motivation and endless patience. I am especially indebted to Mat for the fantastic opportunities provided by this PhD, and the hours of excellent discussions sharing his knowledge about all things tropical rainfall and cycling. I would like to thank Hugo for his infectious enthusiasm, and Rob for teaching me the intricacies and joys of running the UM.

More widely, I would like to thank everyone at Exeter and the Met Office who has helped and inspired me over the past seven years, notably: Chris Ferro, Bob Beare, Philip Gill, Jamie Rae and Gill Martin. I gratefully acknowledge NERC and the Met Office for their funding.

I am very thankful to my parents for encouraging and supporting me to follow my passion of weather to wherever it has taken me. Many thanks also to my brother for inspiring me to follow his footsteps down the academic path.

Thank you to all the friends I've shared an office with on Laver levels six and nine. The python and JASMIN help has been invaluable, as well as the regular tea breaks.

Thanks to the pets: Sprocket, Coppi and Bartali, and the recent addition of Rossby, who has provided much needed distractions whilst writing up.

Mostly, thank you to Lucy for your unwavering love and support throughout, for endlessly listening to me talk about rain, and for your eternal drive to help me reach my dreams.

Contents

List of Tables

List of Figures

Chapter 1

Introduction

> "Situated upon the Equator, and bathed by the tepid water of the great tropical oceans, this region enjoys a climate more uniformly hot and moist than almost any other part of the globe, and teems with natural productions which are elsewhere unknown. The richest of fruits and the most precious of spices are Indigenous here. It produces the giant flowers of the Rafflesia, the great green-winged Ornithoptera..., the man-like Orangutan, and the gorgeous Birds of Paradise."
>
> *A. R. Wallace, The Malay Archipelago, 1869*
> (Describing the maritime continent.)

Present day interannual variability in tropical precipitation affects billions of lives. The largest driver of tropical climate variability is the El Niño-Southern Oscillation (ENSO), where sea surface temperatures fluctuate by a few degrees Celsius in the eastern equatorial Pacific every 2-7 years (McPhaden *et al.*, 2006). This leads to local and remote weather changes (Rasmusson and Carpenter, 1982; Ropelewski and Halpert, 1987), which can contribute to widespread socio-economic and environmental effects (Bell *et al.*, 1999). Meanwhile, both the mean state and variability of tropical precipitation are changing in response to anthropogenic global warming (Hartmann *et al.*, 2013). Twenty first century projections of precipitation change under business-as-usual scenarios highlight the potential for severe impacts (Collins *et al.*, 2013; Christensen *et al.*, 2013). However, the regional pattern and magnitude of projected precipitation changes for any given scenario is relatively uncertain (Knutti and Sedlacek, 2012). This thesis aims to improve our understanding of the mechanisms which control tropical precipitation and its variability, in order to reduce the uncertainty of future projections. A variety of observations and climate model simulations are examined in order to disentangle the competing processes which may contribute to future tropical precipitation changes.

1.1 Present Day Tropical Climate

1.1.1 Tropical Precipitation and the Global Hydrological Cycle

All precipitation originates from moisture evaporated at the Earth's surface. Due to the global atmospheric circulation, falling precipitation may occur quite distant to the original point of evaporation. This adds considerable complexity when examining present day and future precipitation variability. In the global hydrological cycle, over annual time scales, the precipitation minus evaporation surplus over continental land is balanced by a precipitation minus evaporation deficit over ocean. Trenberth *et al.* (2007) provide estimates of these moisture fluxes drawing on a variety of observations and reanalyses for the recent, 1979-2000 period. Over ocean, evaporation and precipitation fluxes were 413×10^3 km^3 yr^{-1} and 373×10^3 km^3 yr^{-1}, whilst over land these fluxes were 73×10^3 km^3 yr^{-1} and 113×10^3 km^3 yr^{-1}, respectively. The 40×10^3 km^3 yr^{-1} imbalance, equivalent to 0.72 mm day^{-1} accumulation over all land areas, is maintained by surface and subsurface runoff from land to ocean, which equals the advection of water vapour from ocean to land by the atmospheric circulation.

The hydrological cycle plays an important role in the Earth's energy budget. Trenberth *et al.* (2009) use a variety of observational datasets to estimate the global mean surface latent heat flux associated with evaporation at 80 W m^{-2}. As this water vapour condenses to form cloud droplets, this leads to an equivalent diabatic heating of 80 W m^{-2} in the troposphere due to precipitation. The net atmospheric advection of moisture from ocean to land constitutes 3.2 PW of moist static energy (Trenberth *et al.*, 2007). An opposing dry static energy transport of 1 PW, leads to a net ocean to land energy transport of approximately 2.2 PW (Fasullo and Trenberth, 2008). Precipitation over the tropics (30°N-30°N), one half of the Earth's surface, accounts for a disproportionately high fraction (58% in GPCP over 1979-2016, see Section 1.2.1) of the global precipitation, with tropical and global mean accumulation rates of 3.1 and 2.7 mm day^{-1}, respectively. Consequently, tropical precipitation variability has an important effect on the global circulation and energy balance.

1.1.2 Tropical Precipitation and Atmospheric Circulation

In the present day, over seasonal and annual time scales, tropical precipitation is generally organised into narrow, zonal bands. This is evident in Figure 1.1, which shows seasonal and annual means for the Global Precipitation Climatology Project (GPCP, Adler *et al.* (2003)) observations (discussed further in Section 1.2.1) over the 1979-2016 period. These zonal bands are termed convergence zones, due to the net moisture convergence at low levels. The most extensive zonal band is the Inter-Tropical Convergence Zone (ITCZ). In the annual mean, the ITCZ generally extends across the northern off-equatorial Pacific and Atlantic oceans, and the equatorial regions of the Indian ocean,

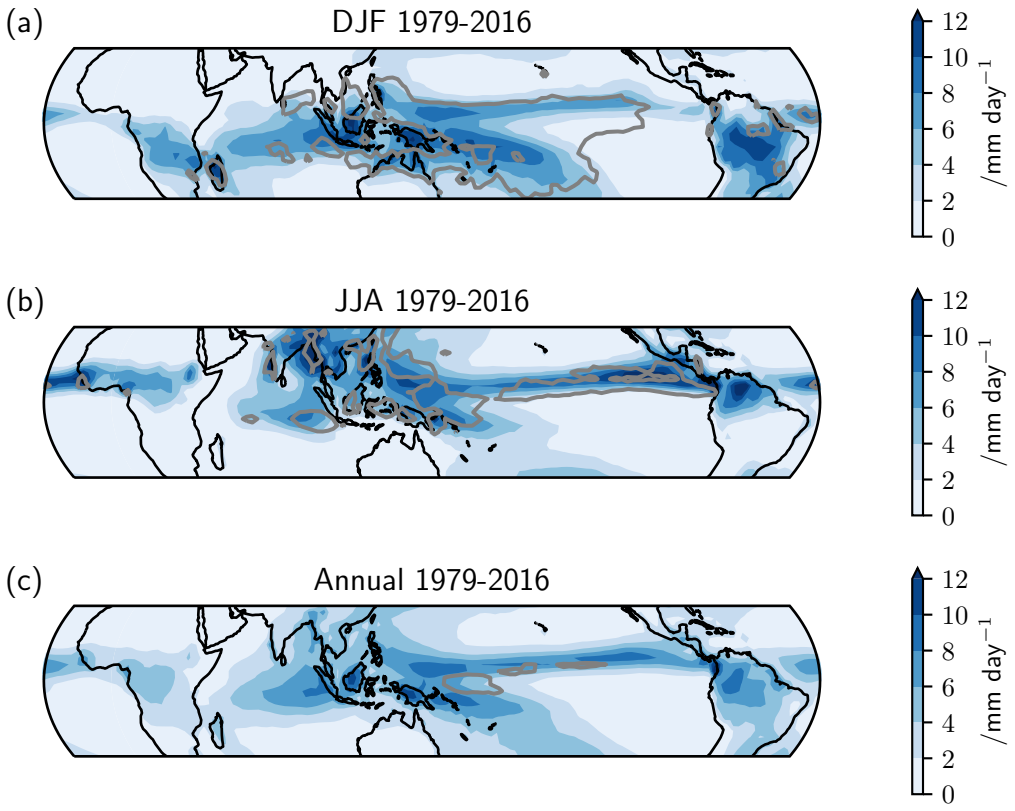

Figure 1.1: Colours show the GPCP December-February (a), June-August (b) and annual mean (c) tropical precipitation over the 1979-2016 period. Grey lines indicate the 2 mm day^{-1} contour of the standard deviation of the corresponding seasonal and annual means.

maritime continent and South America. Over the seasonal cycle, the ITCZ migrates meridionally across the equator, with the zonal mean precipitation maximum generally located in the summer hemisphere, as shown by Figure 1.2. On a regional scale, the South Pacific (SPCZ) and South Atlantic Convergence Zones (SACZ) are two smaller precipitation bands extending south eastward from the equator over their respective ocean basins. These regional convergence zones are most prominent during the austral summer (Haffke and Magnusdottir, 2013).

Over tropical oceans, the location of these convergence zones, and hence the spatial pattern of precipitation, is strongly dependent on coupled atmosphere-ocean processes. A balance between low level moisture convergence and surface evaporation sets the ITCZ location (Charney, 1971). However, as the local correlation between evaporation and precipitation is generally weak across tropical oceans, low level moisture convergence is largely responsible for precipitation from the ITCZ (Neelin and Held, 1987). Sea surface temperature (SST) gradients drive the pattern of low level atmospheric circulation and therefore convergence, modulated by waves within the boundary layer (Holton *et al.*, 1971). Meanwhile, deep convection is favoured over regions of the relatively highest SST and boundary layer moist static energy (Lindzen and Nigam, 1987). This process

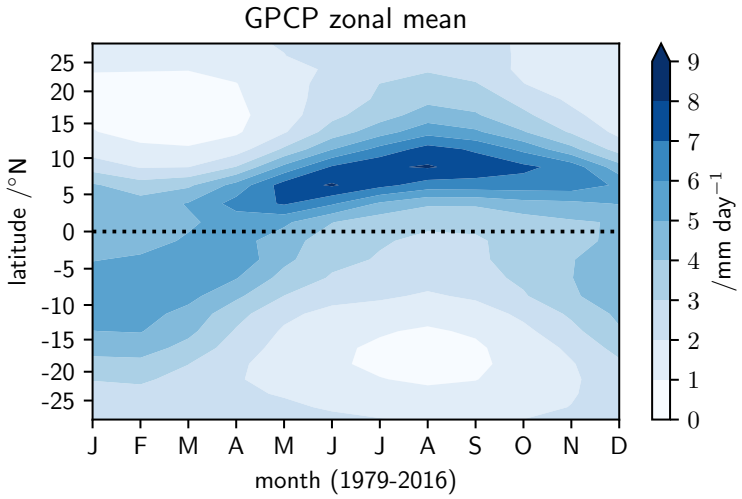

Figure 1.2: Zonal mean GPCP precipitation versus month for the 1979-2016 period. The horizontal dotted line denotes the equator; and the vertical axis is scaled by the cosine of latitude to represent area weighting.

acts as a positive feedback, since deep convection promotes low level convergence, which subsequently provides moisture to sustain the deep convection. A more detailed discussion of convection and different precipitation types is provided in Section 1.1.3.

A number of mechanisms have been proposed to explain the tropical SST pattern and consequently the northward displacement of the ITCZ away from the equator, especially over the Pacific and Atlantic oceans. Common to each mechanism is Earth's zonally asymmetric continental configuration. Takahashi and Battisti (2007) used climate model simulations to demonstrate how the presence of the Andes leads to a climatological descent of low specific humidity air over the eastern Equatorial Pacific. This relatively dry air promotes surface evaporation, causing SST cooling over this region and hence a cross-equatorial SST gradient, which displaces the ITCZ northward of the equator. Furthermore, the asymmetric ocean meridional overturning circulation, especially in the Atlantic, leads to a net northward heat transport at the equator, contributing to the northward ITCZ displacement (Frierson *et al.*, 2013; Loeb *et al.*, 2016). In addition, precipitation and latent heating differences over the Sahel and southern Africa is linked with an asymmetric atmospheric circulation pattern, pushing the annual mean ITCZ north of the equator (Biasutti *et al.*, 2004). At larger scales, inter-hemispheric energy imbalance linked with albedo differences, leads to a net southward energy flux and a compensating northward moisture flux in the atmosphere (Hawcroft *et al.*, 2017). On shorter timescales, free tropospheric relative humidity (Möbis and Stevens, 2012), and the cross-equatorial energy flux linked with ocean heat uptake (Adam *et al.*, 2016) modulate the location of the ITCZ.

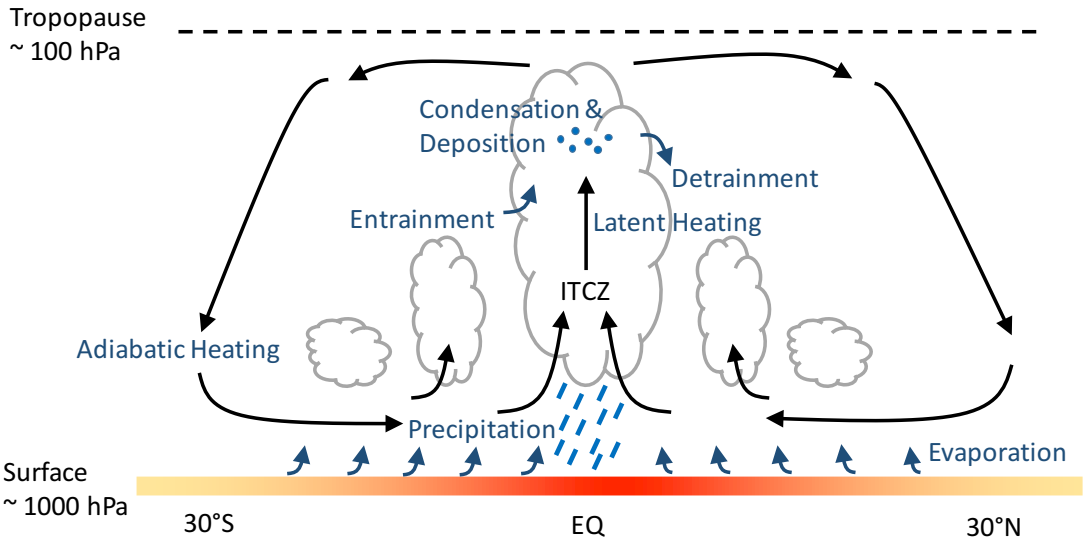

Figure 1.3: Schematic representation of the annual mean Hadley circulation, demonstrating the main processes associated with inter-tropical convergence zone (ITCZ). Warmer and cooler surface temperatures near the equator and subtropics are represented by red and yellow shading, respectively.

Zonally Symmetric Overturning Circulation

On the tropics-wide scale and over the annual mean, the ITCZ represents the ascending branch shared between two meridional overturning cells. This is termed the Hadley circulation, crediting the original source (Hadley, 1735) to explain the basic mechanisms. Figure 1.3 presents a schematic of the Hadley circulation. Deep convection near the equator rapidly lifts moist air parcels towards the tropopause, causing condensation and latent heating aloft, leading to heavy precipitation locally and a poleward outflow in the upper troposphere. These air parcels then gradually subside over the subtropics, warming adiabatically, hence stabilising the troposphere and suppressing convection. At low levels, the returning flow of relatively dry air towards the equator promotes surface evaporation, contributing to the equatorial moisture convergence which sustains the deep convection (Webster, 2004). Since the Earth is rotating, the Coriolis effect leads to an easterly component of the low level flow, causing typically north easterly and south easterly flow, termed the trade winds, in the northern and southern tropics, respectively. Held and Hou (1980) present a theoretical framework which defines the width of each Hadley cell as the lowest latitude where baroclinic eddies are sustained, based on stability constraints, and assuming a dry atmosphere. Hadley circulation dynamics and recent observed changes are explored further in Section 1.2.1.

Zonally Asymmetric Overturning Circulation

Examining the zonal profile of tropical precipitation in Figure 1.1, three regions experience heavier precipitation relative to their surroundings: the maritime continent, equatorial South America and Africa. This inhomogeneity indicates a zonal asymmetry to the tropical circulation, with ascending branches generally located over these three regions. The largest cell is located across the Pacific ocean, termed the Walker circulation by Bjerknes (1969), crediting earlier work by Walker (1923). A schematic of the Walker circulation is presented in Figure 1.4 (Section 1.1.4). Similar to the northward displacement of the ITCZ, the Walker circulation is driven by the zonal SST gradient across the equatorial Pacific. In the mean state, the surface equatorial Pacific is relatively warmer in the west and cooler in the east. This leads to low level easterly flow across the Pacific, caused by and maintaining the convergence and ascent over the western Pacific and maritime continent, with westerly outflow aloft, and large scale returning descent over the eastern Pacific and western shores of equatorial South America. Bjerknes (1969) also demonstrated how the atmospheric and underlying oceanic circulation act as a coupled system, which is pivotal for understanding El Niño-Southern Oscillation (ENSO) dynamics. Commonly termed the Bjerknes feedback, this mechanism will be examined further in Section 1.1.4.

Weak Temperature Gradient Approximation

In equatorial regions, horizontal temperature and density gradients are very weak above the boundary layer, due to the small Coriolis parameter and therefore negligible rotational effects (Charney, 1963). Consequently, the primary energy balance on local scales is between vertical advection and diabatic heating. To first order, the free tropospheric temperature profile, above 700 hPa, can be assumed to be uniform across the tropics. Sobel *et al.* (2001) term this assumption the weak temperature gradient (WTG) approximation, and present a simplified theory for the tropical circulation. Sobel and Bretherton (2000) demonstrated how uncoupled single column models, prescribed with varying surface temperatures and identical free tropospheric temperature profiles, simulate a climatological precipitation pattern similar to that of a full global circulation model (climate models are discussed further in Section 1.3). This demonstrates how the pattern of tropical precipitation is largely linked to surface conditions. The WTG approximation forms the basis of the precipitation diagnosis methodologies presented in Chapters 2 and 3.

1.1.3 Precipitation Classifications: Convective and Stratiform

Precipitation is any form of falling hydrometeor, generally categorised as rain, sleet, hail, graupel or snow. At the surface, the vast majority of tropical precipitation is rain, since low level temperatures are almost entirely above freezing. Processes leading to precipitation cover a spectrum, typically partitioned into two main classifications: stratiform or convective. Stratiform precipitation occurs when the lower troposphere is stably stratified, with widespread weak updrafts aloft. Under these conditions, hydrometeors falling through these updrafts slowly grow by condensation or deposition of environmental moisture. Consequently, stratiform precipitation typically covers a large spatial scale at low intensity. Conversely, convective precipitation results from the narrower and faster updrafts associated with the buoyant ascent of deep convection, due to a conditionally unstable tropospheric lapse rate. In this case, updrafts are of sufficient magnitude to repeatedly lift falling hydrometeors, leading to additional growth through deposition. Deep convection is typically short lived (of the order hours), as condensation and hence latent heating at upper levels stabilises the tropospheric lapse rate. Additionally, resulting cool downdrafts act to restrict the moisture supply at low levels. Consequently, convective precipitation generally occurs over a shorter duration, on smaller spatial scales and at higher intensity relative to stratiform precipitation (Houze, 1993). In reality, tropical precipitation is generally a mixture of both convective and stratiform types, as discussed later in this subsection.

Over the 1998-2000 period in Tropical Rainfall Monitoring Mission (TRMM, Huffman *et al.* (2007)) observations, stratiform precipitation accounted for 73% of the total area and 40% of the total accumulation across the tropics (Schumacher and Houze, 2003). This highlights how tropical convective precipitation occurs on both smaller scales and at greater intensity relative to stratiform precipitation. For example, Schumacher and Houze (2003) estimated that the tropical mean convective precipitation rate was four times larger than the equivalent stratiform rate, with this result typically consistent at smaller scales. However, variations across the tropics exist in the relative spatial extent of convective to stratiform precipitation rates. For instance, over the maritime continent and eastern equatorial Pacific, the stratiform fraction was 25% and 60%, respectively.

The large majority of tropical precipitation is formed within mesoscale convective systems (MCS), which are organised conglomerates of cumulonimbus and stratiform clouds (Houze, 1989). In particular, over the Amazon Basin and the East African Rift region, greater than 80% of precipitation originates from MCS in observations (Roca *et al.*, 2014). Initially, if the lapse rate is unstable, deep convective updrafts from the boundary layer produce towering cumulonimbus clouds. If several of these coalesce a stratiform cloud deck extends between the convective towers and a mesoscale convective system is formed and subsequently matures. Consequently, MCS produce both convective and

stratiform precipitation, contiguous over an area of the order 10-100 km in diameter (Houze, 2004). Over warm ocean regions with low vertical wind shear, sufficiently long lasting MCS can further evolve into tropical cyclones. This leads to deep convection persisting for several days. MCS affect the larger scale tropical circulation by acting as Rossby and Kelvin wave sources (Houze *et al.*, 2000), and play an important role in modulating interannual variability (Chen *et al.*, 1996).

The contrasting processes leading to convective and stratiform precipitation lead to differing tropospheric heating profiles. Hartmann *et al.* (1984) discussed these differences based on theoretical and idealised modelling results, and the implications for large scale circulation. Typically, the buoyant ascent associated with convective precipitation leads to latent or diabatic heating throughout the troposphere. For deep convection, heating is maximal around 500-600 hPa, corresponding to the region of the largest vertical velocities. In contrast for stratiform precipitation, condensation and deposition, and hence latent heating, is limited to the weak updrafts in the upper troposphere. Below the freezing level, a large proportion of the small falling hydrometeors melt and re-evaporate, causing a net latent cooling. Consequently, for MCS producing a mixture of stratiform and convective precipitation, latent heating is concentrated in the upper troposphere above 600 hPa, with a maximum near 400 hPa. This combined convective and stratiform heating drives the tropical scale zonal and meridional overturning circulations, as introduced in Section 1.1.2, by promoting ascent at lower levels and divergence aloft.

1.1.4 El Niño-Southern Oscillation (ENSO) Dynamics

The dominant mode of tropical and global interannual climate variability is the El Niño-Southern Oscillation (ENSO), a coupled ocean-atmosphere process. The oceanic component of ENSO is characterised by quasi-periodic and asymmetric shifts between anomalously warm (El Niño) and cool (La Niña) sea surface temperatures in the central and eastern equatorial Pacific every 2-7 years. The corresponding atmospheric component, the Southern Oscillation, is manifested by changes in convection, precipitation, sea level pressure and hence trade winds across the tropical Pacific. ENSO events lead to a variety of global weather impacts via teleconnections (Ropelewski and Halpert, 1987), which contribute to a number of important socio-economic and environmental effects (Bell *et al.*, 1999). A schematic highlighting the main processes involved with each ENSO phase is presented in Figure 1.4.

The mean state, or ENSO neutral phase, of the tropical Pacific climate was outlined earlier in Section 1.1.2. Low level easterly winds, associated with the Walker circulation, are driven and maintained by an equatorial zonal SST gradient, with a warm western Pacific and relatively cooler eastern Pacific. As introduced previously, this coupling between the zonal SST gradient and atmospheric circulation is termed the Bjerknes feedback.

Along the equator, the resulting zonal wind stress causes a westward surface current, and hence upwelling of cool subsurface water in the eastern equatorial Pacific, maintaining the equatorial cold tongue. Meanwhile, surface water warmed and advected into the western equatorial Pacific forms the western Pacific warm pool. Additionally, the westward surface current leads to a poleward Ekman transport away from the equator due to the Coriolis effect, causing equatorial upwelling of cooler subsurface water. This process is especially strong in the eastern Pacific where the surface wind stress is largest, further reinforcing the zonal SST gradient. During La Niña events, these neutral state conditions are amplified via the Bjerknes feedback and the Walker circulation strengthens, as the zonal SST gradient steepens. This leads to enhanced ascent and increased precipitation over the western Pacific and increased tropospheric stability and reduced precipitation over the central and eastern Pacific (Philander, 1990; Neelin *et al.*, 1998).

During El Niño events, the equatorial Pacific low level easterly winds weaken, or even reverse in extreme cases (Cai *et al.*, 2014), and the Bjerknes feedback operates in reverse to reduce the SST gradient across the Pacific Basin. In this case, the westward equatorial surface current slows and the western Pacific warm pool extends eastward into the central Pacific. Upwelling reduces in the eastern Pacific, further weakening the zonal SST gradient. Correspondingly, the Walker cell shifts eastward as deep convection remains anchored above the expanding warm pool. In the eastern Pacific, the circulation shift further weakens the trade winds, slowing the surface currents and hence reducing upwelling. These mechanisms combine as a positive feedback to amplify the characteristic El Niño warm SST anomalies in the central and eastern equatorial Pacific. The shift in the Walker circulation therefore causes an increase in precipitation over the central and eastern Pacific, and a decrease over the western Pacific. In addition, the eastward shift of the Walker circulation displaces the Atlantic and Indian ocean zonal overturning cells eastward. This consequently leads to precipitation anomalies across many tropical land areas. Moreover, anomalous deep convection over the central equatorial Pacific acts as a Rossby wave source (Trenberth *et al.*, 1998). The poleward and eastward propagation of these waves into the subtropics and mid-latitudes leads to a variety of global weather impacts, termed teleconnections (Rasmusson and Carpenter, 1982; Ropelewski and Halpert, 1987).

In addition to the Bjerknes feedback, the thermocline feedback modulates ENSO intensity. The eastward propagation of Kelvin waves along the thermocline, a region of strong vertical temperature gradient between the warm mixed layer and the cool deep ocean, is particularly important in the evolution of ENSO events. In the neutral state, the thermocline slopes downwards from east to west, due to the location of the west Pacific warm pool and upwelling of cool water in the eastern Pacific. The slope of the thermocline is determined by the surface wind stress, with a deeper thermocline located

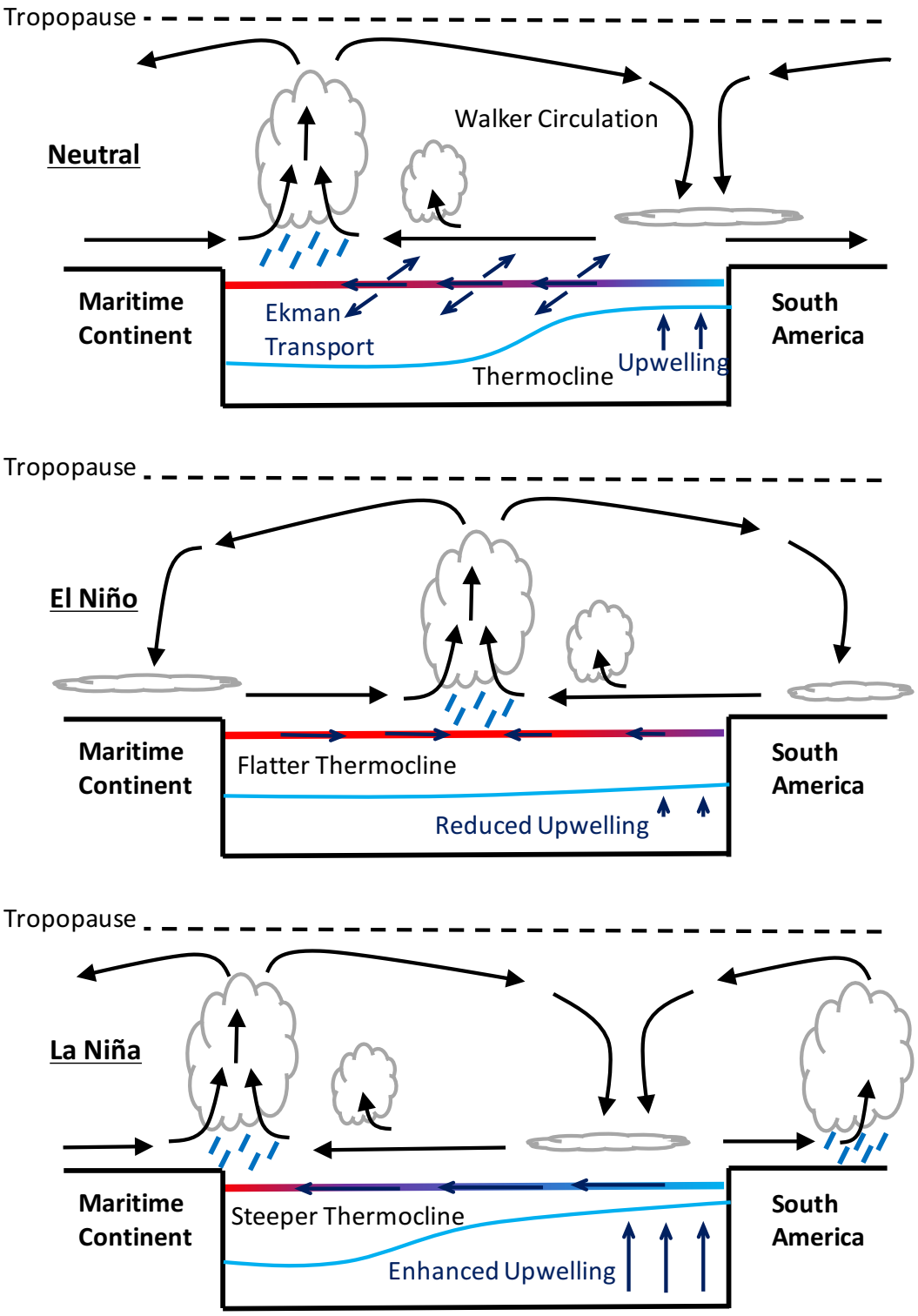

Figure 1.4: Schematic representation of the tropical Pacific and Walker circulation under neutral or mean state (top), El Niño (middle) and La Niña (bottom) conditions. Warmer and cooler sea surface temperatures represented by red and blue shading. Accompanying description in Section 1.1.4.

underneath and eastward of surface temperature anomalies (Neelin *et al.*, 1998). This results in warmer subsurface waters east of the surface anomaly, which warm the surface via upwelling. Hence, the thermocline feedback leads to an eastward propagation of surface temperature anomalies, amplifying El Niño and dampening La Niña conditions.

Further mechanisms are also influential in modulating incipient ENSO events. Increased convection over warm SST anomalies leads to additional cumulonimbus formation in convergence zones, which reduces incoming shortwave radiation and hence weakens surface heating. This mechanism is referred to as the shortwave radiation feedback. Anomalous surface winds affect evaporation, with increased wind speeds cooling SST locally. These SST changes can subsequently influence the surface wind strength by via SST gradient changes, (Xie and Philander, 1994). In addition, during El Niño events, warm surface waters are slowly advected polewards into the subtropics. This poleward transport happens over a longer timescale than the thermocline or Bjerknes feedbacks. This produces a discharged state in the boreal spring after peak El Niño conditions in the winter, which can initiate La Niña development during the following year (Collins *et al.*, 2010).

Over the satellite era, and in a variety of climate model simulations, there is a large diversity in the spatial pattern of El Niño SST anomalies and the corresponding atmospheric teleconnections (Capotondi *et al.*, 2015). El Niño events can broadly be categorised into two types, where positive SST anomalies are constrained to either the central or eastern equatorial Pacific (Yeh *et al.*, 2009). However, there is a great deal of diversity within these two categories. Since 1979, La Niña has typically occurred in the year following El Niño conditions, but 1980, 1992 and 2002 were exceptions. Additionally, individual ENSO events occur quite irregularly in time, due to the careful balance of competing feedbacks. There are a number of asymmetries between El Niño and La Niña, with the magnitude of SST anomalies generally larger for the former. La Niña events often persist for two or more years, whereas El Niño events rarely exceed one year in duration. Timmermann *et al.* (2018) provide a comprehensive overview of our understanding of the processes leading to the spatial and temporal complexity of ENSO, focussing on the theoretical recharge-discharge oscillator model of Jin (1997).

1.2 Recent Tropical Precipitation

1.2.1 Observing Precipitation

Several methods are used to observe precipitation, including surface-based rain gauges and radar, and passive microwave and infra-red imaging from geosynchronous and low-orbit satellites. Measurements from these varying sources are combined to produce observational datasets. In this thesis, the Global Precipitation Climatology Project (GPCP) version 2.3 dataset is frequently used, as it is generally considered the most accurate observational product (Flato *et al.*, 2013). GPCP consists of monthly mean precipitation estimates at a global, $2.5^\circ \times 2.5^\circ$ resolution. Adler *et al.* (2003) give a detailed description of the GPCP dataset, with a summary provided here. GPCP uses rain gauge measurements from 6500-7000 observing stations contributing to the Global Precipitation Climatology Centre dataset from 1986 onwards, and a subset of these contributing to the Global Historical Climate Network or the Climate Assessment and Monitoring System for 1979-1985. After quality control and spatial interpolation, these in situ observations are combined with multiple satellite derived estimates, calibrated against ground based radar measurements. For 1979-present, infra-red (IR) based estimates of cloud top area and outgoing longwave radiation (OLR) measurements (Xie and Arkin, 1998), from geosynchronous and low Earth orbiting satellites, respectively, are used to infer precipitation rates. From 1987 onwards, Special Sensor Microwave Imager (SSM/I) cloud top brightness temperatures are also utilised, with separate algorithms applied for microwave emission and scattering over ocean and land.

Alternative contemporary precipitation observation products include the Tropical Rainfall Monitoring Mission (TRMM, Huffman *et al.* (2007)) and the Climate Prediction Centre (CPC) Merged Analysis of Precipitation (CMAP, Xie and Arkin (1997)) datasets. Similar to GPCP, TRMM uses rain gauge measurements combined with IR and microwave based estimates, focussing only on the period 1998-2015 when a continuous suite of passive microwave sensors was available. CMAP combines the merged rain gauge and satellite estimates from GPCP with precipitation simulations from the NCEP-NCAR reanalysis. Importantly, each of these precipitation datasets has a corresponding error, or bias, compared to reality. In situ rain gauges can underestimate precipitation accumulations due to undercatch, either via evaporation or surface wind effects. Spatial coverage of rain gauges is also weak for sparsely populated and developing land areas, and virtually non-existent over ocean, contributing to systematic errors. For instance, recent CloudSat radar observations suggest GPCP underestimates precipitation over tropical oceans by up to 10% (Berg *et al.*, 2010; Stephens *et al.*, 2012). By definition, satellite-based estimates rely on empirical models calibrated against surface observations to infer precipitation, which provides another source of systematic error.

In this thesis, error in observations refers to the difference between the observational product, such as GPCP data, and what happened in reality. Hence this error represents a combination of instrumentation error and uncertainty from the algorithms used to estimate precipitation from indirect satellite or radar measurements. Adler *et al.* (2012) compare multiple precipitation datasets to estimate their relative error, the standard deviation divided by the mean, in an attempt to quantify the systematic error for the 1988-2007 period. Relative error was found to be higher over the eastern tropical Pacific (20%) in comparison to the western tropical Pacific (10-15%). Generally, relative error was smaller over tropical land due to the greater availability of rain gauge measurements for calibrating satellite-derived estimates.

1.2.2 Precipitation Variability over the Satellite Era

As introduced in Section 1.1.4, the dominant mode of interannual tropical climate variability is ENSO. The central-eastern Pacific SST anomaly in the Niño3.4 region (5°N-5°S, 120°W-170°W) is a commonly used proxy for ENSO amplitude (Trenberth and Stepaniak, 2001), with relatively warm and cool anomalies representing El Niño and La Niña events, respectively. Panel (a) of Figure 1.5 shows the Niño3.4 SST anomaly over the 1979-2016 period in the Extended Reconstructed Sea Surface Temperature (ERSSTv4) dataset (Huang *et al.*, 2015). Figures 1.5(b) and (c) show slope estimates of monthly GPCP precipitation accumulations regressed on the positive and negative Niño3.4 SST anomalies, respectively. In this context, and throughout this thesis, Y regressed on X means the (Gaussian) linear model, $Y \sim \mathcal{N}(\beta_0 + \beta_1 X, \sigma^2)$, is fitted via maximum likelihood. Here, X and Y are considered explanatory and response variables, respectively, and β_0, β_1 and σ^2 represent the intercept, slope and variance parameters, respectively. Hence, Figures 1.5(b) and (c) demonstrate the mean precipitation change, in mm day^{-1}, per unit SST anomaly, in K.

Consistent with the canonical picture, El Niño and La Niña conditions in the recent period are linked with precipitation increases and decreases across the central-eastern Pacific, respectively, with opposite changes over the maritime continent. On the regional scale, a notable skewness is present between the precipitation change between the two ENSO phases. For instance, in the magnitude of precipitation changes are typically amplified for El Niño relative to La Niña conditions, and La Niña increases across the maritime continent are more extensive than equivalent El Niño decreases. This ENSO-related precipitation skewness is due to the underlying asymmetric dynamics modulating ENSO (McPhaden *et al.*, 2006), as discussed in Section 1.1.4.

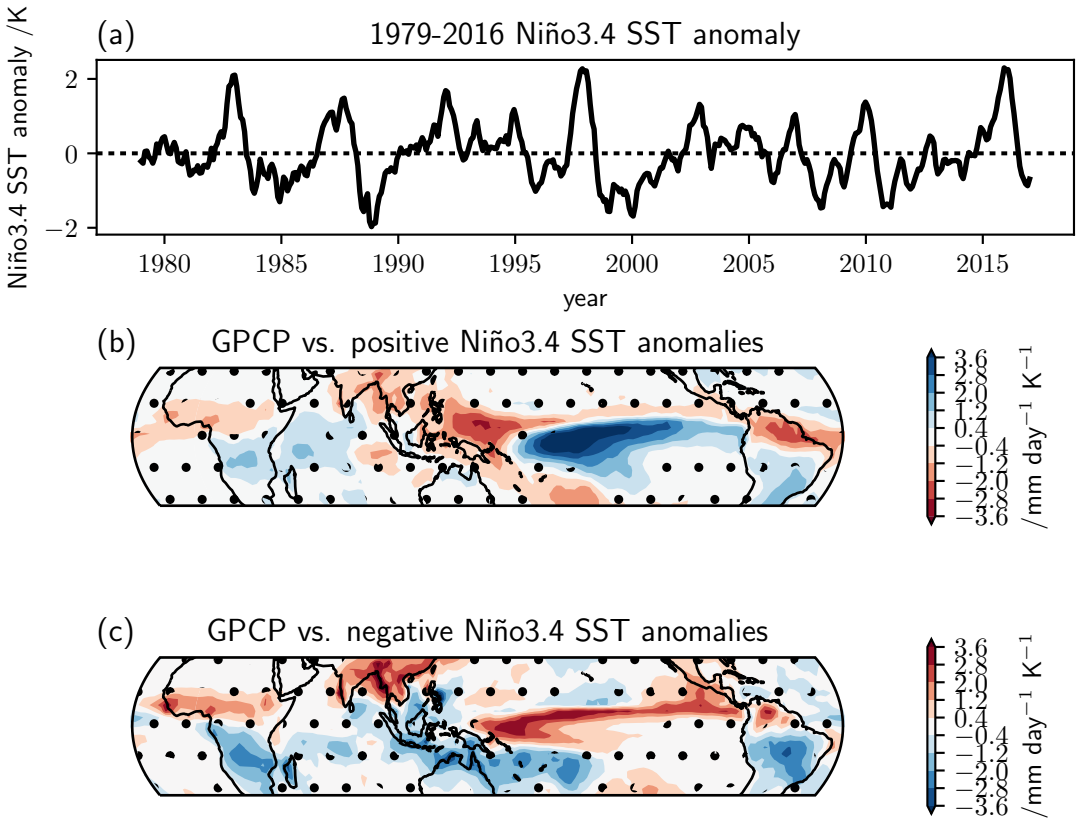

Figure 1.5: ENSO-related precipitation over the satellite era (1979-2016). (a) ERSST (Huang et al., *2015) Niño3.4 SST anomalies, with the dotted horizontal line denoting zero. In (b) and (c), colours show GPCP (Adler* et al., *2003) monthly mean precipitation regressed on positive and negative Niño3.4 SST anomalies, respectively. Stippling covers areas where the regression slope is insignificantly different from zero at the 5% level. Note the opposite colour bars in (b) and (c), with blue colours indicating precipitation increases for increasing Niño3.4 SST anomaly amplitudes.*

1.2.3 Observed Changes over the Satellite Era

Prior to the satellite era, and especially before 1951, regional trends in tropical precipitation are quite uncertain due to sparse observational coverage (Hartmann *et al.*, 2013). As discussed previously, multiple satellite measurements can be combined with rain gauge data to produce more recent spatially complete precipitation estimates. However, systematic errors add an important caveat when computing trends over the recent period. Using SSM/I data, Wentz *et al.* (2007) demonstrate a 1.4 ± 0.5 % decade^{-1} trend in global mean precipitation over 1987-2006. The 95% error bar in this positive trend, ± 0.5 % decade^{-1}, represents errors in the retrieval algorithms, and is estimated by assuming temporally smoothed global precipitation and evaporation balance on monthly timescales. During the 1987-2006 period, global mean surface temperatures increased by 0.19$\pm$0.04 K decade^{-1} (Smith and Reynolds, 2005). Allan and Soden (2007) show that this increase is largely confined to climatological ascent regions, with decreases over descent regions since 1979. Allan *et al.* (2010) updated estimates of these precipitation changes using only the consistent SSM/I period in GPCP (1988-2008). Over ocean, in the highest (wet regimes) and lowest (dry regimes) 30% of precipitation regions, $+1.8$% decade^{-1} and -2.6% decade^{-1} trends were detected, respectively, over this twenty year period. Liu and Allan (2013) extend this analysis to examine different datasets over tropical land, demonstrating that observed trends over wet and dry regimes are sensitive to the data source.

A more robust observed change over the satellite era is the poleward expansion of the Hadley circulation, leading to a broadening and drying of the subtropical descent regions. Theoretically, assuming a dry atmosphere, tropospheric warming and stabilisation, especially in the subtropics, is expected to broaden and deepen the overturning Hadley cells (Held and Hou, 1980). Stratospheric ozone depletion (Hudson *et al.*, 2006) and reanalysis and radiosonde measurements (Seidel and Randel, 2006) indicate an increase in tropopause height, implying Hadley cell deepening. Satellite estimates of mid-latitude and subtropical warming (Fu *et al.*, 2006) and changes in outgoing longwave radiation (OLR), alongside multiple reanalysis products (Hu and Fu, 2007), indicate Hadley cell broadening, especially in the summer and autumn hemispheres. Using a variety of definitions of Hadley cell width, Hu and Fu (2007) detect a significant Hadley cell broadening of 2-4.5° latitude over the period 1979-2006.

Several recent observational studies have found multiple lines of evidence indicating a strengthening of the Walker circulation. After filtering for ENSO variability, Solomon and Newman (2012) found an increasing trend in the Pacific zonal SST gradient since 1900, with relative warming and cooling over the western and eastern equatorial Pacific, respectively. A consistent decrease and increase in sea level pressure over the maritime continent and eastern equatorial Pacific, respectively, is evident since the 1950s

(L'Heureux *et al.*, 2013). This had lead to a strengthening of the low level easterly trades, enhancing upwelling in the eastern Pacific (England *et al.*, 2014). Considering precipitation, Dong and Lu (2013) highlight relative increases over the western Pacific and maritime continent since the 1990s. In addition, Dong and Lu (2013) identify an inverse relationship between the strength of the Pacific (Walker) and Atlantic zonal overturning circulation cells, suggesting the latter has weakened over this recent period. This observed Walker circulation strengthening is contrary to the simulated long term weakening by coupled climate models under a variety of global warming scenarios (as discussed in Section 1.3.1). However, this disparity could be due to the large unforced interdecadal variability in the Pacific climate (Atwood *et al.*, 2016), which could delay the emergence of the forced global warming signal (Dong and Lu, 2013).

1.3 Future Tropical Precipitation

As discussed in the previous section, climate observations are inherently spatially and temporally incomplete. This limits their usefulness in developing our knowledge of climate processes. Numerical models are one approach for improving understanding of tropical precipitation, and the only viable method for simulating future changes under different global warming scenarios. The Intergovernmental Panel on Climate Change (IPCC), under the auspices of the United Nations Environment Programme (UNEP) and the World Meteorological Organisation (WMO), is responsible for organising the international effort to model the Earth's climate and project future changes. Together with the IPCC, the World Climate Research Programme (WCRP) organises the Coupled Model Intercomparison Project (CMIP). Every few years, an assessment report of the state of understanding and future projections of climate change is published. These assessment reports are produced by three working groups, reviewing: 1) the physical science basis, 2) impacts and adaptations and 3) mitigation for climate change.

The contribution of working group 1 to the fifth assessment report (AR5, IPCC (2013)), reviews CMIP phase 5 (CMIP5) state-of-the-art climate model simulations of pre-industrial, present day and a variety of future scenarios from over forty models produced by a variety of international modelling centres (Taylor *et al.*, 2012). This builds upon the equivalent section of the preceding fourth assessment report (AR4, IPCC (2007)), which examined CMIP phase 3 (CMIP3) simulations. Both CMIP3 and CMIP5 climate models generally consist of coupled atmosphere, land surface, ocean and sea ice components. Additional complexity is incorporated with aerosol, carbon cycle, vegetation, atmospheric chemistry and oceanic biogeochemistry components for a subset of Earth system simulations, especially in CMIP5. Between CMIP3 and CMIP5, the vertical and horizontal resolution of the constituent atmosphere and ocean models generally increased, with more realistic stratospheric representation and further improvements to each component. Future scenarios also switched from socio-economic storyline-derived concentration estimates in CMIP3 (IPCC, 2000), to representative concentration pathway (RCP) scenarios in CMIP5. These RCP scenarios are based on late twenty-first century target radiative forcing anomalies, and hence cover a variety of future options for greenhouse gas and aerosol emissions (Moss *et al.*, 2010).

Chapters seven (Boucher *et al.*, 2013), twelve (Collins *et al.*, 2013) and fourteen (Christensen *et al.*, 2013) of AR5 review the processes, projected large scale and regional twenty-first century changes in tropical precipitation, respectively. The following subsections review the future mean state (Section 1.3.1) and variability (Section 1.3.2) changes outlined in AR5, with updates from more recent literature.

1.3.1 Tropical Mean State

A consistent and robust feature amongst CMIP5, CMIP3 and earlier generations of coupled climate models is an increase in global and tropical mean precipitation with global warming. This precipitation scaling is approximately 1-3 % K^{-1} of global mean warming (Allen and Ingram, 2002; Held and Soden, 2006), dependent on the future scenario. Since the global oceans provide an essentially unlimited supply of moisture for evaporation, precipitation is energetically constrained (Mitchell *et al.*, 1987). Increased greenhouse gas (GHG) concentrations reduce the tropospheric net radiative cooling (Held and Soden, 2006), which subsequently mitigates future precipitation changes. Similar to the simulated precipitation change, boundary layer moisture also increases with global warming. Low level specific humidity typically scales at a rate of 7 % K^{-1}, following the saturation value via the Clausius-Clapeyron relation. Following Held and Soden (2006) or Chadwick *et al.* (2013), assume precipitation $P = Mq$, where M is the net mass flux upwards into the free troposphere and q is the mean boundary layer specific humidity. Since q increases faster than P with warming, this implies M must decrease with warming, indicating a weakening of the global mean atmospheric overturning circulation.

Several mechanisms have been identified to explain this mean circulation weakening. Since the Hadley cells dominate the global atmospheric overturning (Section 1.1.2), this discussion focusses on tropical circulation changes. As the tropical lapse rate approximately follows a moist adiabat, surface warming leads to amplified warming in the upper troposphere. Knutson and Manabe (1995) and Lu *et al.* (2008) demonstrated how this leads to tropospheric dry static stability increasing faster than diabatic heating, consequently weakening the overturning circulation. Ma *et al.* (2012) suggested that under tropospheric warming, climatological circulation leads to an upwards advection of warm anomalies in tropical ascent regions, decreasing instability, and downwards advection of cool anomalies in descent regions, increasing stability. This process is termed the mean advection of stratification change (MASC) mechanism. Bony *et al.* (2013) highlighted the direct effect of CO_2 concentration increases in reducing net radiative cooling mainly at upper levels, further stabilising the troposphere and weakening the overturning circulation.

On the zonal mean scale, precipitation generally increases in the climatological ITCZ and decreases over the subtropics. This wet-get-wetter and dry-get-drier response is largely due to the increased low level moisture, advected from the divergent to convergent regions, moderated by the mean circulation weakening (Held and Soden, 2006). In addition, the low precipitation subtropical regions broaden, due to Hadley cell expansion (Lu *et al.*, 2007; Seidel *et al.*, 2008), resulting in a poleward shift of the zonal subtropical jet stream (Lu *et al.*, 2008). Along the boundaries of the ITCZ, precipitation decreases, leading to a narrowing of the zonal precipitation band. This is due to increased dry

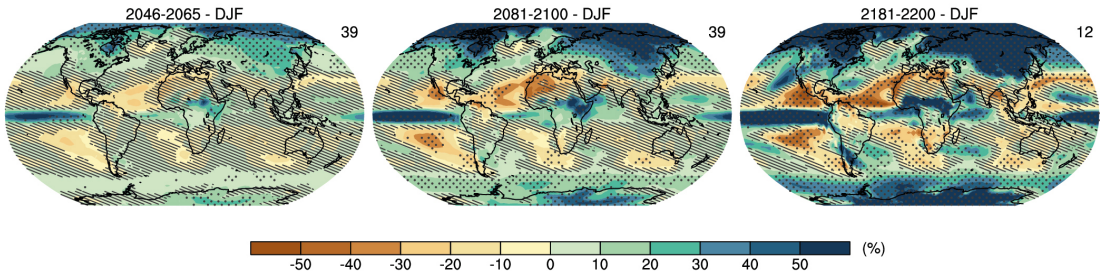

Figure 1.6: Adapted from Figure 12.22 of Collins et al. *(2013). Colours show the simulated fractional change in CMIP5 ensemble and December-February mean precipitation for the RCP8.5 scenario in the mid twenty first (left), late twenty first (middle) and late twenty second centuries (right), relative to 1986-2005 in the historical simulation. The ensemble size is indicated at the top right corner of each panel. Hatching covers areas where the magnitude of these changes is less than one standard deviation of the ensemble mean interannual variability, derived from pre-industrial control simulations. Stippling highlights areas where at least 90% of models agree on the sign of the change, and the ensemble mean magnitude is greater than two standard deviations of interannual variability.*

advection from the subtropics to the margins of convective regions, termed the "upped-ante" mechanism (Neelin *et al.*, 2003; Chou *et al.*, 2009). These large scale responses are relatively consistent and robust across several generations of coupled climate models. In addition, some of these signals are beginning to emerge from interannual variability in observations, as discussed in Section 1.2.3.

At regional scales, between CMIP3 and CMIP5, considerable uncertainty in the tropical precipitation response to global warming persists (Collins *et al.*, 2013; Christensen *et al.*, 2013), and the wet-get-wetter, dry-get-drier paradigm is a poor approximation (Chadwick *et al.*, 2013). Examining ensemble mean changes can also be misleading, due to substantial inter-model variability (Knutti *et al.*, 2010). For example, Figure 1.6 (adapted from Figure 12.22 in Collins *et al.* (2013)) demonstrates low model consensus in CMIP5 for large areas of tropical Africa and the maritime continent. Over tropical oceans a handful of responses are consistent across CMIP5 and supported by well understood mechanisms. Precipitation generally increases over the eastern equatorial Pacific and along the equatorward flank of the ITCZ over the seasonal cycle, and decreases across the subtropical Pacific (Christensen *et al.*, 2013). This pattern is strongly linked to the simulated SST pattern change, with warming of the eastern equatorial Pacific generally greater than the surrounding regions. Deep convection and hence precipitation is favoured over the relatively warmest SSTs, where low level moist static energy is largest (Xie *et al.*, 2010; Chadwick *et al.*, 2013). This mechanism highlights how regional precipitation changes are strongly linked to atmospheric circulation changes. This warmer-get-wetter relationship is common across the CMIP5 ensemble, with differences

in the simulated future SST pattern contributing to approximately one third of differences in the simulated precipitation change (Ma and Xie, 2013).

Over tropical land areas, even greater uncertainty exists in the regional precipitation response to global warming, relative to tropical oceans (Christensen *et al.*, 2013). This is largely due to the surface moisture limitation over land and our incomplete understanding of soil moisture-evaporation-precipitation feedbacks (Joshi *et al.*, 2008). The vegetation response to increased CO_2 and teleconnection shifts due to SST pattern changes are also not yet fully understood. Precipitation over the Sahel, similar to other climatological descent land regions, is major area of CMIP5 model disagreement. In these regions, evaporation increases due to warming are approximately balanced by moisture divergence towards the ITCZ. Consequently, small differences in either of these components modulate the sign of the precipitation change, leading to relatively high uncertainty (Allan, 2012). More recent studies have identified a link between mean state simulated future surface air temperature, relative humidity and precipitation changes over land (Lambert *et al.*, 2017). This novel framework is explored in greater depth in Chapters 2 and 3. An issue central to reducing uncertainty in tropical precipitation projections is the bias in present day simulations (discussed in Chapter 4). An open question is how can we have confidence in projected changes over regions where present day simulations are inaccurate?

To summarise, simulated future mean state tropical precipitation changes are largely a balance of two responses. At large scales, increased low level moisture contributes to a wet-get-wetter and dry-get-drier pattern across the tropics and subtropics, typically termed the thermodynamic response (Held and Soden, 2006). This response is dampened by a tropical mean overturning circulation weakening, linked with increased tropospheric stability. At regional scales, and especially over oceans, shifts in convective regions due to relative warming differences contribute to circulation and hence precipitation changes. Jointly, the effects of circulation weakening and convection shifts can be grouped together as the dynamic precipitation response. The interaction of moisture increases and circulation change is typically termed the nonlinear response. In order to quantify these contributions, and hence understand the mechanisms controlling regional precipitation changes, a number of decomposition frameworks have been presented (for instance: Seager *et al.* (2010), Bony *et al.* (2013) and Chadwick *et al.* (2013)). These are examined in greater detail, and applied to idealised global warming simulations in Chapter 4.

1.3.2 Tropical Variability

As introduced in Section 1.1.4, the dominant mode of interannual tropical and global climate variability is ENSO. At the time of CMIP3, the future response of ENSO to

global warming was quite uncertain (Collins *et al.*, 2010). This was due to the relatively poor representation of the careful balance of feedbacks modulating ENSO in CMIP3 coupled models, contributing to substantial present day biases (Guilyardi *et al.*, 2009). One feature evident in CMIP3 simulations which reliably simulated observed ENSO characteristics was an increase in the frequency of central Pacific El Niño events, relative to canonical, eastern Pacific El Niño events. Yeh *et al.* (2009) suggested this was due to a simulated mean state flattening of the equatorial Pacific thermocline, consistent with observed changes since the mid 1990s.

CMIP5 simulations demonstrate fewer uncertainties surrounding the ENSO response to global warming, relative to CMIP3 (Cai *et al.*, 2015a), due to a general improvement in ENSO representation (Bellenger *et al.*, 2014). Robust projected ENSO changes are largely linked with consistent tropical Pacific mean state changes (Santoso *et al.*, 2013). Thermocline shoaling, flattening and enhanced surface warming in the eastern equatorial Pacific lead to a reduced zonal SST gradient, weakening the Walker circulation via the Bjerknes feedback. This flatter thermocline, reduced SST gradient and weaker easterly trades increases the frequency of extreme El Niño events (Cai *et al.*, 2014). This is because relatively weaker westerly wind anomalies could trigger or amplify incipient El Niño events under future conditions, leading to more extremes. Meanwhile, enhanced warming over the maritime continent, relative to the central Pacific, leads to an equivalent increased frequency of extreme La Niña events (Cai *et al.*, 2015b). The increasingly frequent discharged state following extreme El Niño also contributes to often triggering extreme La Niña in the following year.

In addition to an increasing frequency of extreme ENSO events, several robust changes to ENSO characteristics have been identified in CMIP5 simulations. Equatorward swings of the eastern portion of the SPCZ are often associated with extreme El Niño events, leading to a zonally aligned SPCZ just south of the equator. Borlace *et al.* (2014) identified an increased co-occurrence of these SPCZ shifts with future El Niño events, due to the weakened meridional SST gradient associated with enhanced equatorial warming. Power *et al.* (2013) demonstrated increased precipitation variability over the central and eastern equatorial Pacific, with decreased variability over the western equatorial Pacific. This highlights an amplification of El Niño precipitation anomalies under global warming, which Huang and Xie (2015) suggest is linked with equivalent interannual variability changes in equatorial Pacific SST.

Weakening of the mean state zonal SST gradient in CMIP5 is also linked with enhanced ENSO asymmetry and changes in teleconnections. Huang and Chen (2017) demonstrate an amplified El Niño minus La Niña precipitation anomaly, due to the western-eastern Pacific SST variability asymmetry highlighted by Huang and Xie (2015). Additionally,

the longitude of maximum El Niño SST anomalies is simulated to shift eastward with global warming (Huang, 2016). This leads to an eastward shift in deep convection and hence global teleconnections patterns (Bonfils *et al.*, 2015). Perry *et al.* (2017) demonstrated an increase in the spatial extent of anomalous precipitation and temperature teleconnections over tropical land areas, again linked with this eastward shift in the El Niño SST anomaly.

The relative roles of tropical mean state and variability changes in CMIP5 were recently assessed by Power and Delage (2018). Changes in both components can re-enforce or cancel each other, but regional patterns are relatively uncertain. For policy makers, understanding both changes is particularly important. Chapters 4 and 5 apply a similar framework to Power and Delage (2018) in order to examine ENSO precipitation changes under idealised global warming simulations.

1.4 Research Questions and Thesis Outline

As discussed in this chapter, our knowledge of present day tropical precipitation is imperfect, due to systematic errors in observation systems (Section 1.2.1). Additionally, the regional pattern of future changes under global warming is quite uncertain (Section 1.3). This is due to present day mean state biases (Flato *et al.*, 2013), ENSO representation issues (Bellenger *et al.*, 2014) and model disagreement especially over land (Knutti *et al.*, 2010), even in state-of-the-art CMIP5 coupled models. Consequently, improving our understanding of present day and future tropical precipitation and its variability is the aim of this thesis.

Four research questions are used to guide the anaylsis in this thesis, forming the basis for Chapters 2-5, respectively:

1. Can a consistent mechanism explain both present day tropical precipitation variability and simulated future changes?

2. Can surface condition changes constrain the uncertainty in present day tropical precipitation variability and simulated future changes?

3. What role does atmosphere-ocean coupling play in precipitation mean state and variability changes?

4. Does tropical land warming relative to ocean warming drive the circulation and precipitation response to global warming?

The motivation for questions 1 and 2 is a previous study by Lambert *et al.* (2017), who apply a simple binning method in an attempt to diagnose precipitation changes linked

with surface condition (relative humidity and air temperature) changes. Using CMIP5 coupled global warming simulations, Lambert *et al.* (2017) demonstrate large inter-model diversity in the performance of this method, and hence the strength of this link between the simulated precipitation and surface condition changes. In Chapter 2, the Lambert *et al.* (2017) method is applied to observed present day ENSO precipitation changes and compared to consistent atmosphere-only and coupled ENSO simulations from CMIP5 models. This method performs reasonably well for ENSO observations and simulations, bridging present day variability and future changes with one mechanism. Chapter 2 is heavily based on Todd *et al.* (2018), with only minor additions as noted in the chapter.

Chapter 3 extends the analysis presented in Chapter 2 in order to examine question 2. A more sophisticated, Gaussian process framework is developed to implement the Lambert *et al.* (2017) diagnosis method. This permits a more rigorous assessment of the method assumptions, and a novel technique for quantifying the uncertainty in future precipitation simulations. Tropical precipitation, as a function of surface air temperature and relative humidity tropical quantiles, undergoes minor structural changes under ENSO and global warming conditions. These changes, and hence diagnosis method errors, are largely due to changes in the link between surface and free tropospheric relative humidity, highlighting a regime dependence for the suitability of the Lambert *et al.* (2017) mechanism.

In order to examine question 3, idealised global warming atmosphere-only simulations are compared to more realistic CMIP5 coupled simulations in Chapter 4. The Seager *et al.* (2010) moisture budget decomposition is applied to quantify the dynamic and thermodynamic contributions to precipitation change in response to uniform SST warming, SST pattern change and CO_2 forcing. This builds upon a similar framework presented by Kent *et al.* (2015), He and Soden (2015) and Zappa *et al.* (2018). A novel contribution from this chapter is examining the mechanisms leading to ENSO anomalous precipitation change. This analysis is motivated by the results of Huang and Xie (2015), who examined coupled simulations. By assessing atmosphere-only experiments, uncertainty resulting from atmosphere-only feedbacks is reduced, at the expense of realism. The pattern of anomalous land warming is hypothesised as an important secondary factor affecting tropical circulation and hence precipitation change.

Question 4 and the hypothesis suggested by the results of Chapter 4 motivate a modelling study using HadGEM2-A (discussed further in Section 5.2), presented in Chapter 5. A single model ensemble of idealised global warming simulations is examined to quantify the timescales over which the dynamic and thermodynamic precipitation responses reach equilibrium. This is applied to develop our understanding of causality in the land warming-circulation-precipitation response to global warming. Finally, Chapter 6

presents a synthesis of the conclusions of this thesis, noting the novel and important contributions to climate science. Recommendations for future work are detailed, looking ahead to opportunities from the ongoing CMIP6.

Chapter 2

A Simplified Framework for Diagnosing Tropical Precipitation Shifts

This chapter is predominantly based on the Todd *et al.* (2018) study, with minor structural changes to the introduction (Section 2.1) and discussion (Section 2.7) to link in other chapters. An extended analysis originally omitted from Todd *et al.* (2018) is presented in Section 2.4.3, and the original appendices have been moved into the relevant sections. In addition, map panels on Figures 2.3, 2.5, 2.6, 2.7, 2.8, 2.10, 2.11, and 2.13 have been reproduced using a Mollweide, equal area projection, for consistency throughout this thesis.

2.1 Introduction

The Fifth Assessment Report of the Intergovernmental Panel on Climate Change (IPCC) outlines current projections of tropical precipitation change under anthropogenic global warming (Collins *et al.*, 2013; Christensen *et al.*, 2013). These projections are based on general circulation model (GCM) climate simulations from the Coupled Model Intercomparison Project, phase 5 (CMIP5). Despite modelling improvements since earlier phases of CMIP, persistent inter-model disagreement contributes to uncertainty in patterns of policy-relevant regional and local precipitation change (Knutti and Sedlacek, 2012).

Tropical precipitation change under global warming is typically partitioned into thermodynamic and dynamic contributions (Vecchi and Soden, 2007; Seager *et al.*, 2010), as discussed in Chapter 1. Thermodynamic changes comprise of Clausius-Clapeyron related increases in low-level moisture at 7% K^{-1} of global mean warming. Dynamic changes are related to changes in atmospheric circulation, for instance: spatial shifts in convection (Chadwick *et al.*, 2013); enhancement and narrowing of the inter-tropical convergence zone (ITCZ) (Lau and Kim, 2015; Byrne and Schneider, 2016), Hadley cell

expansion (Seidel *et al.*, 2008) and a tropical mean circulation weakening largely due to reduced tropospheric radiative cooling (Vecchi and Soden, 2007). Thermodynamic increases, modulated by the mean circulation weakening, lead to a large-scale wet-get-wetter pattern of precipitation change (Held and Soden, 2006). On smaller scales, spatial shifts dominate tropical precipitation changes (Chadwick *et al.*, 2013). These precipitation shifts can be linked with a number of mechanisms, such as sea surface temperature (SST) pattern change (Xie *et al.*, 2010), land-sea temperature contrast changes, plant physiological changes and direct responses to carbon dioxide (Chadwick, 2016). However, a simplified theory for understanding the mechanisms contributing to these shifts, and linking precipitation changes over land and ocean, is currently lacking in the literature.

As introduced in Section 1.1.2, weak rotational effects near the equator mitigate horizontal temperature and density gradients above the boundary layer (Charney, 1963). Sobel *et al.* (2001) assume free tropospheric temperature profiles to be relatively uniform across the tropics, and hence demonstrate how circulation largely depends on surface and boundary layer conditions. This assumption is termed the weak temperature gradient (WTG) approximation, which forms the basis of this and the following chapter. Further theoretical and modelling studies demonstrated the suitability of the WTG approximation for representing idealised Walker (Bretherton and Sobel, 2002) and Gill-Matsuno (Bretherton and Sobel, 2003) type circulations.

Lambert *et al.* (2017) present a simplified method for diagnosing tropical precipitation change following the WTG approximation. Assuming relatively uniform free tropospheric temperature profiles, convective initiation is strongly linked with surface conditions (Sobel *et al.*, 2001). Therefore, local precipitation is assumed to depend only on the local relative humidity (RH) and surface air temperature (SAT), relative to the tropical mean RH and SAT, respectively. Therefore, precipitation shifts can be characterised by surface changes in RH and SAT, relative to their tropical means. A physical justification for this simplification is presented by Xie *et al.* (2010) in the form of an idealised two-layer model of tropical moist stability. Moist static energy (MSE) is largely uniform in the tropical free troposphere, due to weak horizontal temperature gradients and relatively low moisture above the boundary layer. Hence, the difference between MSE at the surface and the free troposphere, which modulates convection and therefore precipitation, is mainly controlled by MSE variations at the surface. SAT or surface RH increases would decrease moist stability, enhancing or triggering convection. Surface RH changes could also affect convective initiation by changing the height of the lifting condensation level. Free tropospheric increases in environmental RH would enhance convection via entrainment into convective plumes (Sobel *et al.*, 2001). Although not explicitly included in the Lambert *et al.* (2017) method, lower tropospheric RH is likely to be spatially and temporally

correlated with surface RH, and so the method may implicitly include information about the humidity of entrained environmental air.

In this chapter, we analyse the performance of the Lambert *et al.* (2017) method at diagnosing observed present day shifts in tropical precipitation associated with the El Niño-Southern Oscillation (ENSO). ENSO is the leading mode of interannual climate variability, with atmosphere-ocean feedbacks linking sea surface temperature (SST) anomalies and precipitation in the tropical Pacific, and teleconnections leading to tropical and extra-tropical weather impacts (McPhaden *et al.*, 2006). ENSO-related precipitation anomalies are evident in both recent observations, reanalyses and a variety of present day CMIP5 climate model simulations (Bellenger *et al.*, 2014). A detailed description of ENSO dynamics is presented in Section 1.1.4. Diagnosing ENSO precipitation shifts for a range of data sources is considered to be a necessary test of the Lambert *et al.* (2017) method.

The first question to guide this analysis is: (i) does the Lambert *et al.* (2017) method adequately diagnose present day ENSO precipitation shifts? A key finding of Lambert *et al.* (2017) is the substantial inter-model variability in the diagnosis method performance for global warming driven precipitation changes in an ensemble of CMIP5 model simulations. This motivates a second question: (ii) what factors influence the performance of the diagnosis method for ENSO and global warming precipitation shifts? The remainder of this chapter is structured as follows. In Section 2.2, we describe the data sources used and in Section 2.3 we explain our implementation of the Lambert *et al.* (2017) method. ENSO representation and diagnosed shifts for observations and climate model simulations is discussed in Sections 2.4 and 2.5. In Section 2.6, we examine relationships between ENSO and global warming diagnosed precipitation changes and finally Section 2.7 presents our conclusions.

2.2 Data

2.2.1 Observations - precipitation

The source for monthly mean precipitation observations is the Global Precipitation Climatology Project (GPCP) version 2.3 dataset (Adler *et al.*, 2003). The GPCP dataset combines both satellite and in situ precipitation gauge measurements, and has spatially complete coverage at $2.5^{\circ} \times 2.5^{\circ}$ resolution. Present day observations between January 1979 and December 2008 are used in this study, since this coincides with the range of the atmosphere-only amip experiment for the CMIP5 ensemble.

Model	Institute	piControl periods		Spatial Correlation		
		El Niño	Neutral	amip El Niño	piControl El Niño	abrupt4xCO2 global warming
ACCESS1-0	CISRO-BOM	7	14	0.63	0.70	0.46
ACCESS1-3	CISRO-BOM	7	18	0.62	0.63	0.71
BNU-ESM	GCESS	12	5	0.78	0.71	0.59
CanESM2[1]	CCCMA	10	9	0.79	0.69	0.61
CCSM4	NCAR	10	7	0.66	0.72	0.30
CNRM-CM5	CNRM-CERFACS	8	12	0.67	0.72	0.47
CSIRO-Mk3-6-0	CSIRO-QCCCE	3	19	0.68	0.67	0.81
FGOALS-s2	LASG-IAP	10	8	0.71	0.66	0.41
GFDL-CM3	NOAA GFDL	7	13	0.70	0.74	0.47
GISS-E2-R	NASA GISS	6	18	0.68	0.61	0.61
HadGEM2-ES[1]	MOHC	7	15	0.62	0.71	0.47
inmcm4	INM	4	20	0.51	0.51	0.38
IPSL-CM5A-LR	ISPL	7	16	0.71	0.75	0.35
IPSL-CM5A-MR	ISPL	7	12	0.71	0.75	0.42
IPSL-CM5B-LR	ISPL	9	11	0.70	0.82	0.48
MIROC5	MIROC	8	10	0.74	0.87	0.65
MRI-CGCM3	MRI	4	17	0.80	0.76	0.66
NorESM1-M	NCC	11	10	0.77	0.77	0.38
MME-mean				0.78	0.82	0.64

Table 2.1: CMIP5 models, piControl ENSO representation and diagnosis performance. The two leftmost columns show the eighteen model names, and corresponding institutes, for the CMIP5 simulations used in this study. The third and fourth columns denote the number of El Niño and (ENSO) neutral July-June periods in the last 30 years of each model's piControl simulation, respectively, classified using the Oceanic Niño Index (as discussed in Section 2.3.1). The three rightmost columns show the diagnosed versus simulated precipitation change spatial correlations for the amip El Niño, piControl El Niño and abrupt4xCO2 global warming cases for each model. [1]*For amip, the CanAM4 and HadGEM2-A configurations were used in place of CanESM2 and HadGEM2-ES, respectively.*

2.2.2 Reanalysis - temperature and relative humidity

For reanalysis data, the European Centre for Medium Range Weather Forecasting Reanalysis (ERA-Interim) (Dee *et al.*, 2011) is used. ERA-Interim is constructed by prescribing observed SST and land surface conditions and assimilating observations into an atmosphere GCM. Monthly mean SAT is available directly. Monthly mean RH cannot be estimated directly from monthly means of temperature and dew point temperature due to the nonlinear relationship between temperature and specific humidity. Therefore, daily RH is estimated using daily reanalysis of surface air temperature and dew point temperature and formula (7.5) presented in ECMWF (2016). The mean of these daily values for each month provides the monthly mean RH. All ERA-Interim data is interpolated onto the GPCP 2.5° grid. In this analysis, we term ERA-Interim SAT and RH and GPCP observed precipitation jointly as ERA-Interim-GPCP.

2.2.3 CMIP5 model simulations

Monthly mean simulated surface air temperature, RH and precipitation from the first ensemble member (r1i1p1) of eighteen CMIP5 models are used, as listed in Table 2.1. For MPI-ESM-LR, MPI-ESM-MR and bcc-csm1-1 where surface RH is unavailable, RH from the lowest pressure level above orography is used as a proxy. For consistency, equivalent air temperature data is used as a proxy. We examine the multi-model ensemble (MME) present day simulations between 1979 and 2008 from the amip experiment, where the observed monthly mean SST conditions are prescribed. Additionally, we use the coupled piControl experiment, where greenhouse gas forcing and aerosol concentrations are fixed at pre-industrial levels, and the temporal evolution of the atmosphere and ocean are simulated. In order to explore idealised global warming changes, we compare piControl with the abrupt4xCO2 simulations, following Lambert *et al.* (2017). The abrupt4xCO2 experiment involves instantaneously quadrupling the concentration of atmospheric carbon dioxide. For each model we limit our analysis to the last thirty years of the long-running piControl and abrupt4xCO2 (years 121–150) simulations, to minimise transient effects during the spin up period. Hereafter, we refer to abrupt4xCO2 minus piControl as global warming, for brevity. All model simulated data are interpolated onto the GPCP 2.5° grid to enable intercomparison. Further details of the amip, piControl and abrupt4xCO2 experiment designs are described by Taylor *et al.* (2012).

2.3 Methods

2.3.1 Constructing El Niño composites

We focus on the tropical region in the latitude band between 30°N and 30°S in this analysis. In each ENSO data source, we examine the twelve month periods between each July and the following June. This period is chosen as it represents the typical El

Niño growth and decay stages and a variety of teleconnections (Ropelewski and Halpert, 1987). Each twelve month period is classified as either El Niño or neutral via the Oceanic Niño Index (ONI) (NOAA, 2015). The ONI is based on spatial mean SST anomalies in the Niño3.4 ($5°$N-$5°$S, $120°$W-$170°$W) region. The amplitude of anomalies in this region are commonly used to represent the magnitude of the oceanic component of an ENSO event (Trenberth and Stepaniak, 2001). The ONI identifies an El Niño event if five consecutive and overlapping three month periods have a Niño3.4 SST anomaly greater than $+0.5$ K, a La Niña event if the SST anomaly is less than -0.5 K, and neutral conditions otherwise. In ERA-Interim-GPCP and the amip MME, eight El Niño and nine neutral events are identified from the prescribed SST conditions. In the piControl MME, there is a broad variety in the frequency of ENSO events, as detailed in Table 2.1. El Niño and neutral SAT, RH and precipitation composites are constructed by calculating the mean of each of the El Niño and neutral periods, respectively.

2.3.2 Implementing the Lambert et al. (2017) method

A detailed description of the precipitation change diagnosis method is presented in Lambert *et al.* (2017). Consider one month in a control scenario, for instance a neutral ENSO or piControl composite. The method proceeds by producing an ordered vector of grid point control RH and partitioning it into n equally sized bins ($n = 10$ is fixed in this study). Subsequently, within each RH bin, the ordered vector of grid point control SAT is partitioned into n equally sized bins, resulting in an $n \times n$ space of RH and SAT values. Figures 2.1(a) and (b) demonstrate the mean RH and SAT, respectively, within each bin for the ERA-Interim July-June composite means. We note that absolute RH increases with RH bin number from 60% to 82%, and this is relatively uniform within each SAT bin. This absolute RH increase with RH bin number is nonlinear, with the steepest gradient in low RH bins. In contrast, absolute SAT increases more linearly with SAT bin number but varies greatly across RH bins. For instance, mean SAT increases from 290 K to 298 K, and 296 K to 300 K, in RH bins 2 and 9, respectively.

Subsequently, the mean control precipitation, P_{ij}, for grid points in RH bin i and SAT bin j is calculated (Figure 2.1(c) provides an example for GPCP precipitation in ERA-Interim RH and SAT bins). Next, for one month in a perturbation scenario, such as an El Niño or abrupt4xCO2 composite, grid point RH and SAT is binned following the same procedure as the control scenario. Each tropical grid point is then a member of RH bins i and i', and SAT bins j and j', in the control and perturbation scenarios, respectively. The diagnosed precipitation change, ΔP, at each grid point is then $\Delta P = sP_{i'j'} - P_{ij}$, where s is the fractional change in tropical mean precipitation. Hence, s largely represents the thermodynamic precipitation change, and spatial shifts in convection are diagnosed through changes in RH or SAT bins. Under global warming on a tropics-wide scale, the thermodynamic precipitation increase is opposed by a mean circulation

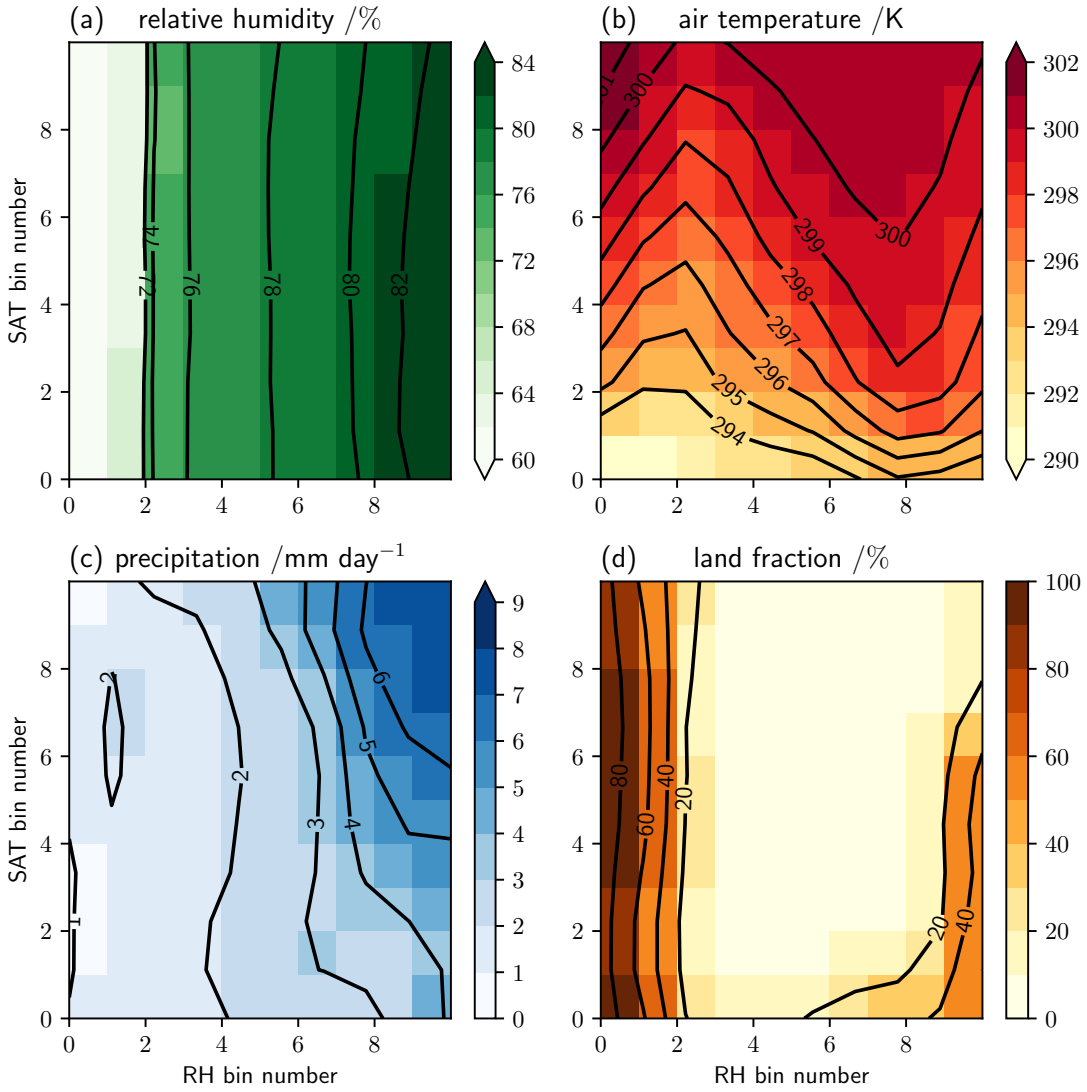

Figure 2.1: Colours show the July-June neutral composite mean ERA-Interim surface (a) relative humidity and (b) air temperature, GPCP precipitation (c) and land fraction (d) in each ERA-Interim RH-SAT bin. Black contour lines show the July-June El Niño composite means.

weakening (Vecchi and Soden, 2007), as discussed in the Introduction. We note that other factors controlling tropical mean precipitation changes, such as poleward energy transport (Held and Soden, 2006), are implicitly incorporated in this framework. The scaling factor s is expected to modulate the magnitude of precipitation changes under global warming (Chadwick *et al.*, 2013), but to be less important during El Niño events, where tropical mean temperature and circulation changes are much smaller compared to spatial variations (Neelin *et al.*, 1998; McPhaden *et al.*, 2006).

In order to remove the seasonal cycle, we calculate the temporal means of the observed or simulated and diagnosed precipitation anomaly composites. For ERA-Interim-GPCP, and the amip and piControl simulations, the temporal means represent July-June, and for the global warming simulations, the temporal means represent January-December. To quantify the performance of the diagnosis method, we calculate the area-weighted, grid point (spatial) correlation between the temporal means of the simulated and diagnosed anomalies. Spatial correlation is a commonly used performance metric in the assessment of climate models (Flato *et al.*, 2013) and forecasts of spatial fields (Jolliffe and Stephenson, 2012).

A primary assumption of the diagnosis method is that the precipitation pattern in RH-SAT space, P_{ij}, is relatively invariant between the control and perturbation scenarios, except for a scaling by the tropical mean precipitation change. In GPCP observations, the tropical mean precipitation decreases by 0.43% from neutral to El Niño composites. Notably, there is relatively large variability in tropical mean precipitation between each neutral or El Niño July-June period, as demonstrated by Figure 2.2. Hence the composite mean El Niño precipitation decrease is not a consistent feature. Using more recent observations over the 2000-2015 period, Stephens *et al.* (2018) found increased precipitation in tropical ascent regimes under El Niño conditions, attributed to positive feedbacks between increased latent and radiative heating, circulation changes and an enhanced hydrological cycle. Figure 2.1(c) displays neutral and El Niño composite mean GPCP precipitation as a function of ERA-Interim RH-SAT bin number. The precipitation patterns appear similar for both composites, with a small decrease in the relatively warmest and most humid bins from neutral to El Niño, consistent with the tropical mean change. Therefore, there is evidence in observations to support the assumption that precipitation as a function of local RH and SAT, relative to the tropical mean, is largely invariant under present day shifts.

For ERA-Interim-GPCP, Figure 2.1(c) demonstrates that precipitation increases more rapidly with RH bin number in comparison to SAT bin number. This highlights the non-linear relationship between precipitation and RH or SAT bin numbers. Under the WTG

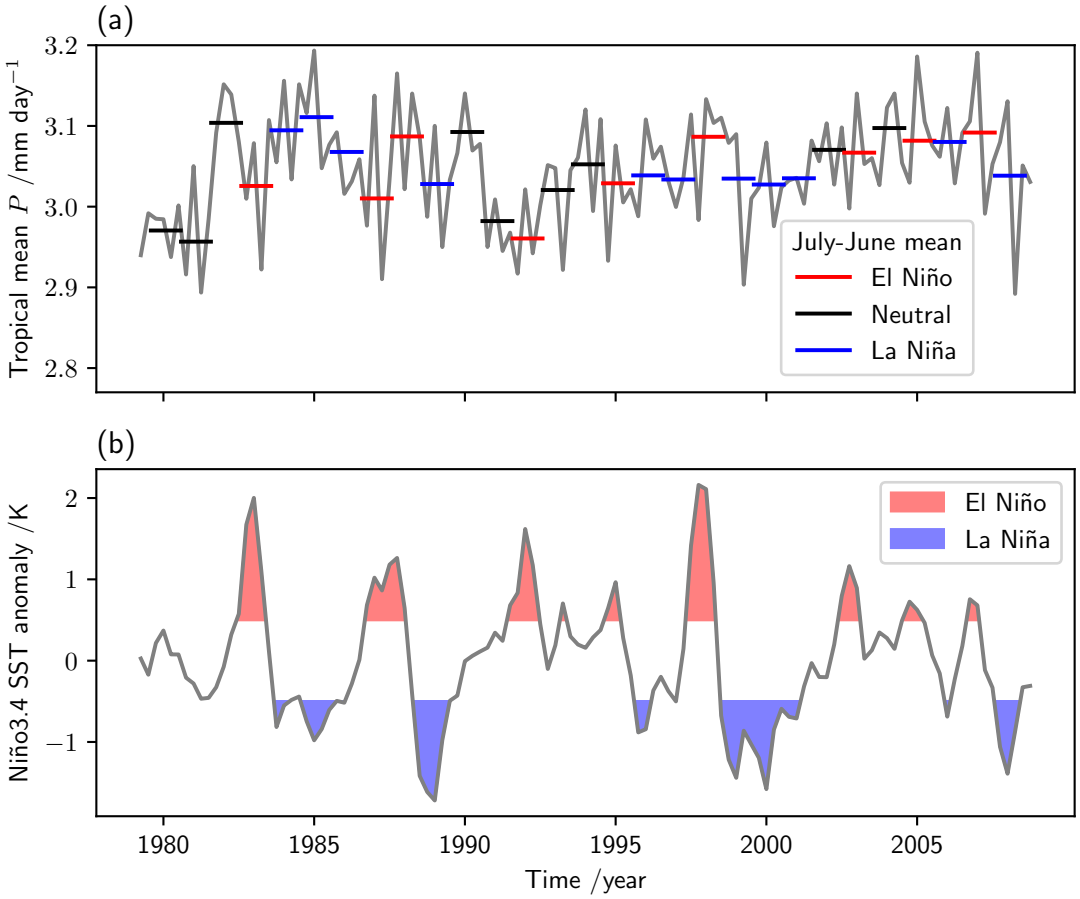

Figure 2.2: Seasonal tropical (30N-30S) mean precipitation in GPCP (a) and Niño3.4 (5N-5S, 120-170W) mean SST anomaly in ERSSTv4 (b) over the 1979-2008 period. Red, black and blue horizontal bars in (a) indicate the July-June tropical mean precipitation for each El Niño, neutral and La Niña period, respectively. In (b), red and blue shading denote El Niño and La Niña conditions, respectively, where the magnitude of the Niño3.4 SST anomaly is greater than 0.5 K.

assumption, SAT bin number changes could alter the difference between the boundary layer and free tropospheric temperature, and therefore affect dry static stability. Similarly, RH bin number changes may affect vertical gradients in equivalent potential temperature, and hence moist static stability. Consequently, changes in either SAT or RH bin numbers can be linked with precipitation changes. As discussed previously, absolute RH varies nonlinearly with the RH bin number, and similarly for SAT. Hence, the relationship between precipitation and RH or SAT bin numbers may mask a simpler relationship between precipitation and absolute RH or SAT.

An implicit assumption of the Lambert *et al.* (2017) method is a spatial and temporal relationship between surface and lower tropospheric RH. This is evident in ERA-Interim, since there is a moderate spatial correlation between surface and 700 hPa El Niño RH anomalies over both land (0.57) and ocean (0.62). Consequently, surface RH bin number changes may reflect free tropospheric RH changes, leading to large changes in column water vapour (CWV) (Bretherton *et al.*, 2004; Holloway and Neelin, 2009). In observations (Schiro *et al.*, 2016) and climate model simulations (Kuo *et al.*, 2017), precipitation sharply increases above a CWV threshold over both land and ocean. Relatively high CWV increases entrainment of environmental moisture, deepening convection and leading to heavier precipitation. This mechanism may explain why precipitation increases more rapidly with RH bin number than with SAT bin number.

Comparing Figure 2.1(c) with Supplementary Figure 1 of Lambert *et al.* (2017), we note that these results for ERA-Interim-GPCP are consistent with the majority of CMIP5 model piControl simulations, with the exception of FGOALS-s2. In FGOALS-s2, the heaviest precipitation occurs in the highest SAT bin of middle ranking RH bins. Figure 2.1(d) demonstrates that the majority of tropical land areas are classified either in the highest RH bin or two lowest RH bins for both the El Niño and neutral ERA-Interim-GPCP composites. The presence of tropical land in the highest RH bin indicates that RH decreases could plausibly lead to a lowering of RH bin number for land grid points. This result is consistent with a number of the CMIP5 model piControl simulations. However, as discussed by Lambert *et al.* (2017), the FGOALS-s2, IPSL-CM5A-LR and IPSL-CM5A-MR piControl experiments do not simulate significant areas of tropical land in the highest RH bin. This highlights an inconsistency between these model simulations and present day conditions in ERA-Interim.

2.4 ENSO in observations and reanalysis

In present day observations, ENSO events are characterised by anomalous warming in the eastern or central equatorial Pacific, leading to both tropical and extra-tropical precipitation shifts (McPhaden *et al.*, 2006). Figures 2.3(a) and (b) demonstrate the ERA-Interim composite mean RH and SAT El Niño anomalies, respectively. The magnitude of RH changes are typically larger over land in comparison to ocean. A decrease in RH is observed over a majority of tropical land (62%) and ocean (53%) areas, including South America, southern Africa, the Sahel, south east Asia, Australia and the subtropical Pacific. Furthermore, an increase in SAT is observed over a high proportion of tropical land (83%) and ocean (75%) areas. GPCP observed precipitation anomalies are displayed in Figure 2.3(c). Precipitation increases are evident over the western Indian Ocean, central and eastern equatorial Pacific and eastern Asia. In addition, there are precipitation decreases over the tropical maritime continent, the western Pacific, South America and the subtropical central Pacific.

There is a moderate spatial correlation between the El Niño precipitation and RH anomalies over ocean (0.51) and land (0.59), as well as an anticorrelation between El Niño RH and SAT anomalies over land (-0.56). The magnitude of spatial correlations between anomalous precipitation and SAT are weaker over both land (-0.43) and ocean (0.41). These spatial correlations are qualitatively consistent with temporal correlations for in situ observation sites (Pfhal and Neidermann, 2011). Over both land and ocean, ENSO circulation and precipitation changes lead to surface RH changes through changes in moisture advection and re-evaporation in the boundary layer. Additionally, RH changes over land can be linked with soil moisture changes, which feedback on evaporation and precipitation, and moisture advection from neighbouring ocean regions (Chadwick *et al.*, 2016; Byrne and O'Gorman, 2016).

2.4.1 Diagnosing ENSO Precipitation Changes

Applying the Lambert *et al.* (2017) method using ERA-Interim El Niño changes in RH and SAT bin numbers and GPCP precipitation, the El Niño precipitation change is diagnosed. In this case, the diagnosed precipitation change, ΔP, is estimated using $\Delta P = sP_{i'j'} - P_{ij}$, where s is the fractional change in tropical mean precipitation, $P_{i'j'}$ is the neutral precipitation in the (i', j') El Niño RH-SAT bin, and P_{ij} is the neutral precipitation in the (i, j) neutral RH-SAT bin. Figure 2.3(d) shows the spatial pattern of the diagnosed precipitation change (cf. Figure 2.3(c) showing the observed precipitation change). The spatial correlation between the observed and diagnosed tropical changes is 0.69 (0.71 over ocean, 0.46 over land), suggesting moderately good performance, especially over ocean grid points. In addition, we note that the sign of the large scale features are correctly diagnosed: increased precipitation in the western Indian Ocean

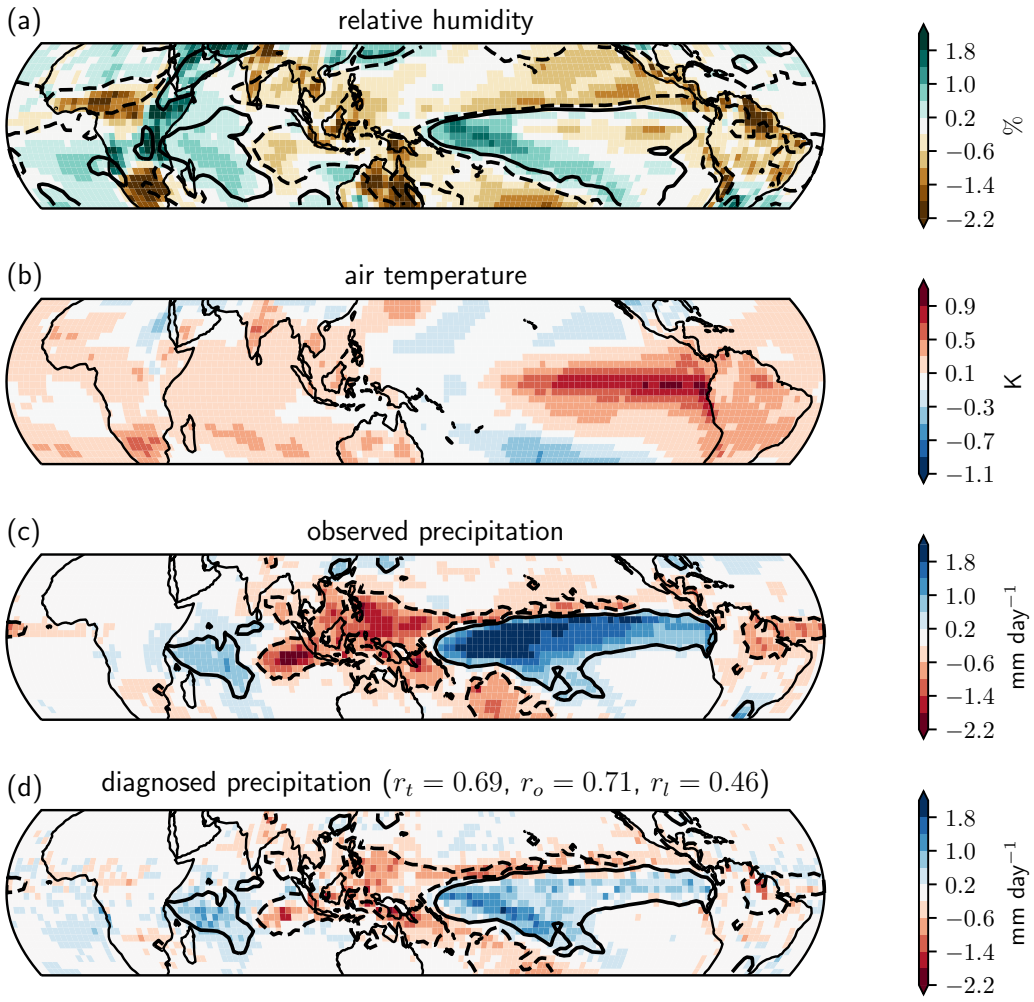

Figure 2.3: Colours show the July-June composite mean (El Niño minus neutral) anomalies: ERA-Interm (a) surface relative humidity and (b) air temperature, GPCP (c) precipitaton and (d) diagnosed precipitation from the Lambert et al. *(2017) method. Black contour lines in (a) indicate the -1% (dashed) and $+1\%$ (solid) 700 hPa relative humidity anomaly, and in (c) and (d) indicate the -0.5 (dashed) and 0.5 (solid) mm day^{-1} GPCP precipitation anomaly. Spatial correlations between the observed and diagnosed precipitation anomalies for tropical, oceanic and land grid points are denoted by r_t, r_o and r_l, respectively.*

and the central and eastern Pacific Ocean, and decreased precipitation over the eastern Indian Ocean, the maritime continent and equatorial South America. However, there is a general under-estimation of the magnitude of the precipitation anomalies. Regressing the diagnosed on the observed precipitation changes, the slope estimate is 0.41, with a 95% confidence interval of [0.40, 0.43]. This is consistent with the weaker magnitudes of diagnosed compared to simulated global warming shifts as presented in Lambert *et al.* (2017). A reason for the weaker diagnosed magnitudes is the aggregation process in the diagnosis method, since bin averaging smooths precipitation as a function of RH and SAT relative to their tropical means.

Differences in diagnosis performance over land and ocean are related to how closely the tropical troposphere satisfies the assumptions of the Lambert *et al.* (2017) method. The ocean surface is essentially flat and homogeneous, in contrast to orographic, vegetation and soil moisture variations over land. These surface attribute differences lead to spatial variability in latent and sensible heating over land, affecting boundary layer dynamics. For example, there is a significantly stronger diurnal cycle of convective intensity over land in comparison to ocean, linked with enhanced boundary layer destabilisation following daytime surface heating (Nesbitt and Zipser, 2003). Differences in aerosol constituents over land and ocean may also affect convection via microphysical processes and their effects on buoyancy (Rosenfeld *et al.*, 2008). Consequently, several competing processes modulate conditional instability and hence deep convection over land and ocean (Schiro *et al.*, 2016). Furthermore, over the Amazon and Congo basins sparse observational coverage may increase uncertainty in the ERA-Interim reanalysis (Cowtan and Way, 2014). This observational uncertainty may contribute to weaker diagnosis performance over these areas.

Boundary layer variations over land may lead to horizontal temperature gradients in the lower troposphere, compromising the WTG approximation. This suggestion is supported by Figure 2.4, showing the seasonal magnitude of the ERA-Interim zonal mean horizontal temperature gradient at 500 hPa, $|\nabla T|$. Between 15°N-30°N, $|\nabla T|$ is larger over land in both neutral and El Niño composites. The difference between land and ocean $|\nabla T|$ is especially large during northern hemisphere autumn and winter, as shown by Figures 2.4(a) and (b). Generally, in all seasons, the magnitude of horizontal temperature gradients, which are largely meridional, increase poleward from the equator. Since there is more land than ocean between 20°N-30°N, there is a larger fraction of land grid points where the WTG approximation is only weakly satisfied and variations in free tropospheric moisture may be relatively large.

As discussed in Section 2.3.2, an implicit assumption of the diagnosis method is a link between surface and lower tropospheric RH. There is evidence of this link in ERA-Interim,

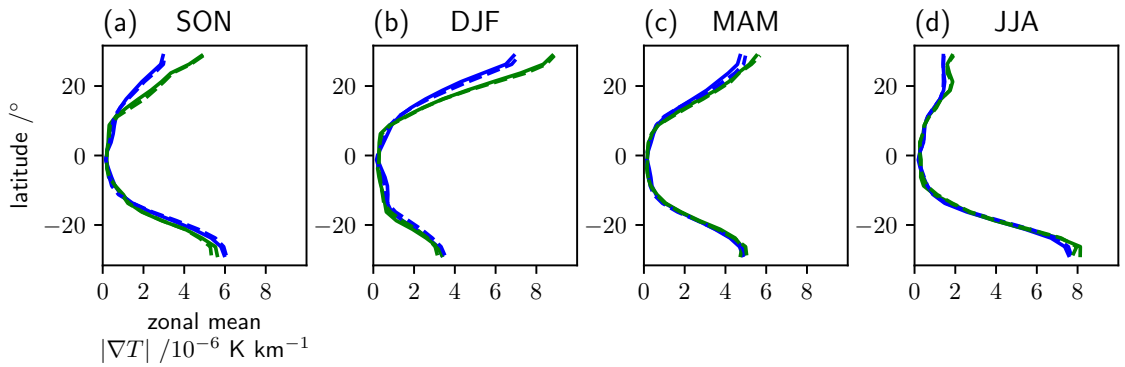

Figure 2.4: Zonal mean magnitude of the ERA-Interim horizontal temperature gradient at 500 hPa, $|\nabla T|$, versus latitude for each season. Blue lines indicate the neutral (solid) and El Niño (dashed) composite means over ocean grid points. Green lines indicate the neutral (solid) and El Niño (dashed) composite means over land grid points.

where 63% and 66% of tropical land and ocean areas, respectively, have a correlation in temporal variability between surface and 700 hPa RH greater than 0.5. Areas with low or anti-correlation are subtropical Africa, Australia and South America. These regions are typically climatological descent regions, with weak vertical mixing and relatively high stratification (Sherwood *et al.*, 2010). Examining Figure 2.3(a), there is evidence of spatial variability in the link between surface and 700 hPa RH El Niño anomalies. There is large-scale sign agreement over much of tropical Africa, the equatorial Indian, western and central Pacific Oceans and Southern America. However, there is weaker sign agreement, or disagreement, over the equatorial eastern Pacific and western Atlantic Oceans. These areas demonstrate relatively weak diagnosis performance in Figure 2.3(d), with the magnitude of the precipitation changes generally underestimated. Differences in the link between surface temperatures and precipitation over land and ocean could also be linked to the diagnosis performance disparity. Over land, descent conditions lead to greater sunlight and the limited soil moisture restricts latent heating, leading to warmer surface temperatures. In contrast, over ocean, warmer temperatures and unlimited moisture lead mainly to latent heating, enhancing ascent, and hence heavy precipitation (Trenberth and Shea, 2005).

In order to assess the relative influence of RH and SAT changes in diagnosis performances, we examine four new configurations of the Lambert *et al.* (2017) method. Firstly, we bin (ENSO) neutral precipitation using neutral RH, and use the El Niño change in RH bin numbers to diagnose the El Niño change in precipitation. This configuration is termed *RH 1-D*, since it uses only one surface variable (RH). A second, corresponding, *SAT 1-D* configuration uses El Niño SAT bin number changes to diagnose the precipitation change. A third configuration involves binning neutral precipitation using both RH and SAT (as described in Section 2.3(2.3.2)), and using the El Niño change in RH bin number, as well as the neutral SAT bin number, to diagnose the El Niño precipitation change.

This configuration is termed *RH partial 2-D* since it considers El Niño changes in only one of two surface variables (RH). The fourth configuration, *SAT partial 2-D*, uses El Niño SAT bin number changes, and neutral precipitation binned on RH and SAT, to diagnose precipitation changes. For completeness, we refer to the original configuration as *2-D* for the remainder of this study.

Diagnosed precipitation changes for the four new configurations are presented in Figure 2.5. Both the RH 1-D and partial 2-D configurations diagnose a precipitation pattern similar to the 2-D configuration, as displayed in Figure 2.3(d). Precipitation increases (> 0.5mm day^{-1}) are diagnosed over the tropical western Indian Ocean and across the central and eastern Pacific Ocean, with decreases (< -0.5mm day^{-1}) diagnosed over the maritime continent and much of the subtropical Pacific Ocean. In contrast, the SAT 1-D and partial 2-D configurations diagnose quite a different precipitation change pattern, with weaker increases (< 0.5mm day^{-1}) confined to the eastern equatorial Pacific, and weak decreases (> -0.5mm day^{-1}, in SAT partial 2-D) over the western tropical Pacific. The SAT 1-D and partial 2-D methods diagnose increases in the eastern equatorial Pacific, due to the relatively strong surface warming associated with El Niño SST changes. The RH 1-D diagnosis method performs considerably better (0.56) than the SAT 1-D method (0.27). In particular, over land grid points, the SAT 1-D diagnosed precipitation changes are weakly anti-correlated (-0.28) with the observed changes, whilst the RH 1-D changes are positively correlated (0.51). Comparable differences in the performance of the RH (0.62) and SAT (0.39) partial 2-configurations are also demonstrated. These results suggest that observed precipitation changes are more strongly linked with RH bin number changes in comparison to SAT bin number changes. In particular, both the RH 1-D and RH partial 2-D configurations over land perform equivalently well (0.51), and better than the 2-D method (0.46), which uses changes in RH and SAT bin numbers. We note that the relative importance of RH changes in comparison to SAT changes is only weakly linked with relative contributions to low level moist static energy (MSE) changes, as discussed in the next subsection.

The sum of the partial 2-D changes, RH partial 2-D plus SAT partial 2-D, represents the diagnosed precipitation change due to independent changes in RH and SAT bin numbers. This sum is strongly correlated (0.96) and linearly related with the 2-D diagnosed change, as shown by Figure 2.6(a). Similarly, the sum of 1-D changes, RH 1-D plus SAT 1-D, is well correlated (0.75) with the 2-D diagnosed changed. This indicates that for the majority of grid points, precipitation changes are linked with either RH or SAT bin number changes. Additionally, given the base state SAT or RH bin in each case, the diagnosis performance improves. The magnitudes of the differences between the 2-D changes and the sum of the partial 2-D changes, as displayed in Figure 2.6(b), are typically small (< 0.5 mm day^{-1}) across the tropics. In a small area of the central

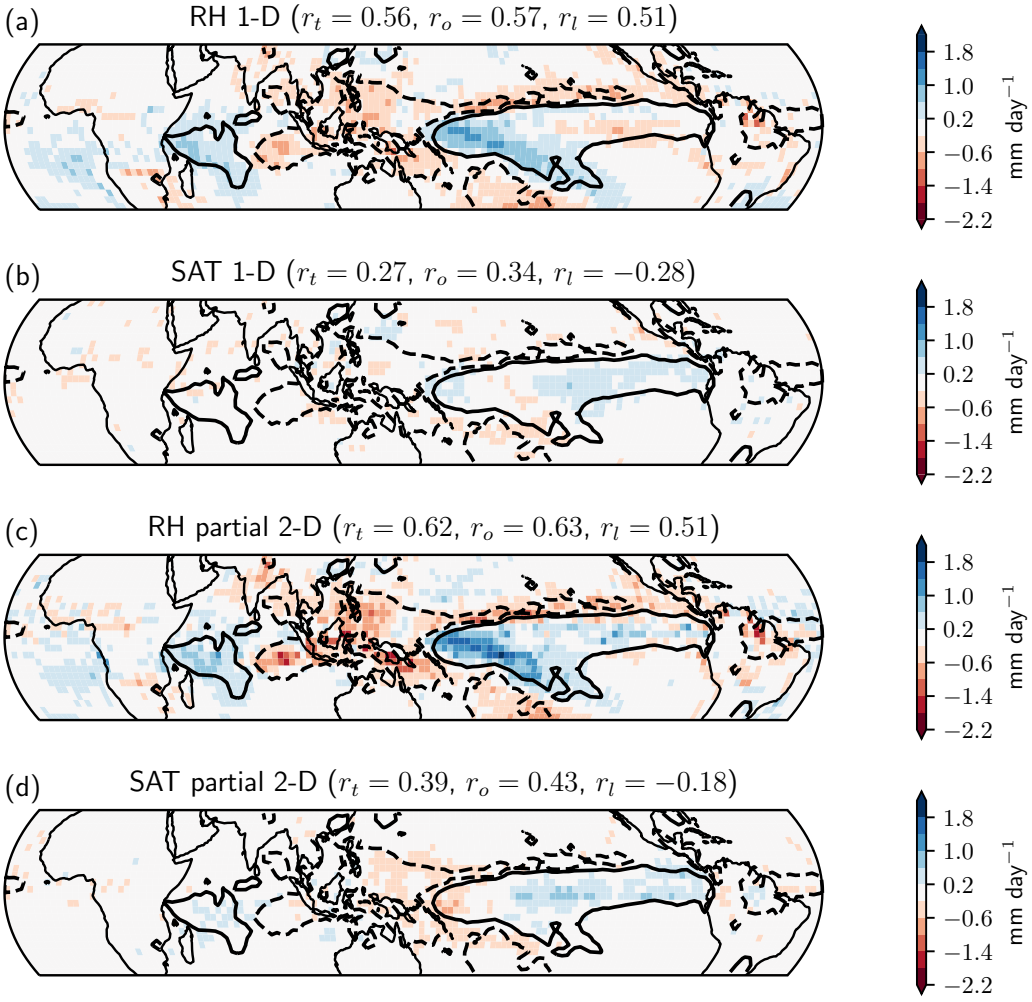

Figure 2.5: Colours show the July-June mean diagnosed precipitation anomaly for four configurations of the Lambert et al. *(2017) method: (a) 1-D using RH changes, (b) 1-D using SAT changes (c) partial 2-D using RH changes and (d) partial 2-D using SAT changes. Black contour lines in (a-d) indicate the -0.5 (dashed) and 0.5 (solid) mm day^{-1} GPCP precipitation anomaly and r_t, r_o and r_l as in Figure 2.3.*

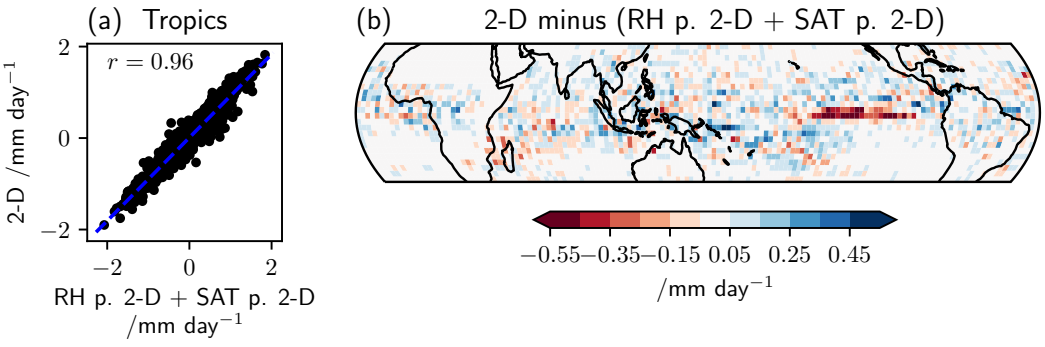

Figure 2.6: (a) ERA-Interim-GPCP July-June mean 2-D diagnosed precipitation changes versus the sum of the RH partial 2-D and SAT partial 2-D diagnosed precipitation changes, with the blue dashed line indicating the regression slope. (b) 2-D diagnosed precipitation changes minus the sum of the RH partial 2-D and SAT partial 2-D diagnosed precipitation changes. Note the smaller range of the colour scale in comparison to Figure 2.5.

equatorial Pacific, both RH and SAT bin numbers increase, leading to large increases in precipitation, which is underestimated by independent changes in RH and SAT bin numbers. This demonstrates how the 2-D and partial 2-D methods capture the non-linear relationship between precipitation, RH and SAT bin changes.

2.4.2 Relative Contributions of RH and SAT to Low-Level MSE

In order to examine the relative effects of RH and SAT changes to precipitation changes, we decompose low level moist static energy (MSE) changes. Low level MSE is defined as $L_v q + c_p T$, where q and T are surface specific humidity and air temperature, respectively, and $L \approx 2.50 \times 10^6$ J kg^{-1} is the latent heat of vaporization of water and $c_p \approx 1005$ J kg^{-1} K^{-1} is the specific heat capacity of air at constant pressure. Specific humidity is a function of relative humidity and temperature. A component of specific humidity change linked the Clausius-Clapeyron relation, Δq_{CC}, is due to a fractional change in saturated vapour pressure with temperature change. The residual component of specific humidity change, $\Delta q_{RH} = \Delta q - \Delta q_{CC}$, is therefore linked with relative humidity changes (Chadwick *et al.*, 2013). Changes in low level MSE can thus be decomposed into three terms: $\Delta MSE = L_v \Delta q_{RH} + L_v \Delta q_{CC} + c_p \Delta T$. Here, $L_v \Delta q_{RH}$ and $L_v \Delta q_{CC} + c_p \Delta T$ represent MSE changes associated with RH and SAT changes, respectively.

ERA-Interim El Niño changes in low level MSE are moderately correlated with GPCP precipitation changes over ocean (0.58), but uncorrelated over land (0.07), as demonstrated by Figure 2.7(a). This suggests that different mechanisms may control precipitation changes over land and ocean. The decomposition of the low level MSE change is shown in Figures 2.7(b-d). The RH related component, $L_v \Delta q_{RH}$ is correlated with pre-

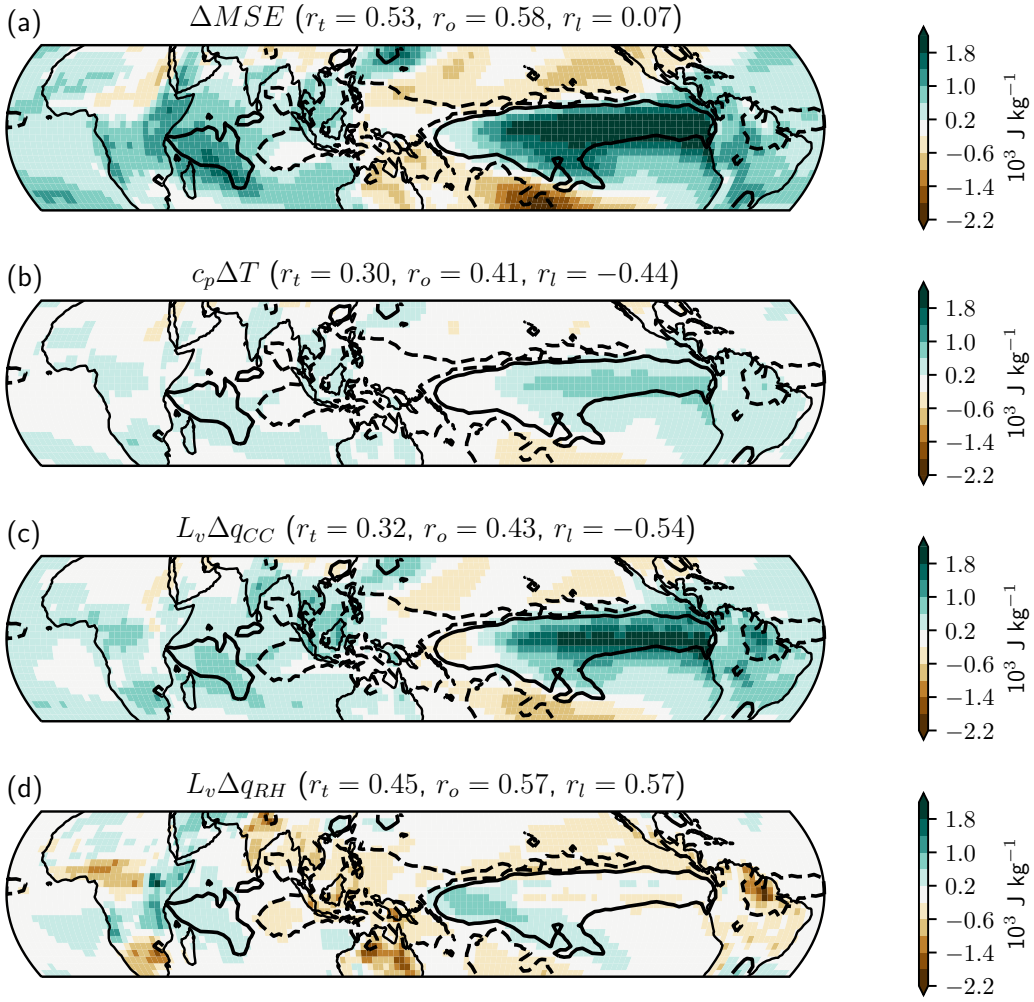

Figure 2.7: Colours show the July-June El Niño minus neutral mean surface MSE change (a) and its' decomposition: (b) MSE changes directly due to temperature changes (c) MSE changes due to the effect of temperature change on specific humidity change and (d) MSE changes due to relative humidity changes. Black contour lines in (a-d) indicate the -0.5 (dashed) and 0.5 (solid) mm day^{-1} GPCP precipitation change and r_t, r_o and r_l indicate the spatial correlation with the precipitation change.

cipitation changes over both land (0.57) and ocean (0.57). In contrast, the SAT related components, $c_p\Delta T$ and $L_v\Delta q_{CC}$, are anti-correlated with precipitation change over land. These results indicate that the dominance of RH changes over SAT changes for diagnosing ENSO precipitation changes is not simply explained by their relative contributions to low level MSE changes. Other mechanisms such as changes in lifting condensation level or entrainment may be important for determining changes in convection.

2.4.3 ENSO Diagnosis Across Multiple Observations

The previous subsection demonstrated successful El Niño precipitation diagnosis performance using ERA-Interim RH and SAT reanalyses and GPCP observations. In this section, this result is explored using alternative data sets to assess robustness. Firstly, ERA-Interim precipitation forecasts are examined. Secondly, HadCRUT (version 4.6, Morice *et al.* (2012)) SAT and HadCRUH (Willett *et al.*, 2008) RH estimates, based on in-situ observations, are used. In HadCRUH, air temperature and dew point temperature measurements from buoys and ships over ocean, and stations on land, are used to infer relative humidity. Similar input measurements are used in the HadCRUT data set. These observational products are available at 5° resolution, and HadCRUH only extends over the period 1973-2003. Consequently, this subsection focuses on diagnosing DJF El Niño minus neutral tropical precipitation changes over the twenty five year, 1979-2003 period with ERA-Interim and GPCP data bilinearly interpolated to the HadCRUT and HadCRUH 5° resolution. Due to their in-situ observational basis, HadCRUT and HadCRUH (jointly referred hereafter as HadCRUX) datasets are spatially incomplete. Hence the Lambert *et al.* (2017) binning method is modified to omit masked grid points in the diagnosis procedure. At 5° resolution there are 864 tropical grid points, 24% of which are land, and 90 grid points (10%) are masked: 60 land and 30 ocean.

El Niño anomalous precipitation diagnoses are presented in Figure 2.8 for the various observational and reanalysis sources. Performance is slightly stronger for the ERA-Interim only case, in comparison to ERA-Interim-GPCP, with spatial correlations of 0.64 and 0.58, respectively. This suggests that for ERA-Interim, the Lambert *et al.* (2017) method is marginally better at diagnosing the reanalysis model's own precipitation, in comparison to an independent observed precipitation product. Examining the ERA-Interim-GPCP, tropics-wide performance is equivalent for the HadCRUX masked and unmasked cases, and slightly reduced over land in the masked case. This may be linked with with relatively high proportion (67%) of masked grid points over land, which is explored further later in this subsection. However, even with approximately 10% of the tropical grid points masked the performance remains largely consistent. In each of these three cases, performance is generally better over ocean in comparison to land areas, consistent with higher resolution and longer period ERA-Interim-GPCP result presented in Section 2.4.

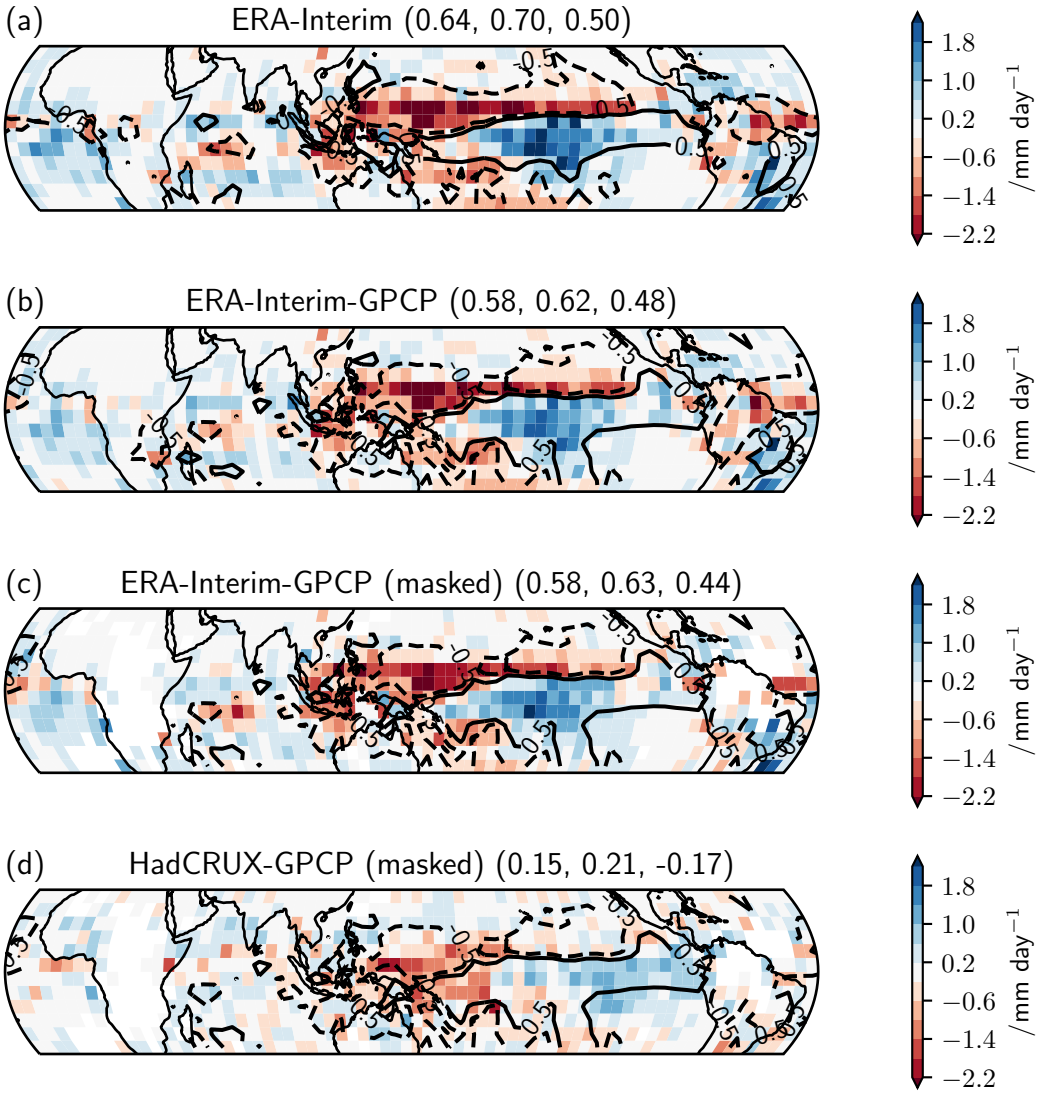

Figure 2.8: Colours show the December-February (1979-2003) diagnosed El Niño minus neutral precipitation anomalies using: (a) ERA-Interim data, (b) ERA-Interim RH and SAT and GPCP precipitation, (c) as in (b) with the HadCRUT4-HadCRUH (HadCRUX) mask applied and (d) HadCRUX RH and SAT and GPCP precipitation. Black lines demonstrate the ± 0.5 mm day^{-1} observed precipitation changes. The 3-tuples indicate the spatial correlation over all tropical, ocean and land grid' points, respectively.

For HadCRUX-GPCP, the spatial correlation is considerably weaker (0.15), relative to the ERA-Interim only and ERA-Interim-GPCP cases. However, the large scale pattern of increases and decreases over the eastern and western equatorial Pacific, respectively, is correctly diagnosed. Notably, there are considerable uncertainties in HadCRUH over tropical oceans (Willett *et al.*, 2008), which may contribute to this relatively weak performance. These results demonstrate how the Lambert *et al.* (2017) method successfully diagnoses at least the large scale pattern of observed El Niño precipitation anomalies for a variety of data sets.

In order to examine the effect of masking on diagnosis performance, a resampling approach using 100 random masks of 90 grid points, an equal size to HadCRUX, with a varying land-to-ocean ratio is applied to the ERA-Interim-GPCP data. As previously, diagnosis performance is measured using the tropics-wide spatial correlation. For the HadCRUX land fraction (67%), the median correlation (0.57) for random masks is quite close to the HadCRUX mask (0.58), which is at the seventy-first percentile. Hence performance under the HadCRUX mask is generally consistent with a random mask covering a similar land fraction. Figure 2.9 demonstrates the distribution of El Niño diagnosis performance versus the land proportion of the 90 masked points at eleven increments between 0 and 1. Performance generally increases with the land proportion of the mask, with median correlations increasing from approximately 0.54 to 0.58 for entirely ocean to entirely land masks. In addition, performance consistency amongst masks, either the interquartile or interdecile range of the correlations, typically decreases with the land proportion. These results indicate generally better and more consistent El Niño performance when a larger proportion of masked grid points are land. This highlights how in this case, ocean grid points are relatively more influential in the Lambert *et al.* (2017) method for diagnosing precipitation changes.

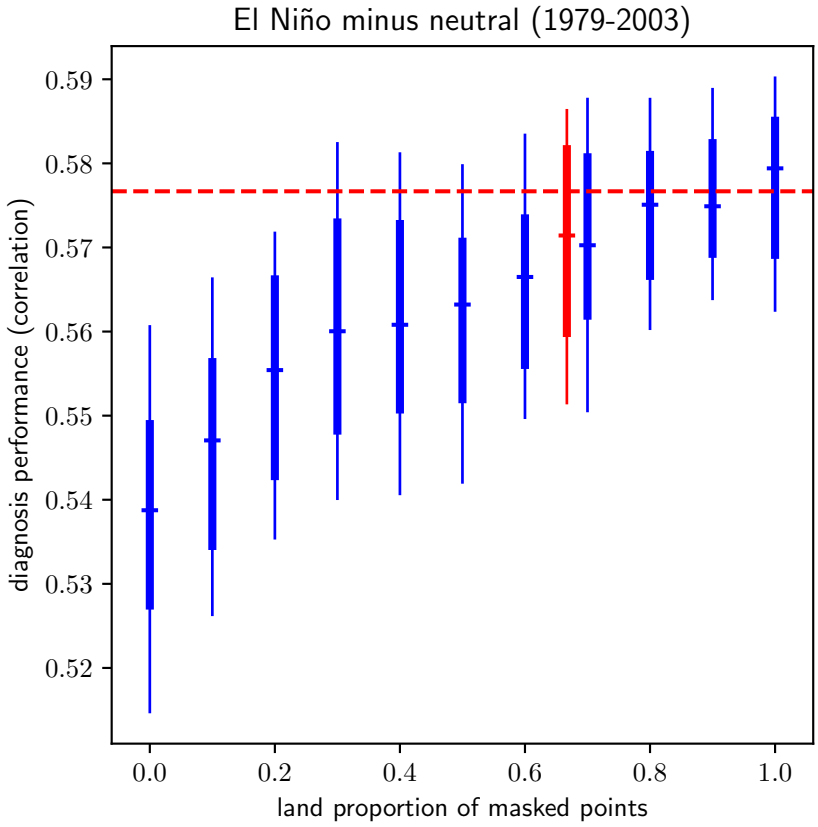

Figure 2.9: Boxplots show the distribution of December-February (1979-2003) El Niño minus neutral diagnosis performance (tropical spatial correlation) versus the land proportion of 90 masked grid points for ERA-Interim-GPCP data. Thin and thick vertical lines represent the interdecile and interquartile ranges, respectively, with horizontal lines denoting the median. The red boxplot is consistent with HadCRUX, with 60 masked grid points over land, and the red dashed horizontal line shows the ERA-Interim-GPCP performance with the HadCRUX mask applied. At each discrete land proportion, distributions are estimated using 100 randomly selected masks.

2.5 ENSO in climate model simulations

In Section 2.4, we demonstrated that the Lambert *et al.* (2017) method performs fairly well at diagnosing ENSO precipitation shifts in present day observations and reanalysis. In this section, we examine whether consistent performance is evident for climate model ENSO simulations. Specifically, we test atmosphere-only (amip) and coupled (piControl) experiments for a multi-model ensemble of eighteen climate models contributing to CMIP5.

The spatial correlation between simulated and diagnosed amip El Niño precipitation anomalies is 0.78 for the MME mean, and ranges between 0.51 and 0.8 for individual models. For piControl El Niño precipitation anomalies, the MME mean spatial correlation is 0.82, and for individual models, correlations range between 0.5 and 0.87. Hence, for both experiments in all models, the method performs relatively well at diagnosing El Niño precipitation shifts. The MME mean patterns of SAT, RH and precipitation are smoother than those of individual models. This is likely to contribute to the high performance of the MME mean, for both experiments, relative to the individual models. For comparison, the spatial correlation between observed and predicted ERA-Interim-GPCP El Niño precipitation anomalies is 0.69. Therefore, the diagnosis performance of ERA-Interim-GPCP lies within both the amip and piControl MME variability.

Consistent with ERA-Interim-GPCP observations, the diagnosis method performs better over ocean than land in each model, and the MME mean, for both the amip and piControl El Niño simulations. The majority of models, in both experiments, simulate a decrease in precipitation over the eastern Amazon basin, which agrees well with GPCP observations. In each case, the diagnosis method typically underestimates the magnitude and spatial extent of this precipitation decrease, diminishing the overall land performance. The observed El Niño precipitation decreases over southern Africa and increases over eastern China and equatorial Africa are only weakly simulated by the MME, especially in the piControl experiment. Hence, the simulated precipitation change signal over the majority of tropical land areas is relatively weak. As discussed in Section 2.4, a number of factors affect boundary layer dynamics, modulating deep convection differently over land and ocean, influencing diagnosis performance. Differences in the suitability of the Lambert *et al.* (2017) method assumptions contributes to the varying disparity in land and ocean diagnosis performance for each model.

Examining Figure 2.10, the amip simulated El Niño precipitation anomalies are similar to the GPCP observed precipitation anomaly (see Figure 2.3(c)). There is moderate inter-model variability in the simulated precipitation anomalies, especially over tropical Africa and South America. This variability is likely to be linked with differences in atmospheric simulation. However, the key observed features and good diagnosis performance

are evident in all models. For example, each model simulates a precipitation increase (> 0.5 mm day^{-1}) in the central and eastern equatorial Pacific and a precipitation decrease (< -0.5 mm day^{-1}) in the western and off-equatorial Pacific. The Lambert *et al.* (2017) method adequately diagnoses this shift in precipitation for each model, given the simulated El Niño changes in RH and SAT.

The coupled model piControl simulated and diagnosed El Niño precipitation anomalies are displayed in Figure 2.11. There is greater inter-model variability in these patterns in comparison to the amip simulations and diagnoses. This increased variability is due to model differences in simulated El Niño SST anomalies and ocean-atmosphere feedbacks (Guilyardi *et al.*, 2009). Despite this variability, the Lambert *et al.* (2017) method performs relatively well at diagnosing El Niño precipitation changes across the tropics in each model. Moreover, the MME range of spatial correlations between simulated and diagnosed precipitation changes is similar for both prescribed SST (atmosphere-only) and coupled (atmosphere-ocean) experiments. This suggests that the Lambert *et al.* (2017) method is flexible and capable of diagnosing shifts linked with a variety of El Niño SST anomalies.

Inter-model variability in the diagnosis performance is linked with how well each model satisfies the method assumptions, as outlined in Section 2.3. There is a significant correlation in inter-model variability between amip and piControl El Niño diagnosis performance across the tropics (0.63) and over tropical ocean grid points (0.64). To support these correlations, Figure 2.12 displays scatter plots of amip versus piControl diagnosis performance. There is evidence of a positive, linear association in performance between the atmosphere-only and the coupled experiments over ocean. This indicates that the performance of the Lambert *et al.* (2017) method over ocean grid points is relatively independent of how the model simulates SST, and so atmospheric processes are the main source of model differences in diagnosis performance over ocean.

Comparing amip and piControl diagnosis performance over land, the correlation in inter-model variability is much weaker (0.16), and Figure 2.12(c) suggests there is little evidence of a linear relationship. Several factors may contribute to this inconsistency in comparison to amip and piControl performance over ocean. Performance over land is uniformly weaker than over ocean in observations, as discussed in Section 2.4. Therefore, the smaller magnitude of the spatial correlations may inhibit any clear performance association between the amip and piControl diagnoses. In addition, there is larger inter-model variability of El Niño teleconnection patterns over land in piControl simulations in comparison to amip simulations, as displayed in Figures 2.10 and 2.11. Consequently, amip and piControl El Niño precipitation shifts may be located over areas where the suitability of the WTG approximation changes.

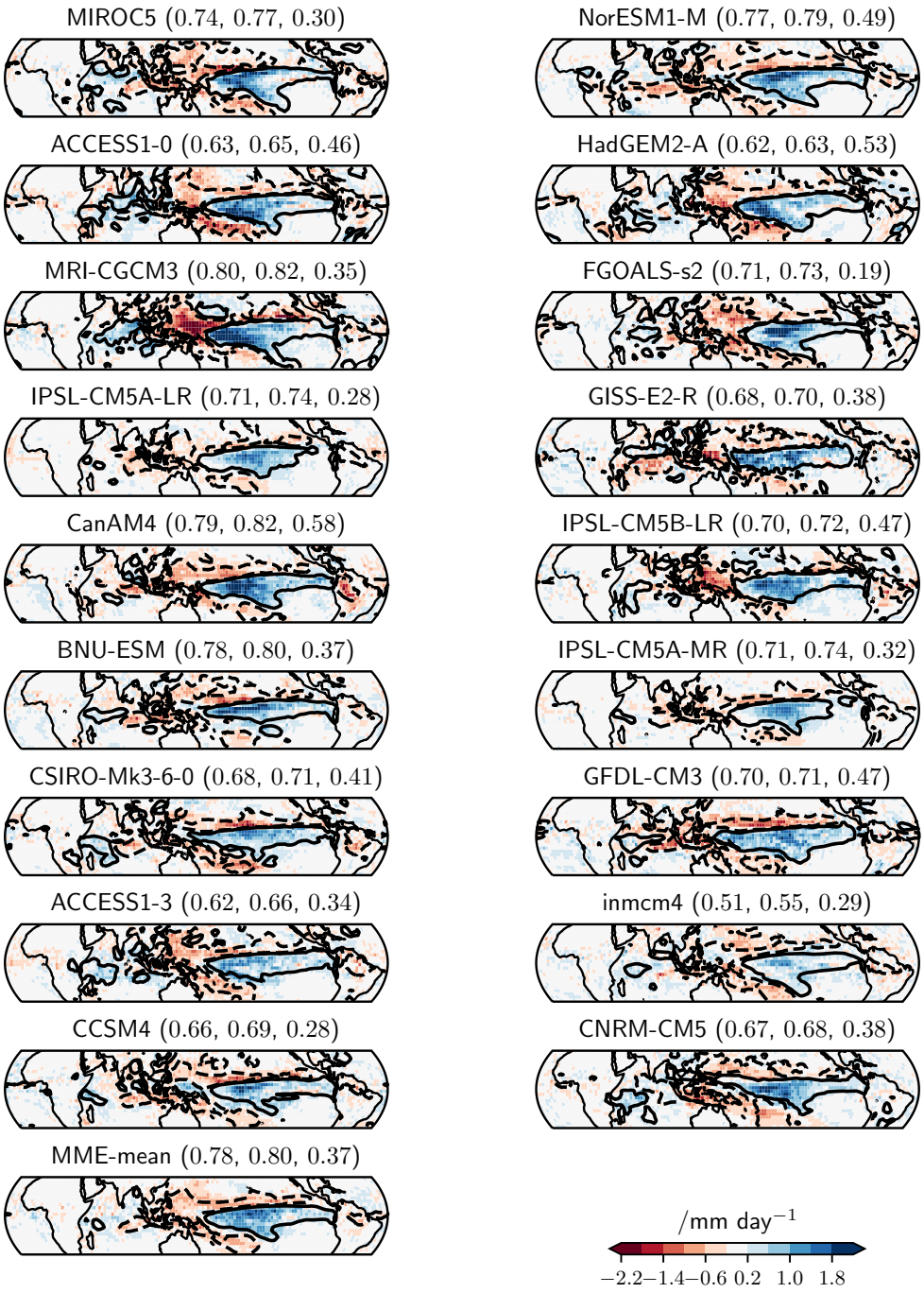

Figure 2.10: Colours show amip El Niño diagnosed precipitation anomalies for eighteen models and the MME mean. Dashed and solid lines indicate the simulated -0.5 mm day^{-1} and 0.5 mm day^{-1} contours, respectively. The 3-tuples, (r_t, r_o, r_l), indicate the spatial correlation over the tropical, ocean and land grid points, respectively.

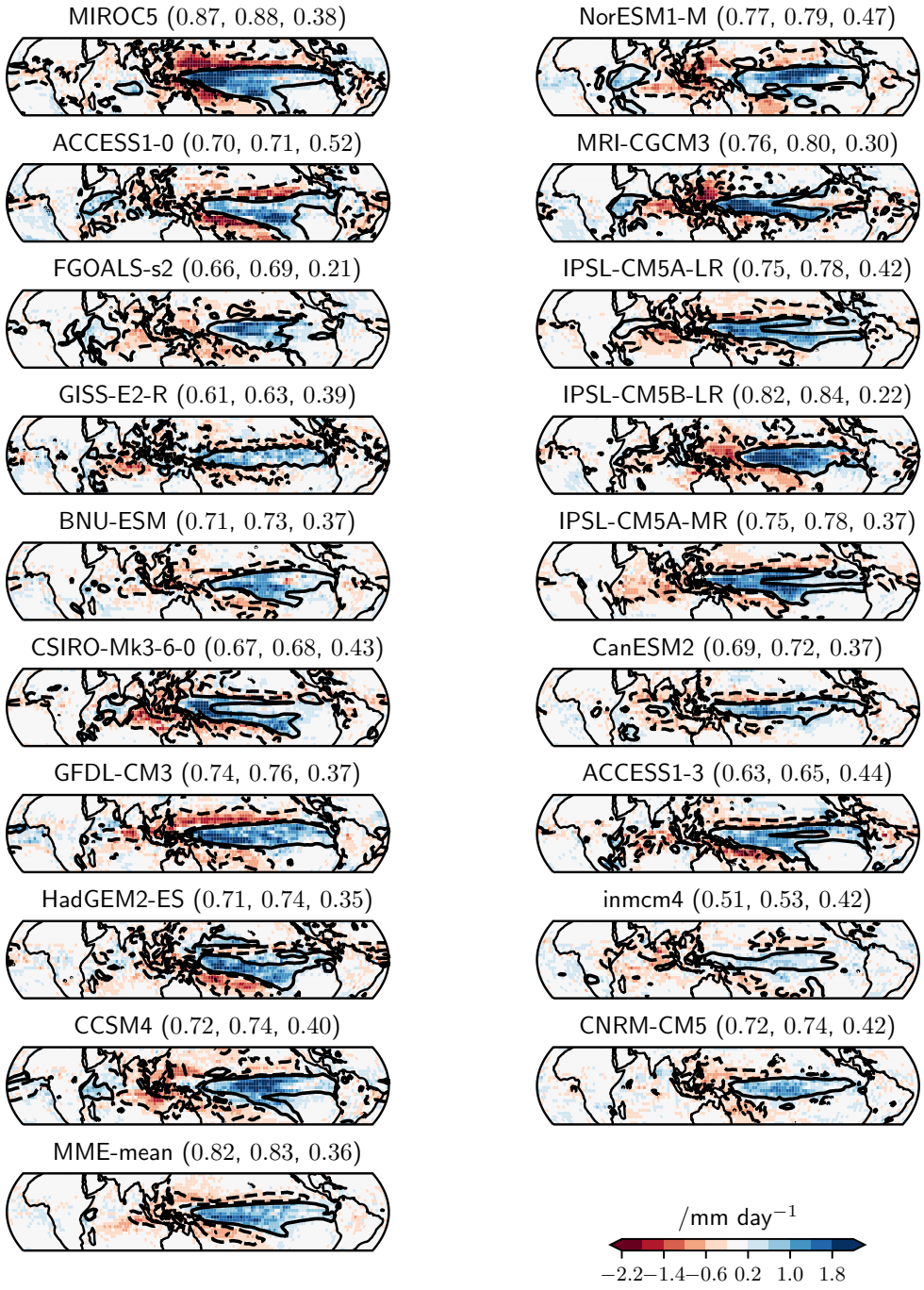

Figure 2.11: Colours show piControl El Niño diagnosed precipitation anomalies for eighteen models and the MME mean. Dashed and solid lines indicate the simulated -0.5 mm day^{-1} and 0.5 mm day^{-1} contours, respectively. The 3-tuples as in Figure 2.10.

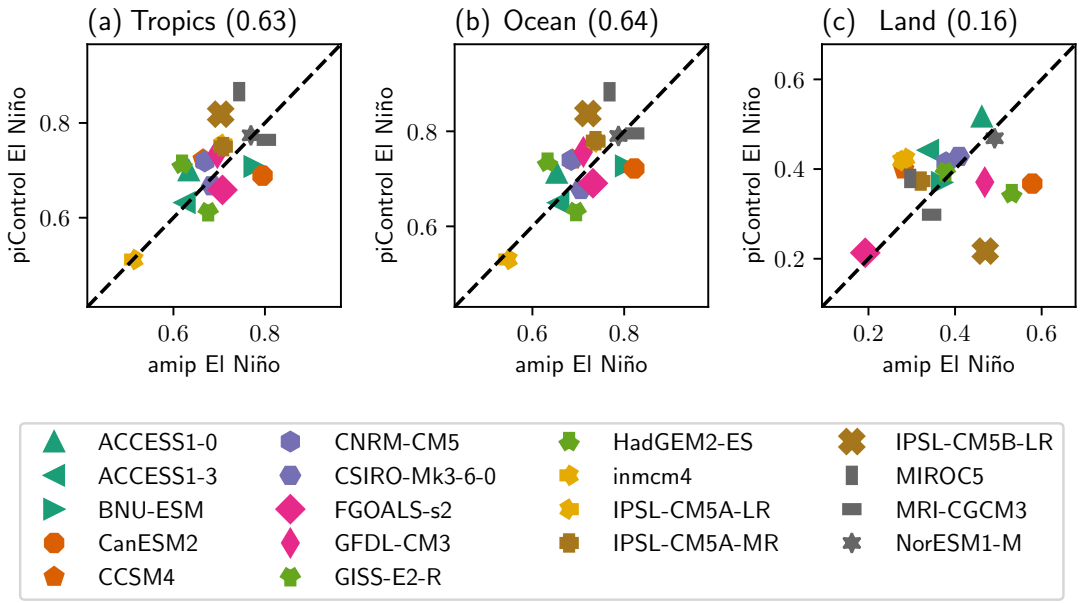

Figure 2.12: Spatial correlations between simulated and diagnosed precipitation anomalies for July-June mean amip El Niño versus piControl El Niño, over the tropics (a), tropical oceans (b) and tropical land (c). The dashed black line indicates the diagonal.

2.6 Relating ENSO and global warming precipitation change diagnoses.

In this section, we extend our analysis of the Lambert *et al.* (2017) method to examine the diagnosis performance for simulated global warming precipitation changes. We note that the tropical mean precipitation changes under global warming (6.0% for the MME mean) are substantially larger than El Niño-related changes (0.1% for the amip MME mean). This highlights the importance of the thermodynamic-circulation weakening scaling for applying the diagnosis method to simulated global warming precipitation changes.

Spatial correlations between simulated and diagnosed global warming precipitation anomalies range between 0.30 and 0.81 for individual models, and the MME mean spatial correlation is 0.64. Hence, there is a broader inter-model range of performance for global warming in comparison to amip and piControl El Niño diagnosed precipitation changes. Figure 2.13 displays the simulated and diagnosed global warming precipitation anomalies for each model in the MME. We note large inter-model variability in the sign of precipitation changes, especially over tropical Africa and the maritime continent. However, the majority of models indicate precipitation increases over the equatorial Pacific, and decreases over tropical South America. Model differences in SST pattern change and convergence zone shifts contribute to this inter-model variability in simulated precipitation change (Xie *et al.*, 2010; Chadwick *et al.*, 2013), as discussed in the Introduction.

Similar to El Niño observations and climate model simulations, diagnosis performance is weaker over land in comparison to ocean for the majority of the MME for global warming simulations. A number of models, such as CNRM-CM5 and CSIRO-Mk3-6-0 simulate small precipitation changes over tropical land. Other models, such as GFDL-CM3, GISS-E2-R, MIROC5 and IPSL-CM5A-LR simulate small-scale, local precipitation changes with large spatial heterogeneity. Subsequently, the diagnosis method fails to detect these weak signals. Regionally, diagnosis performance is quite model-dependent. Examining larger-scale simulated precipitation changes over tropical Africa, the correct sign is diagnosed for ACCESS1-3 and BNU-ESM. However, CCSM4, HadGEM2-ES, CanESM2 and NorESM1-M simulate increases in precipitation which are falsely diagnosed as decreases. Diagnosis performance for the MME is stronger over tropical South America, where the simulated precipitation decreases are correctly diagnosed for ACCESS1-0, ACCESS1-3, CanESM2, CCSM4 and NorESM1-M. Diagnosis performance over land is related to the satisfaction of the method assumptions for each model simulation, as discussed in Section 2.5.

Comparing RH partial 2-D diagnoses for amip El Niño and global warming precipitation changes, there is a significant correlation in inter-model variability in performance

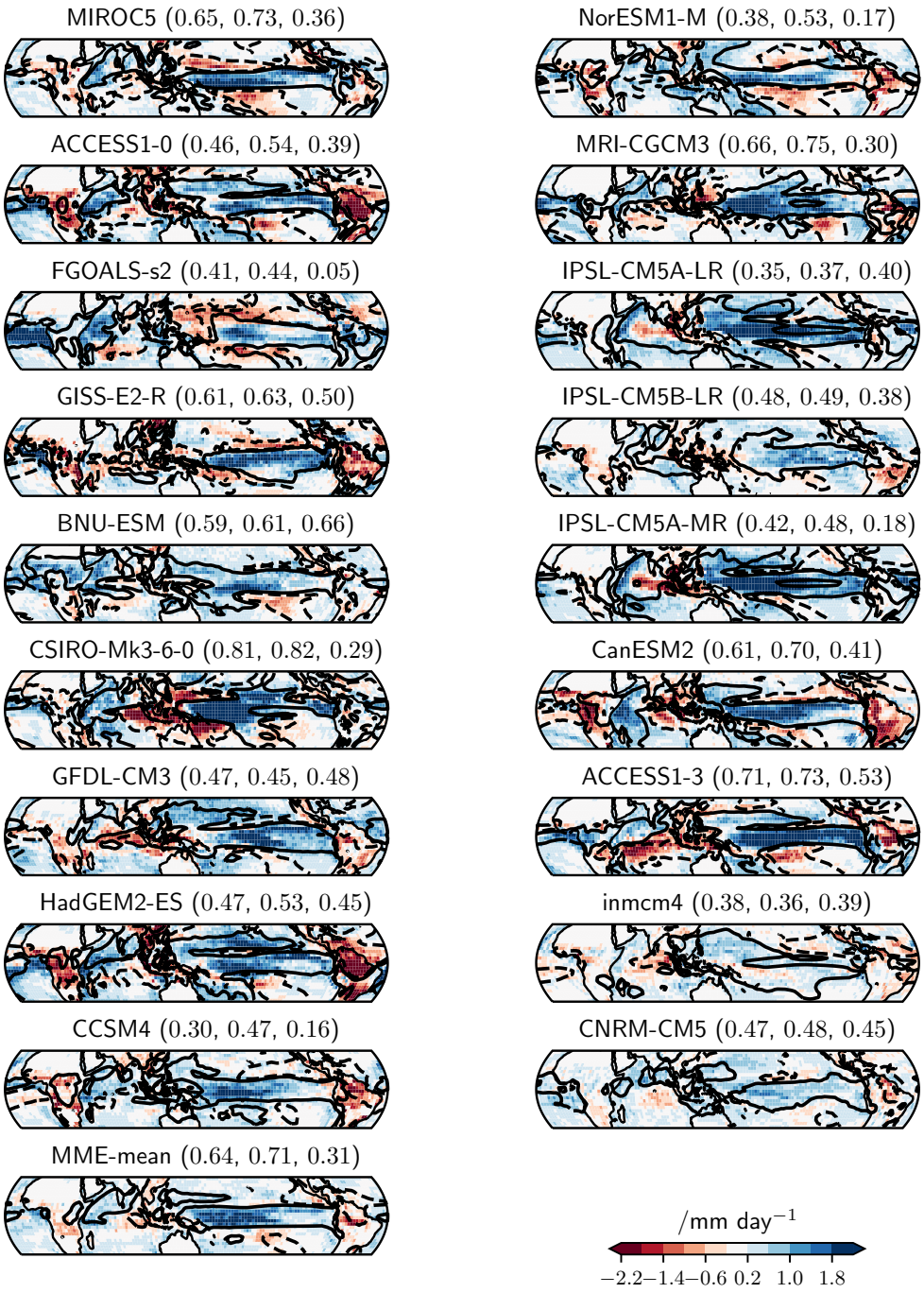

Figure 2.13: Colours show abrupt4xCO2 minus piControl January-December mean diagnosed precipitation anomalies for eighteen models and the MME mean. Dashed and solid lines indicate the simulated -0.5 mm day^{-1} and 0.5 mm day^{-1} contours, respectively. The 3-tuples as in Figure 2.10.

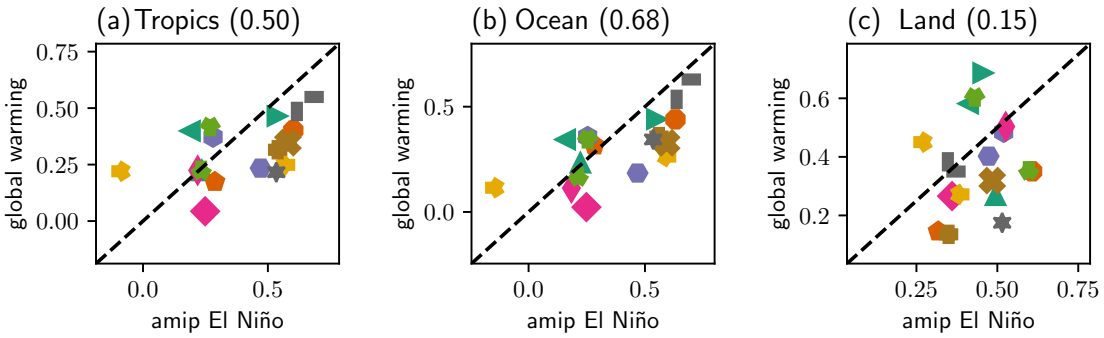

Figure 2.14: RH partial 2-D diagnosis performance (spatial correlation) for amip El Niño versus abrupt4xCO2 minus piControl global warming for the tropics (a), tropical ocean (b) and land (c) grid points. The dashed black line indicates the diagonal, markers as in Figure 2.12.

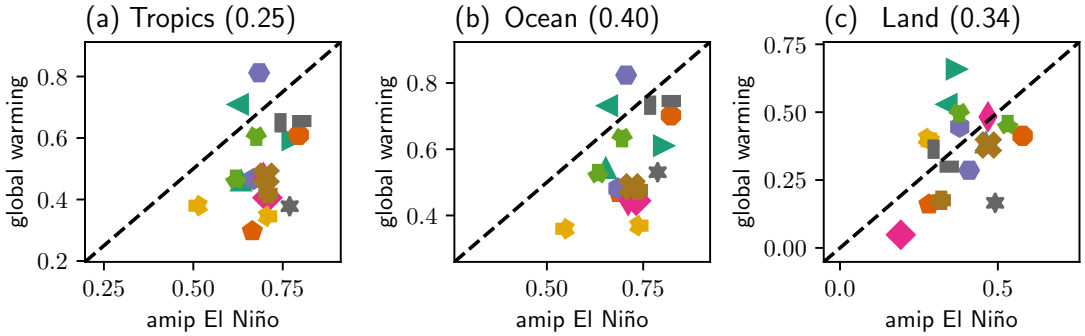

Figure 2.15: 2-D diagnosis performance (spatial correlation) for amip El Niño versus abrupt4xCO2 minus piControl global warming for the tropics (a), tropical ocean (b) and land (c) grid points. The dashed black line indicates the diagonal, markers as in Figure 2.12.

over ocean (0.68). This contributes to a positive correlation in performance across the tropics (0.5), despite a very weak correlation in performance over land (0.15). In addition, Figure 2.14(b) demonstrates evidence of a linear association between amip El Niño and global warming RH partial 2-D performance over ocean. Similarly, the inter-model correlation between piControl El Niño and global warming performance over ocean is larger (0.53) than for performance over land (0.15). Therefore, in models where the RH partial 2-D method performs well over ocean at diagnosing El Niño shifts, typically the method also performs well at diagnosing global warming shifts, and vice versa.

Notably, correlations in inter-model variability between the 2-D diagnosis method performance for amip El Niño and global warming precipitation changes are weaker across the tropics (0.25) and over tropical ocean (0.40). Similar weaker relationships between piControl El Niño performance and global warming performance over the tropics (-0.03) and tropical oceans (0.1) are also present. This suggests that the inclusion of SAT

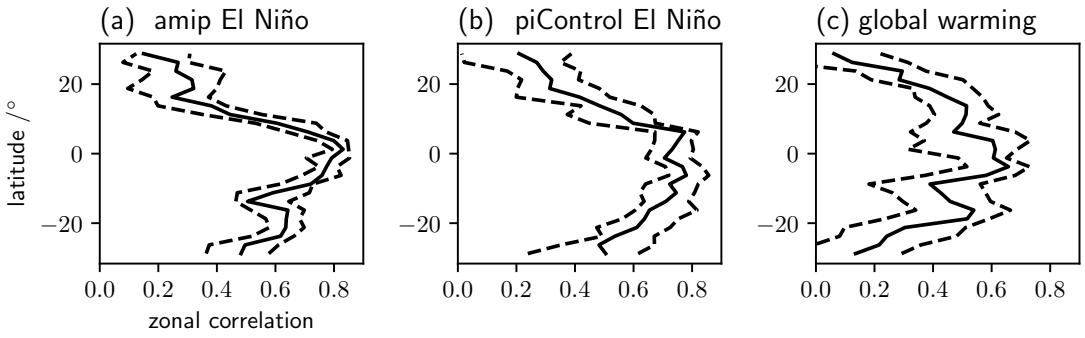

Figure 2.16: Zonal correlation versus latitude for simulated and diagnosed precipitation anomalies for amip El Niño (a), piControl El Niño (b) and abrupt4xCO2 minus piControl global warming (c). Black lines show the median (solid) and upper and lower quartiles (dashed) of the CMIP5 multi-model ensemble variability.

bin number changes affects the method performance differently for El Niño and global warming precipitation changes, mainly over tropical oceans. For amip El Niño diagnoses, including SAT bin number changes in the 2-D configuration improves weaker performance greatly and stronger performance more weakly. For example, the inmcm4 spatial correlations increase from -0.15 to 0.51, whereas the MRI-CGCM3 spatial correlations increase from 0.65 to 0.8. In contrast, using SAT bin number changes in the 2-D configuration improves performance more uniformly for diagnosed global warming precipitation changes. These results indicate that the precipitation-RH bin link over ocean is consistent within models for both El Niño and global warming precipitation changes. The relationship between RH partial 2-D and 2-D performance in the MME is discussed further in the next subsection.

A more consistent result linking El Niño and global warming diagnoses is presented by assessing spatial variations in the performance of the Lambert *et al.* (2017) method. We define the zonal correlation as the grid point correlation between simulated and diagnosed precipitation changes along each 2.5° latitude band. These zonal correlations are calculated for each model in the MME for the amip and piControl El Niño and global warming precipitation changes. The MME median and inter quartile range of these zonal correlations for each case are displayed in Figure 2.16. The inter quartile ranges are relatively narrow, especially for the El Niño cases, suggesting that the MME median is representative of each model. Zonal correlation is largest near the equator for the amip (0.8) and piControl (0.7) El Niño and for the global warming (0.65) diagnosed precipitation changes. In each case, the MME median zonal correlation decreases rapidly poleward. Correspondingly, the magnitude of simulated free tropospheric temperature gradients are weakest near the equator, and increase poleward, in similarity to ERA-Interim as discussed in Section 2.4. Additionally, the link between surface and lower tropospheric RH is weakest in subtropical regions. This suggests that the Lambert *et*

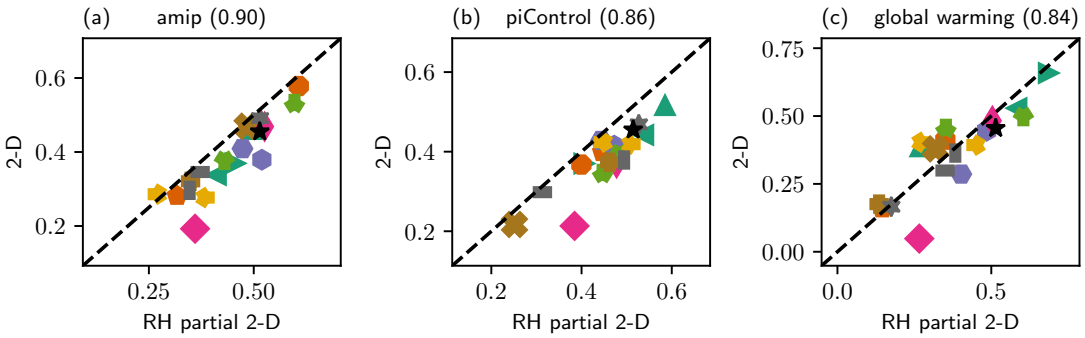

Figure 2.17: RH partial 2-D versus 2-D diagnosis performance (spatial correlation) over land grid points for amip El Niño (a), piControl El Niño (b) and abrupt4xCO2 minus piControl (c). The dashed black line indicates the diagonal, markers as in Figure 2.12 and the black star indicates ERA-Interim-GPCP for reference.

al. (2017) method performs best in the deep tropics, and weaker in subtropical regions, for both El Niño and global warming precipitation changes. Furthermore, this variation in performance is consistently linked in each model with the suitability of the method assumptions.

2.6.1 Comparing RH Partial 2D and 2D Configurations of the Lambert et al. (2017) Method

Inter-model variability demonstrates that RH partial 2-D and 2-D performance over land and ocean is well correlated for amip (0.9, 0.88) and piControl (0.86, 0.79) El Niño precipitation changes, as well as global warming precipitation changes (0.84, 0.55). Additionally, Figure 2.17 indicates that RH partial 2-D and 2-D performance over land is linearly related and approximately equivalent in each model for the three cases. This suggests that including SAT bin number changes in the 2-D diagnosis method does not substantially effect performance over land. However, Figure 2.18 demonstrates that the 2-D configuration consistently outperforms the RH partial 2-D configuration over ocean. This highlights the influence of SAT bin number changes in contributing to El Niño and global warming precipitation changes over ocean. This supports results in the literature suggesting that tropical SST and precipitation pattern changes under global warming are likely to be strongly linked (Xie *et al.*, 2010).

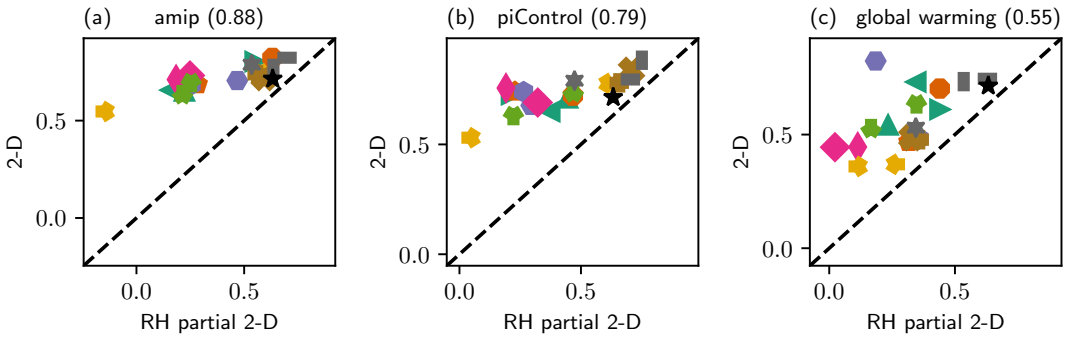

Figure 2.18: RH partial 2-D versus 2-D diagnosis performance (spatial correlation) over ocean grid points for amip El Niño (a), piControl El Niño (b) and abrupt4xCO2 minus piControl (c). The dashed black line indicates the diagonal, markers as in Figure 2.12 and the black star indicates ERA-Interim-GPCP for reference.

2.7 Summary and conclusions

Returning to the Section 2.1, the first question to address in this chapter is "does the Lambert *et al.* (2017) method adequately diagnose present day ENSO precipitation shifts?" The results presented in Sections 2.4 and 2.5 demonstrate moderately good performance of the diagnosis method for observations and reanalysis (ERA-Interim-GPCP), and climate model simulations. Furthermore, in ERA-Interim-GPCP, the method performs successfully as the main assumptions are well justified. Precipitation as a function of local RH and SAT is similar for both El Niño and neutral conditions, supported by Figure 2.1(a). This is perhaps a necessary result to suggest that precipitation as a function of relative RH and SAT may remain invariant under future climate perturbations. In addition, the disparity in performance over tropical land and ocean may be linked with the applicability of the WTG approximation over these domains.

Considering diagnoses of ENSO simulated precipitation shifts in climate models, performance disparity over land and ocean is a consistent feature with the observations and reanalysis. Overall performance across the tropics is quite good in a variety of model simulations in both atmosphere-only and coupled experiments. This demonstrates that the method is flexible since it performs well for a variety of simulated El Niño SST patterns. Moreover, there is evidence of a linear relationship (0.64) in performance over ocean between the two experiments. This suggests that the ability of the method to diagnose precipitation shifts over ocean is relatively independent of how SST conditions are simulated. Therefore, model differences in atmospheric processes are a likely source of method performance variability. Analysing different configurations of the Lambert *et al.* (2017) method, surface RH is more important than SAT for ENSO precipitation diagnosis. In particular, including SAT changes in the method generally does not improve the performance over land.

A second question presented in Section 2.1 is "what factors influence the performance of the diagnosis method for ENSO and global warming precipitation shifts?" Section 2.6 presents some evidence of a linear relationship (correlation of 0.68) in diagnosis performance over ocean between amip ENSO and abrupt4xCO2 minus piControl global warming simulations for the RH partial 2-D method. We suggest that this link in performance is associated with a common RH and precipitation change process over ocean for both simulated ENSO and global warming. An interesting question for future work is why SAT affects diagnosis performance differently for ENSO and global warming precipitation changes. A robust relationship between the spatial performance of the diagnosis method and the suitability of the WTG approximation is present for both simulated El Niño and global warming precipitation changes, with the method performing better in the equatorial regions in both cases. Furthermore, method performance weakens as horizontal temperature gradients increase polewards of the deep tropics for both ENSO and global warming.

Linking to Lambert *et al.* (2017), an important finding of this work is that areas of relatively high RH are observed over land in the present day. Therefore, simulated decreases in RH under global warming could plausibly lead to reduced precipitation via the diagnosis method presented here. In addition, some CMIP5 model piControl simulations have a large negative RH bias over land and hence are inconsistent with present day observations. These models simulate an increase in tropical precipitation over some tropical land areas under global warming, which may be unrealistic due to this RH bias.

A few caveats and important areas of future work are associated with this study. There are large differences in the magnitude of observed ENSO and simulated global warming RH and SAT changes. Performance of the diagnosis method over land for observed El Niño shifts is quite weak (0.46), and there is broad inter-model variability for both amip (0.19 to 0.58) and piControl (0.21 to 0.52) simulations. It is also important to note that the majority of large, observed ENSO precipitation changes are over ocean, so the ENSO signal is relatively weaker over tropical land. Additionally, various conflicting factors may contribute to this poor performance over land, as discussed in Section 2.4. Further work is required to quantify the relative contributions from each factor, to build a more complete theory to explain tropical precipitation changes. In addition, another extension would be to implement the Lambert *et al.* (2017) method in an appropriate statistical modelling framework, in order to calculate uncertainty estimates for the diagnosed precipitation shifts. This is explored in Chapter 3, and permits a more robust assessment of the diagnosis method performance.

The Lambert *et al.* (2017) diagnosis method postulates that precipitation changes can be characterised by relative changes in SAT and RH. From the results presented in this study, we suggest that the performance of this diagnosis method is related to the satisfaction of three main assumptions: (1) tropical precipitation as a function of SAT and RH bin number is structurally similar under climate perturbations; (2) free tropospheric horizontal temperature gradients are small, so relative surface conditions influence convection; (3) surface and lower tropospheric RH changes are linked. This study and the Lambert *et al.* (2017) method improve our understanding of the problems surrounding prediction of future precipitation shifts. Markedly different mechanisms contribute to simulated precipitation change for ENSO and global warming. However, a consistent feature across observations, reanalysis, atmosphere-only and coupled climate model simulations is that the heaviest tropical precipitation is typically anchored above the relatively warmest and most humid locations. This chapter illustrates how under climate perturbations such as ENSO or global warming, shifts in tropical precipitation can be largely determined by changes in surface relative humidity and air temperature.

Chapter 3

An Improved Framework for Diagnosing Tropical Precipitation Shifts

In Chapter 2, a simplified method for linking tropical precipitation shifts with surface relative humidity and air temperature changes was presented. A more sophisticated, statistical framework, is explored in this chapter.

3.1 Introduction

Two major issues are associated with the Lambert *et al.* (2017) diagnosis method, when applied to ENSO and global warming precipitation changes, as discussed in Chapter 2. Firstly, the diagnosed anomaly magnitudes are typically too weak relative to the observed or simulated anomalies. This issue is linked with the aggregation process in the binning procedure, which smooths the largest and smallest precipitation values within each bin, therefore reducing the diagnosed anomaly magnitudes relative to observations. Secondly, there is consistent disparity in the performance of the diagnosis method over tropical land and ocean areas, with land performing worse than ocean, for both observed and simulated precipitation changes. Additionally, diagnosed precipitation changes are point estimates within the Lambert *et al.* (2017) framework. Without an estimate of uncertainty of these diagnosed changes, our inference is inherently limited.

In this chapter, a novel methodology is developed where precipitation observations and simulations are considered as random variables. A well-resolved function of precipitation in terms of RH and SAT relative to their tropical means is estimated. A Bayesian approach is taken to quantify the uncertainty in diagnosed precipitation changes given RH and SAT changes. This framework tests the association between precipitation and surface meteorological regime changes, providing a useful method for understanding the drivers of precipitation changes (Allan, 2012; Lambert *et al.*, 2017). The remainder

of this chapter is as follows. Section 3.2 describes the data used in this analysis and Section 3.3 presents the novel methodology. Results, discussion and conclusions are presented in Sections 3.4 and 3.5.

3.2 Data

We focus on the tropical region within the latitude band between 30°N and 30°S for this analysis. Consistent with Chapter 2, monthly mean ERA-Interim (Dee *et al.*, 2011) surface air temperature and relative humidity reanalyses and GPCP (Adler *et al.*, 2003) precipitation data are used to represent present day observations. However, in this chapter, we now examine the longer 1979-2016 period in order to increase the sample size to 37 years and to include observations of the recent 2015-2016 extreme El Niño event (Hu and Fedorov, 2017). Twelve El Niño (1982-83, 1986-87, 1987-88, 1991-92, 1994-95, 1997-98, 2002-03, 2004-05, 2006-07, 2009-10, 2014-15, 2015-16) and ten La Niña (1984-85, 1988-89, 1995-96, 1998-99, 1999-2000, 2000-01, 2007-08, 2008-09, 2010-11, 2011-12) two-year events are identified via the Oceanic Niño Index (NOAA, 2015). The remaining 15 two-year periods in the 1979-2016 period are subsequently classified as (ENSO) neutral events.

Simulated monthly mean surface relative humidity, air temperature and precipitation from the first ensemble member (r1i1p1) of 27 models contributing to CMIP5 archive (Taylor *et al.*, 2012) are used, as presented in Table 3.1. For models where surface relative humidity is unavailable, data from the pressure level nearest the surface is selected as a proxy (indicated in Table 3.1), as in Chapter 2. Two coupled atmosphere-ocean experiments are examined; historical and representative concentration pathway (RCP) 8.5, for the late twentieth (1980-1999) and twenty-first century (2080-2099), respectively. In the historical experiment, nineteenth and twentieth century observations of greenhouse gases, aerosols and land use changes are prescribed. RCP8.5 is a future scenario, where greenhouse gas emission increases, aerosol and land use changes lead to a CO_2 concentration of 1370 ppm by 2100 and a target radiative forcing of $+8.5$ Wm^{-2} (Moss *et al.*, 2010). For reference, global mean CO_2 concentrations in 2016 were approximately 400 ppm (NOAA/ESRL, 2019). The RCP8.5 scenario is more realistic than the $4\times CO_2$ global warming experiment used in Chapter 2, and hence provides a more policy relevant test of the diagnosis method. To enable intercomparison, all reanalysis and climate model data is bilinearly interpolated onto the GPCP $2.5°$ grid.

Model	Institute ID	Atmospheric Resolution (latitude $\times$ longitude)
ACCESS1-0	CSIRO-BOM	$1.25° \times 1.875°$
ACCESS1-3	CSIRO-BOM	$1.25° \times 1.875°$
BNU-ESM	BNU	$2.767° \times 2.812°$
CCSM4	NCAR	$0.942° \times 1.25°$
CESM1-BGC	NSF-DOE-NCAR	$0.942° \times 1.25°$
CESM1-CAM5	NSF-DOE-NCAR	$0.942° \times 1.25°$
CNRM-CM5	CNRM-CERFACS	$1.389° \times 1.406°$
CSIRO-Mk3-6-0	CSIRO-QCCCE	$1.85° \times 1.875°$
CanESM2	CCCma	$2.767° \times 2.812°$
GFDL-CM3	NOAA GFDL	$2.0° \times 2.5°$
GFDL-ESM2G	NOAA GFDL	$1.517° \times 2.5°$
GFDL-ESM2M	NOAA GFDL	$1.517° \times 2.5°$
GISS-E2-H	NASA-GISS	$2.0° \times 2.5°$
GISS-E2-H-CC	NASA-GISS	$2.0° \times 2.5°$
GISS-E2-R	NASA-GISS	$2.0° \times 2.5°$
GISS-E2-R-CC	NASA-GISS	$2.0° \times 2.5°$
HadGEM2-CC	MOHC	$1.25° \times 1.875°$
HadGEM2-ES	MOHC	$1.25° \times 1.875°$
MIROC-ESM	MIROC	$2.767° \times 2.812°$
MIROC-ESM-CHEM	MIROC	$2.767° \times 2.812°$
MIROC5	MIROC	$1.389° \times 1.406°$
MRI-CGCM3	MRI	$1.112° \times 1.125°$
NorESM1-M	NCC	$1.895° \times 2.5°$
NorESM1-ME	NCC	$1.895° \times 2.5°$
bcc-csm1-1	BCC	$2.767° \times 2.812°$
bcc-csm1-1-m	BCC	$1.112° \times 1.125°$
inmcm4	INM	$1.5° \times 2.0°$

Table 3.1: Model names, institutes and atmospheric resolutions for the CMIP5 ensemble. Abbreviations: Commonwealth Scientific and Industrial Research Organisation (CSIRO), Bureau of Meteorology (BOM), Beijing National University (BNU), National Center for Atmospheric Research (NCAR), National Science Foundation-Department of Energy (NSF-DOE), Centre National de Recherches Meteorologiques-Centre Europeen de Recherches et de Formation Avancee en Calcul Scientifique (CNRM-CERFACS), Queensland Climate Change Centre of Excellence (QCCCE), Canadian Centre for Climate Modelling and Analysis (CCCma), National Oceanic and Atmospheric Administration-Geophysical Fluid Dynamics Laboratory (NOAA-GFDL), National Aeronautics and Space Administration-Goddard Institute for Space Studies (NASA-GISS), Met Office Hadley Centre (MOHC), Model for Interdisciplinary Research on Climate (MIROC), MRI (Meteorological Research Institute), NCC (Norwegian Climate Centre), BCC (Beijing Climate Center), INM (Institute for Numerical Mathematics)

3.3 Methods

In this section, a novel statistical framework, building upon the Lambert *et al.* (2017) method is discussed. Grid point tropical quantiles of relative humidity, q_H, and surface air temperature, q_T, are used to define geographical locations relative to the rest of the tropics. We then estimate precipitation as a function of these tropical quantiles by fitting a log-normal Gaussian process model. Local changes in q_H and q_T under climate perturbations can then be used to diagnose precipitation changes. Note that $_H$ and $_T$ subscripts are used in these definitions to distinguish this notation from the use of q to represent specific humidity as in Chapters 4 and 5. This choice uses the general notation q_X to represent the quantile of X.

3.3.1 Locations in (q_H, q_T)-space

The shape, scale and location of the distributions of tropical grid point surface air temperature (SAT) and relative humidity (RH) are very similar in ERA-Interim for both the 1979-2016 El Niño and neutral composite means. This is demonstrated by the quantile-quantile plots in Figures 3.1(a, b). For each composite, the median SAT and RH is approximately 298 K and 78%, respectively. For both surface variables, the distributions are strongly negatively skewed and clustered closely about the respective medians. For example, the RH interquartile range (IQR) is 5%, whilst the (total) range is 77%. The equivalent SAT IQR and range are 4 K and 40 K, respectively. Generally consistent results are evident when comparing the CMIP5 ensemble mean historical (1980-1999) and RCP8.5 (2080-2099) tropical RH and SAT distribution shapes and scales, and the tropical RH distribution locations (Figures 3.1(c, d)). In this case, for SAT, there is evidence of an approximately $+4$ K tropics-wide warming, highlighted by historical and RCP8.5 medians of 298 K and 302 K, respectively. Comparing ERA-Interim and the CMIP5 ensemble mean, SAT and RH ranges are slightly smaller for the latter, especially for SAT, but the IQR and medians are very similar.

Generally, Figure 3.1 demonstrates that the shape and scale of RH and SAT distributions remains relatively constant under either observed El Niño or simulated global warming conditions. Therefore, El Niño quantiles are approximately equal to neutral quantiles, and similarly for future global warming and present day quantiles. Consequently, local quantile changes represent similar absolute RH or SAT changes in both cases. This motivates the method presented in the next subsection (3.3.2), which applies local quantile changes to diagnose absolute precipitation changes.

Regions in (q_H, q_T)-space can be related to geographical locations by separating tropical

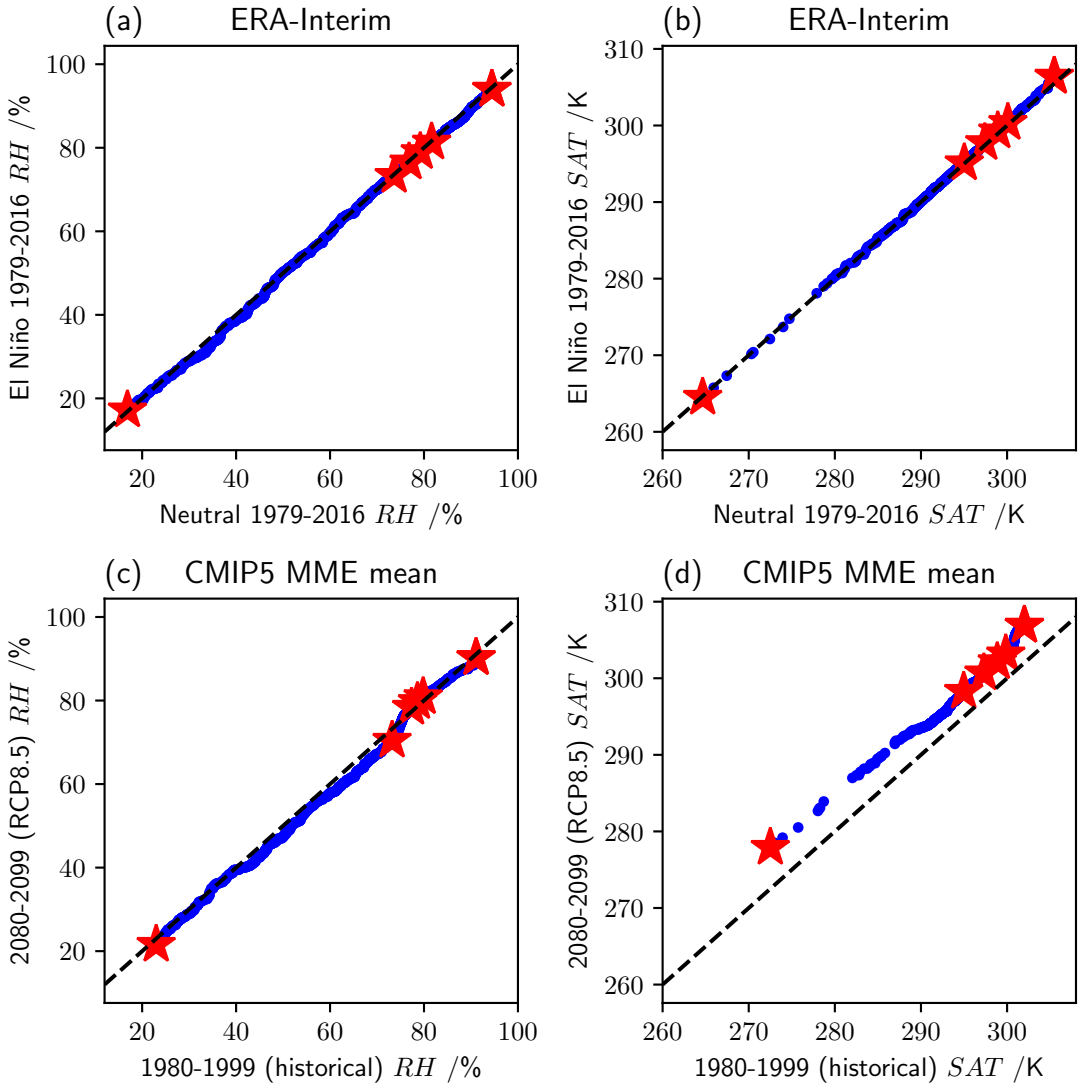

Figure 3.1: Quantile-quantile plots comparing tropical: ERA-Interim 1979-2016 El Niño versus neutral surface relative humidity (a) and air temperature (b) distributions, and corresponding CMIP5 ensemble mean RCP8.5 (2080-2099) versus historical (1980-1999) distributions (c, d). Blue circles indicate each grid point, with red stars denoting the distribution quintiles (0^{th}, 20^{th}, 40^{th}, 60^{th}, 80^{th} and 100^{th} percentiles) and black dashed lines indicating the diagonal.

grid points into clusters of similar q_H and q_T values. A commonly used, general purpose clustering algorithm is K-means (MacQueen, 1967), where N_c initial cluster centres are prescribed and an iterative approach minimises the within cluster variance. To ensure robust results, this clustering algorithm is repeated several times with distant initial cluster centres (Arthur and Vassilvitskii, 2007). Setting $N_c = 6$ is physically motivated, as tropical land and ocean are expected to exhibit three regimes: equatorial, summer and winter. The locations of each cluster in (q_H, q_T)-space are demonstrated in Figures 3.2 and 3.3, for the DJF and June-August (JJA) ERA-Interim climatologies, respectively. In both seasons, the relatively warmest and most humid cluster (6) has the highest mean precipitation (5.4 and 6.7 mm day^{-1} for DJF and JJA, respectively) and consists of mainly deep convective tropical oceanic grid points (3 and 10% land fraction, for DJF and JJA respectively). The adjacent, relatively cooler cluster (5) has lower precipitation, especially in JJA, (5.3 and 3.8 mm day^{-1}) and contains a more even mixture of oceanic and land grid points (43 and 48% land fraction, for DJF and JJA respectively). In both seasons, cluster (5) includes the tropical rainforests of the Amazon and Congo basins, the islands of the maritime continent, as well as parts of the eastern equatorial Pacific and subtropical oceans.

Examining differences between clusters in (q_H, q_T)-space supports the assumption that tropical precipitation may be strongly linked with the surface conditions. Compared to the most humid regions, situated in clusters (5-6), relatively less humid locations, within clusters (1-4), have substantially lower mean precipitation: 1-2.1 mm day^{-1} in DJF and 1.2-3.7 mm day^{-1} in JJA. The warmest and least humid clusters, (4) and (2) in DJF and JJA respectively, largely contain the arid land regions of the summer hemisphere: central Australia in DJF and the Saharan and Arabian deserts in JJA. Conversely, the coolest and least humid cluster, (1) in DJF and JJA, represent these arid land areas in the winter hemisphere. The intermediate cluster (3), containing the tropical median RH and SAT, consists largely of oceanic grid points (12% and 7% land fraction, for DJF and JJA respectively) neighbouring the deep tropical and heavy precipitation regions in cluster (6).

Panel (c) of Figures 3.2 and 3.3 demonstrates the grid point precipitation at each location in (q_H, q_T)-space for DJF and JJA, respectively. In each season, we note that precipitation typically increases with both q_H and q_T. This suggests a relatively smooth curve could interpolate these data, in order to estimate precipitation at new points in (q_H, q_T)-space. However, there are regions in this space where observations are relatively sparse, for instance near $(0.2, 0.8)$ and $(0.6, 0.2)$ in both seasons. In these areas, this data sparsity would lead to only a weak constraint on the shape of the smooth curve. Additionally, outside the convex hull of the observation points the shape of the curve is unconstrained and hence a form of extrapolation would be required. In the following

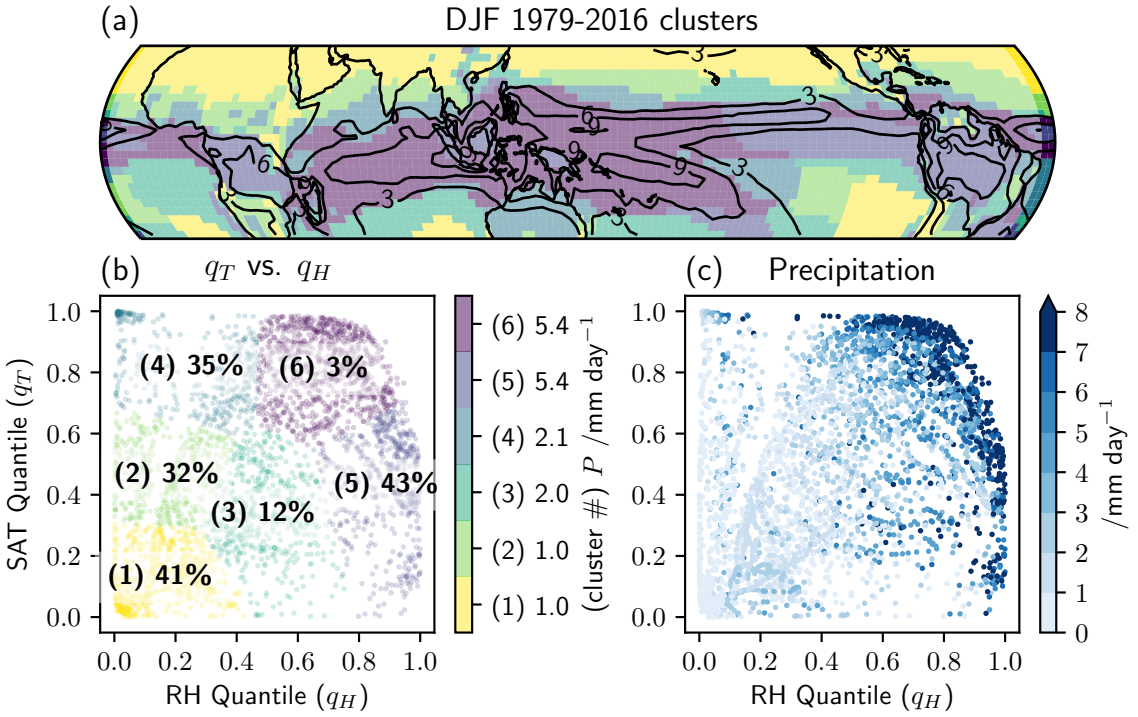

Figure 3.2: (a) Colours represent tropical grid points located within six (q_H, q_T)-space clusters for the ERA-Interim 1979-2016 DJF composite mean. Black contour lines indicate the corresponding GPCP composite mean precipitation at 3 mm day^{-1} intervals. (b) Tropical surface air temperature quantiles, q_T, versus relative humidity quantiles, q_H. Colours denote six clusters selected via a K-means algorithm, ordered by cluster mean precipitation. Percentages represent the land fraction within each cluster, located at each cluster centroid. (c) q_T versus q_H with blue shading showing grid point precipitation.

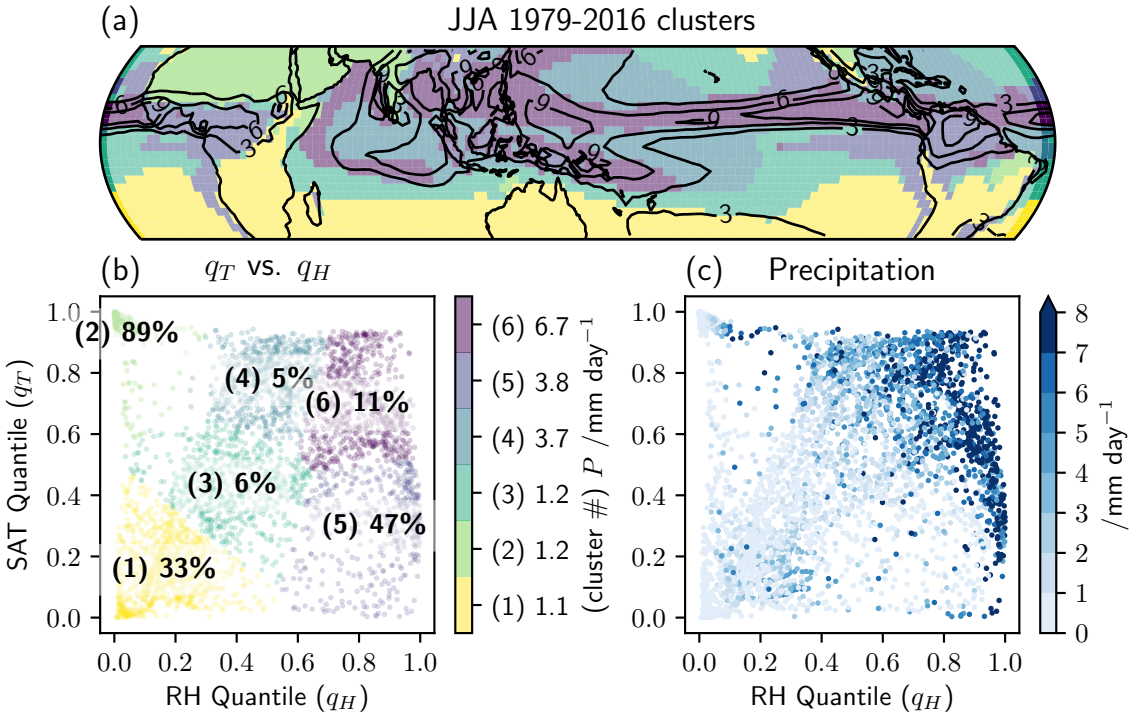

Figure 3.3: As in Figure 3.2 for the ERA-Interim-GPCP JJA composite mean.

section, we apply a statistical framework to estimate the shape of this function and rigorously explore its properties.

3.3.2 Tropical Precipitation Gaussian Process Model

In a statistical framework, assume observed or simulated tropical precipitation in (q_H, q_T)-space, P, varies about a smooth function, $\hat{P}$. Therefore, $P = \epsilon\hat{P}$, where $\epsilon = \epsilon(P, q_H, q_T)$ is a noise term, which may depend on the precipitation and location in (q_H, q_T)-space. Assuming a log multivariate normal (MVN) distribution for P ensures physically realistic, positive values, and is a common choice in the literature (for example, see Cho *et al.* (2004)). These assumptions naturally lead to a Gaussian process (GP) model of the form:

$$\log P(q_H, q_T) \sim \mathcal{GP}\left(m(q_H, q_T), k((q_H, q_T), (q'_H, q'_T))\right), \tag{3.1}$$

where $m = \log\hat{P}$ and k are the mean and covariance functions, respectively, and $\mathcal{GP}$ represents a Gaussian process.

A priori, tropical precipitation is assumed to increase with both q_H and q_T, since relatively humid and warm locations are most favourable for triggering and sustaining deep convection, as discussed in Lambert *et al.* (2017) and Chapter 2. From this assumption, locations with $(q_H, q_T) = (0, 0)$ and $(1, 1)$ would experience the lowest and highest precipitation, respectively. For the framework presented in Equation 3.1, a prior mean function of the form:

$$m(q_H, q_T) = \alpha(q_H + q_T - 1) \tag{3.2}$$

is assumed, where α is a constant. Choosing $\alpha = 3$ yields $\hat{P}(0, 0) = 0.05$ mm day^{-1} and $\hat{P}(1, 1) = 20$ mm day^{-1}, which is relatively consistent with the 1979-2016 monthly tropical precipitation range in GPCP observations. Alternative choices for α in the range 2.5-3.5 lead to qualitatively consistent results.

The functional form of k determines the strength of the association between precipitation in neighbouring regions of (q_H, q_T)-space. Consequently, the choice of k controls the smoothness properties of the mean function. In this framework, a Matérn covariance function is selected since this is a common and appropriate choice for many machine learning and geospatial statistical models (Guttorp and Gneiting, 2006). For a Matérn covariance function, the covariance, R, between locations separated by a distance r_i in the i-th direction is given by:

$$R(|r_i|) = \frac{\eta^2}{\Gamma(\nu)2^{\nu-1}}\left(\frac{\sqrt{2\nu}|r_i|}{l_i}\right)^{\nu} K_\nu\left(\frac{\sqrt{2\nu}|r_i|}{l_i}\right) \text{ with } \eta, l_i, \nu > 0 \text{ for } i = 1, 2, ..., N,$$

for N directions, where Γ and K_v are the gamma and modified Bessel functions, respectively. Typically, the smoothness parameter, ν, is chosen a priori, with larger values

increasing the smoothness of the mean function. In the special case where $\nu = p + 1/2$ and p is a positive integer, $R(|r_i|)$ can be expressed as the product of an exponential and a polynomial of order p, and is therefore p-times differentiable (Rasmussen and Williams, 2006). For instance, when $\nu = 3/2$,

$$R(|r_i|) = \eta^2 \left(1 + \frac{\sqrt{3}|r_i|}{l_i}\right) \exp\left(-\frac{\sqrt{3}|r_i|}{l_i}\right) \text{ for } i = 1, 2. \tag{3.3}$$

For the proposed model (Equation 3.1), there are $N = 2$ explanatory variables, and an anisotropic Matérn covariance function is chosen, with $\nu = 3/2$ fixed and a non-zero nugget, and therefore:

$$k((q_H, q_T), (q'_H, q'_T)) = \eta^2 R(|q_H - q'_H|, |q_T - q'_T|; l_1, l_2) + \sigma^2 \delta_{(q_H, q_T)(q'_H, q'_T)} \tag{3.4}$$

Here, $\sigma^2 \delta_{(q_H, q_T)(q'_H, q'_T)}$ represents the nugget variance, with $\delta_{(q_H, q_T)(q'_H, q'_T)}$ the Kronecker-δ function, such that $\delta_{(q_H, q_T)(q'_H, q'_T)} = 1$ if and only if $(q_H, q_T) = (q'_H, q'_T)$, and $\delta_{(q_H, q_T)(q'_H, q'_T)} = 0$ otherwise. $R(\cdot, \cdot; l_1, l_2)$ is the Matérn covariance function with $\nu = 3/2$ fixed (Equation 3.3), with l_1 and l_2 the unknown length scales in the q_H and q_T directions, respectively. Hence $\theta = (\eta, \sigma, l_1, l_2)$ represents the hyperparameters of this model, and $k = k(\cdot, \cdot; \theta)$, with the fitting procedure described in the next subsection.

This choice of k permits different decorrelation length scales in the RH quantile- and SAT quantile-directions and ensures the mean function is not overly smooth. Physically, large precipitation gradients in (q_H, q_T)-space are expected, as observational (Schiro *et al.*, 2016) and climate modelling (Kuo *et al.*, 2017) studies demonstrate sharp increases in tropical precipitation with column water vapour (CWV), and tropical CWV and surface RH variations are strongly linked (Holloway and Neelin, 2009). Importantly, repeating this analysis with different values of ν leads to qualitatively consistent results, supporting this methodological approach.

Model Fitting and Prediction

Let $y = (\log P_1, \log P_2, ..., \log P_n)$ denote the log-precipitation training data for n grid points and $X = ((q_{H1}, q_{T1})', (q_{H2}, q_{T2})', ..., (q_{Hn}, q_{Tn})')$ denote the corresponding $n \times 2$ matrix of (q_H, q_T) training data, where $'$ indicates the transpose, and recall $\theta = (\eta, \sigma, l_1, l_2)$. In addition, define the vector $m(X)$ as the prior mean function (Equation 3.2) evaluated at X, and the matrix $K = k(X, X)$ as the covariance function including the nugget (Equation 3.4) evaluated on the training data.

Via Bayes' Theorem, the posterior density function for the hyperparameters is:

$$p(\theta|X,y) = \frac{p(\theta)p(y|X,\theta)}{p(y|X)} \propto p(\theta)p(y|X,\theta) \tag{3.5}$$

where $p(\theta)$ is the prior on the hyperparameters, $p(y|X,\theta)$ is the likelihood for a given θ, and $p(y|X)$ is a normalising constant which does not depend on θ. In setting the hyperparameter priors an objective approach is taken, using uninformative $Gamma(2,1)$ distributions for η, σ, l_1 and l_2, ensuring each hyperparameter is positive. The model (Equation 3.1) is fitted to the training data (X,y) using the maximum a posteriori (MAP) estimate for θ, $\hat{\theta}_{MAP}$, which satisfies:

$$\begin{aligned}\hat{\theta}_{MAP} &= \arg\max_{\theta} p(\theta|X,y) \\ &= \arg\max_{\theta} p(\theta)p(y|X,\theta)\end{aligned}$$

In the present framework, a marginal likelihood implementation is used, since $p(y|X,\theta)$, the product of the GP prior and the likelihood integrated over all GP functions, is a MVN density function with mean $m(X)$ and covariance K (Rasmussen and Williams, 2006). $\hat{\theta}_{MAP}$ is estimated numerically by applying the Broyden-Fletcher-Goldfarb-Shanno (BFGS, Byrd *et al.* (1995)) algorithm to the 4-dimensional log-posterior density function,

$$\log p(\theta|X,y) = \log p(\theta) + \log p(y|X,\theta).$$

Alternative choices for the hyperparameter priors lead to qualitatively similar results in the following analysis. A second, more computationally expensive method for estimating θ is to sample directly from the posterior, $p(\theta|X,y)$, using Markov Chain Monte Carlo (MCMC) techniques, which avoids issues associated with a multi-modal posterior distribution. However, as with varying the hyperparameter priors, this leads to similar results to MAP estimation for ERA-Interim-GPCP test cases, and hence due to limited computational resources, MAP estimation is used throughout.

Once the model is fitted via MAP estimation, it can be used for prediction. Define X_* and y_* as the (q_H, q_T) and $\log P$ testing data, respectively, and let $f = \log P$ represent the Gaussian process for compactness. The posterior predictive distribution at the testing points X_* is a MVN with a mean vector:

$$E[f(X_*)|X,y] = m(X_*) + k(X_*,X)k(X,X)^{-1}(y - m(X)) \tag{3.6}$$

and covariance matrix:

$$Cov[f(X_*)|X,y] = k(X_*,X_*) - k(X_*,X)k(X,X)^{-1}k(X,X_*), \tag{3.7}$$

where $k = k(\cdot, \cdot; \hat{\theta}_{MAP})$ is the covariance function evaluated at the hyperparameter MAP estimate. The posterior estimate for $\hat{P}$ is hence:

$$\hat{P}(X_*) = \exp\left(E[f(X_*)|X, y]\right), \tag{3.8}$$

with a $100\alpha\%$ posterior prediction interval for point estimates given by:

$$(\exp(E[f(X_*)|X, y] \mp z_{(1+\alpha)/2}\sqrt{Cov[f(X_*)|X, y]})), \tag{3.9}$$

where $z_{(1+\alpha)/2}$ is the $(1 + \alpha)/2$ quantile of the standard normal distribution.

3.3.3 Diagnosing Precipitation Shifts

Analogous to Chapter 2, tropical precipitation changes under climate perturbations are diagnosed using a GP model fitted to control conditions, and evaluating this model at the perturbed surface RH and SAT tropical quantiles. Consider control and perturbation scenarios, such as neutral and El Niño observations, or late twentieth and twenty-first century climate model simulations. Let P, q_H and q_T represent the control scenario tropical precipitation, RH and SAT quantiles respectively. Similarly, let P', q'_H and q'_T represent the perturbation scenario tropical precipitation, RH and SAT quantiles, respectively. For compactness, define $X = (q_H, q_T)$ and $X' = (q'_H, q'_T)$ as the control and perturbation locations in (q_H, q_T)-space, respectively. To diagnose the precipitation change from the control to perturbation scenarios, $P' - P$, firstly we fit the model (Equation 3.1) to the control data, $\log P \sim \mathcal{GP}(m(X), k(\cdot, \cdot))$, as discussed in Section 3.3.2. The diagnosed precipitation change,

$$\Delta P = s\hat{P}(X') - \hat{P}(X), \tag{3.10}$$

is then calculated by evaluating $\hat{P}$ (Equation 3.8) at the control and perturbation locations in (q_H, q_T)-space. As in Lambert *et al.* (2017) and Todd *et al.* (2018) (Chapter 2), s is the fractional change in tropical mean precipitation. For global warming scenarios, generally $s > 1$, representing a thermodynamic increase in precipitation change, modulated by a tropical mean circulation weakening (Held and Soden, 2006). An alternative choice would be to examine the fractional change in precipitation, $s\hat{P}(X')/\hat{P}(X)$. However, for consistency with Chapter 2, absolute changes are examined in this chapter.

Once the GP model has been fitted to control conditions (P, q_H and q_T), resamples can be drawn to estimate properties of the diagnosed precipitation change. Let $\mathbf{P} = (P_1, P_2, ..., P_{N_s})$ represent N_s samples drawn from the posterior predictive distribution at the control locations, X. Similarly, let $\mathbf{P'} = (P'_1, P'_2, ..., P'_{N_s})$ represent N_s samples randomly drawn from the posterior predictive distribution at the perturbation locations, X'. These samples can then be used to estimate a sample of diagnosed

precipitation changes:

$$\Delta P_i = sP_i' - P_i \text{ for } i = 1, 2, ..., N_s, \tag{3.11}$$

from the distribution $p(\Delta P|X, y, X')$, where $y = \log P$ and P is the control precipitation as in Section 3.3.2. Using this sample, $\mathbf{\Delta P} = (\Delta P_1, \Delta P_2, ..., \Delta P_{N_s})$, and assuming a good model fit, two tests can be performed. Firstly, the probability that the diagnosed precipitation change is positive, $p(\Delta P > 0|X, y, X')$, can be estimated as:

$$p(\Delta P > 0|X, y, X') \approx \frac{1}{N_s}\Sigma_{i=1}^{N_s}\mathbb{1}(\Delta P_i > 0), \tag{3.12}$$

where $\mathbb{1}$ is the indicator function. If $p(\Delta P > 0|X, y, X')$ is greater than a high threshold, the model suggests an increase in precipitation associated with the location change in (q_H, q_T)-space is likely, and vice-versa for a low threshold. These thresholds are chosen as 10% and 90% in this analysis. Secondly, the upper and lower quartiles of $\mathbf{\Delta P}$ can be estimated and differenced to yield a proxy for the prediction interval width:

$$\Delta P_{IQR} = \Delta P_{(0.75N_s)} - \Delta P_{(0.25N_s)} \tag{3.13}$$

where $\cdot_{(j)}$ is the j-th order statistic. If ΔP_{IQR} is large, ΔP is only weakly constrained by (q_H, q_T)-space changes. Alternatively, if ΔP_{IQR} is small, ΔP is well constrained by (q_H, q_T)-space changes. In this analysis, $N_s = 1000$ is fixed due to computational constraints. Qualitatively consistent results obtained for test cases with $N_s = 5000$.

3.3.4 Tropical Precipitation Gaussian Process Model Validation

In order to justify using the model proposed (Equation 3.1) in Section 3.3.2 for diagnosing precipitation changes, its goodness of fit requires testing. In this section, climatological seasonal means of GPCP precipitation observations and ERA-Interim reanalyses of SAT and RH for the 1979-2016 period are used for validation. Similar validation for CMIP5 data is presented alongside the results in the following section. Within the 30°S-30°N tropical region, there are 3456 grid points at 2.5° resolution. For training and testing data, the $n = 1728$ even, (X, y), and odd, (X_*, y_*), numbered grid points are used, respectively. Table 3.2 presents the hyperparameter MAP estimates for each model fitted to the seasonal training data. The hyperparameter estimates are similar across each seasonal climatology, with the q_T decorrelation length scale, $\hat{l_2}$, consistently larger than the q_H decorrelation length scale, $\hat{l_1}$.

The top row of Figure 3.4 demonstrates how both X and X_* data provide relatively good coverage of (q_H, q_T)-space in each seasonal climatology. Fitting the GP model to (X, y), the posterior mean precipitation, $\hat{P}$, evaluated on a 0.01×0.01 mesh in (q_H, q_T)-space, increases with both increasing q_H and q_T, with a similar pattern in each season.

	DJF	MAM	JJA	SON
$\hat{\eta}$	2.00	1.53	1.60	1.30
$\hat{\sigma}$	0.85	0.78	0.89	0.93
$\hat{l_1}$	0.16	0.11	0.19	0.15
$\hat{l_2}$	0.78	0.68	0.37	0.58

Table 3.2: Maximum a posteriori hyperparameter estimates for the GP model (Equation 3.1) fitted to ERA-Interim-GPCP 1979-2016 seasonal climatologies.

In addition, the posterior precipitation inter-decile range (estimated using Equation 3.9) is also consistent across the seasons. For the majority of (q_H, q_T)-space, the posterior precipitation inter-decile range is less than 3mm day^{-1}, except towards $(q_H, q_T) = (1, 1)$ where it rapidly increases due to data sparsity.

Following Bastos and O'Hagan (2009), a useful metric for assessing GP model fit is the credible interval diagnostic,

$$D_{CI}(y_*) = 1 - \frac{1}{N}\Sigma_{i=1}^{N}\mathbb{1}(y_{*,i} \in CI_i), \tag{3.14}$$

where CI_i is the 95% posterior predictive interval at the point $X_{*,i}$, and $D_{CI}(y_*)$ is close to 5% if the model is well fitted. For the four seasonal climatology test cases, $D_{CI}(y_*)$ ranges between 6.3-6.7%, indicating relatively good model fit. A more comprehensive approach is to assess model fit is using diagnostic plots. The second row of Figure 3.4 demonstrates quantile-quantile (QQ) plots of the uncorrelated standardised errors,

$$D_G(y_*) = G^{-1}(y_* - E[f(X_*)|X, y]), \tag{3.15}$$

versus equivalent quantiles of a Student t distribution on $n-2$ degrees of freedom. Here, G satisfies $Cov[f(X_*)|X, y] = GG^T$ and is estimated using a Cholesky decomposition. For each season, the majority of points on the QQ plot lie close to the 45° diagonal line, indicating the normality assumption in the GP model is justified. However, especially for March-May (MAM) and June-August (JJA), the lower tails demonstrate a substantial deviation from the diagonal. This could be due to the bounded property of precipitation observations. For P close to zero, the underlying process for $\log P$ may be poorly represented by a Gaussian.

The standardised errors,

$$D_I(y_*) = \frac{y_* - E[f(X_*)|X, y]}{\sqrt{diag(Cov[f(X_*)|X, y])}}, \tag{3.16}$$

are plotted against the posterior fitted values, $E[f(X_*)|X, y]$, in the third row of Figure 3.4 to check for systematic errors in the mean function (Bastos and O'Hagan, 2009).

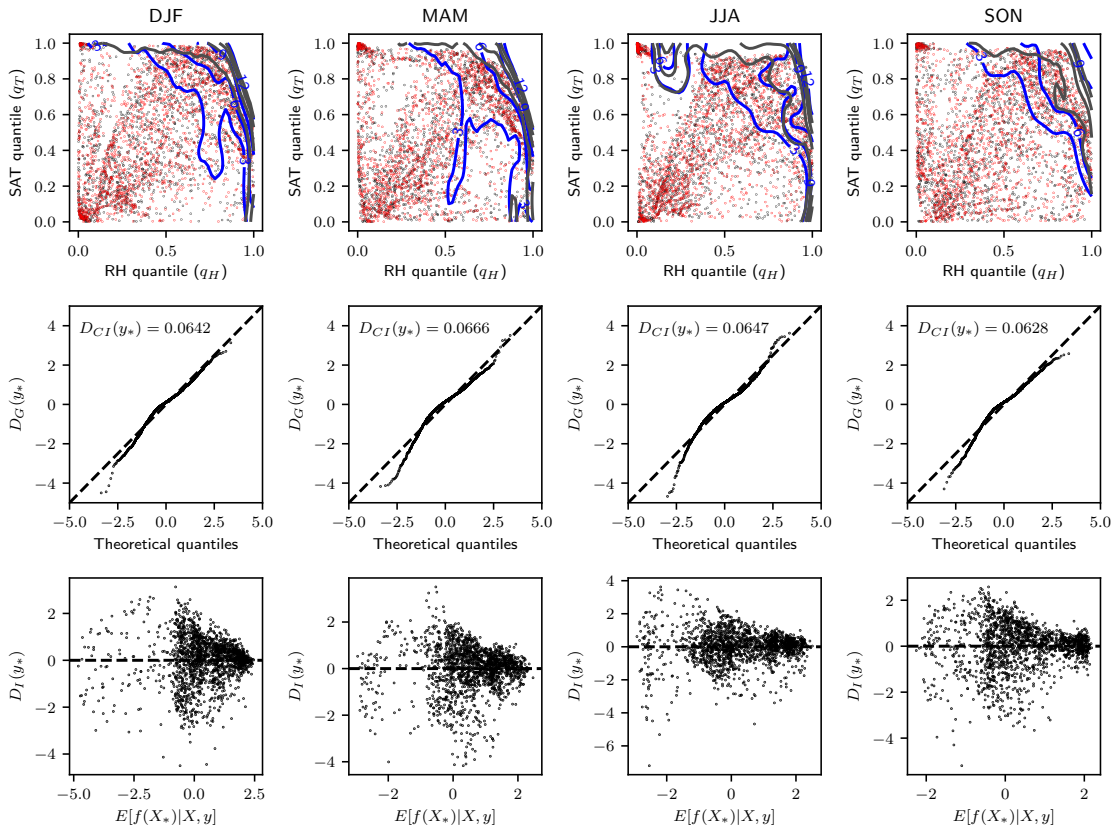

Figure 3.4: Diagnostic plots for GP models fitted to ERA-Interim-GPCP 1979-2016 seasonal climatologies. In the top row, black and red points indicate the training (X) and testing (X_*) locations in (q_H, q_T)-space, respectively. Blue and grey contours represent the posterior $\hat{P}$ and inter-decile ranges, evaluated on a 0.01×0.01 mesh, at intervals of 3 mm day^{-1}, respectively. The second row displays quantile-quantile plots, showing the uncorrelated standardised errors, $D_G(y_*)$ (Equation 3.15) versus theoretical quantiles from a Student t distribution on $n-2$ degrees of freedom. The dashed line indicates the 45° diagonal, and $D_CI(y_*)$ (Equation 3.14) reports the 95% credible interval diagnostic. The third row shows standardised errors, $D_I(y_*)$ (Equation 3.16), versus the posterior fitted values, with the dashed horizontal line at $D_I(y_*) = 0$.

The standardised errors are quite symmetrically distributed about zero for each season, demonstrating a well fitted mean function given the training data. The magnitude of $D_I(y_*)$ tends to increase for smaller values of $E[f(X_*)|X, y]$, suggesting the posterior predictive variance may be too small in these regions. As with the QQ plots, this could be due to the lower boundedness of precipitation values, compromising the log-Gaussian assumption.

In order to further test the GP model fit, it is helpful to examine profiles across (q_H, q_T)-space. Figure 3.5 demonstrates $\hat{P}$ and 95% prediction interval profiles for points nearby to $q_T = 0.2, 0.4, 0.6$ and 0.8 for the December-February (DJF) climatology. As identified by the QQ and standardised error versus posterior mean value plots, model fit is relatively

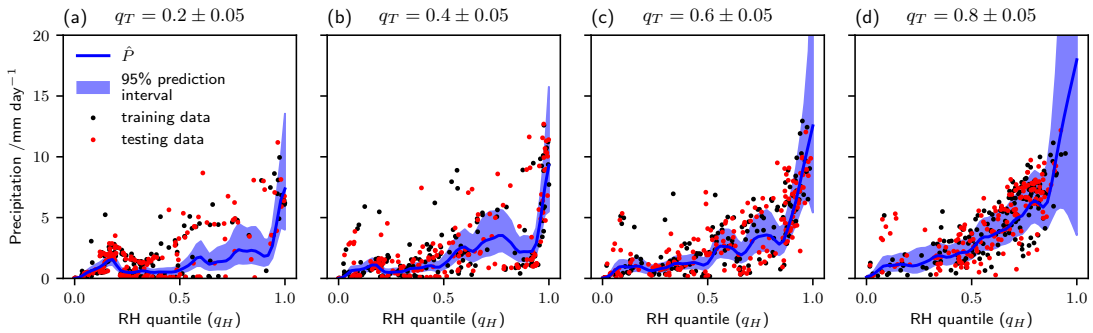

Figure 3.5: Profile plots for the GP model fitted to the ERA-Interim-GPCP DJF seasonal climatology. Blue lines and shading indicate the posterior mean $\hat{P}$ and 95% prediction interval as a function of q_H across each q_T band: (a) 0.2 ± 0.05, (b) 0.4 ± 0.05, (c) 0.6 ± 0.05 and (d) 0.8 ± 0.05. Black and red points indicate the training and testing data, respectively, within each corresponding q_T band.

weak for low precipitation values, especially in the $q_T = 0.2$ case. However, for larger precipitation values better model fit is observed. For $q_T = 0.8$, the majority of both nearby training and testing points lie within the 95% posterior prediction interval. In regions of data sparsity, such as for $q_T = 0.4$ and $0.7 < q_H < 0.8$ the posterior prediction interval broadens accordingly. Additionally, in the region near $(q_H, q_T) = (1, 1)$ where there is no data, the posterior prediction interval is very broad and $\hat{P}$ tends toward the prior mean.

Consequently, for this ERA-Interim-GPCP validation data, the GP model fit is reasonably good, especially in regions of (q_H, q_T)-space where the mean precipitation is not close to zero. This provides confidence in applying fitted GP models to diagnose tropical precipitation changes, as presented in the following section. However, a caveat is that diagnosis performance in a minority of regions where the mean state precipitation is close to zero may be affected by weaker model fit.

3.4 Results

In this section, the performance of the revised diagnosis method for observed ENSO and simulated global warming precipitation shifts is evaluated. Subsequently, the assumption that precipitation as a function of RH and SAT relative to their tropical means is invariant under climate perturbations is examined.

3.4.1 Gaussian Process Method Diagnosis Performance

Applying the Lambert *et al.* (2017) method produces a point estimate of tropical precipitation changes linked with surface air temperature and relative humidity changes. With the revised statistical framework presented in Section 3.3.3, diagnosed precipitation changes, ΔP are now considered as random variables. Using the posterior predictive distribution, two tests can be performed. Firstly, the probability that $\Delta P > 0$ is estimated using Equation 3.12. If this probability is between 0.1 and 0.9 and the GP model is well fitted, there is little evidence to support the sign of the diagnosed precipitation change. Secondly, the inter-quartile range of ΔP can be estimated using Equation 3.13. If this inter-quartile range is large, there is a broad spread in the magnitude of the diagnosed precipitation change.

Present Day El Niño-Southern Oscillation

The GP method performs relatively well at diagnosing El Niño minus neutral precipitation changes using ERA-Interim-GPCP for the period 1979-2016, as displayed by Figure 3.6. These results are quite confident, since the GP model fits this ERA-Interim-GPCP data relatively well, as discussed in Sections 3.3.4. Spatial correlations between the observed and diagnosed changes are 0.55, 0.66 and 0.73 for JJA(0), SON(0) and D(0)JF(1), respectively. The sign of observed major precipitation shifts ($|\Delta P| \geq 1$ mm day^{-1}) over the Indian and Pacific oceans, South America and the Maritime Continent are correctly diagnosed as positive in the majority of regions for each season in the El Niño growth and mature stages. Despite the correctly diagnosed sign, the inter-quartile range estimates are relatively large (> 4 mm day^{-1}), across a majority of equatorial regions. Furthermore, the slope estimates from regressing the diagnosed on observed changes, 0.44, 0.41 and 0.53 for JJA(0), SON(0) and D(0)JF(1), respectively, are smaller than one, and hence the magnitudes are typically underestimated. Physically, this result suggests that El Niño relative changes in SAT and RH are strongly linked with the sign of precipitation changes. However, additional factors may be responsible for modulating the size of these changes, which will be discussed further in Section 3.4.2.

Contrasting the diagnosis results from the GP method with the binning method, modest improvements in diagnosis performance are evident, as shown in Table 3.3. The spatial correlation performance improvement is largely driven by higher pattern correlations over

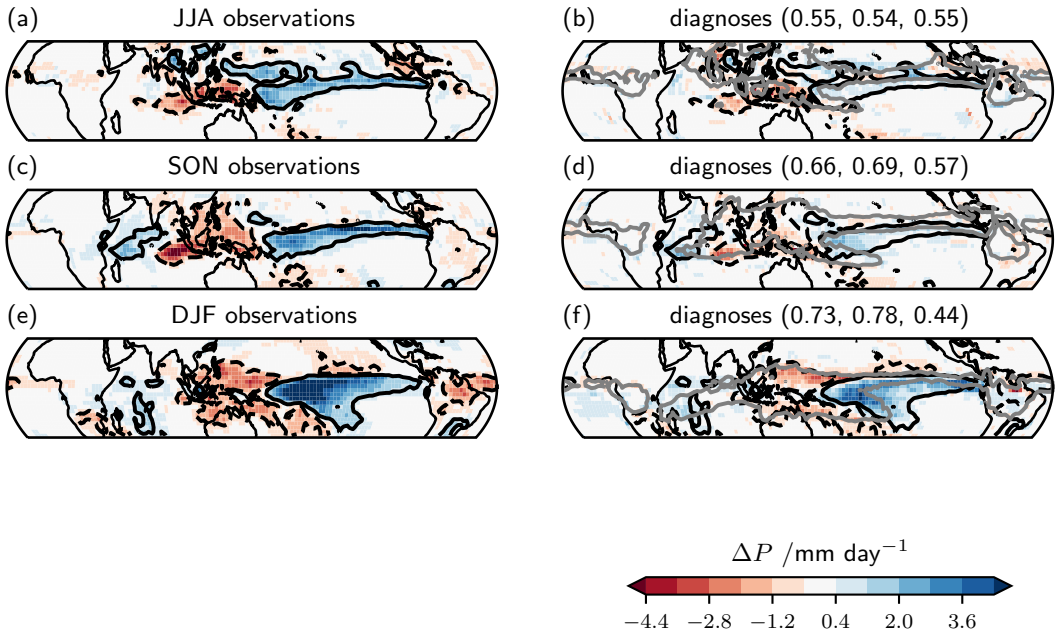

Figure 3.6: Colours show the 1979-2016 composite mean El Niño minus neutral seasonal GPCP observed (a, c, e) and diagnosed (b, d, f) precipitation anomalies. Solid and dashed black contour lines in (a-f) indicate the ± 1 mm day^{-1} GPCP anomalies. In (b, d, f), areas where the estimated probability of a positive diagnosed anomaly (Equation 3.12) is between 0.1 and 0.9 are masked. Grey lines show the 4 mm day^{-1} contour of the predictive inter-quartile range, ΔP_{IQR} (Equation 3.13).Triplets in parentheses in (b, d, f) indicates the spatial correlation over the whole tropics, oceanic, and land grid points, respectively.

	El Niño minus neutral				La Niña minus neutral			
	GP Method		L17 Method		GP Method		L17 Method	
	r	$\hat{\beta}$	r	$\hat{\beta}$	r	$\hat{\beta}$	r	$\hat{\beta}$
JJA	0.55	0.44	0.53	0.47	0.45	0.36	0.43	0.37
SON	0.66	0.41	0.60	0.37	0.48	0.37	0.45	0.35
DJF	0.73	0.53	0.69	0.41	0.69	0.55	0.67	0.47

Table 3.3: Performance metrics for seasonal El Niño and La Niña precipitation diagnoses: correlation, r, and slope estimates, $\hat{\beta}$, for the respective Gaussian Process (GP) and Lambert et al. *(2017) (L17 or binning) methods.*

tropical oceans, a consistent result in all seasons. Over tropical land there is no consistent improvement in pattern correlations when comparing the GP and binning method diagnoses. A second area of minor improvement is the slightly more realistic magnitudes from the GP method for the SON and DJF seasons (Table 3.3). These two areas of improvement are likely to be linked to the greater fidelity of the precipitation function for the GP method. In the Lambert *et al.* (2017) binning framework, for 2.5° ERA-Interim-GPCP data, 34 grid points are aggregated within each RH-SAT bin to estimate the bin mean precipitation. As discussed in Chapter 2, this leads to a relatively smooth function of precipitation versus SAT and RH bin number. In contrast, by using a Matérn covariance function with $\nu = 1.5$, the GP framework better resolves precipitation as a function of (q_H, q_T)-space, as shown by Figure 3.5. Consequently, precipitation changes can be diagnosed from smaller SAT or RH changes in the GP method in contrast to the binning method, relatively improving performance for the former.

Diagnosis results for the GP method applied to ERA-Interim-GPCP La Niña minus neutral precipitation changes are displayed in Figure 3.7. Both the GP and binning method La Niña diagnosed changes perform less well than the equivalent El Niño diagnosed changes. One explanation for this performance disparity could be due to the nonlinearity of ENSO precipitation anomalies. La Niña precipitation changes are characterised as an intensification of the climatological state, with the magnitude of anomalies slightly weaker relative to El Niño changes. In contrast, El Niño precipitation changes which are largely represented by shifts in convergence zones away from the climatology (as discussed in Section 1.1.4). These results suggest the Lambert *et al.* (2017) framework may be better at diagnosing precipitation spatial shifts instead of pattern amplification. Despite the relatively weaker La Niña diagnosis performance for the GP method, the majority of spatial correlations and regression slope estimates improve relative to the binning method (Table 3.3). This is a consistent result with the El Niño diagnosis performance discussed previously.

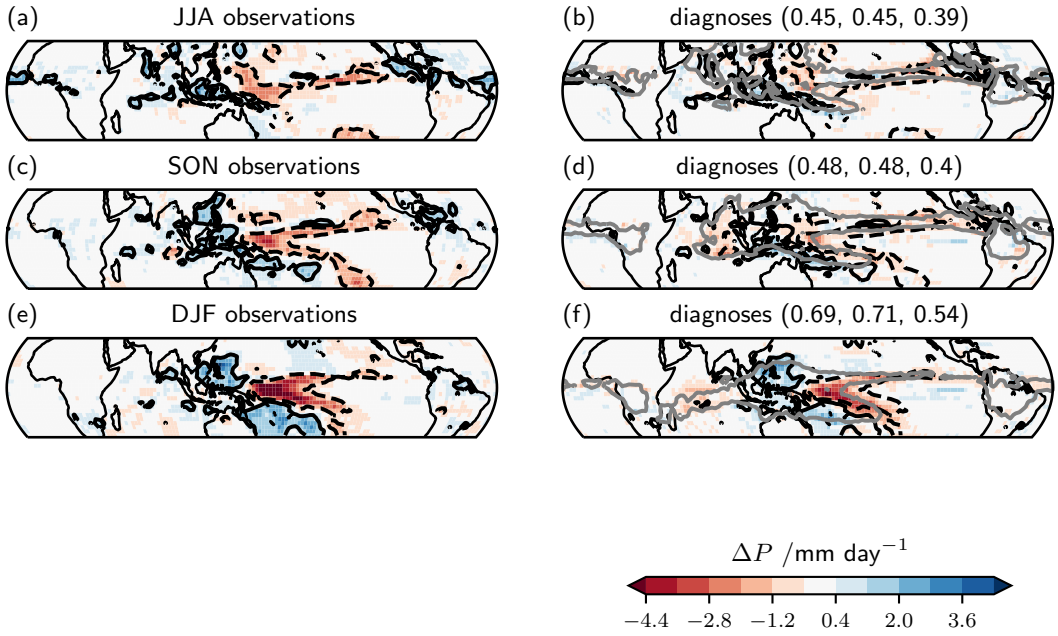

Figure 3.7: As in Figure 3.6, but for the 1979-2016 composite mean La Niña minus neutral precipitation anomalies.

Twenty-First Century Global Warming

The GP diagnosis method is next applied to CMIP5 simulated twenty-first century precipitation changes (2080-2099 minus 1980-1999) following the RCP8.5 scenario (Moss *et al.*, 2010). Only DJF composite mean changes are discussed, as qualitatively consistent results apply for the MAM, JJA and SON composite means. Consistent with the ERA-Interim-GPCP results, the MAP estimates for the q_T decorrelation length scale are generally smaller than the corresponding q_H decorrelation length scale for each model, as shown by Figure 3.8. Generally models with a larger noise hyperparameter estimate, $\hat{\sigma}$, have a smaller compensating decorrelation length scales and vice-versa.

In order to assess model fit, an equivalent validation method to that presented in Section 3.3.4 is performed on the CMIP5 data. Even and odd numbered grid points for each CMIP5 model's 1980-1999 historical DJF climatologies are used for training and testing data, respectively. Generally, GP model fit for CMIP5 historical simulations is consistent with GP model fit to the ERA-Interim-GPCP data. Quantile-quantile plots for GP models fitted to the historical DJF climatologies are presented in Figure 3.9. For the majority of CMIP5 models, the uncorrelated standardised errors, $D_G(y_*)$, only substantially deviate from quantiles of a Student t distribution on $n-2$ degrees of freedom in the lower tails. Hence the normality assumption of log-precipitation is typically well satisfied except in small regions of (q_H, q_T)-space. For a minority of CMIP5 models where the diagnosis method performs relatively weakly (as discussed later in this section), such as NorESM1-ME, ACCESS1-0, HadGEM2-CC, GFDL-ESM2M, bcc-csm1-1-m and bcc-csm1-1, there are additional deviations of $D_G(y_*)$ in the upper tails. This could be

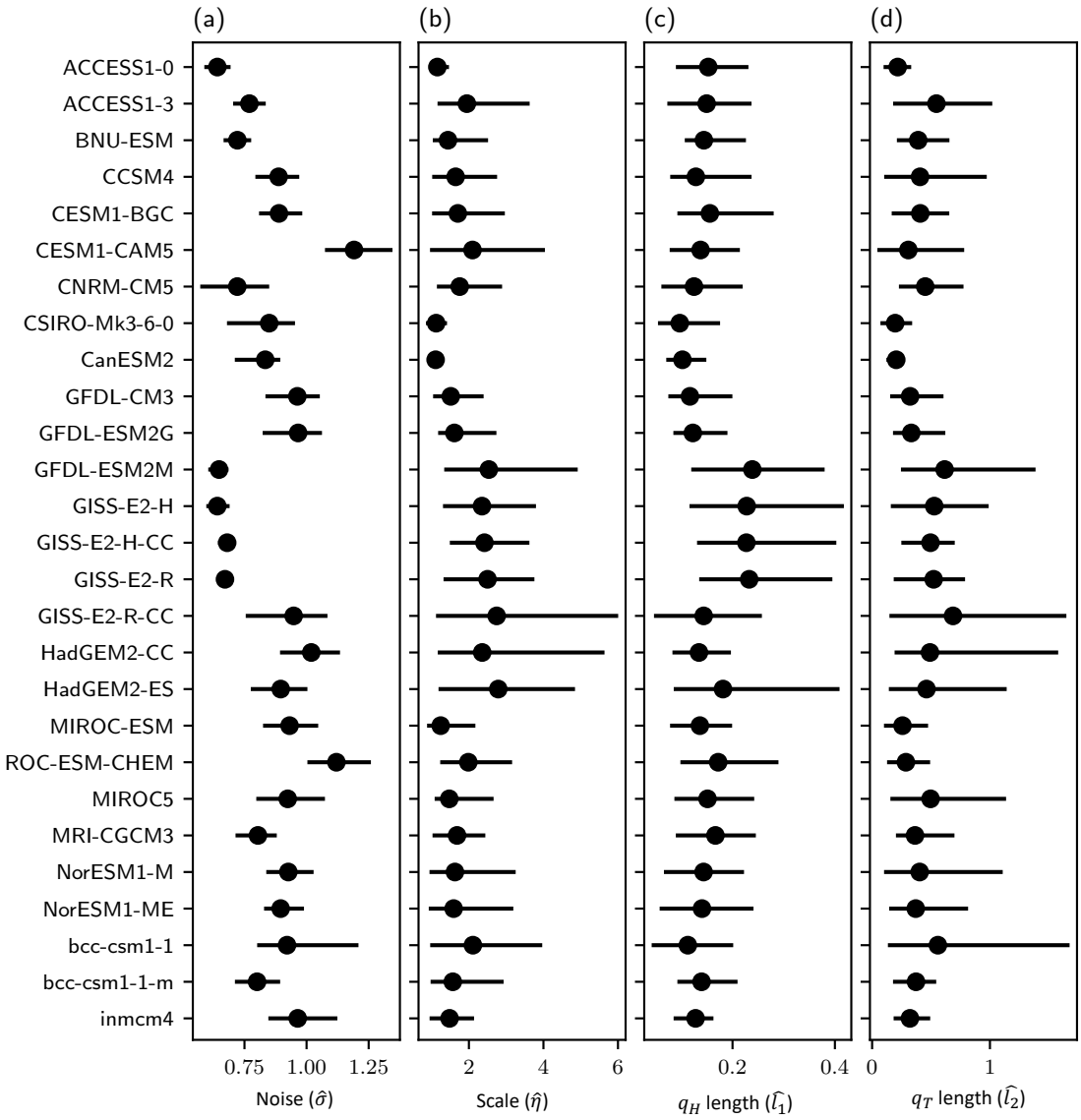

Figure 3.8: Maximum a posteriori hyperparameter estimates for GP models fitted to CMIP5 1980-1999 historical monthly climatologies. Horizontal bars indicate the range of (a) $\hat{\sigma}$, (b) $\hat{\eta}$, (c) $\hat{l_1}$ and (d) $\hat{l_2}$ estimates for each model across the twelve monthly climatologies, with points indicating the respective mean hyperparameter estimates.

an contributing factor leading to the weak diagnosis performance.

Standardised error versus fitted value diagnostic plots for the CMIP5 historical data are displayed in Figure 3.10. The errors are generally distributed symmetrically about zero in each model. Similarly to the ERA-Interim-GPCP case, the error magnitudes are larger for smaller fitted values. This indicates that the GP mean functions are well fitted for the majority of regions in (q_H, q_T)-space, but the posterior variance is underestimated for low precipitation values. 95% credible interval diagnostics for the twenty seven ensemble members range between 0.063 and 0.098. This is slightly larger than the theoretical value of 0.05 for a perfectly fitted model, but still indicates generally good model fit.

Precipitation change diagnosis performance varies broadly across the CMIP5 ensemble, as demonstrated by Figure 3.11. For models where the GP method performs best, diagnosed global warming precipitation changes are typically the correct sign, however the magnitudes of these changes are generally too weak. Similar to the El Niño and La Niña cases, the inter-quartile range of the diagnosed precipitation changes exceeds 4 mm day^{-1} for large regions of the tropics.

The Lambert *et al.* (2017) binning method is also applied to the simulated RCP8.5 twenty-first century precipitation changes. A comparison of diagnosis performance for the binning and GP methods across the CMIP5 ensemble is displayed in Figure 3.12. Spatial correlation ranges are consistent for both methods: 0.15 to 0.74 and 0.21 to 0.62 for the binning and GP methods, respectively. Furthermore, the performance of both methods for RCP8.5 is comparable with the performance of the binning method applied to abrupt4xCO2 simulations, as presented in Lambert *et al.* (2017) and Chapter 2. Spatial correlations between simulated and diagnosed changes increase for a majority (78%) of CMIP5 models for the GP method relative to the binning method (Figure 3.12(a)).

The largest changes in diagnosis performance, measured via spatial correlations are for the MIROC and CESM1 (increases), and HadGEM2 and bcc-csm1 (decreases), model families. Examining spatial correlations over tropical ocean and land regions, overall performance changes between the binning and GP methods are mainly linked with performance changes over ocean. These results suggest that the improved fidelity of $\hat{P}$ affects diagnosis performance differently for each model in CMIP5. Similar to the ENSO results discussed previously, there is a slight improvement comparing GP and binning method diagnosed precipitation change magnitudes. This is reflected in slope estimates closer to unity for a majority models, when regressing diagnosed on simulated changes, for the GP method (Figure 3.12(b)). Factors influencing the performance of the GP method for global warming simulations are explored further in Section 3.4.3.

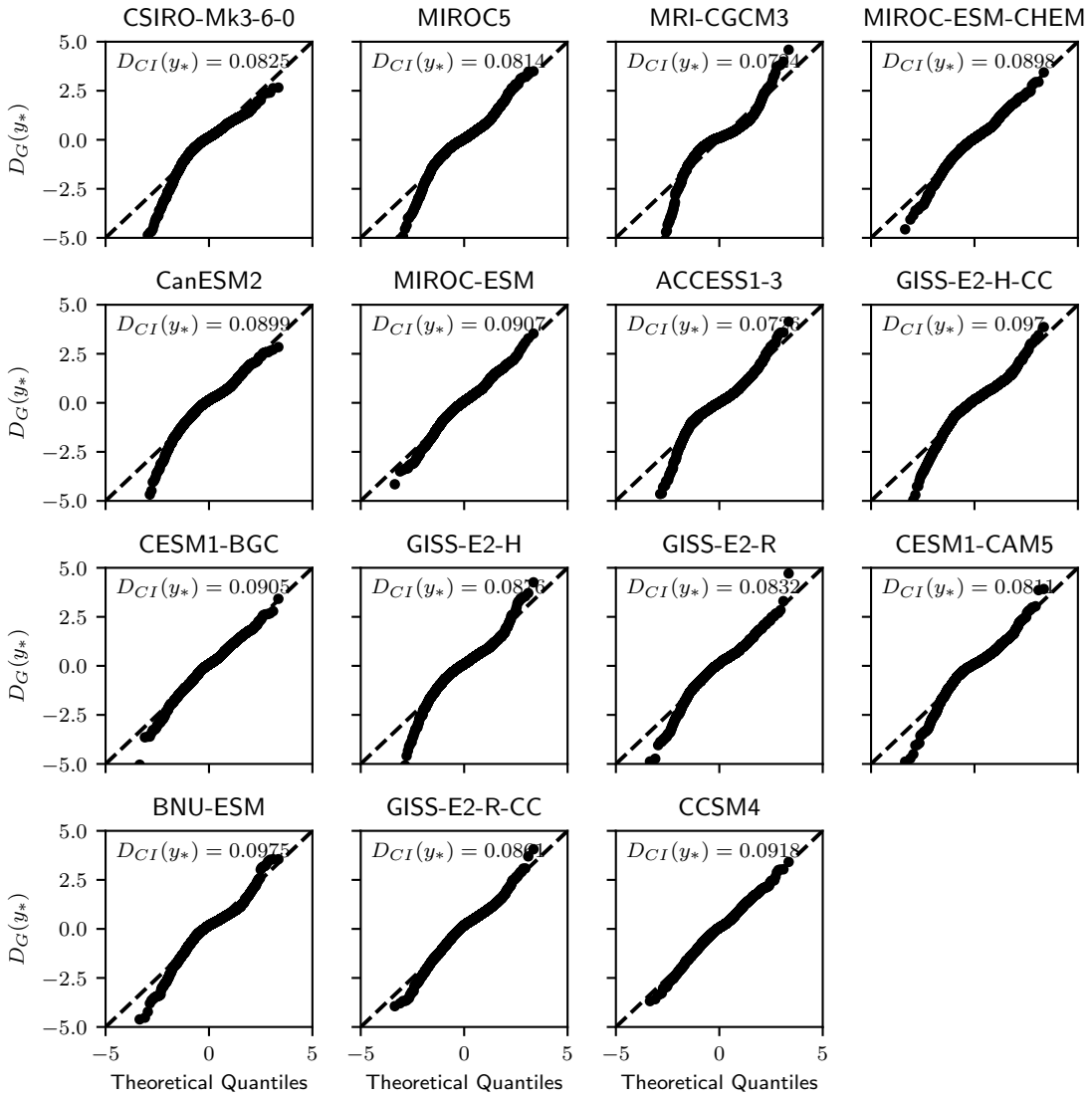

Figure 3.9: Quantile-quantile diagnostic plots for GP models fitted to historical 1980-1999 DJF climatologies for 27 CMIP5 models, in descending order of diagnosis performance. Each panel shows the uncorrelated standardised errors, $D_G(y_*)$ (Equation 3.15) versus theoretical quantiles from a Student t distribution on $n-2$ degrees of freedom. The dashed line indicates the 45° diagonal, and $D_CI(y_*)$ (Equation 3.14) reports the 95% credible interval diagnostic.

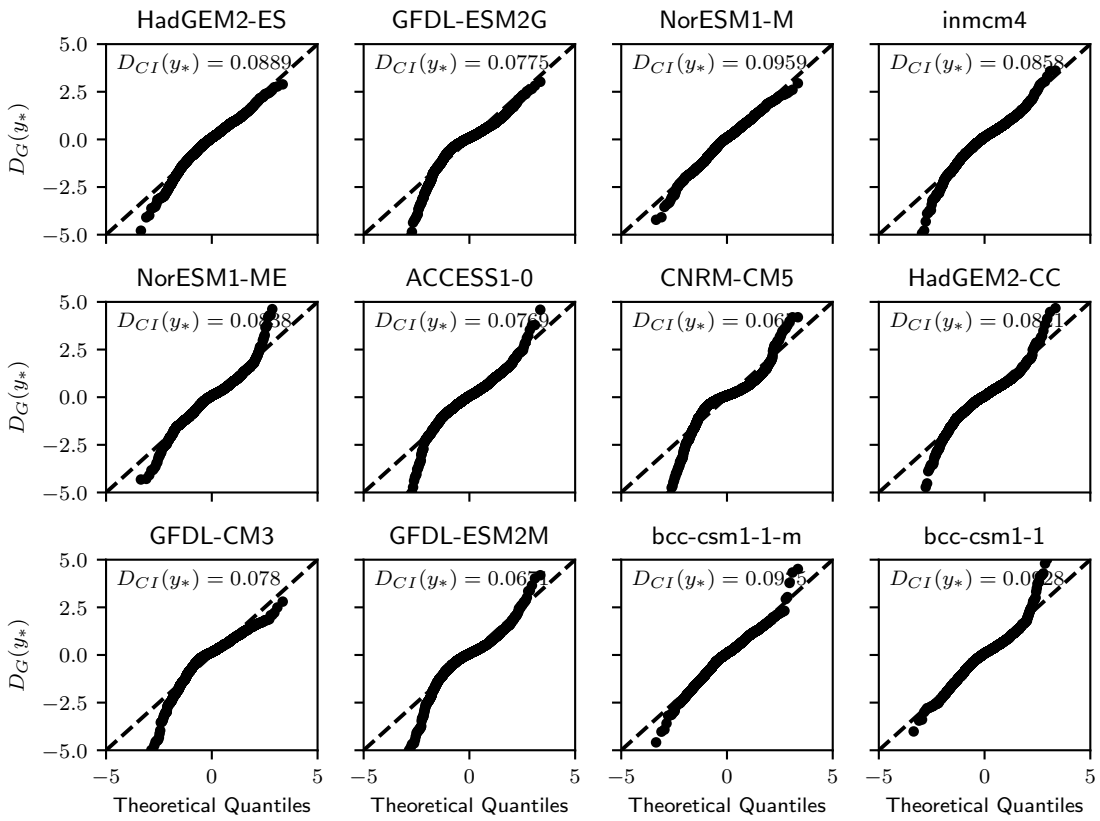

Figure 3.9 (Continued)

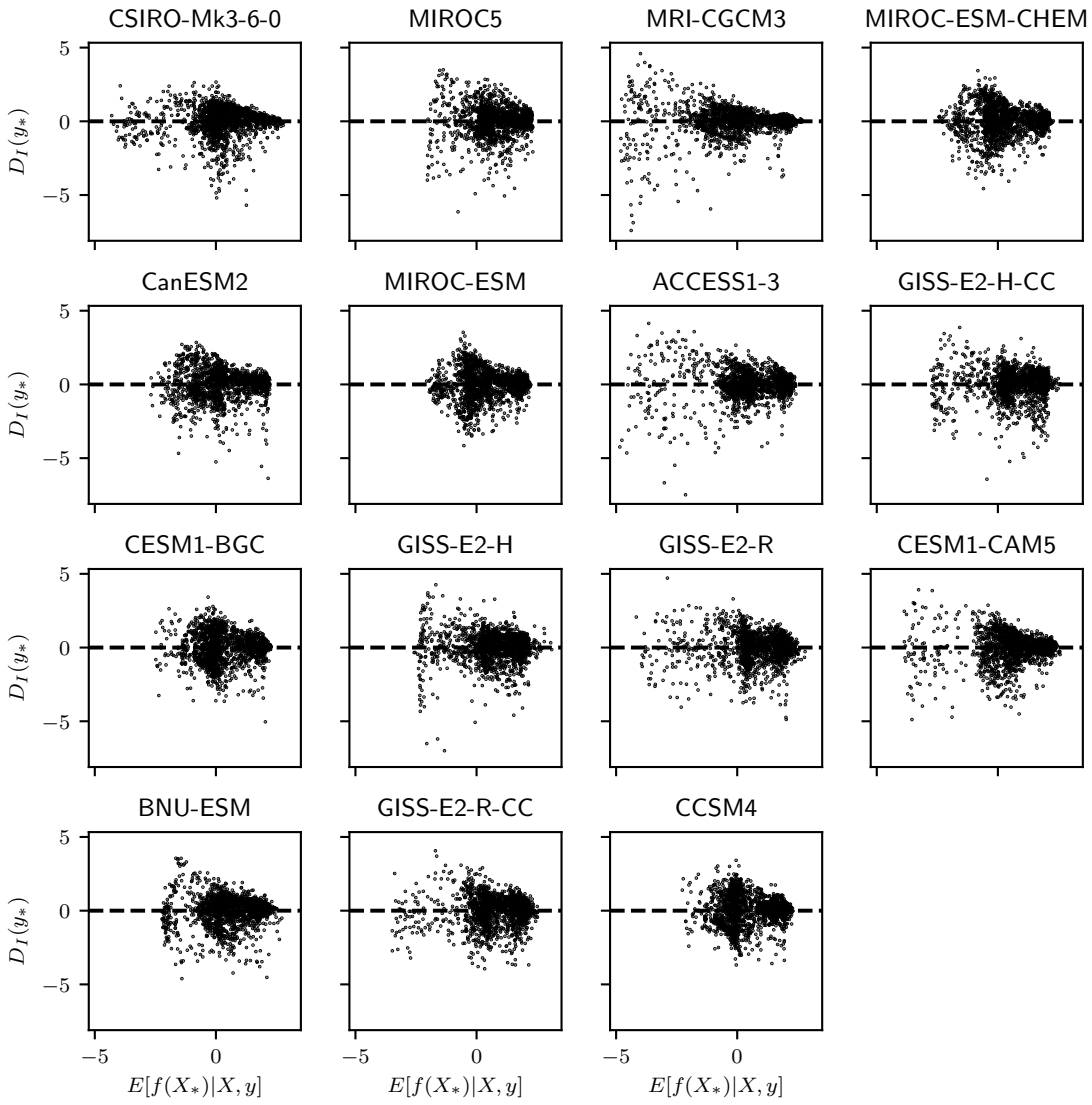

Figure 3.10: Standardised error diagnostic plots for GP models fitted to historical 1980-1999 DJF climatologies for 27 CMIP5 models, in descending order of diagnosis performance. Each panel shows standardised errors, $D_I(y_*)$ (Equation 3.16), versus the posterior fitted values, with the dashed horizontal line at $D_I(y_*) = 0$.

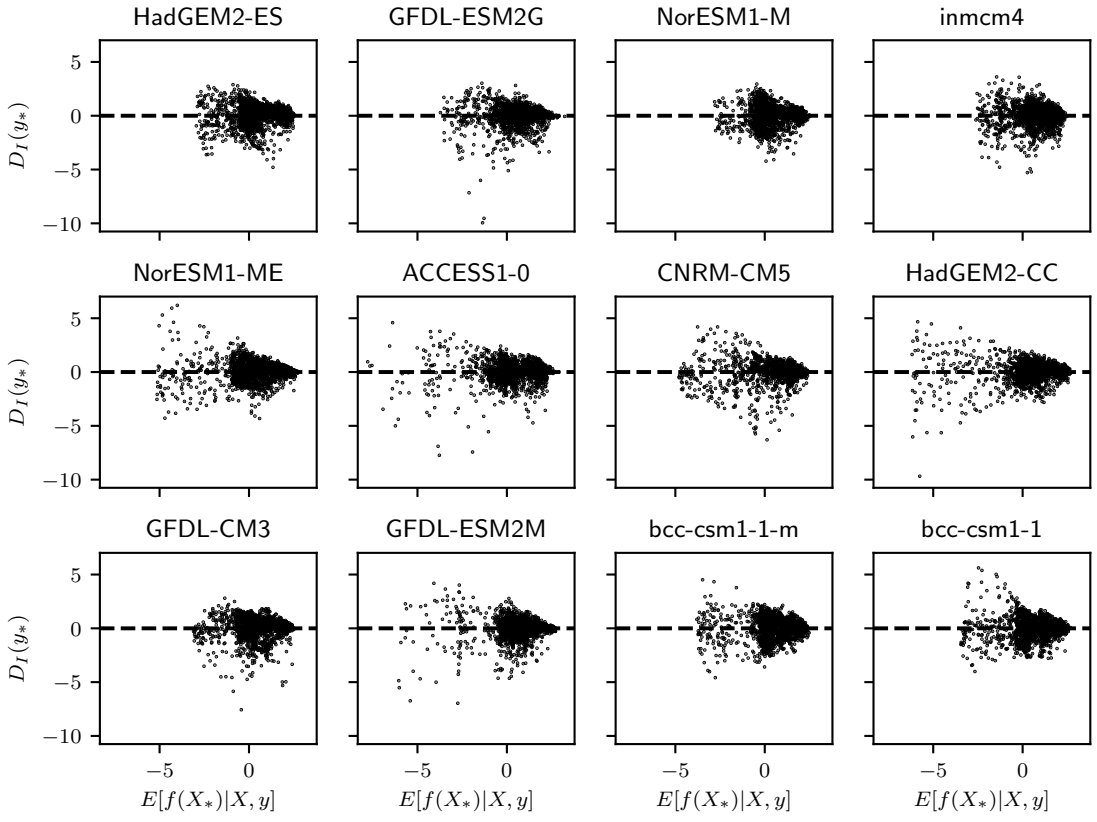

Figure 3.10 (Continued)

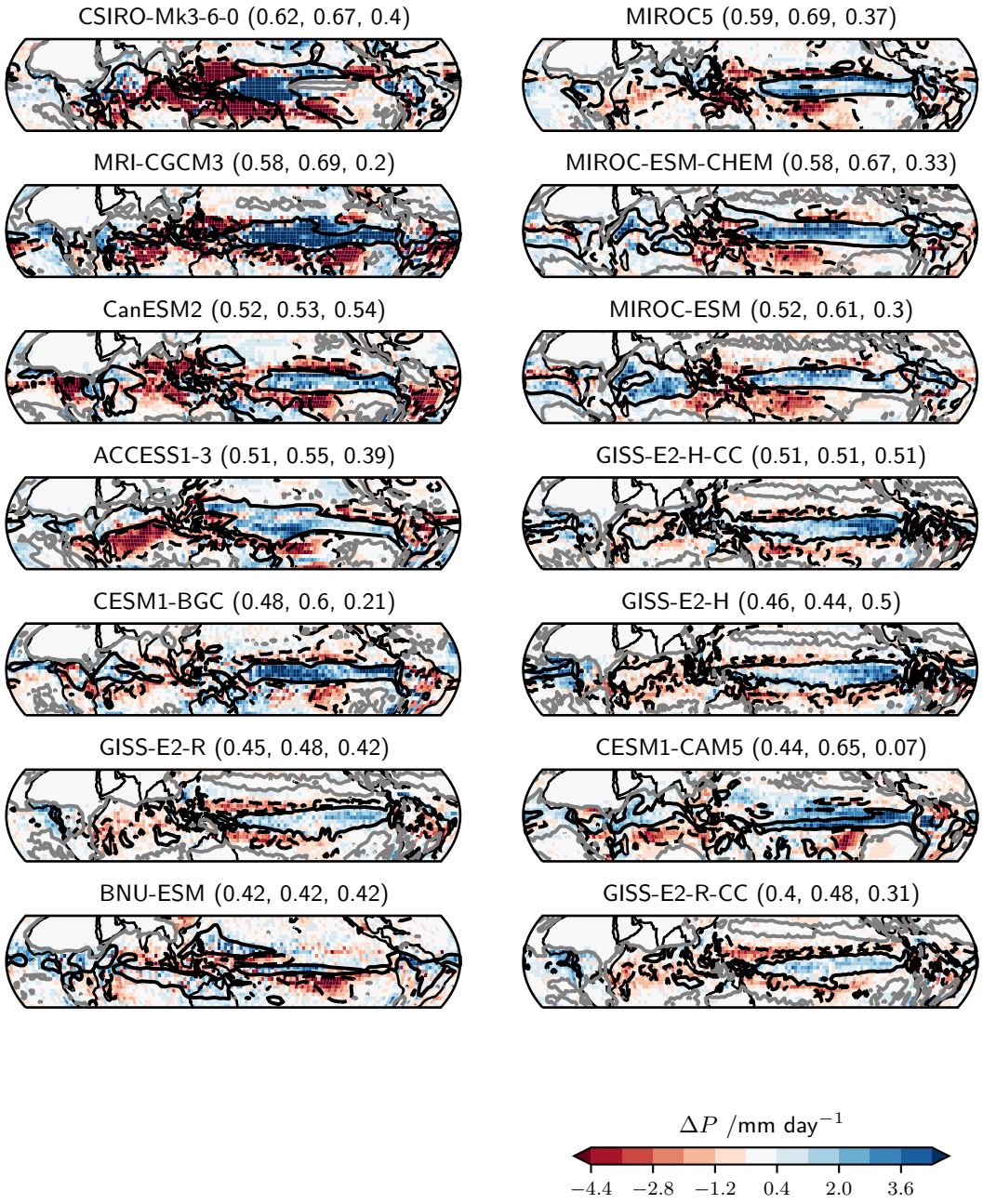

Figure 3.11: 2080-2099 (RCP8.5) minus 1980-1999 (historical) DJF composite mean simulated and diagnosed precipitation anomalies for 27 CMIP5 models in descending order of diagnosis performance. Solid and dashed black contour lines in indicate the ± 1 mm day^{-1} simulated precipitation anomalies. Colours show the diagnosed precipitation anomaly, and areas where the estimated probability of a positive diagnosed anomaly (Equation 3.12) is between 0.1 and 0.9 are masked. Grey lines show the 4 mm day^{-1} contour of the predictive inter-quartile range, ΔP_{IQR} (Equation 3.13). The triplets in parentheses indicate the spatial correlation over the tropical, oceanic, and land grid points, respectively.

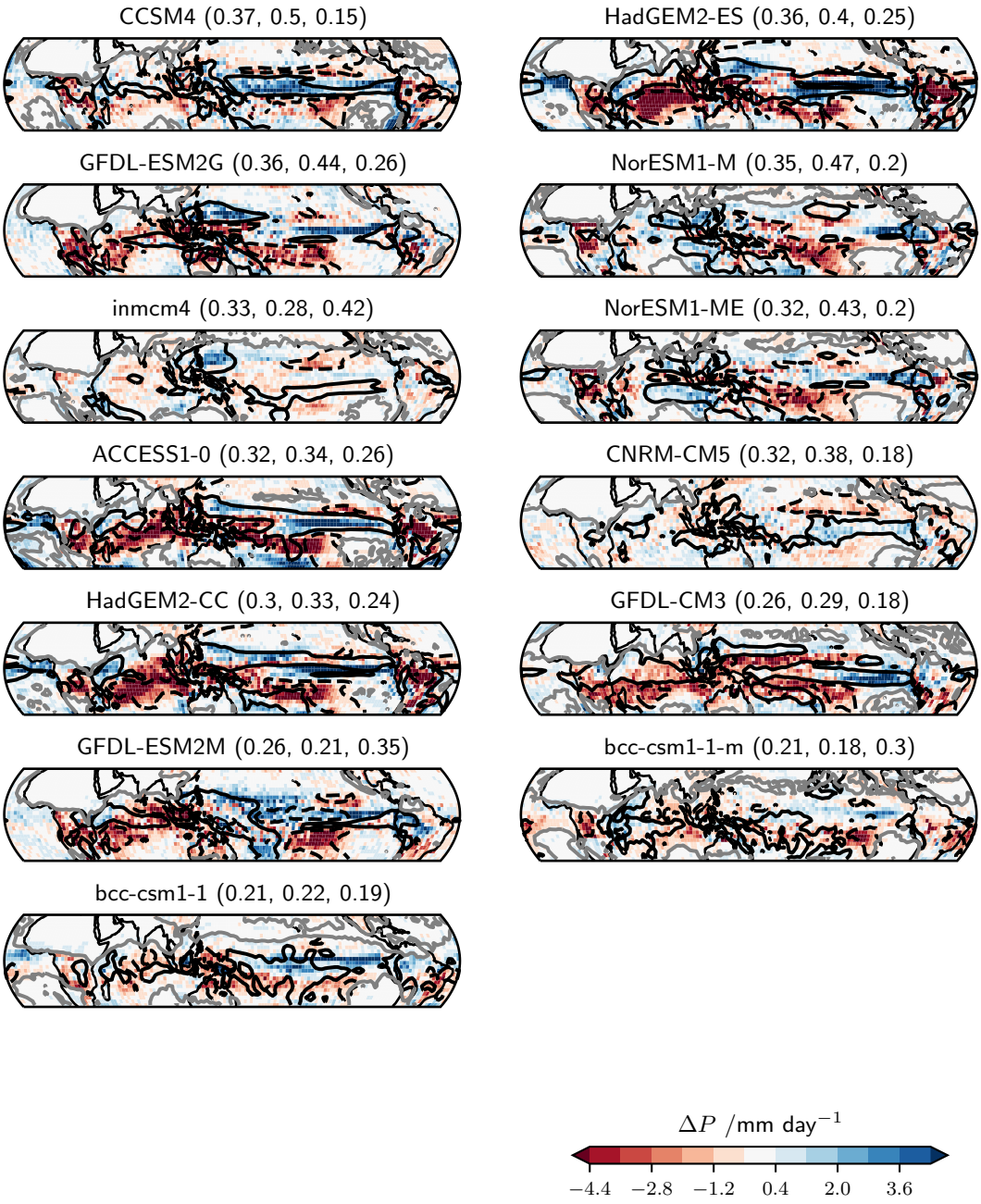

Figure 3.11 (Continued)

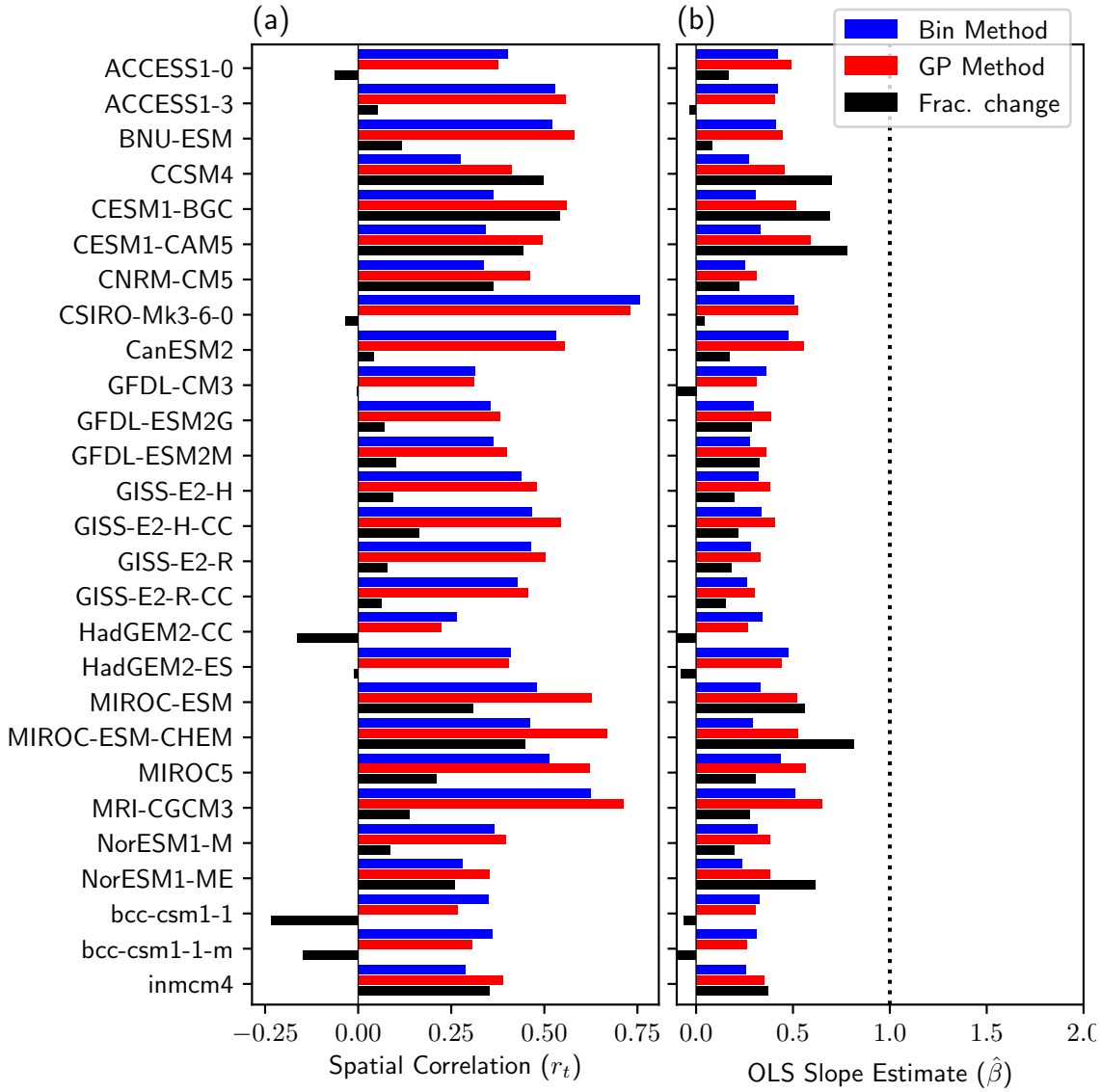

Figure 3.12: Comparison of diagnosis performance for the 2080-2099 (RCP8.5) minus 1980-1999 (historical) simulated precipitation change for 27 models in CMIP5: (a) spatial correlations between simulations and diagnoses and (b) slope estimate from regressing diagnosed on simulated changes. Blue bars indicate the Lambert et al. *(2017) binning method, red bars show the revised GP method (Section 3.3.3) and black bars demonstrate the difference.*

3.4.2 $\hat{P}$ Changes and Climate Perturbations

The binning (Lambert *et al.*, 2017) and revised GP (Section 3.3.3) diagnosis methods, share a major simplification. Both methods assume tropical precipitation as a function of SAT and RH, relative to their tropical means, is invariant under climate perturbations, except for a scaling by the fractional change in tropical mean precipitation. Returning to the GP method framework, let $\hat{P}'$ be the mean precipitation from the GP method fitted to perturbation conditions, such as El Niño observations or global warming simulations. Consistent with Section 3.3.2, let $\hat{P}(q_H, q_T)$ represent control precipitation as a function of the control tropical quantiles. As the diagnosed precipitation change is $\Delta P = s\hat{P}(q_{H'}, q_{T'}) - \hat{P}(q_H, q_T)$, optimal performance would be achieved if:

$$s\hat{P}(q_{H'}, q_{T'}) = \hat{P}'(q_{H'}, q_{T'}), \tag{3.17}$$

where s is the corresponding fractional change in tropical mean precipitation.

Testing the equality in Equation 3.17 is equivalent to testing whether $\hat{P}' - s\hat{P}$ is significantly different from zero. In the following sections, we evaluate $s\hat{P}$ and $\hat{P}'$ on a fine, 0.01×0.01 mesh of values in (q_H, q_T)-space for control and perturbation months. A Kolmogorov-Smirnov test is applied to seasonal composites of $s\hat{P}$ and $\hat{P}'$ to examine whether the distributions change significantly, at the 5%-level, in regions of (q_H, q_T)-space between the perturbation and scaled control conditions. Subsequently, if significant changes are detected for certain regions, we examine tropical grid points located within those regions under either control or perturbation conditions.

El Niño-Southern Oscillation $\hat{P}$ Changes

Comparing the DJF composite mean El Niño precipitation, $\hat{P}_{EN}$, and the corresponding scaled neutral precipitation, $s\hat{P}_{neutral}$, the magnitude differences are less than 1 mm day^{-1} for the majority of (q_H, q_T)-space, as shown by Figure 3.13(a). Only two small regions in (q_H, q_T)-space demonstrate a significant change via a Kolmogorov-Smirnov test at the 5% level: increases surrounding $(0.9, 0.3)$ (A) and decreases near $(0.96, 0.5)$ (B). During 40-50% of neutral DJF periods, grid points in the eastern equatorial Pacific populate region (A) of (q_H, q_T)-space (Figure 3.13(b)). Under El Niño conditions, sea surface warming in this area reduces the zonal SST gradient across the Pacific, contributing to an eastward shift in the Walker circulation via the Bjerknes feedback. This results in substantial precipitation increases over the central and eastern equatorial Pacific. Consequently, eastern equatorial Pacific grid points are only within (A) for 20% or fewer El Niño DJF periods due to the large relative SAT changes (Figure 3.13(c)). Furthermore, across the tropics only a handful of grid points are consistently within (A)

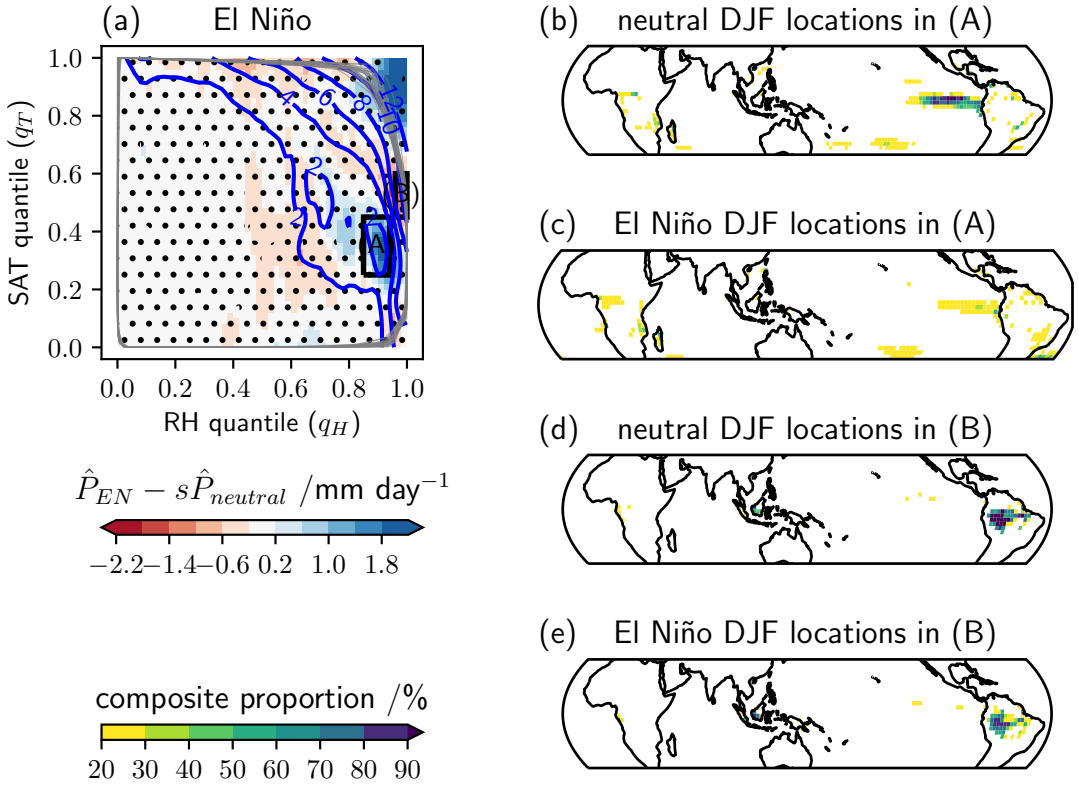

Figure 3.13: (a) Colours indicate differences between the 1979-2016 DJF El Niño composite mean precipitation, $\hat{P}_{EN}$, and the corresponding neutral composite mean precipitation, $\hat{P}_{neutral}$, scaled by the El Niño minus neutral fractional mean change in tropical precipitation, s, in (q_H, q_T)-space. Stippling shows where these differences are insignificant, via a Kolmogorov-Smirnov test at the 5% level, relative to interannual variability. Grey lines demarcate the convex hulls of grid points in (q_H, q_T)-space for each El Niño and neutral month in the composites. Blue contour lines denote $s\hat{P}_{neutral}$ at 2 mm day^{-1} intervals. Black boxes highlight two regions (A, B) of large, significant differences. (b, c) Colours show the composite proportion for grid points within region (A) of (q_H, q_T)-space for neutral and El Niño events, respectively. (d, e) As in (b, c), but for grid points within region (B) of (q_H, q_T)-space.

during El Niño events in comparison to neutral events. The depopulation of (A) during El Niño conditions weakens the constraint on the shape of $\hat{P}$, which may contribute to the non-zero $\hat{P}_{EN} - s\hat{P}_{netural}$. However, this weaker constraint would result in larger GP model confidence intervals in this region, and hence the precipitation change is likely insignificant with respect to GP model uncertainty (Section **??**).

In contrast, region (B) is consistently populated by grid points in tropical rainforest regions of the maritime continent and the Amazon basin for both El Niño and neutral DJF periods, as shown by Figures 3.13(d, e). This suggests precipitation as a function of RH and SAT quantiles significantly changes over these tropical land areas during El Niño events. Hence, other factors such as free tropospheric moisture or temperature changes

may affect precipitation changes in these locations, inconsistent with the method assumptions. For instance, if RH increases near the surface but decreases aloft, with no change in the lapse rate, convection near the surface would be enhanced. However, entrainment of relatively drier free tropospheric air would suppress convective plumes, mitigating or even reversing any enhancement from the surface. These additional factors affecting the diagnosis method performance are examined further in Section 3.4.3.

Despite these performance issues with regions (A) and (B), both areas of (q_H, q_T)-space are situated very close to the convex hull of the observation points. Consequently, the shape of $\hat{P}_{EN}$ and $\hat{P}_{neutral}$ is weakly constrained, with relatively high GP model uncertainty. Furthermore, (A) and (B) are quite minor areas of (q_H, q_T)-space, containing a small fraction of, albeit important, tropical grid points during El Niño and neutral events. Therefore, the non-zero $\hat{P}_{EN} - s\hat{P}_{neutral}$ in regions (A) and (B) may only substantially affect diagnosis performance in spatially small areas, relative to the rest of the tropics. Indeed, the observed El Niño precipitation increases over the eastern equatorial Pacific, and decreases over the Amazon basin, are only weakly over-estimated or miss-diagnosed, as shown by Figure 3.6(e, f).

Similar to the El Niño changes, the DJF composite mean La Niña precipitation, $\hat{P}_{LN}$, minus $s\hat{P}_{neutral}$ changes in (q_H, q_T)-space are relatively small (Figure 3.14). Two small regions demonstrate significant changes: decreases near $(0.96, 0.3)$ (A) and weak increases surrounding $(0.9, 0.62)$ (B). Under La Niña conditions, region (A) is more frequently populated with with grid points in the eastern equatorial Pacific, relative to neutral conditions. This is the opposite result for the similarly defined region (A) for the El Niño $\hat{P}$ changes. Subsequently, the shape of $\hat{P}$ in (A) may be much better constrained for La Niña events compared to neutral events. In addition, region (A) contains a large fraction of tropical rainforest grid points in both cases, again highlighting diagnosis performance issues over these areas. Region (B) broadly represents the ITCZ over the Atlantic, Indian and eastern Pacific oceans for both neutral and La Niña periods. In these areas, factors other than local SAT and RH changes may be affecting precipitation changes. However, in (B), the typical magnitude of $\hat{P}_{LN} - s\hat{P}_{neutral}$, 0.2-0.6 mm day^{-1}, is quite small relative to $s\hat{P}_{neutral}$, which ranges between 3-9 mm day^{-1}. Therefore, the differences between $\hat{P}_{LN}$ and $s\hat{P}_{neutral}$ only lead to minor issues with diagnosis performance. Referring back to Figures 3.7(e,d), we note small over-estimated precipitation decreases over the Atlantic, central Indian and eastern Pacific oceans, relative to observations. Similar to the El Niño case, this is consistent with the differences between $\hat{P}_{LN}$ and $s\hat{P}_{neutral}$ in these regions.

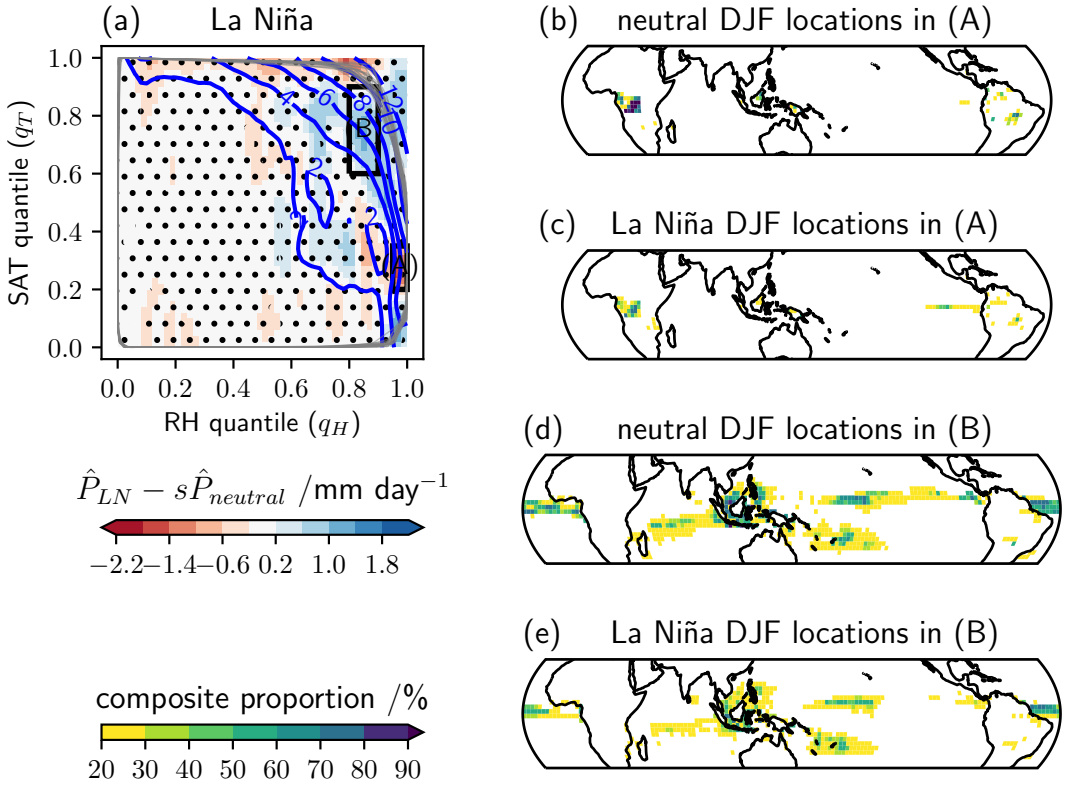

Figure 3.14: As in Figure 3.13, but for the 1979-2016 DJF La Niña composite.

Global Warming $\hat{P}$ Changes

Following the ENSO analysis, this subsection examines differences between the 2080-2099 (RCP8.5) mean precipitation, $\hat{P}_{rcp85}$, and the corresponding scaled 1980-1999 (historical) mean precipitation, $s\hat{P}_{hist.}$, for the CMIP5 multi-model ensemble (MME). Results are presented for DJF means, for direct comparison with the ENSO changes. However, qualitatively similar results are obtained for the other seasons. Figure 3.15 shows $\hat{P}_{rcp85} - s\hat{P}_{hist.}$ for each model, the MME mean, and the equivalent ERA-Interim-GPCP El Niño and La Niña $\hat{P}$ differences for comparison. The MME mean indicates only relatively minor $\hat{P}_{rcp85} - s\hat{P}_{hist.}$ differences across (q_H, q_T)-space, with generally small increases ($\hat{P}_{rcp85} > s\hat{P}_{hist.}$) for $q_H > 0.5$ and $q_T > 0.5$ and decreases ($\hat{P}_{rcp85} < s\hat{P}_{hist.}$) for $q_H < 0$. Comparing this pattern to $s\hat{P}_{hist.}$, this indicates a slight wet-get-wetter and dry-get-drier response. However, magnitude of the differences are largely less than 0.6 mm day^{-1}, suggesting for the MME mean relatively small $\hat{P}$ changes under simulated global warming. This is consistent with the ENSO results, discussed previously, where the shape of $\hat{P}$ is similar for ERA-Interim-GPCP El Niño, neutral and La Niña composites.

Amongst the CMIP5 ensemble, several groups of models display relatively consistent anomaly patterns in (q_H, q_T)-space. These similarities could partially be due to shared or related model components (Knutti *et al.*, 2013), for instance the HadGEM2 and ACCESS1 families use a common atmosphere model. In addition, similar $\hat{P}$ differences could also be due to a shared physical behaviour under global warming between quite

independent models. We focus on three model groups for practicality. Firstly, group 1 models (ACCESS1-0, ACCESS1-3, CanESM2, CSIRO-Mk3-6-0) generally indicate large increases ($\hat{P}_{rcp85} - s\hat{P}_{hist.} \geq 2$ mm day^{-1}) near $q_T = 0.8$ for $0.3 \leq q_H \leq 0.9$ and weaker decreases ($\hat{P}_{rcp85} - s\hat{P}_{hist.} \leq -1$ mm day^{-1}) near $(0.95, 0.2)$. Secondly, models in group 2 (MRI-CGCM3, MIROC-ESM-CHEM, CESM1-CAM5, HadGEM2-CC, GFDL-CM3) show increases more focussed around $(0.4, 0.9)$ with decreases near $(0.8, 0.9)$. Finally, in group 3 (HadGEM2-ES, HadGEM2-CC), large increases are evident near $(0.85, 0.6)$ and large decreases ($\hat{P}_{rcp85} - s\hat{P}_{hist.} \leq -2$ mm day^{-1}) around $(0.4, 0.9)$. In the remainder of this section, one representative model from each group will be explored in greater detail: ACCESS1-0, MRI-CGCM3 and HadGEM2-ES, for groups 1-3, respectively.

The DJF composite $\hat{P}_{rcp85} - s\hat{P}_{hist.}$ differences for ACCESS1-0 are demonstrated by Figure 3.16. Region (A), representative of areas where $\hat{P}_{rcp85}$ is significantly larger than $s\hat{P}_{hist.}$, generally contains grid points from the equatorial Atlantic, Indian and Pacific oceans, as well as equatorial South America, during the late twentieth century simulation. In the late twenty-first century simulation, there is a large decrease in equatorial South America grid points typically populating region (A). Therefore, (A) represents a mixture of land and ocean grid points in the late twentieth century, but mainly ocean grid points in the late twenty-first century. As discussed in Chapter 2, orography and vegetation over tropical land erode the suitability of the weak temperature gradient (WTG) approximation, relative to tropical oceans. Hence, for ACCESS1-0 in region (A), the assumptions of the diagnosis method are likely better satisfied in the late twenty-first century simulation. Consequently, factors other than surface conditions may contribute more to the shape of $s\hat{P}_{hist.}$, relative to $\hat{P}_{rcp85}$, leading to $s\hat{P}_{hist.} - \hat{P}_{rcp85}$ differences.

For ACCESS1-0 in region (B) (Figure 3.16), $\hat{P}_{rcp85}$ is significantly less than $s\hat{P}_{hist.}$, and mainly consists of southern subtropical ocean grid points in both present day and global warming simulations (Figure 3.16). Similar to region (A), weaknesses in the WTG approximation over the subtropics (Chapter 2 and Figure 2.4) are likely to contribute to $\hat{P}$ differences in region (B). For instance, subtropical stratiform precipitation changes, such as along the southern flank of the SPCZ, are mainly due to large scale circulation changes (Widlansky *et al.*, 2012). These are only indirectly linked with local surface RH and temperature changes. Additional factors affecting $\hat{P}$ changes and diagnosis performance are examined further in Section 3.4.3.

Comparing the ACCESS1-0 (Figure 3.16(a)) with HadGEM2-ES $\hat{P}_{rcp85} - s\hat{P}_{hist.}$ (Figure 3.17(a)), differences are evident across (q_H, q_T)-space, despite a common atmosphere model. This suggests some sensitivity of $\hat{P}$ differences to the ocean and land surface model components and the coupling scheme. For HadGEM2-ES, in region (A), $q_T > 0.85$ and $0.2 < q_H < 0.6$, $\hat{P}_{rcp85}$ is significantly less than $s\hat{P}_{hist.}$, whereas there are

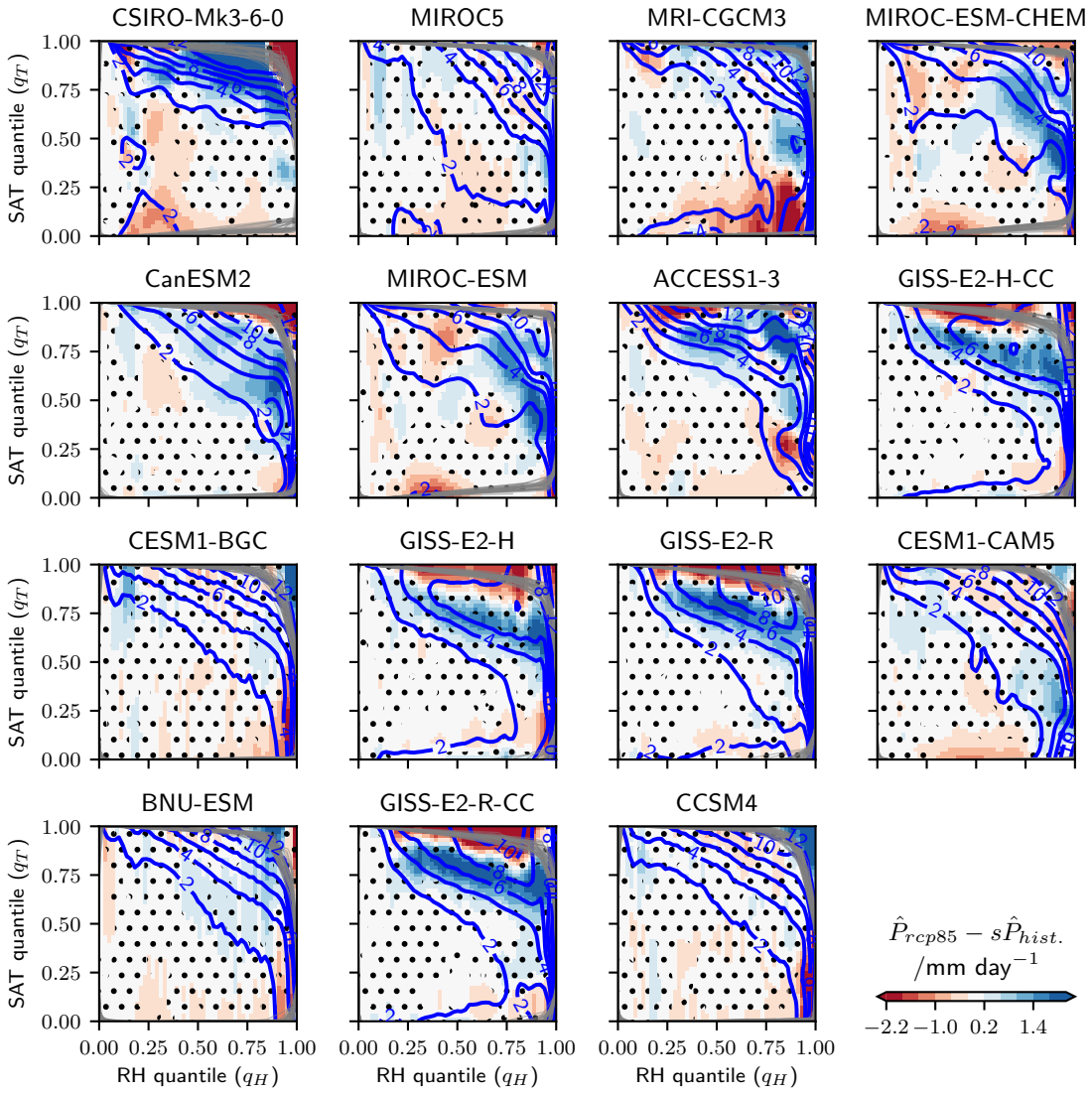

Figure 3.15: Colours indicate differences between the 2080-2099 (RCP8.5) DJF composite mean precipitation, $\hat{P}_{rcp85}$, and the corresponding 1980-1999 (historical) composite mean precipitation, $\hat{P}_{hist.}$, scaled by the corresponding fractional change in tropical mean precipitation, s, in (q_H, q_T)-space for 27 CMIP5 model simulations, ordered by diagnosis performance (c.f. Figure 3.11), and the CMIP5 multi-model ensemble mean (MME-mean). Stippling shows where these differences are insignificant, via a Kolmogorov-Smirnov test at the 5% level, relative to interannual variability. Grey lines demarcate the convex hulls of grid points in (q_H, q_T)-space for each month over the 2080-2099 or 1980-1999 periods. Blue contour lines denote $s\hat{P}_{hist.}$ at 2 mm day^{-1} intervals. Equivalent ERA-Interim-GPCP El Niño and La Niña $\hat{P}$ changes from Figures 3.13(a) and 3.14(a) are repeated for comparison.

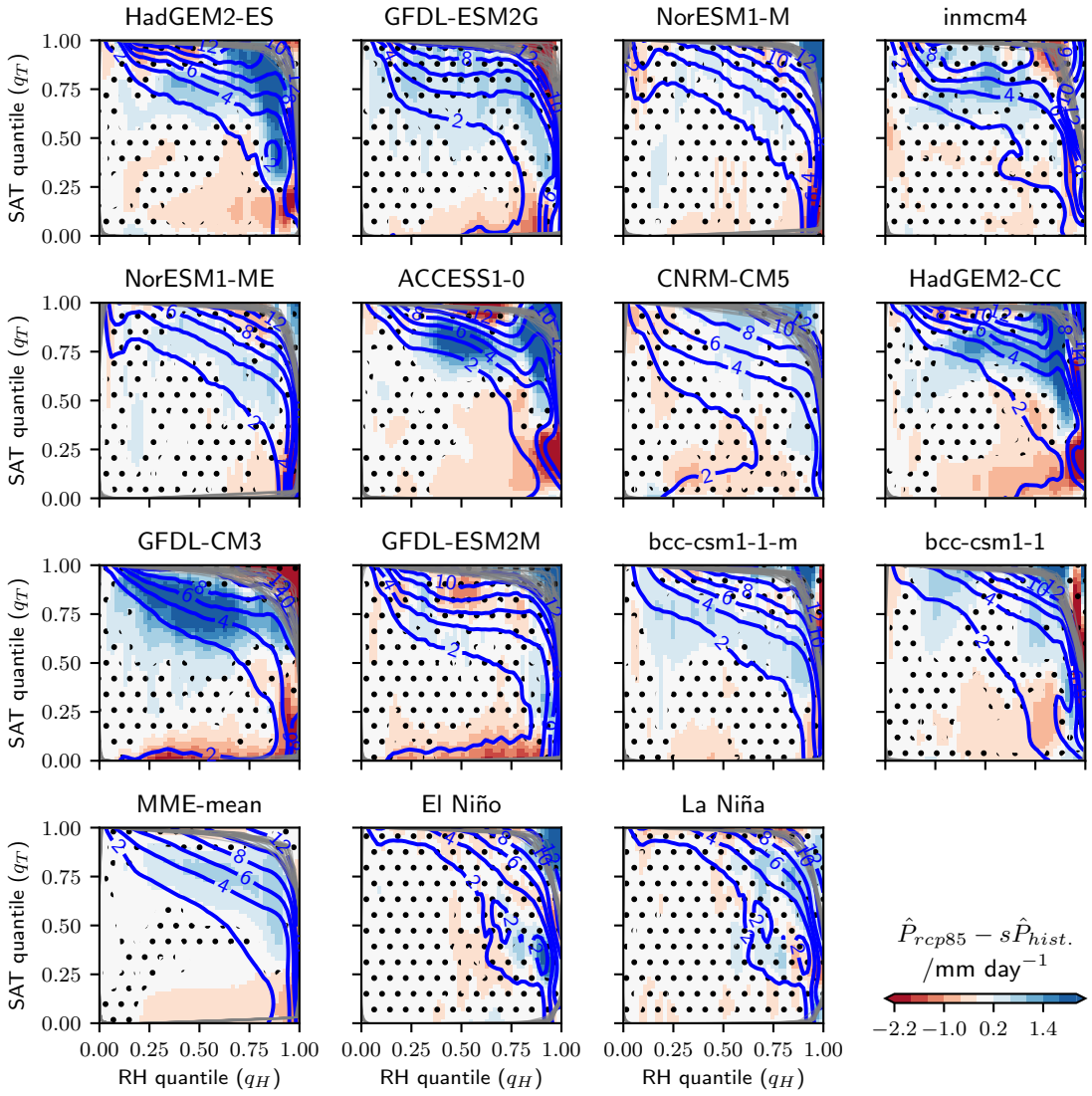

Figure 3.15 (Continued)

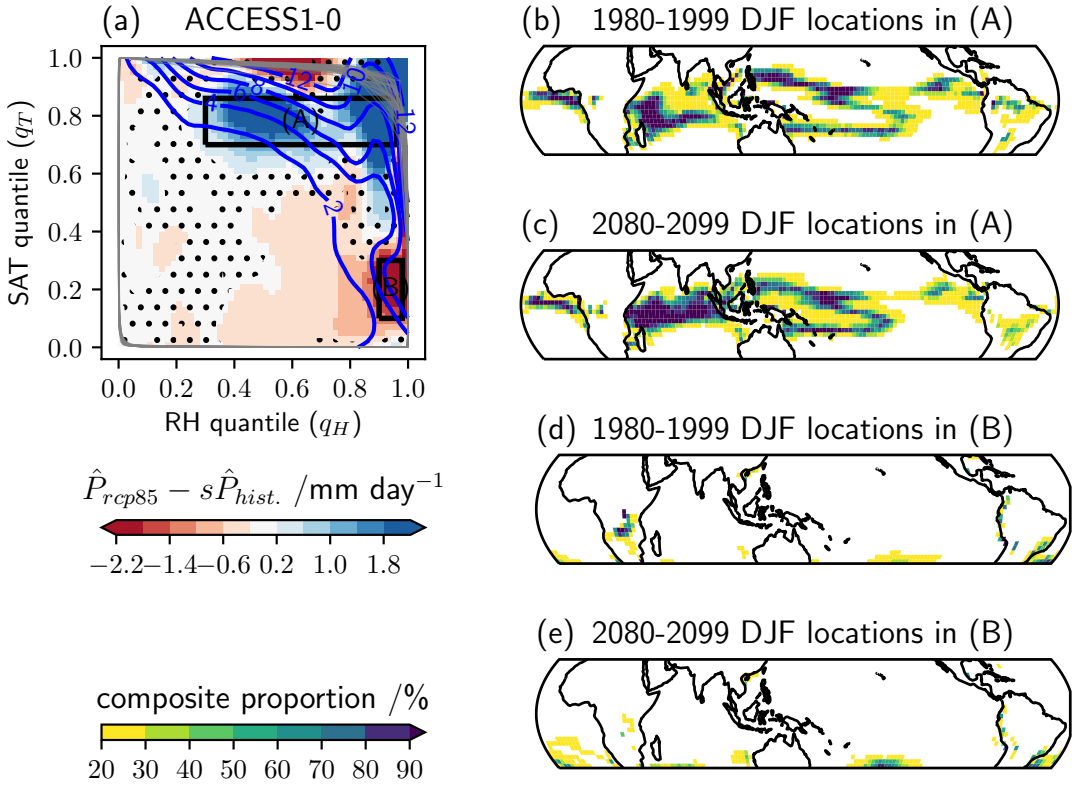

Figure 3.16: As in Figure 3.13, but for the ACCESS1-0 simulated 2080-2099 (RCP8.5) minus 1980-1999 (historical) DJF composite mean precipitation anomaly.

few significant differences for ACCESS1-0. Examining region (A) for HadGEM2-ES, it is consistently populated with grid points in the western equatorial Pacific in both present-day and global warming simulations, and grid points in the eastern Indian Ocean largely in the present-day simulation. Consequently, $\hat{P}$ is well constrained by similar oceanic grid points in both periods, so factors other than surface RH and SAT changes may be affecting simulated precipitation changes in this region. A second area of substantial differences between ACCESS1-0 and HadGEM2-ES $\hat{P}_{rcp85} - s\hat{P}_{hist.}$ differences is region (B), where $0.3 < q_T < 0.8$ and $q_H \approx 0.85$, and $\hat{P}_{rcp85}$ is significantly larger than $s\hat{P}_{hist.}$ in HadGEM2-ES,. Consistent with region (A), the grid points within (B) represent similar locations, in the off-equatorial eastern Pacific, in both simulations. Therefore, for HadGEM2-ES, over large tropical ocean areas, $\hat{P}$ significantly changes between present day and global warming simulations.

The MRI-CGCM3 $\hat{P}_{rcp85} - s\hat{P}_{hist.}$ pattern is substantially different across (q_H, q_T)-space relative to both ACCESS1-0 and HadGEM2-ES, as shown by Figure 3.18. Notably, in cool and relatively high RH locations (region (A)), $\hat{P}_{rcp85}$ is substantially less than $s\hat{P}_{hist.}$. For near median SAT and relatively high RH locations (region (B)) $\hat{P}_{rcp85}$ is significantly greater than $s\hat{P}_{hist.}$. These MRI-CGCM3 differences are quite different those of ACCESS1-0 and HadGEM2-ES, which may be linked with differences in model parametrisations, since the atmosphere and ocean components of MRI-CGCM3 are quite

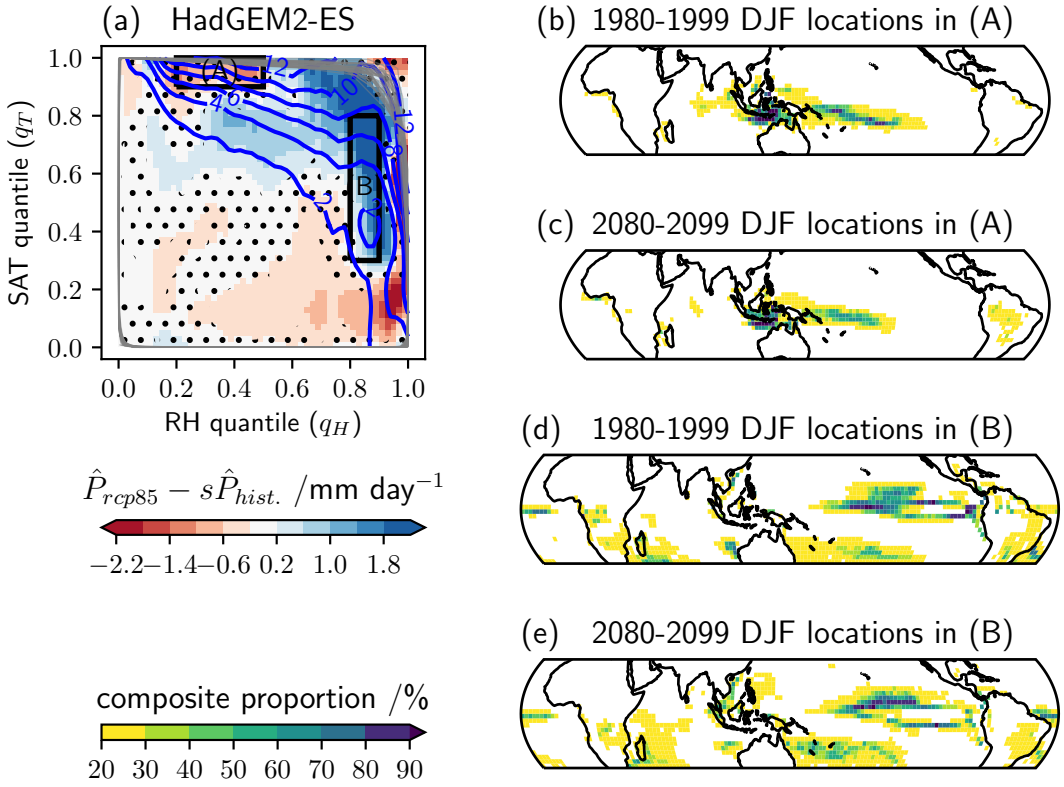

Figure 3.17: As in Figure 3.16, but for the HadGEM2-ES simulated 2080-2099 (RCP8.5) minus 1980-1999 (historical) DJF composite mean precipitation anomaly.

distinct from ACCESS1-0 and HadGEM2-ES. A more consistent result for MRI-CGCM3 is that similar, oceanic grid points populate regions (A) and (B) in both present day and global warming periods, again suggesting factors other than surface RH and SAT changes may be linked with the simulated precipitation changes.

3.4.3 Additional Factors Affecting Diagnosis Performance

In the previous section, we established how weak diagnosis performance of global warming precipitation changes is linked with significant $\hat{P}$ changes in regions of (q_H, q_T)-space under climate perturbations. One reason for these changes could be due to differences in the suitability of the WTG approximation between present day and future scenarios. This would imply factors other than surface condition changes would be linked with precipitation changes. This is explored further in this section, alongside model $\hat{P}$ biases relative to present day observations.

Surface-Free Troposphere RH changes under Global Warming

Several processes contribute to a coupling between tropical near surface, boundary layer and free troposphere, linking relative humidity at the surface and aloft. In large scale ascent regimes, boundary layer RH anomalies are vertically advected into the lower free troposphere. In deep convective plumes, strong updrafts vertically transport moisture vapour and small hydrometeors. Concordant with these convective plumes, entrainment

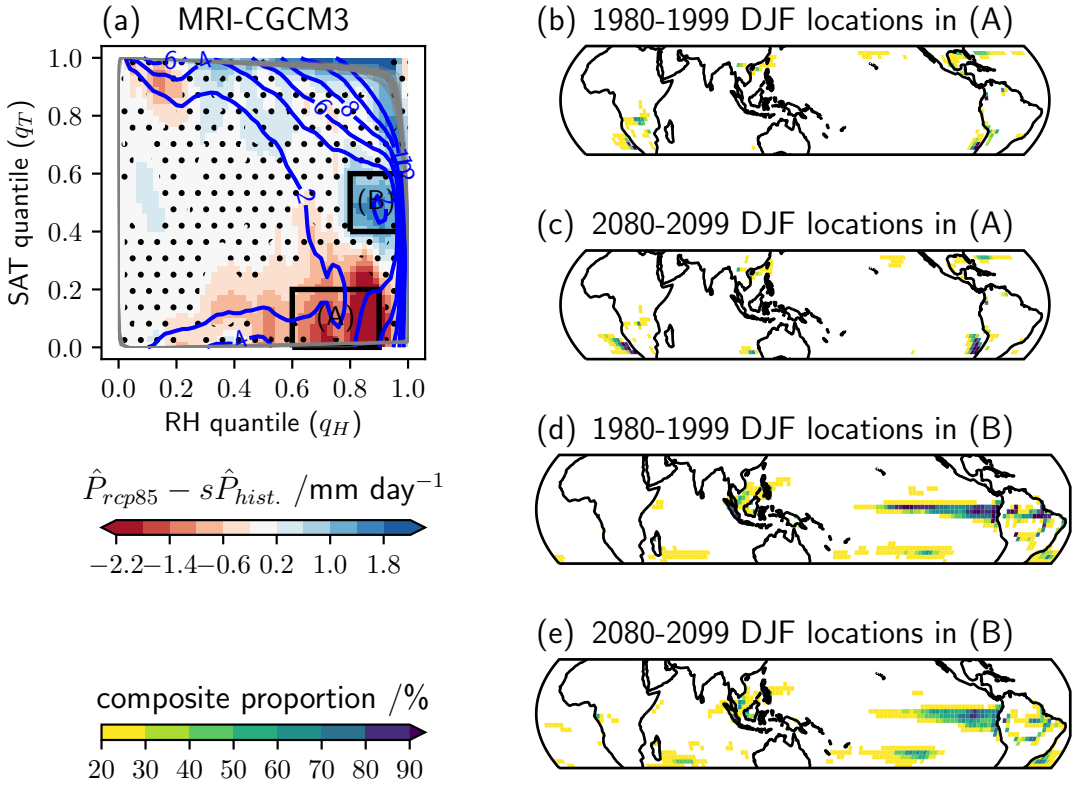

Figure 3.18: As in Figure 3.16, but for the MRI-CGCM3 simulated 2080-2099 (RCP8.5) minus 1980-1999 (historical) DJF composite mean precipitation anomaly.

in the boundary layer and detrainment aloft acts to link free tropospheric RH to the near surface RH. At smaller scales, turbulence and diffusion across the boundary layer-free troposphere interface also contributes to vertical mixing and hence RH coupling.

One hypothesis to explain weak diagnosis performance is a change in the local vertical coupling between the boundary layer and free troposphere. Consider a region with high surface RH and SAT relative to the tropical mean, under both present day and global warming mean state conditions. Hence, convective initiation in the boundary layer over this region is highly favourable in both cases, due to the relatively high low-level moist static energy. Assuming a strong coupling between surface and free tropospheric RH in the present day, convective plumes over this region would deepen via entrainment of high environmental RH aloft, leading to heavy precipitation. Under global warming conditions, if RH aloft increases relative to surface RH, enhanced entrainment would amplify convection, increasing precipitation. Conversely, if RH aloft decreases relative to surface RH, detrainment would act to suppress or even cap convective plumes at lower levels, resulting in reduced precipitation. Free tropospheric RH changes under global warming would largely affect precipitation only if deep convection continues to be triggered in the boundary layer. Hence, if surface conditions become unfavourable for convective initiation, RH increases aloft may only lead to mid-level convection, contributing to relatively smaller precipitation changes.

In order to examine vertical RH coupling, near surface RH (RH'_{surf}) versus 850 hPa RH changes (RH'_{850}), for observed El Niño minus neutral and CMIP5 RCP8.5 minus historical simulations, are compared in Figure 3.19. Two distinct regimes are evident in the ENSO case and for each model of the CMIP5 ensemble. One regime is an approximately linear association, where $RH'_{surf} \approx RH'_{850}$. There is relatively high inter-model variability in the spread of simulated RH changes under global warming. For instance, in the ACCESS1 and HadGEM2 model families, RH'_{surf} typically ranges between -25% to +10%, whereas for bcc-csm1-1 this range is -10% to +5%. El Niño changes cover an even smaller range, between -5% to +5%. The second regime is characterised by relatively constant surface RH or only weak ($< +5\%$) increases, and large variability in the RH'_{850} changes, encompassing both increases and decreases. There is little evidence of a comparable regime where RH aloft remains quite constant but RH at the surface varies widely. This suggests that under ENSO or global warming changes, surface RH changes only if RH changes aloft. However, RH changes aloft can occur independently of changes at the surface.

The two regimes identified in the scatter plots of Figure 3.19 imply a regional sensitivity to changes in boundary layer-free tropospheric coupling, under El Niño or global warming perturbations. To explore this further, Figure 3.20 demonstrates maps of $RH'_{850} - RH'_{surf}$ for each case. Small magnitude $RH'_{850} - RH'_{surf}$ areas indicate $RH'_{850} \approx RH'_{surf}$, and larger positive and negative regions denote $RH'_{850} > RH'_{surf}$ and $RH'_{850} < RH'_{surf}$, respectively. For El Niño minus neutral conditions in ERA-Interim, RH aloft increases more than at the surface along the central and eastern equatorial Pacific. Over the eastern subtropical Atlantic, Indian and Pacific oceans, RH decreases aloft but remains relatively constant at the surface. Conversely, for eastern equatorial South America, RH decreases at the surface whilst RH aloft stays quite constant. The remaining tropical land and ocean regions demonstrate surface and aloft RH changes of an equivalent magnitude.

The El Niño minus neutral pattern of $RH'_{850} \approx RH'_{surf}$ is quite consistent with the simulated global warming changes. Across the CMIP5 ensemble, the largest $RH'_{850} - RH'_{surf}$ magnitudes are over tropical oceans, where the surface RH change is mainly weakly positive. Aloft, generally there are amplified RH increases over equatorial regions and RH decreases over the eastern subtropical ocean basins. Hence, comparing the RCP8.5 and historical simulations, or the ERA-Interim El Niño and neutral composites, RH aloft mainly increases in climatological ascent regions and decreases in descending regions. Under global warming, one mechanism for these changes over oceans is the simulated large scale circulation change, as introduced in Section 1.1.2. These circulation changes are linked with enhanced moisture convergence along the ITCZ, contributing the equato-

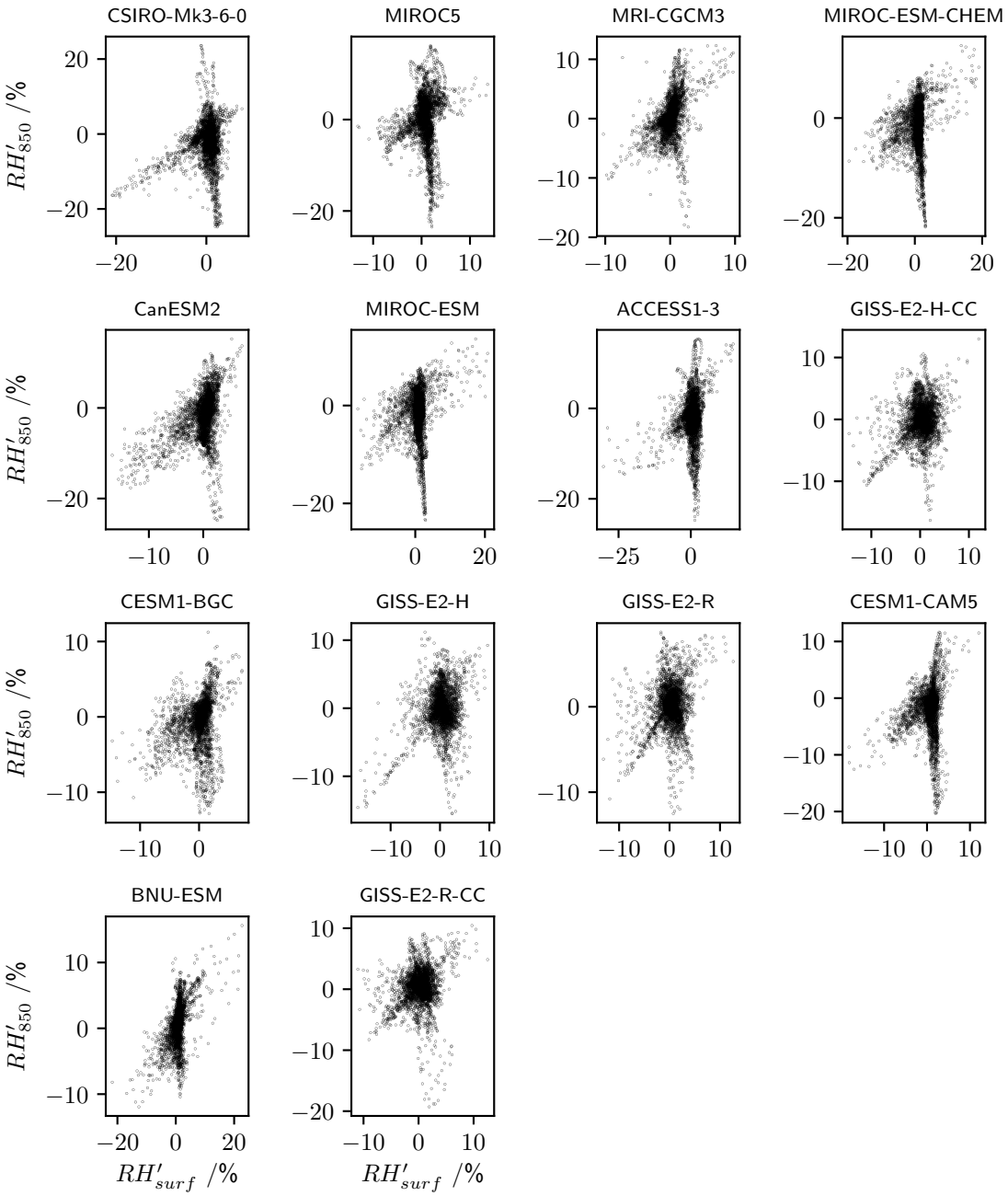

Figure 3.19: Scatter plots demonstrate grid point surface RH changes, RH'_{surf}, versus 850 hPa RH changes, RH'_{850}, for DJF El Niño minus neutral conditions in ERA-Interim-GPCP (final panel), and RCP8.5 minus historical conditions for 27 CMIP5 models (remaining panels, continued overleaf), ordered by diagnosis performance (c.f. Figure 3.11).

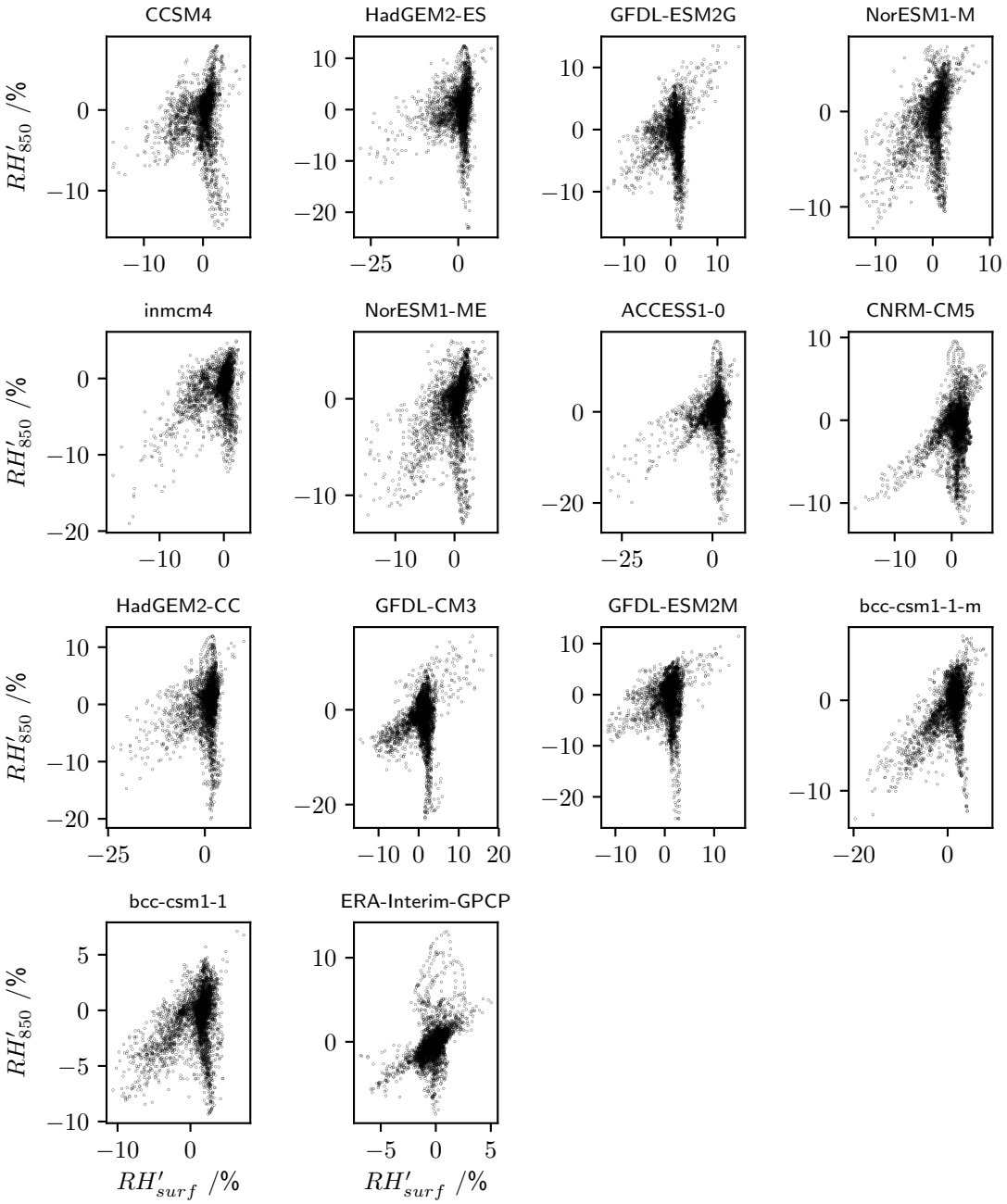

Figure 3.19 (Continued)

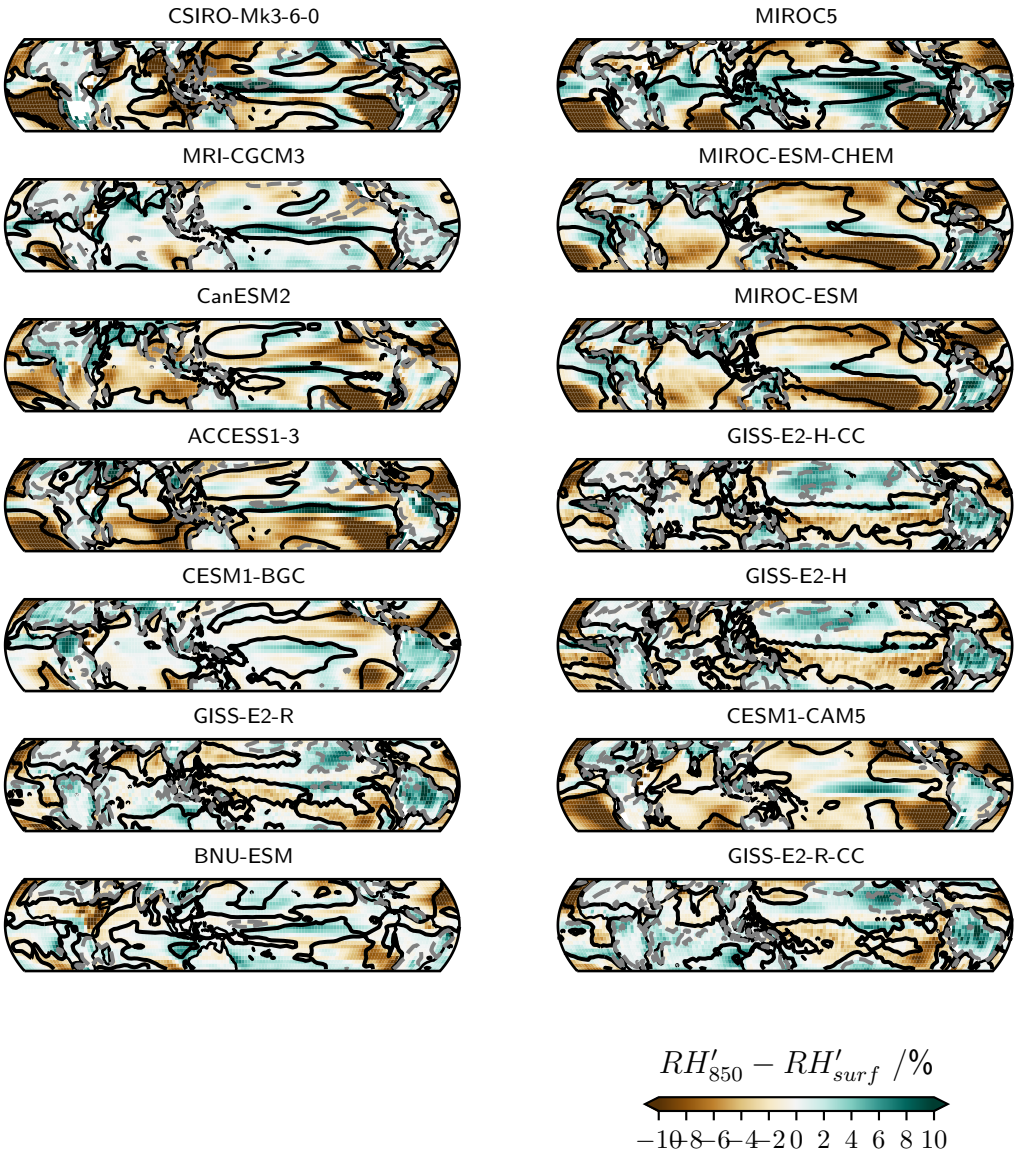

Figure 3.20: Colours show 850 hPa RH changes minus surface RH changes, $RH'_{850} - RH_{surf}$, for DJF El Niño minus neutral conditions in ERA-Interim-GPCP (final panel), and RCP8.5 minus historical conditions for 27 CMIP5 models (remaining panels, continued overleaf), ordered by diagnosis performance (c.f. Figure 3.11). Black solid and grey dashed lines denote the ±1 % surface RH change contours, respectively.

Figure 3.20 (Continued)

rial RH increases aloft, and tropospheric stabilisation over subtropical oceans, leading to reduced RH aloft (Sherwood *et al.*, 2010). Additionally, the tropical lapse rate generally follows a moist adiabat, with warming amplified aloft. Hence, without specific humidity changes, vertical advection of temperature anomalies would increase RH aloft in ascent regions and reduce RH aloft in descent regions.

Examining tropical land regions, global warming $RH'_{850} - RH'_{surf}$ differences are generally positive over equatorial South America, Africa and northern Australia. In these areas, surface RH typically decreases, implying relatively weaker RH decreases or even increases aloft. One hypothesis for why RH decreases over land are weaker aloft relative to the surface is based on differences in moisture limitation. Unlike tropical oceans, over the land surface RH changes are largely constrained by changes in evaporation from the limited soil moisture. Near-surface warming over land contributes to simulated RH decreases (Richter and Xie, 2008). Aloft, moisture supply over land is less restricted relative to the surface, due to horizontal advection and mixing from surrounding oceans, and hence RH decreases are typically smaller than at the surface.

Spatial variations in cloud feedback processes, due to differences in surface-free troposphere coupling, may also affect the pattern of $RH'_{850} - RH'_{surf}$. Atmosphere GCM simulations with uniform SST warming can demonstrate a large decrease in subtropical stratocumulus, leading to a strong positive cloud feedback on surface temperatures. This cloud reduction, and hence negative $RH'_{850} - RH'_{surf}$, is linked with a restricted surface evaporation increase due to weakened surface wind speeds, atmosphere-ocean temperature contrasts, and increasing surface RH (Webb and Lock, 2012). In heterogeneous SST warming experiments, the magnitude of the cloud feedback strongly depends on the pattern of surface temperature change. Isolated warming in the eastern subtropical Pacific, a climatological subsidence region, decreases lower tropospheric stability, reducing cloud cover and lower tropospheric RH. Conversely, surface warming in the climatological ascent region of the western tropical Pacific leads to enhanced warming in the free troposphere, increasing lower tropospheric stability and mitigating the cloud feedback in subsidence regions (Andrews and Webb, 2018).

In order to explore the effect of changes in boundary layer-free tropospheric coupling on diagnosis performance, Figure 3.21 compares observed or simulated precipitation changes, ΔP_{obs}, diagnosed precipitation changes, ΔP_{diag}, and $RH'_{850} - RH'_{surf}$ for observed El Niño and simulated global warming. One feature is consistent in several cases where the GP diagnosis method performs well (spatial correlation > 0.5), and ΔP_{obs} and ΔP_{diag} are quite linearly related, is that $RH'_{850} - RH'_{surf}$ generally increases with ΔP_{obs}. This is evident in the El Niño ERA-Interim changes and also CSIRO-Mk3-6-0, MRI-CGCM3, ACCESS1-3 and BNU-ESM global warming simulations. The inmcm4

simulation demonstrates similar behaviour, but the ΔP_{obs} magnitudes are relatively weak compared to other models, possibly leading to the smaller spatial correlation (0.39). Generally, in these cases, $RH'_{surf} \approx RH'_{850}$ for small precipitation increases ($\Delta P_{obs} < 5$ mm day^{-1}), $RH'_{850} > RH'_{surf}$ for larger increases and vice-versa for decreases. As discussed earlier, in regions where the magnitude of $RH'_{850} - RH'_{surf}$ is large, RH'_{surf} is typically weakly positive, such as across tropical oceans. Hence, for the GP method to diagnose large precipitation change in these areas, surface temperatures must change substantially relative to the tropical mean. This highlights the importance of SST pattern change in controlling tropical precipitation shifts over oceans (Xie *et al.*, 2010).

In CMIP5 models where the global warming precipitation change diagnosis performance is weaker (spatial correlation < 0.5), a general positive association between $RH'_{850} - RH'_{surf}$ and ΔP_{obs} is less evident. For HadGEM2-ES and HadGEM2-CC, equivalent regions where RH increases aloft are greater than at the surface have negative ΔP_{obs} and ΔP_{diag}, and the spatial correlations are 0.38 and 0.17, respectively. However, in MIROC-ESM and MIROC-ESM-CHEM, a similar feature is evident whilst the diagnosis method performance is much stronger (spatial correlations of 0.65 and 0.67, respectively). These model global warming results are quite inconsistent with El Niño observations, where amplified RH increases aloft and large precipitation increases are co-located. This highlights a discrepancy between simulated changes and observed variability in RH and precipitation.

For observed El Niño and simulated global warming, the assumption that surface and lower free tropospheric RH changes are equivalent, suggesting a vertical coupling, is only suitable for a portion of the tropics (Figure 3.19). In these regions, diagnosis performance is typically quite strong, and hence precipitation changes are largely characterised by SAT and RH changes. Over tropical oceans, under global warming, generally surface RH weakly increases, but changes aloft can be either strongly negative or positive. These surface-free troposphere differences are linked with circulation changes (Sherwood *et al.*, 2010). In models where the diagnosis method performs well, both simulations and diagnoses indicate precipitation increases where RH aloft increases relative to the surface, and vice-versa. This is consistent with El Niño observations in ERA-Interim. However, several models simulate different relationships between changes in the vertical RH profile and precipitation, inconsistent with present day variability. These results highlight the non-trivial relationship between the performance of Lambert *et al.* (2017) or GP methods and changes in the boundary layer-free troposphere coupling.

Present day model biases

To constrain which global warming projections are physically plausible, it is important to validate present day climate model simulations against comparable observations (Flato

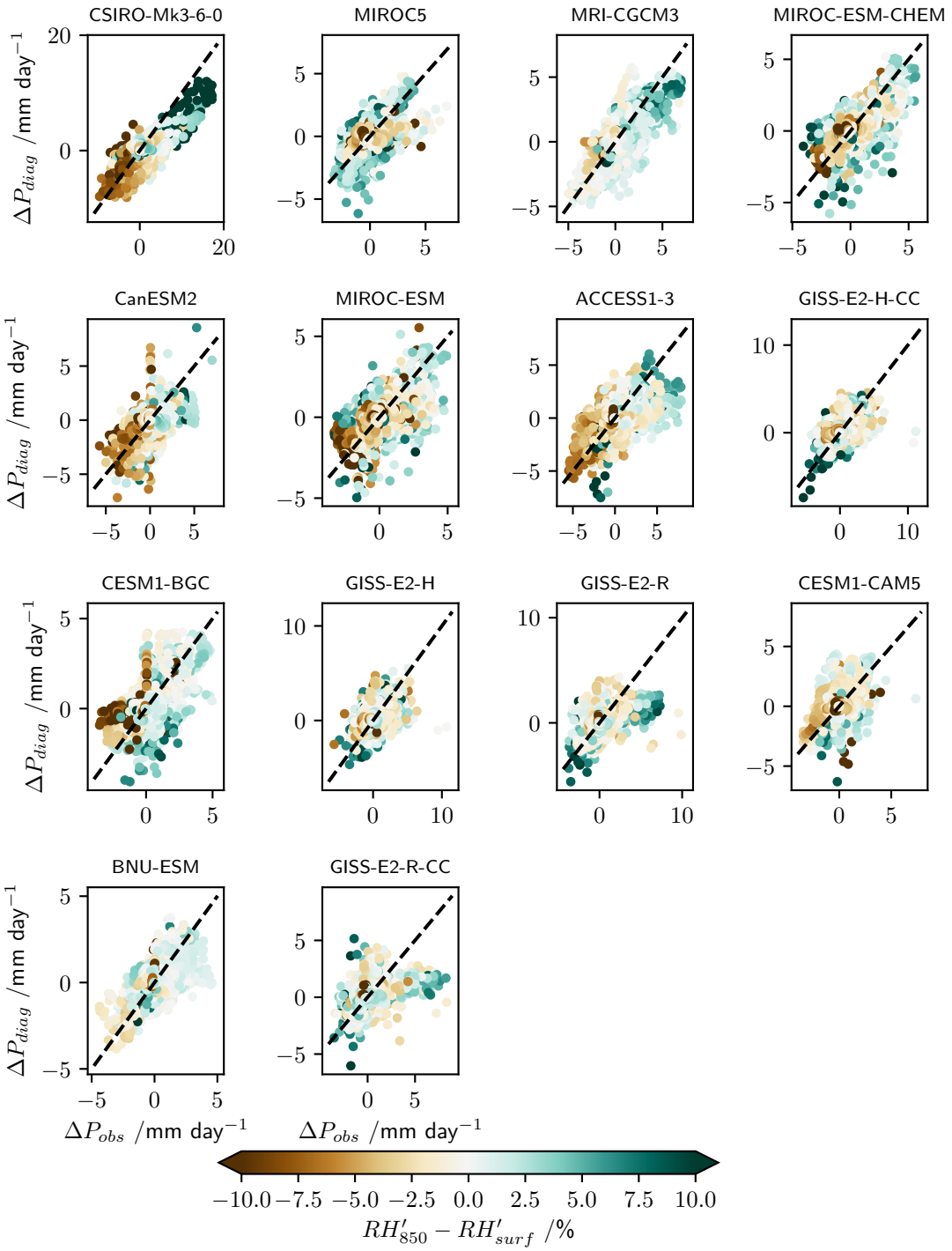

Figure 3.21: Diagnosed versus observed or simulated grid point precipitation changes for DJF El Niño minus neutral conditions in ERA-Interim-GPCP (top left corner), and RCP8.5 minus historical conditions for 31 CMIP5 models (remaining panels, continued overleaf), ordered by diagnosis performance (c.f. Figure 3.11). Colours indicate $RH'_{850} - RH_{surf}$ and dashed black lines show the diagonal.

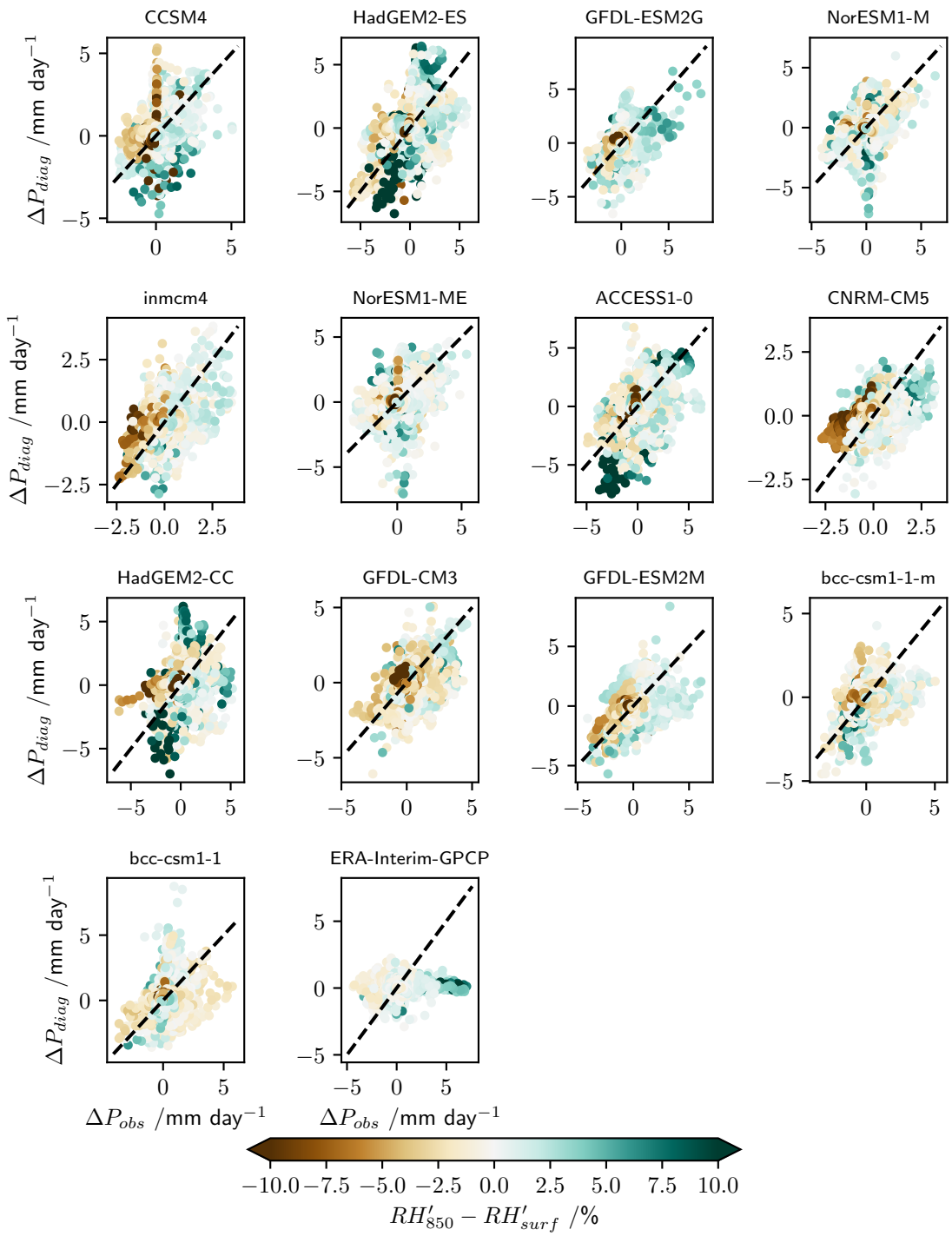

Figure 3.21 (Continued)

et al., 2013). Within the diagnosis framework, evaluating model minus observational precipitation bias in (q_H, q_T)-space is a useful and novel method for assessing present day tropical climate simulations. We compare $\hat{P}$ fitted to CMIP5 1980-1999 (historical) simulations with the ERA-Interim-GPCP observations, $\hat{P}_{obs}$, over the equivalent period. Results are presented here for the DJF composite means, however qualitatively similar results are evident for other seasons. The DJF model biases are demonstrated in Figure 3.22. The majority of CMIP5 models indicate a large positive bias > 2 mm day^{-1} for the majority of the relatively warmest locations ($q_T > 0.8$, $0.2 < q_H < 0.8$), as indicated by the multi-model ensemble mean (MME-mean) panel. This implies that the tropical maximum precipitation typically occurs at a warmer and less humid location relative to the observations. A small proportion of models (CanESM2, CSIRO-Mk3-6-0, MIROC-ESM-CHEM, MIRCO-ESM and HadGEM2-ES) also simulate a weaker negative bias < 1 mm day^{-1} close to the most humid and median temperature locations.

These CMIP5 model biases in (q_H, q_T)-space indicate significant differences in precipitation as a function of tropical RH and SAT quantiles amongst each climate model and relative to observations. The consistent positive precipitation bias in the relatively warmest regions of (q_H, q_T)-space is representative of the persistent and significant double ITCZ issue in climate models, where precipitation rates in the southern off-equatorial eastern Pacific are too large (Lin, 2007). Locally, this issue is linked with poor representation of ocean-atmosphere feedbacks, where simulated precipitation is overly sensitive to SST increases, relative to the observations (Lin, 2007). More remotely, extratropical cloud biases (Hwang and Frierson, 2013; Li and Xie, 2014) lead to a cross-equatorial energy transport imbalance, displacing the ITCZ southwards relative to observations. These differing model biases further contributes to the broad variety in diagnosis performance amongst the CMIP5 ensemble.

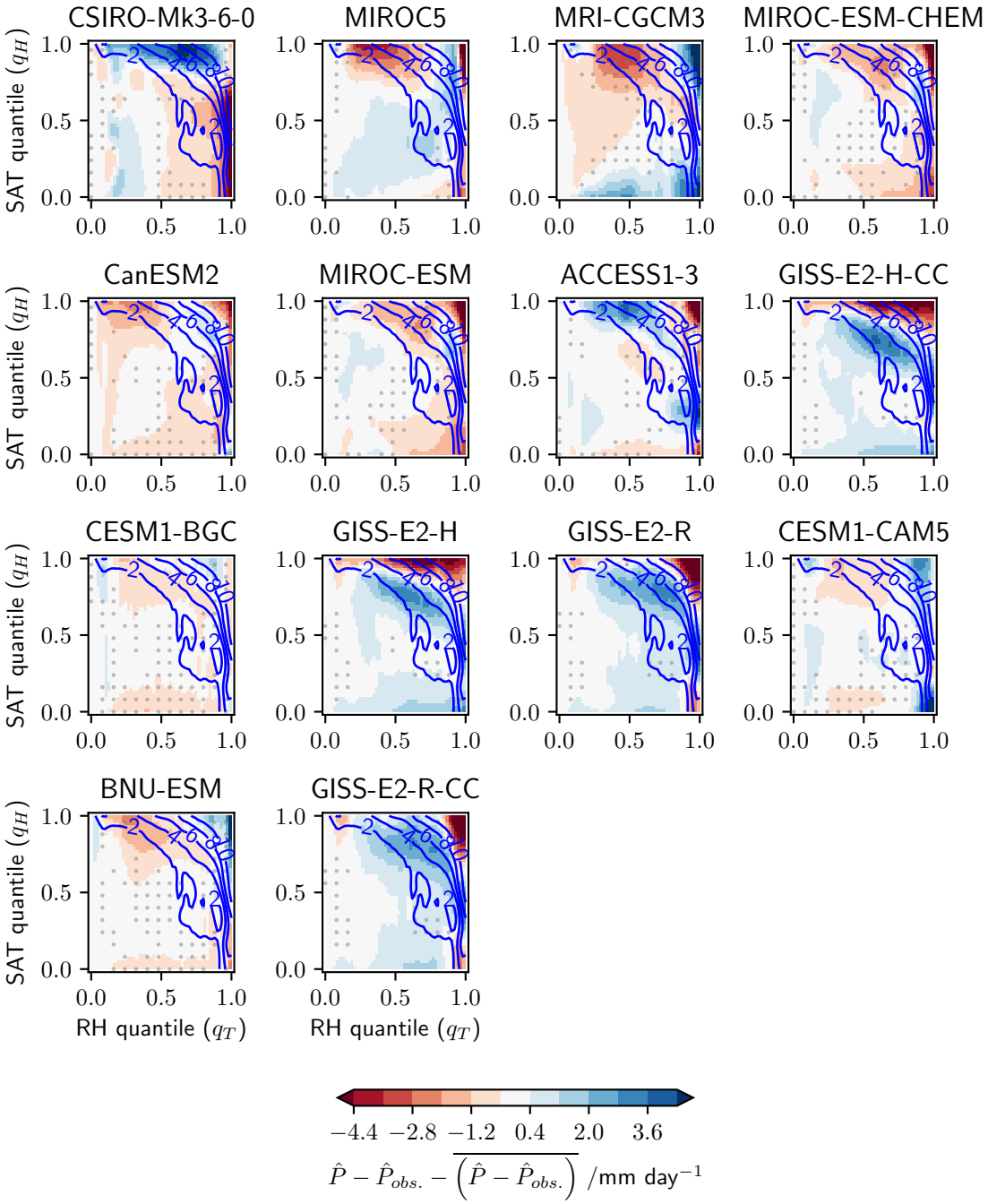

Figure 3.22: As in Figure 3.15, but for the 1980-1999 (historical) simulations minus ERA-Interim-GPCP observations.

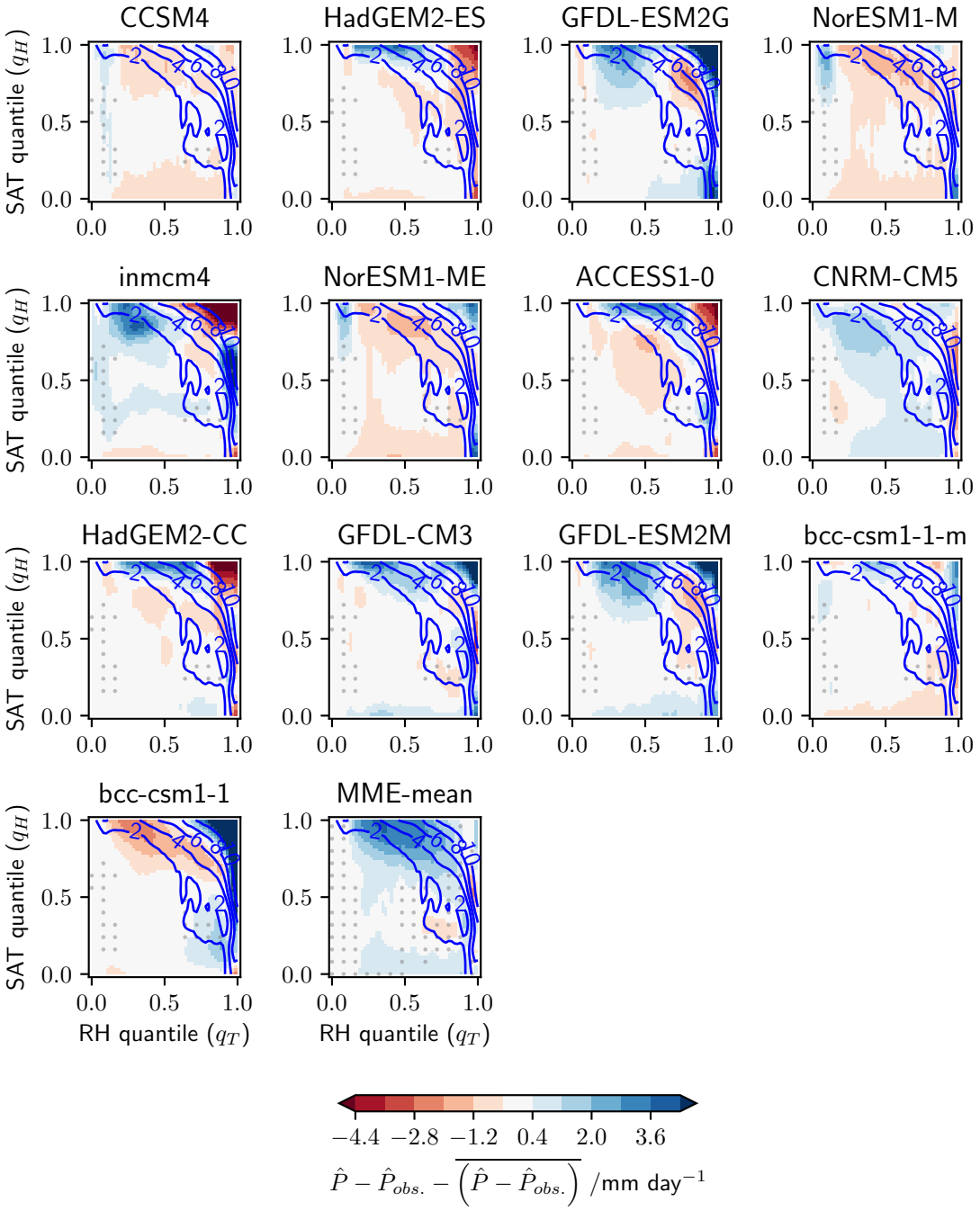

Figure 3.22 (Continued)

3.5 Discussion and Conclusions

A novel statistical framework for diagnosing tropical precipitation shifts has been examined in this chapter. The application of this framework, based upon the Lambert *et al.* (2017) method, builds on the results presented in Chapter 2 by improving our understanding of mechanisms linked with present day ENSO and global warming tropical precipitation changes.

Comparing the GP to the binning method diagnoses, we note a minor improvement in magnitudes for both observed ENSO and simulated global warming precipitation changes, as demonstrated in Section 3.4.1. This improvement is likely linked with the improved fidelity of the precipitation function, due to reduced aggregation, in using the Gaussian process framework. For ENSO, we note a minor performance improvement in terms of the spatial correlation between the observations and the diagnoses. For instance, considering the DJF composite mean El Niño minus neutral conditions, the spatial correlations are 0.69 and 0.73 for the binning and GP methods, respectively. For RCP8.5 global warming simulations, we note a similar minor correlation increase for a majority (78%) of models in the CMIP5 ensemble. However, issues with diagnosis performance over tropical land areas persist with the revised method. Together, these results suggest areas of modest improvement in the ability to correctly diagnose tropical precipitation shifts using the revised Gaussian process method.

Another benefit of the GP method, in contrast to the binning method, is the improved ability to assess where and why diagnoses differ from the observations or simulations. As discussed in Section 3.4.2, weak diagnosis performance is largely linked with the failure of the assumption that scaled tropical precipitation as a function of tropical relative humidity and surface air temperature quantiles (q_H and q_T, respectively) is invariant under climate perturbations. Significant changes in this function, relative to interannual variability, are typically larger across (q_H, q_T)-space and more extensive for global warming simulations in comparison to the ENSO observations. This is consistent with the weaker spatial correlations for the former. Notably, significant changes occur in well populated regions of (q_H, q_T)-space within the convex hull of the (q_H, q_T) points. This result suggests factors other than surface relative humidity or air temperature changes could be linked with precipitation changes. This is consistent with the result that the GP method prediction interval width, ΔP_{IQR}, is relatively large (> 4 mm day^{-1}) across much of the tropics, despite the method broadly diagnosing the correct sign of the anomalies. Furthermore, there is a large diversity amongst the CMIP5 ensemble in the extent and magnitude of the significant changes in the precipitation function, and hence satisfaction of this method assumption. This highlights an important model dependency in the mechanisms leading to tropical precipitation changes.

Precipitation as a function of q_H and q_T may be sensitive to climate perturbations due to changes in the vertical coupling between the boundary layer and free troposphere. An implicit assumption of the diagnosis method is that the interdependence between surface and free tropospheric RH remains invariant under climate perturbations. In Section 3.4.3, this assumption was explored, and generally two regimes are evident for El Niño and global warming changes. In one regime, consisting of off-equatorial tropical ocean and land, surface and 850 hPa RH changes are typically linearly related. In the second regime, largely comprising of the equatorial central Pacific and South America, and the oceanic subtropical descent regions, surface RH changes are marginal whilst RH changes vary substantially aloft. In models where the diagnosis method performs well, both simulated and diagnosed precipitation increases where RH changes aloft are greater than at the surface, and vice-versa. This is consistent with El Niño changes using ERA-Interim and GPCP data. However, in regions where RH aloft increases are much larger than at the surface in the HadGEM2 models, large precipitation decreases are diagnosed but not simulated. This behaviour is physically inconsistent with the observed El Niño changes, highlighting how different mechanisms lead to future tropical precipitation changes in these models.

Several areas of further work could develop the results presented in this chapter. As noted in Section 3.3, given more computational resources, the diagnosis confidence intervals could be more robustly estimated. Additionally, alternative choices in the statistical modelling framework, such as the form of the covariance function, could be explored to optimise diagnosis performance. In Section 3.4.2, an in-depth analysis of the extra twenty eight CMIP5 models may identify further mechanisms acting in addition to RH and SAT changes to affect precipitation changes. However, the motivation for developing the diagnosis method was to explore a simplified tool for understanding tropical precipitation changes. Therefore, a more detailed analysis of the physical mechanisms is beyond the scope of this chapter. Instead, in Chapters 4 and 5, we'll take a dynamics based viewpoint and assess the competing mechanisms leading to tropical climate change, in order to improve our understanding of future precipitation changes.

Chapter 4

Future Tropical Precipitation Change Mechanisms in CMIP5

4.1 Introduction

Chapters 2 and 3 introduced and developed a physically motivated, simplified framework relating precipitation change with surface relative humidity and air temperature changes. This chapter takes a more dynamics-based stance, examining the mechanisms which contribute to future mean state and variability changes under simulated global warming. This is motivated by the relatively high uncertainty in coupled projections of future tropical precipitation changes, due to disagreement amongst the CMIP5 ensemble (Christensen *et al.*, 2013; Collins *et al.*, 2013). In order to improve our understanding of the mechanisms, idealised global warming simulations in atmosphere-only models are used, providing a proxy for more realistic coupled simulations. This method is commonly applied in the literature (for instance: Kent *et al.* (2015); He and Soden (2015); Chadwick (2016); Zappa *et al.* (2018)), and permits an assessment of the relative roles of SST warming and CO_2 forcing.

The remainder of this chapter is split into four sections. Section 4.2 introduces the atmosphere-only simulations in CMIP5 and the statistical significance tests applied throughout this chapter. Section 4.3 examines CMIP5 simulated changes in the mean state and variability of tropical precipitation, applying the contemporary moisture budget decomposition approach of Seager *et al.* (2010). Finally, Section 4.4 presents a summary and discussion of the results.

4.2 Data and Methods

4.2.1 AMIP Experiments

A detailed description of the CMIP5 protocol is presented by Taylor *et al.* (2012), a summary is provided here for the constituent atmosphere model intercomparison project (AMIP) experiments: amip, amip4K, amipFuture and amip4xCO2. In amip, observed SST and sea ice concentration (SIC) conditions between 1979-2008 are prescribed in an atmosphere general circulation model (AGCM). To obtain these boundary conditions, monthly mean observations are adjusted to representative mid-month values from which daily fields are then linearly interpolated (Taylor *et al.*, 2000). This procedure ensures the prescribed monthly mean SST and SIC are consistent with observations. In the atmosphere, CO_2 concentrations and aerosols also follow observations, equivalent to the CMIP5 historical experiment. In amip4K and amipFuture, identical SIC, CO_2 and aerosol conditions are prescribed as in amip. For amip4K, a spatially uniform $+4$ K warming is applied to the prescribed SST fields. For amipFuture, the SST anomaly pattern from the CMIP3 ensemble mean 1% year^{-1} CO_2 at year 70 ($\approx 2\times CO_2$) is applied, after scaling to ensure a global mean SST warming of $+$ 4K. In amip4xCO2, SST, SIC and aerosol conditions are as in amip, but the CO_2 prescribed to the model's radiation scheme is quadrupled, relative to amip. Consequently, amip4K and amipFuture, hereafter the SST perturbation experiments, represent uniform and more realistic twenty-first century patterned warming, respectively. Meanwhile, amip4xCO2 simulates the effect of increased CO_2 forcing to the atmosphere, with SST fixed at present day levels.

In addition to the idealised global warming, atmosphere-only simulations, a pair of atmosphere-ocean coupled simulations are used in this chapter: the CMIP5 historical and RCP8.5. These experiments were initially presented in Chapter 3, and prescribe greenhouse gas and aerosol concentrations representing realistic present-day conditions and a business-as-usual future scenario, respectively. This analysis focuses solely on the late twentieth century (1980-1999) and late twenty first century (2080-2099) periods of the historical and RCP8.5 simulations, respectively. An evaluation of the atmosphere-only and coupled precipitation biases, and a comparison of the simulated global warming changes is presented in Section 4.3.1.

Ten models performed simulations for each of the four AMIP experiments, as well as the coupled historical and RCP8.5 experiments, as detailed in Table 4.1. This analysis examines specific humidity and horizontal wind simulations on twelve standard pressure levels (1000, 925, 850, 700, 600, 500, 400, 300, 250, 200, 150 and 100 hPa) profiling the troposphere, as stratospheric humidity makes a negligible contribution to the surface moisture budget (Seager and Henderson, 2013). Surface pressure simulations are used to mask grid points at pressure levels beneath orography. Consistent with Chapters 2

and 3, all model data is bilinearly interpolated onto a common 2.5° grid to enable inter-comparison, and tropical region within the latitude band between 30°N and 30°S is the focus of this analysis. In Section 4.3, monthly mean data is examined since the effect of transient eddies on the moisture budget is minimal in the tropics (Seager *et al.*, 2010).

CMIP5 Model	Institute ID	Atmospheric Resolution (latitude $\times$ longitude)
CNRM-CM5	CNRM-CERFACS	$1.389^\circ \times 1.406^\circ$
CanAM4[1]	CCCma	$2.767^\circ \times 2.812^\circ$
HadGEM2-A[1]	MOHC	$1.25^\circ \times 1.875^\circ$
IPSL-CM5A-LR	IPSL	$1.895^\circ \times 3.75^\circ$
IPSL-CM5A-MR	IPSL	$1.268^\circ \times 2.5^\circ$
MIROC5	MIROC	$1.389^\circ \times 1.406^\circ$
MPI-ESM-LR[2]	MPI	$1.875^\circ \times 1.875^\circ$
MPI-ESM-MR[2]	MPI	$1.875^\circ \times 1.875^\circ$
MRI-CGCM3	MRI	$1.112^\circ \times 1.125^\circ$
bcc-csm1-1	BCC	$2.767^\circ \times 2.812^\circ$

Table 4.1: Model names, institutes and atmospheric resolutions contributing AMIP simulations to the CMIP5 ensemble. Abbreviations defined in Table 3.1, in addition: MPI (Max Plank Instut für Meteorologie). [1]*In CMIP5, the coupled configuration of CanAM4 and HadGEM2-A is CanESM2 and HadGEM2-ES, respectively.* [2]*MPI-ESM-MR and MPI-ESM-LR have an equivalent atmospheric horizontal resolution, but 47 and 95 vertical levels and 1.5° and 0.4° ocean resolution in coupled configuration, respectively.*

4.2.2 ENSO Composites

Section 4.3 focuses on the boreal winter, December-February (DJF) season, since this is the ENSO mature phase when the magnitude of surface temperature and precipitation anomalies is largest (Rasmusson and Carpenter, 1982). Consistent with Chapters 2 and 3, a development of the Oceanic Niño Index (ONI, NOAA (2015)) is applied to categorise ENSO events. If the DJF mean Niño3.4 (5°N-5°S, 120°W-170°W) SST anomaly is < -0.5 K or $> +0.5$ K, a La Niña or El Niño event is identified, respectively, otherwise the DJF is classified as neutral. This categorisation identifies ten El Niño seasons: (December) 1979, 1982, 1986, 1987, 1991, 1994, 1997, 2002, 2004 and 2006, and nine La Niña seasons: (December) 1983, 1984, 1988, 1995, 1998, 1999, 2000, 2005 and 2007 in the observations prescribed to the AMIP experiments.

For the historical 1980-1999 simulation an equivalent categorisation method is applied as in the AMIP simulation, with a caveat noted here. In coupled simulations, uncertainty in the ocean-atmosphere feedbacks controlling ENSO leads to less realistic SST anomalies (Guilyardi *et al.*, 2009). For instance, Bellenger *et al.* (2014) used long-running piControl simulations (as described in Chapter 2) to identify which CMIP5 coupled models correctly

simulate the switch from positive to negative in the shortwave-SST feedback between subsident and convective regimes over the eastern equatorial Pacific, respectively, during El Niño events. From their analysis, of the AMIP ensemble members only CanAM4 (in coupled configuration as CanESM2) correctly simulates this transition, whilst CNRM-CM5 and MIROC5 remain locked in a negative feedback. Each of the other seven models persist in a positive feedback. One choice would be to only examine CanESM2 in this analysis, as it correctly simulates this change in the shortwave-SST feedback, as in observations. However, this would prohibit applying significance tests, as is possible when using an ensemble approach. Consequently, this study considers all ten coupled models, with the caveat that a mixture of ENSO representation is included.

4.2.3 Determining Statistical Significance

When maps of ensemble mean changes are presented in this analysis, stippling is applied to cover areas where the mean changes is insignificant with respect inter-model variability. To determine statistical significance, a paired t-test is applied, for instance comparing each model's present day and future simulated value. The null hypothesis for each t-test is zero change in ensemble the mean. For temperature simulations, a Gaussian distribution is a reasonable assumption and the t-test is applied directly. In contrast, precipitation values are log-transformed, following Chapter 3, before applying the t-test. Qualitatively similar results are obtained by applying the non-parametric Kolmogorov-Smirnov (KS) test. In contrast to a t-test, a KS test assesses for any distributional changes, and is hence sensitive to both scale and shape changes. Following Wilks (2016), p-values from the t-tests are adjusted to ensure a false detection ratio (FDR) no greater than 10%, as changes at local grid points cannot be assumed independent of each other. The FDR is the expected fraction of incorrectly rejected null hypotheses. Therefore, stippling covers an area where at least 90% of each local null hypothesis is correctly rejected.

4.3 Future Tropical Precipitation in CMIP5

In this section, an analysis of CMIP5 coupled and atmosphere-only simulations of future tropical precipitation is presented. Firstly, biases and uncertainties in present day simulations are examined, in order to frame the projected changes under global warming. A proxy for the more realistic, coupled simulations is developed. This proxy combines atmosphere-only experiments using SST perturbations and CO_2 forcing, in order to disentangle the competing processes leading to simulated precipitation change. A moisture budget decomposition (Seager *et al.*, 2010) is applied to develop our understanding of the mechanisms controlling these changes.

4.3.1 Atmosphere-only and Coupled Simulations

Present Day Precipitation Biases

Several similarities exist between mean state precipitation biases, relative to GPCP, in the CMIP5 atmosphere-only (amip) and coupled (historical) simulations, as demonstrated by Figures 4.1(a) and (b), respectively. Ensemble means of DJF precipitation in both simulations have a positive bias over large areas of the tropical oceans, and a negative bias over the Amazon basin, northern Australia and the maritime continent. A major source of bias, and model differences, are the convective parametrisation schemes used in global circulation models (GCMs) (Flato *et al.*, 2013). As GCM resolution is too coarse to explicitly resolve convection, its effects are estimated from the simulated temperature and humidity profiles. Typically, instability is assessed at low- and mid-tropospheric levels. Entrainment and detrainment, with rates dependent on the humidity profile, are then applied to candidate buoyant air parcels. This process is then repeated to stabilise the tropospheric profile, and estimate the convective mass flux, condensation and hence precipitation rates. A more detailed description of the convective parametrisation in HadGEM2, the Met Office GCM contributing to CMIP5, is presented in Section 5.2.1.

Atmosphere-only precipitation simulations can be biased due to unrepresented atmosphere-ocean feedbacks. For instance, in heavy precipitation regions, extensive cloud cover limits the downwelling shortwave radiation, reducing SST and hence precipitation over time (Feng *et al.*, 2018). However, biases in coupled simulations are typically stronger relative to equivalent atmosphere-only cases, due to the additional effect of SST biases and errors in simulated surface feedbacks in coupled models, leading to greater circulation biases (Toh *et al.*, 2018). For instance, the persistent equatorial cold tongue bias, linked with an unrealistic coupling interval (Misra *et al.*, 2008), leads to deficient precipitation in the central equatorial Pacific. Furthermore, southern hemisphere cloud biases contribute to excessive precipitation in the SPCZ (Li and Xie, 2014). Whilst examining these biases, it is also important to note the relatively high uncertainty in GPCP observations, especially in areas without rain gauge measurements, such as over tropical oceans and

sparsely populated rainforest regions (Adler *et al.*, 2003). In particular, GPCP is found to underestimate precipitation over tropical and mid-latitude oceans (Stephens *et al.*, 2012). Hence, model and observational biases may be confounded in many regions.

Examining El Niño precipitation anomalies, biases are weaker in the atmosphere-only simulations, consistent with the mean state simulations, as shown in Figures 4.1(c) and (d). The large scale features of the amip ensemble mean, with positive biases in the central equatorial Pacific and negative biases in the off-equatorial Pacific, simulate a realistic pattern but strengthened magnitude relative to observed El Niño precipitation anomalies. In contrast, the pattern of El Niño anomalous precipitation in coupled simulations is quite different relative to both atmosphere-only simulations and observations. Positive precipitation anomalies extend too far westward over the maritime continent, and negative anomalies are too weak over the Amazon basin. These El Niño biases in coupled models are largely due to issues in representing ocean-atmosphere feedbacks in the tropical Pacific, which also contribute to mean state biases (Ferrett *et al.*, 2018). For instance, a majority of CMIP5 coupled models fail to simulate the nonlinearity of the observed SST-shortwave feedback (Bellenger *et al.*, 2014), as discussed in Section 4.2.2. Therefore, simulated El Niño SST anomalies in coupled models may lead to an unrealistic atmospheric heating response, further affecting the simulated convection and hence precipitation. However, a complete understanding of future coupled ocean-atmosphere variability is lacking in the literature.

An Atmosphere-only Proxy for Coupled Simulations: amipTotal

The idealised global warming AMIP simulations can be combined to form amipTotal, an atmosphere-only proxy for more realistic future scenario coupled simulations. Define:

$$\begin{aligned}\text{amipTotal} &= (\text{amip4K} - \text{amip}) + (\text{amipFuture} - \text{amip4K}) + (\text{amip4xCO2} - \text{amip}) + \text{amip} \\ &= \text{amipFuture} + \text{amip4xCO2} - \text{amip}\end{aligned}$$

Decomposing amipTotal enables an approximate comparison of the contributions due uniform SST warming $(\text{amip4K} - \text{amip})$, SST pattern change $(\text{amipFuture} - \text{amip4K})$ and CO_2 forcing to the atmosphere $(\text{amip4xCO2} - \text{amip})$ in the coupled RCP8.5 simulation. This framework is a common choice in the literature for understanding the coupled response (for instance: Kent *et al.* (2015), He and Soden (2015), Zappa *et al.* (2018)). However, combining these contributions linearly may be unrealistic due to the unrepresented feedbacks in atmosphere-only simulations.

Five caveats are important to consider when applying the amipTotal framework. 1) The atmosphere-only simulations prescribe aerosols at present day concentrations, whereas in RCP8.5 a future scenario of decreasing aerosol concentrations is implemented (Riahi

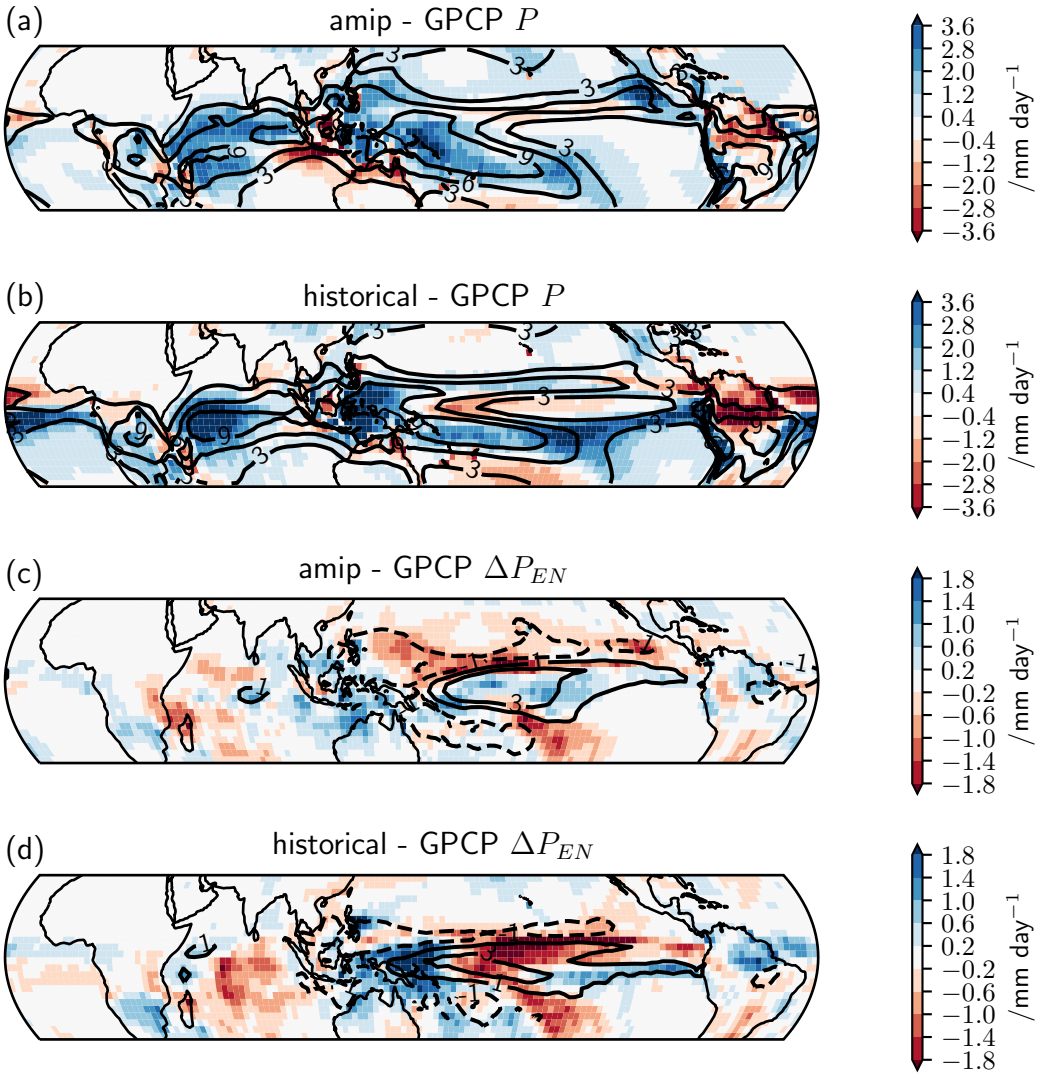

Figure 4.1: Colours show the DJF ensemble mean simulated precipitation minus GPCP observations, for the amip (a, 1979-2008) and historical (b, 1980-1999) experiments, with black contour lines show the simulated precipitation. (c-d) display the corresponding amip and historical composite mean El Niño precipitation anomalies, respectively.

et al., 2007). 2) CO_2 increases steadily in RCP8.5 in contrast to abrupt quadrupling in amip4xCO2, mixing the transient and equilibrium responses in the coupled simulation. 3) CO_2 forcing is applied to both the atmosphere and land surface in RCP8.5, in comparison to just the atmospheric radiation scheme in amip4xCO2, leading to an additional plant physiological effect in the former. 4) In amipFuture, an identical mean state SST pattern change is applied to each atmosphere model, whereas the coupled models themselves each produce a distinct SST pattern change. 5) Finally, similar to the model precipitation biases discussed previously, the present day SST pattern in the amip and historical simulations differs. Considering these caveats, the following subsection presents a comparison of the amipTotal and RCP8.5 simulated precipitation and temperature changes.

Future Tropical Temperature and Precipitation Simulations

Consider a simulated weather variable, X, such as temperature or precipitation. Let $\bar{X}$ represent the present day mean state, for instance from the amip or historical experiments. Similarly, define ΔX_{EN} as the present day composite mean ENSO anomaly. For a composite mean of future ENSO events, such as under RCP8.5 or amipTotal, the simulated weather variable can then be written as the sum of four terms:

$$\bar{X} + \Delta X_{EN} + \bar{X}' + \Delta X'_{EN} \tag{4.1}$$

Here, $\bar{X}'$ is the future minus present day change in the time mean or (ENSO) neutral state, and $\Delta X'_{EN}$ is the corresponding change in the ENSO anomaly. This partitioning enables a comparison of changes in the base climate, $\bar{X}'$, and climate variability, $\Delta X'_{EN}$. For the remainder of this chapter, T represents surface air temperature and P represents precipitation.

CMIP5 ensemble mean DJF $\bar{T}'$, the mean state surface air temperature change, for the atmosphere-only and coupled simulations is demonstrated in Figure 4.2.The primary feature of both amipTotal minus amip and RCP8.5 minus historical is a significant land-ocean warming contrast, with subtropical land areas warming substantially more than surrounding oceans. This contrast is principally due to surface moisture limitations over land, leading to differing lapse rates in the boundary layer, amplifying warming near the land surface in response to warming aloft (Joshi *et al.*, 2008). This feature is evident in both the amip4K minus amip and amip4xCO2 minus amip simulations, indicating that both uniform SST warming and CO_2 forcing contribute significantly to the amipTotal response. Over the tropical Pacific, the coupled RCP8.5 minus historical $\bar{T}'$ pattern is greater eastern equatorial warming relative to the western equatorial and surrounding off-equatorial regions. This change, similar to that prescribed in amipFuture minus amip4K, is partially due to the ocean dynamical response in response to a weakened

Walker circulation (DiNezio *et al.*, 2009), and related surface heat flux changes (Xie *et al.*, 2010). A similar, albeit weaker warming disparity is also present in the tropical Atlantic ocean. Qualitatively similar results are present for other seasons, however DJF remains the focus of this chapter as it coincides with the ENSO mature phase when El Niño and La Niña SST and precipitation anomalies are largest.

The corresponding $\bar{P}'$ changes are presented in Figure 4.3. Pattern agreement between amipTotal minus amip and RCP8.5 minus historical simulations is weaker relative to $\bar{T}'$, with spatial correlations of (0.64) and (0.87), respectively. Qualitatively, there is relatively good agreement between these two cases over the eastern tropical Pacific, central America and tropical Atlantic. Agreement is much weaker over the eastern Indian ocean, where amipTotal simulates large decreases (< -2 mm day^{-1}) and RCP8.5 simulates moderate increases (approximately $+1$ mm day^{-1}). This disparity is due to the relative differences in present day SST future warming over these regions. The amipTotal linearity assumption is well justified since atmosphere GCMs prescribed with SST patterns from their coupled configurations typically produce a very similar precipitation pattern (Chadwick, 2016). Hence regional differences between amipTotal and RCP8.5 precipitation over ocean are likely linked with the different SST changes. Nonetheless, examining the different atmosphere-only simulations remains useful for disentangling the more realistic coupled response.

Subsection 4.3.2 provides a detailed analysis of the mechanisms contributing to tropical precipitation change in each atmosphere-only simulation. Here, a brief summary of the simulated changes is provided in the context of recent literature. In amip4K minus amip, demonstrated in Figure 4.3(a), uniform SST warming leads to significant mean state precipitation increases in the present day convergence zones over tropical ocean areas: the ITCZ over the equatorial Indian and eastern equatorial Pacific, and the SPCZ over the western Pacific. At large scales, this is mainly a thermodynamic response; low level moisture increase due to the nonlinear Clausius-Clapeyron relation enhances present day precipitation (Held and Soden, 2006). Over land, significant decreases are evident over southern Africa and northern Australia. This highlights the dynamic response on smaller scales; where circulation changes lead to spatial shifts in convective regions (Chadwick *et al.*, 2013).

The amipFuture minus amip4K mean state change, shown in Figure 4.3(b), highlights a strong link between precipitation and SST pattern change. Physically, deep convection and convergence are favoured where SST is warmer relative to the tropical mean (Xie *et al.* (2010), Chapters 2 and 3). Ensemble mean $\bar{P}'$ is positive, large (> 2mm day^{-1}) and significant in the equatorial central Pacific, western Atlantic and Indian oceans, coincident with significant mean state temperature increases relative to the tropical mean

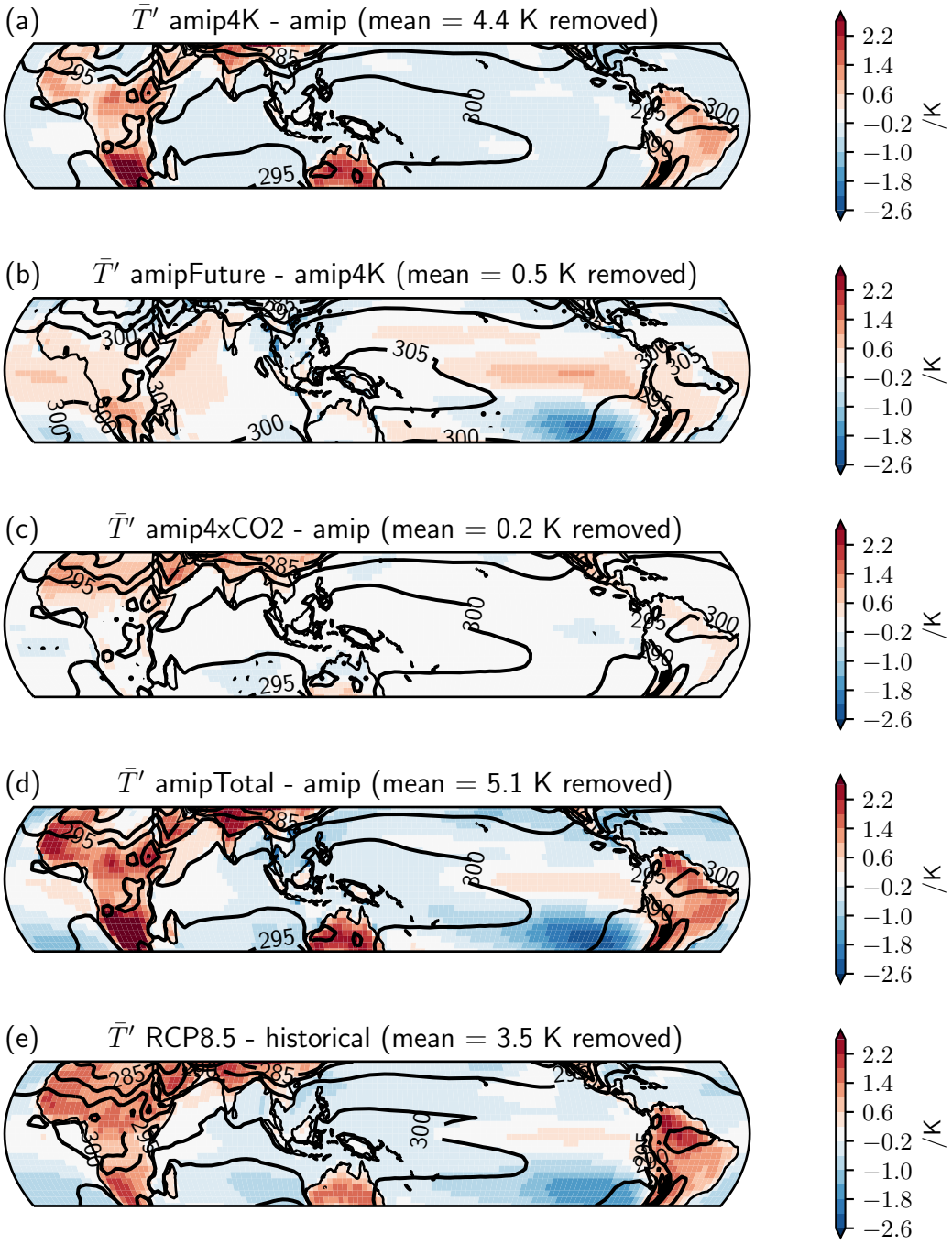

Figure 4.2: Colours show the global warming DJF ensemble mean simulated temperature changes, T': amip4K - amip (a), amipFuture - amip4K (b), amip4xCO2 - amip (c), amipTotal - amip (d) and RCP8.5 - historical (e). Black contours lines indicate the corresponding amip (a,c,d), amip4K (b) and historical (e) temperature, T at 5 K intervals. Stippling covers areas where changes are insignificant via a t-test with adjusted p-values to ensure a false detection ratio of 5%, as discussed in Section 4.2.3.

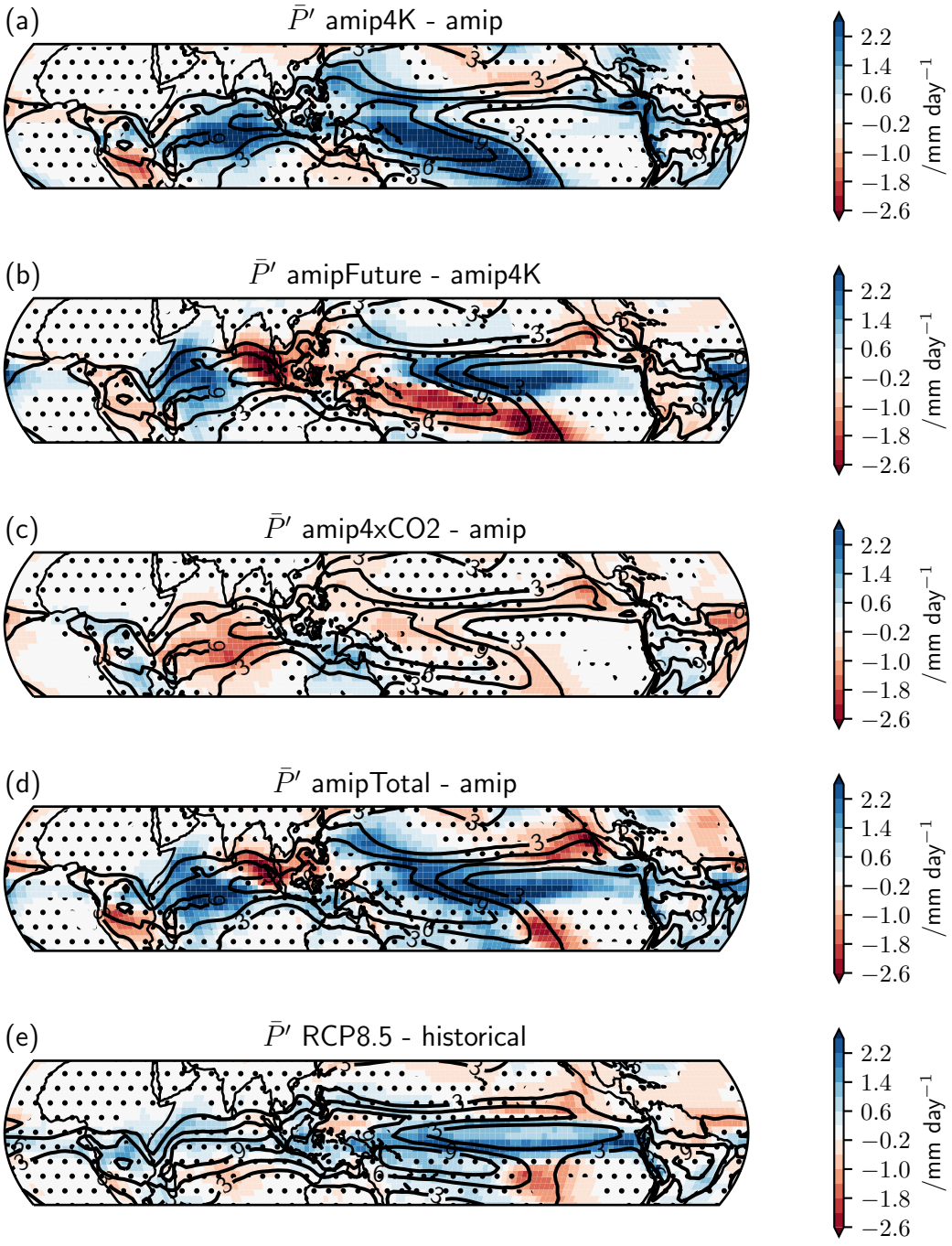

Figure 4.3: Colours, contours and stippling as in Figure 4.2, except for global warming simulated precipitation changes, P'.

warming (Figure 4.2(b)). Conversely, $\bar{P}'$ is significantly negative over the eastern Indian and southern subtropical Pacific oceans, where mean state warming is less than the tropical mean warming. In amip4xCO2 minus amip, precipitation weakly decreases ($\bar{P}' \approx -1$mm day^{-1}) in the present day convergence zones over tropical oceans, and increases ($\bar{P}' \approx 1$mm day^{-1}) over northern Australia and southern Africa, as demonstrated by Figure 4.3(c). The direct response to increased CO_2 forcing is to reduce the net radiative cooling of the atmosphere, leading to tropospheric warming and stabilisation, hence weakening the overturning circulation (Bony *et al.*, 2013). Additionally, with fixed SST as in amip4xCO2, the surface land-sea temperature contrast strengthens (Joshi *et al.*, 2008), as shown by Figure 4.2(c). This relatively favours convection and hence precipitation increases over tropical land areas. However, there is a regional sensitivity to this mechanism, as negligible ensemble mean changes are simulated over, for instance, the Amazon basin. In summary, uniform SST warming, SST pattern change and CO_2 forcing each lead to markedly different and significant precipitation changes.

The El Niño anomaly changes in temperature, $\Delta T'_{EN}$, and precipitation, $\Delta P'_{EN}$, for each simulation are shown in Figures 4.4 and 4.5, respectively. Similarly to the mean state temperature changes, the amipTotal anomaly pattern is relatively consistent with RCP8.5. Each case simulates enhanced warming ($> +0.5$ K) across northern Africa, eastern tropical Asia and tropical South America, and weak cooling (amipTotal) or negligible change (RCP8.5) over southern Africa, Australia and subtropical South America. Decomposing the amipTotal anomaly, both the uniform and patterned SST experiment anomalies simulate a similar $\Delta T'_{EN}$ pattern. Both experiments simulate enhanced anomalous land warming over tropical northern Africa, eastern Asia and South America, and relative cooling over Australia and subtropical South America. The amip4xCO2 anomaly change is generally weaker ($|\Delta T'_{EN}| < 0.3$ K), with a small contribution to warming over northern Africa and eastern Asia. Consistent with mean state changes, these results demonstrate how uniform SST warming, SST pattern change and CO_2 forcing each contribute to substantial El Niño anomaly temperature changes over land.

Similarly to the mean state precipitation changes, the $\Delta T'_{EN}$ anomalies are linked with circulation changes, and therefore $\Delta P'_{EN}$ anomalies. Pattern agreement, measured via spatial correlation, between the amipTotal and RCP8.5 anomalies is slightly weaker for precipitation (0.57) relative to temperature (0.63). However, the sign of large scale features in the tropical Pacific are generally consistent, and hence decomposing amipTotal remains useful for developing our understanding. In amip4K minus amip, the present day western Pacific negative anomaly strengthens, whilst only the southern flank of the central Pacific positive anomaly is significantly amplified. The amipFuture minus amip4K simulation indicates a zonal narrowing of the present day anomalous precipitation pattern in the central Pacific, with large ($|\Delta P'_{EN}| > 2$ mm day^{-1}) equatorial increases and

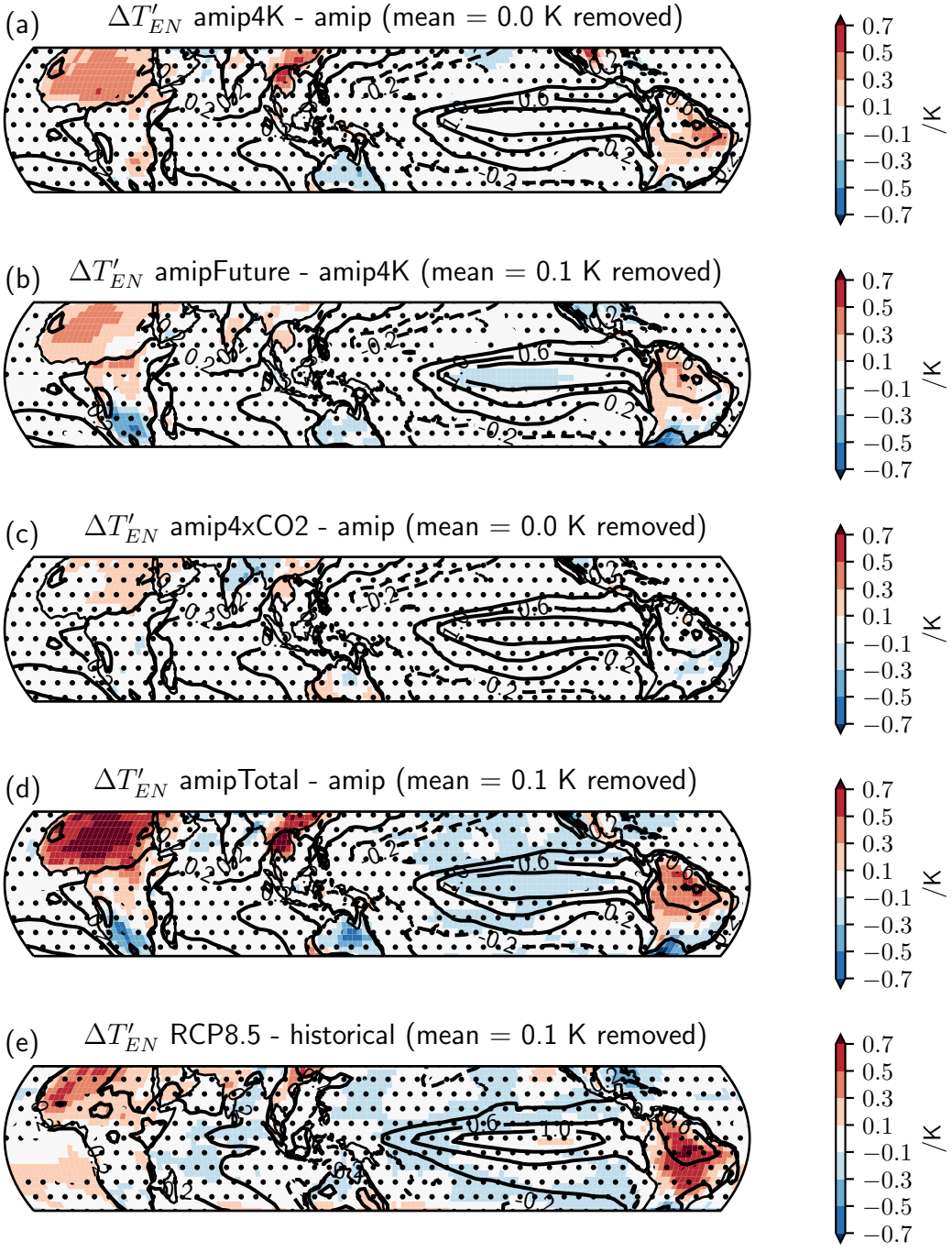

Figure 4.4: Colours, contours and stippling as in Figure 4.2, except for El Niño anomaly simulated changes, $\Delta T'_{EN}$.

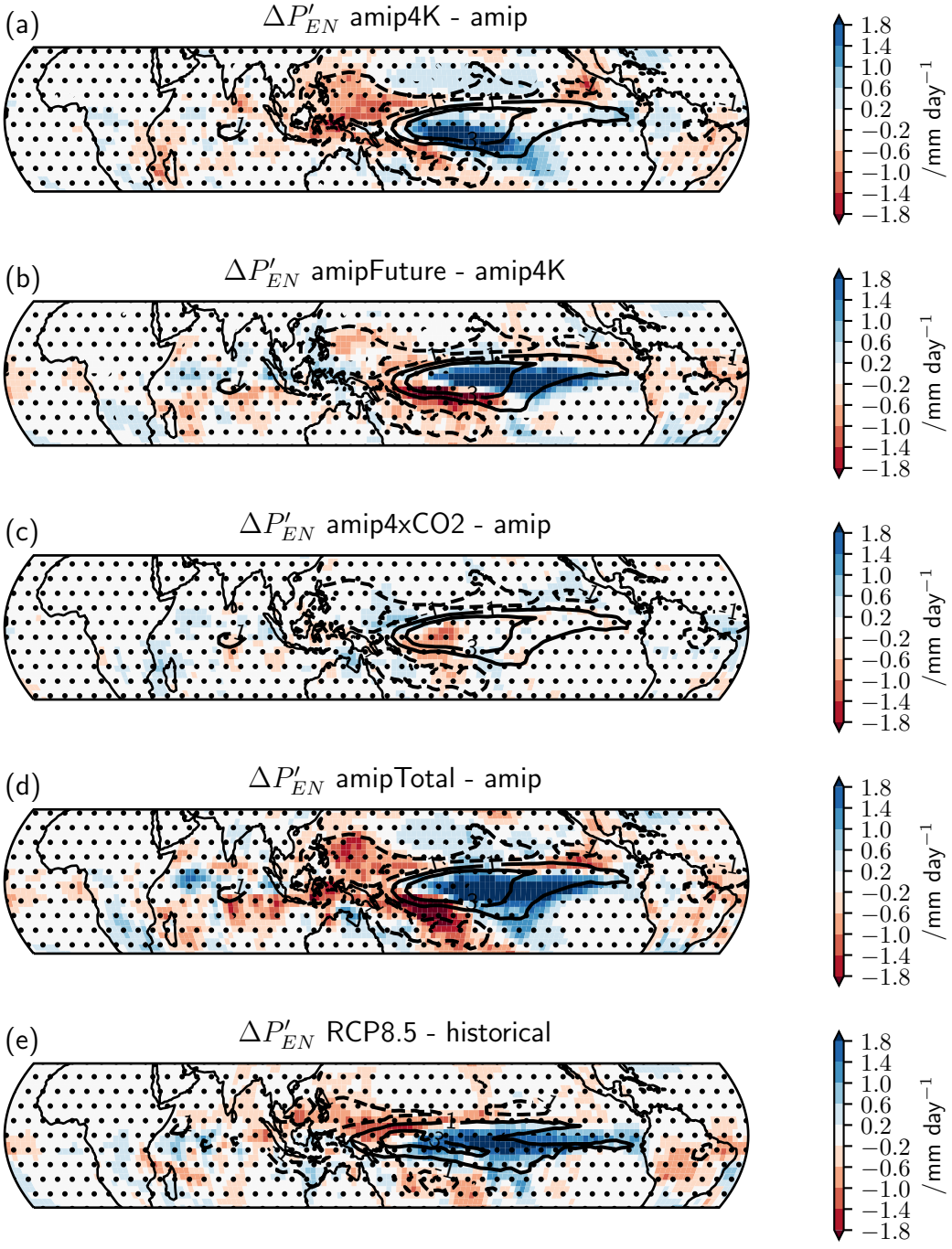

Figure 4.5: Colours, contours and stippling as in Figure 4.2, except for El Niño anomaly simulated changes, $\Delta P'_{EN}$.

southern off-equatorial decreases. The amip4xCO2 minus amip anomaly change is relatively much weaker and less significant, with dampened El Niño anomalous increases and decreases in the central and western Pacific, respectively. Examining the mechanisms controlling $\bar{P}'$ and $\Delta P'_{EN}$ in greater detail forms the basis of the next subsection.

4.3.2 Decomposing CMIP5 Tropical Hydrological Cycle Changes

In the previous subsection, the mean state and El Niño anomaly temperature and precipitation changes were presented for idealised, atmosphere-only and more realistic, coupled global warming simulations. In this subsection, a moisture budget framework is used to evaluate the thermodynamic contributions, due to moisture changes, and dynamic contributions, due to circulation changes, to these precipitation changes.

Moisture Budget Decompositions

Several methods for decomposing simulated precipitation changes are proposed in the literature. For instance, Chadwick *et al.* (2013) build on the assumption of Held and Soden (2006) that tropical precipitation, P, is the product of convective mass flux from the boundary layer to the free troposphere, M, and boundary layer specific humidity, q. Chadwick *et al.* (2013) partition M changes into one component due to tropical mean circulation weakening (Vecchi and Soden, 2007), and a residual term representing spatial shifts in regions of deep convection. Additionally, q changes are split into one term reflecting the Clausius-Clapeyron relation with constant relative humidity (RH), and a second term reflecting changes in RH. Subsequently, P changes can be decomposed into four main terms, due to: tropical mean circulation weakening, circulation shifts, thermodynamic effects and RH changes; plus a nonlinear term due to changes in both M and q acting together.

Alternative decompositions, such as those of Bony *et al.* (2013) and Seager *et al.* (2010) are based upon closing the atmospheric moisture budget. The methodology of Bony *et al.* (2013) assumes deviations about a fixed vertical structure of tropical vertical velocity, ω, are small. Then, dynamic contributions to precipitation changes can be estimated from simulated vertical velocity changes. In contrast, Seager *et al.* (2010) make fewer physical assumptions, instead using horizontal winds anomalies to estimate column moisture divergence and advection changes. Hence, in this analysis the latter methodology is applied as a more complete choice.

Let P, E, $\mathbf{u}$, ω, and q represent the present day precipitation, evaporation, horizontal wind vector, vertical wind in pressure units and specific humidity, respectively. In addition, let t, z and p denote the time, vertical displacement and pressure coordinates, respectively. Following Trenberth and Guillemot (1995), consider mass continuity in pressure coordinates:

$$\nabla \cdot \mathbf{u} + \frac{\partial \omega}{\partial p} = 0, \tag{4.2}$$

and moisture conservation in a horizontal layer of atmosphere:

$$\frac{Dq}{Dt} \equiv \frac{\partial q}{\partial t} + \mathbf{u} \cdot \nabla q + \omega \frac{\partial q}{\partial p} = e - c, \tag{4.3}$$

where $\frac{D}{Dt}$ represents the Lagrangian derivative. In Equation 4.3, e represents the rate of evaporation of cloud droplets and hydrometeors, and c is the moisture condensation rate. Multiplying Equation (4.2) by q, and adding it to the advective term in Equation (4.3):

$$\begin{aligned}\mathbf{u}\cdot\nabla q+\omega\frac{\partial q}{\partial p}&=\mathbf{u}\cdot\nabla q+\omega\frac{\partial q}{\partial p}+q(\nabla\cdot\mathbf{u})+q\frac{\partial\omega}{\partial p}\\&=\nabla\cdot(q\mathbf{u})+\frac{\partial}{\partial p}(q\omega)\end{aligned}$$

and hence, Equation (4.3) can be rearranged and written as:

$$\frac{\partial q}{\partial t}+\nabla\cdot(q\mathbf{u})+\frac{\partial}{\partial p}(q\omega)=e-c. \tag{4.4}$$

Vertically integrating Equation (4.4) over the depth of the atmosphere, we have:

$$E-P=\frac{\partial}{\partial t}\int_0^H q dz+\int_0^H\nabla\cdot(q\mathbf{u})dz+\int_0^H\frac{\partial}{\partial p}(q\omega)dz, \tag{4.5}$$

where H represents the top of the atmosphere. Since $\omega=0$ at the surface and the top of the atmosphere, the third term of the right hand side of Equation (4.5) is zero. Over climate timescales, the time mean (Trenberth and Guillemot, 1995) of $\frac{\partial}{\partial t}\int_0^H q dz$ and its simulated change under global warming (Seager *et al.*, 2010) are negligible. Therefore, evaporation minus precipitation at the surface is approximately balanced by moisture flux divergence aloft:

$$E-P\approx\int_0^H\nabla\cdot(q\mathbf{u})dz \tag{4.6}$$

Now, let $'$ represent the global warming minus present day difference, for instance if present day precipitation is P and global warming precipitation is $P+P'$, the difference between the latter and former is P'. Seager *et al.* (2010) consider changes in q and $\mathbf{u}$ in order to decompose precipitation changes into four terms:

$$P'=E'-\int_0^H\nabla\cdot(q'\mathbf{u})dz-\int_0^H\nabla\cdot(q\mathbf{u}')dz-\int_0^H\nabla\cdot(q'\mathbf{u}')dz. \tag{4.7}$$

The second, third and fourth terms on the right hand side of Equation (4.7) represent the thermodynamic, dynamic and nonlinear contributions to precipitation change, respectively.

As discussed in Section 4.2.1, monthly mean q and $\mathbf{u}$ are available on twelve standard pressure levels in the CMIP5 archive. Therefore, in order to estimate the vertical integrals in Equation (4.7), hydrostatic balance is assumed, so $\frac{\partial p}{\partial z}=-\rho g$, where ρ is density and

g the acceleration due to gravity ($g \approx 9.8$ m s^{-1}). Hence, vertical displacement can be converted to pressure coordinates for evaluating vertical integrals, $\int_0^H \cdot dz = -\frac{1}{g}\int_{p_s}^{p_t} \cdot dp$, where p_s and $p_t = 0$ are the surface and top of atmosphere pressure, respectively. In this analysis, $p_s = 1000$ hPa, as this is the lowest archived pressure level, and $p_t = 100$ hPa since this approximately represents the tropopause and moisture above this level is negligible. In addition, using monthly means neglects the effect of transient eddies, due to sub-monthly variations in q and $\mathbf{u}$. However, these contributions are minimal in the tropics (Seager and Henderson, 2013), and hence the assumptions for this moisture budget decomposition are suitable.

In order to decompose mean state precipitation changes, $\bar{P}'$, the Seager *et al.* (2010) method is applied directly to monthly data. Present day or control conditions (amip or historical) are represented by E, q and $\mathbf{u}$, with future or perturbation anomalies (amip4K, amip4xCO2, amipTotal or RCP8.5) denoted by E', q' and $\mathbf{u}'$. To isolate the effect of SST pattern changes, amip4K and amipFuture are taken as control and perturbation conditions, respectively. Anomalous El Niño precipitation changes, $\Delta P'_{EN}$, are examined by applying the Seager *et al.* (2010) method twice. Firstly, future El Niño anomalies are decomposed, taking the future time mean as control and the future El Niño composite mean (as described in Section 4.2.2) as perturbed conditions. This provides the contributions to $\Delta P_{EN} + \Delta P'_{EN}$, where ΔP_{EN} is the present day El Niño precipitation anomaly. Secondly, ΔP_{EN} is similarly decomposed, using present day time mean and El Niño composite mean conditions. Differences in the Seager *et al.* (2010) components between future and present day El Niño anomalies are subsequently used to evaluate the contributions to $\Delta P'_{EN}$.

Decomposing Mean State Precipitation Changes

Components of the Seager *et al.* (2010) moisture budget decomposition applied to the simulated RCP8.5 minus historical mean state precipitation change are shown in Figure 4.6. Evaporation changes, as displayed in Figure 4.6(a), are weakly positive ($\sim$ 0.2-0.6 mm day^{-1}) over the majority of tropical oceans, and negligible over most land areas. This evaporation component weakly contributes to the precipitation increase along the equator, and opposes the precipitation decrease over the eastern subtropical Pacific (Figure 4.7(a)). The evaporation response to global warming over oceans is positive due to the surface warming, moderated by increased near surface stability and weakened surface wind speeds (Richter and Xie, 2008). Evaporation increases contribute to an approximately uniform and weak precipitation increase over ocean. In contrast, it is evident that both horizontal wind and specific humidity changes substantially contribute to the pattern of precipitation changes on a regional scale. The thermodynamic component, $-\int_0^H \nabla \cdot (q'\mathbf{u})dz$ as shown in Figure 4.6(b), indicates a general pattern of increases in present day convergence zones, and decreases in subtropical descent regions. This

wet-get-wetter, dry-get-drier contribution is due to a relatively uniform spatial pattern of specific humidity increases in the lower troposphere, via the nonlinear Clausius-Clapeyron relation (Held and Soden, 2006). This result holds since simulated global warming mean state RH changes are modest, especially over tropical oceans (Sherwood *et al.*, 2010).

The dynamic component, $-\int_0^H \nabla \cdot (q\mathbf{u}')dz$ as shown in Figure 4.6(c), contributes substantial precipitation changes of a similar magnitude (~ 2 mm day^{-1}) to the thermodynamic term, largely dominating the precipitation change pattern (Figure 4.7(c)). Circulation changes and hence convergence zone shifts, acting without specific humidity changes, lead to precipitation increases in the central and eastern equatorial Pacific and decreases over the subtropical Pacific and maritime continent. These convergence zone shifts are strongly linked with the underlying SST pattern (Xie *et al.*, 2010; Chadwick *et al.*, 2013) and land surface changes (Chadwick, 2016), the effects of which will be explored further in Chapter 5. The nonlinear term, $-\int_0^H \nabla \cdot (q'\mathbf{u}')dz$ as shown in Figure 4.6(d), is typically weaker in comparison to the thermodynamic and dynamic contributions. The pattern of $-\int_0^H \nabla \cdot (q'\mathbf{u}')dz$ is similar to $-\int_0^H \nabla \cdot (q\mathbf{u}')dz$, again because specific humidity increases are largely positive and relatively uniform in the lower troposphere. These results indicate that both the dynamic and thermodynamic contributions to the RCP8.5 minus historical precipitation change are substantial and of a similar magnitude. Meanwhile, the evaporation term is relatively uniform across tropical oceans, and, along with the nonlinear term (Figure 4.7(d)), has a relatively small magnitude and weak contribution to the precipitation change.

The equivalent Seager *et al.* (2010) moisture budget decomposition of the amipTotal minus amip mean state precipitation change is demonstrated by Figure 4.8. Generally, each component is consistent with the respective RCP8.5 minus historical decomposition presented in Figure 4.6. Similarly, the relative dominance of the dynamic component contribution to the precipitation change is consistent for amipTotal, as shown by Figure 4.9. Evaporation weakly increases across the majority of tropical ocean areas, with insignificant changes or weak decreases over land. Similar to RCP8.5, the amipTotal thermodynamic term contributes a wet-get-wetter and dry-get-drier pattern whilst the dynamic term leads to substantial convergence zone shifts and precipitation changes. In contrast to the decomposition of the coupled simulation, the nonlinear term reaches an equivalent magnitude to the dynamic and thermodynamic components in amipTotal. This is likely due to the greater magnitude of tropical mean warming in amipTotal (5.1 K), relative to RCP8.5 (3.5 K), leading to larger magnitude changes of both q and $\mathbf{u}$.

Examining the amip4K minus amip component of amipTotal, each term in the Seager *et al.* (2010) decomposition significantly contributes to the mean state precipitation

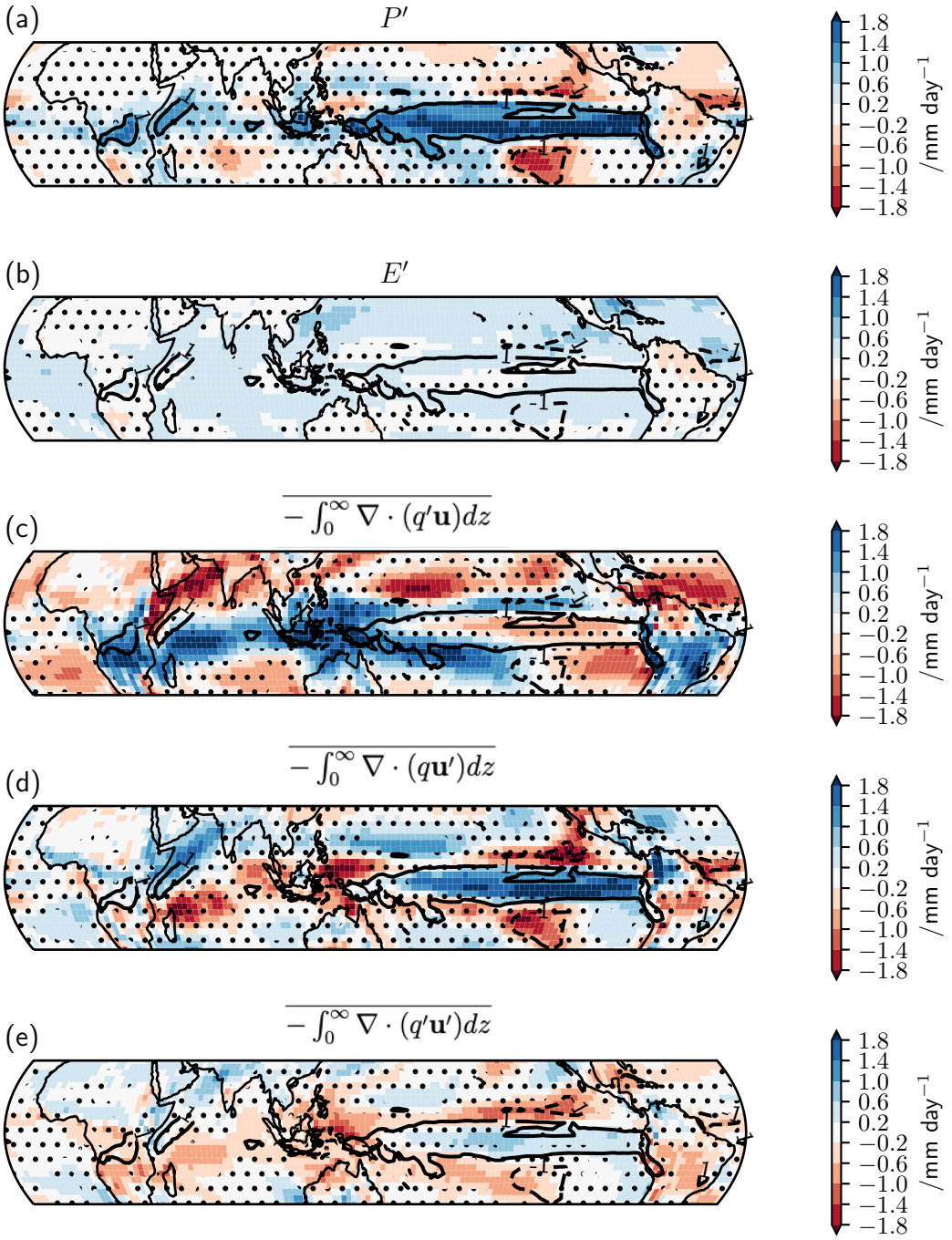

Figure 4.6: Colours show the DJF ensemble mean precipitation (a), evaporation (b), thermodynamic (c), dynamic (d) and nonlinear (e) terms in the Seager et al. *(2010) decomposition, applied to the RCP8.5 minus historical mean state precipitation change. Black lines indicate the ± 1 mm day^{-1} contours of this precipitation change. Stippling covers areas where the ensemble mean change is insignificant, relative to ensemble spread.*

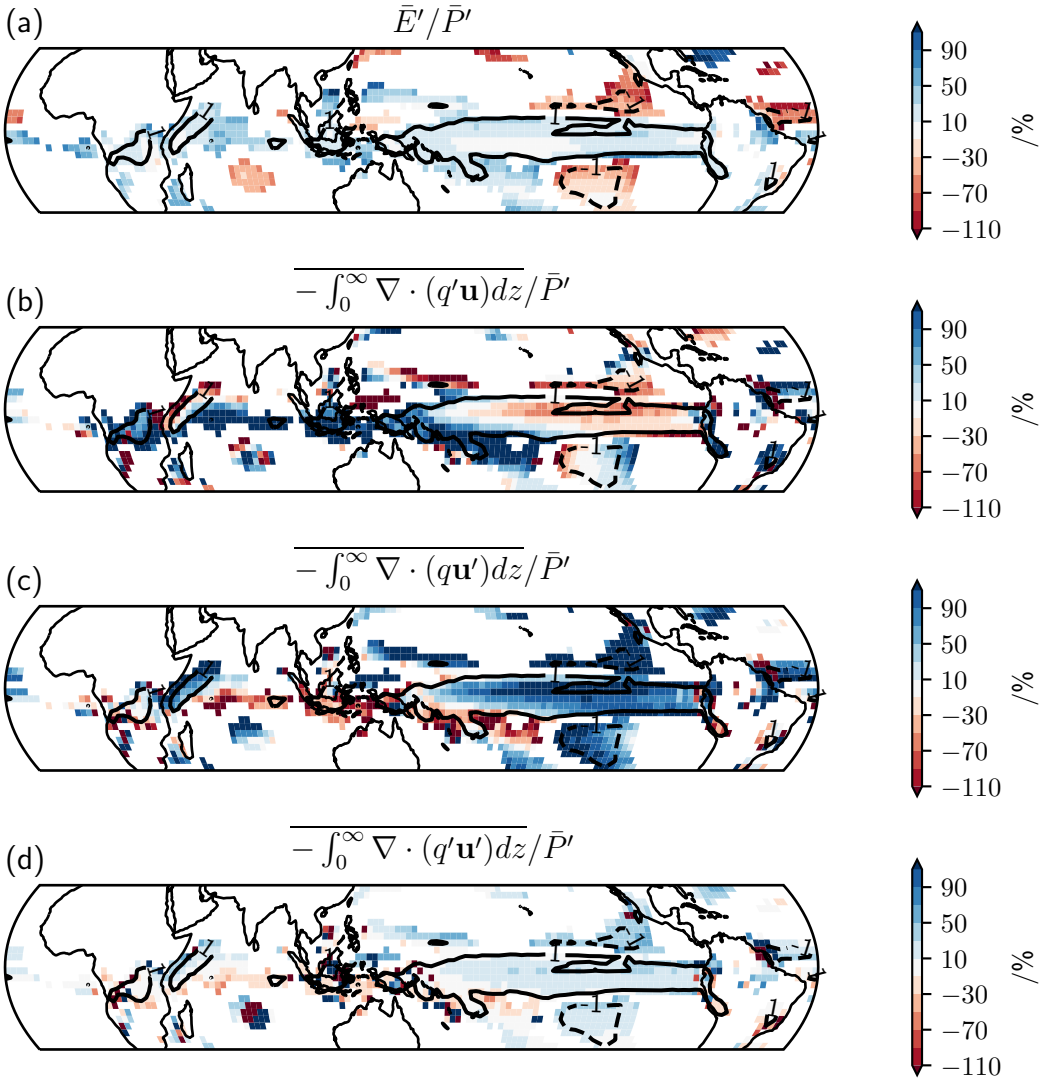

Figure 4.7: Colours show the DJF ensemble mean evaporation (a), thermodynamic (b), dynamic (c) and nonlinear (d) terms in the Seager et al. *(2010) decomposition, applied to the RCP8.5 minus historical mean state precipitation change, as a percentage of the corresponding precipitation change, $\bar{P}'$. Regions where $|\bar{P}'| < 0.5$ mm day^{-1} are masked. Black lines indicate the ± 1 mm day^{-1} contours of this precipitation change.*

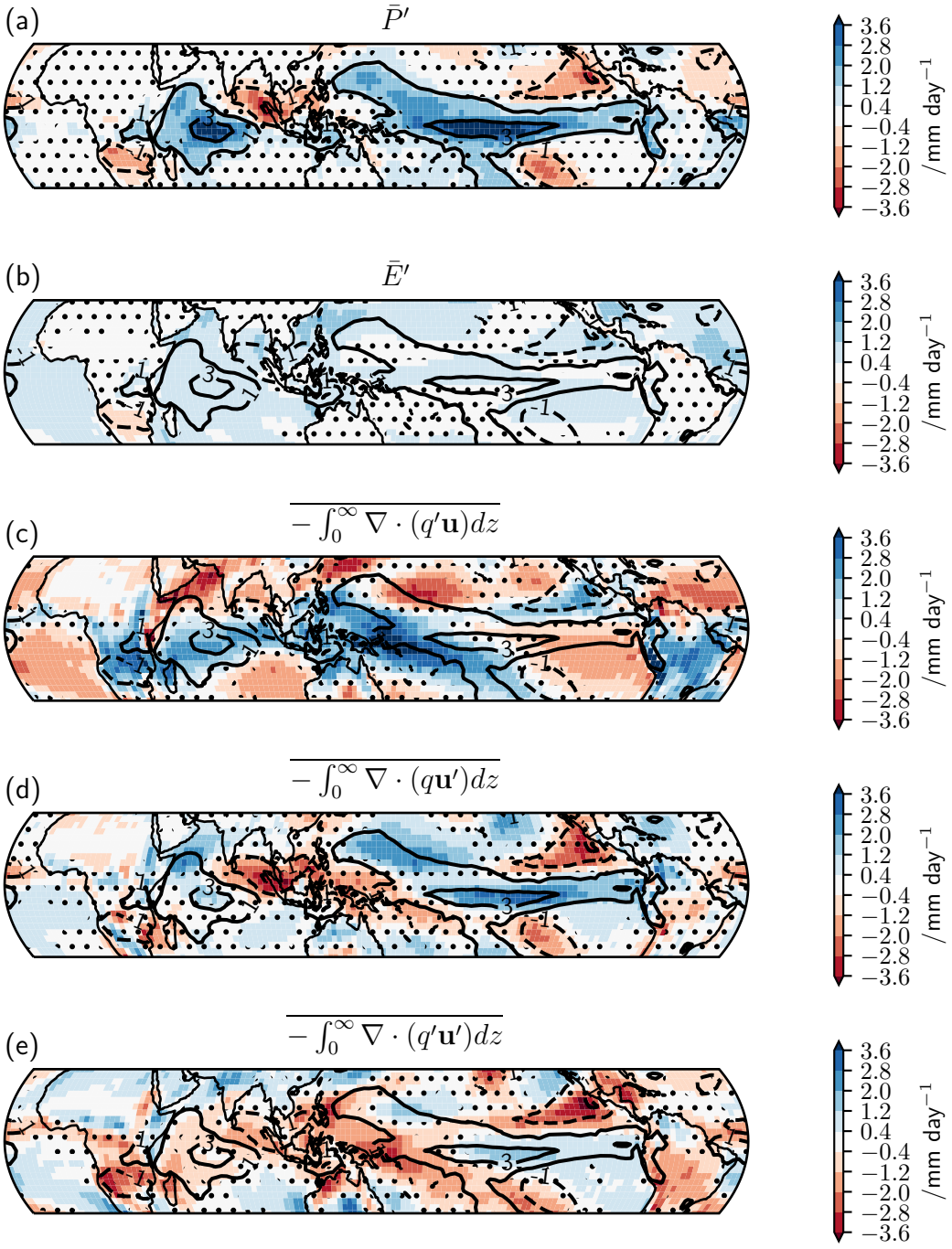

Figure 4.8: As in Figure 4.6, except for the amipTotal minus amip precipitation change.

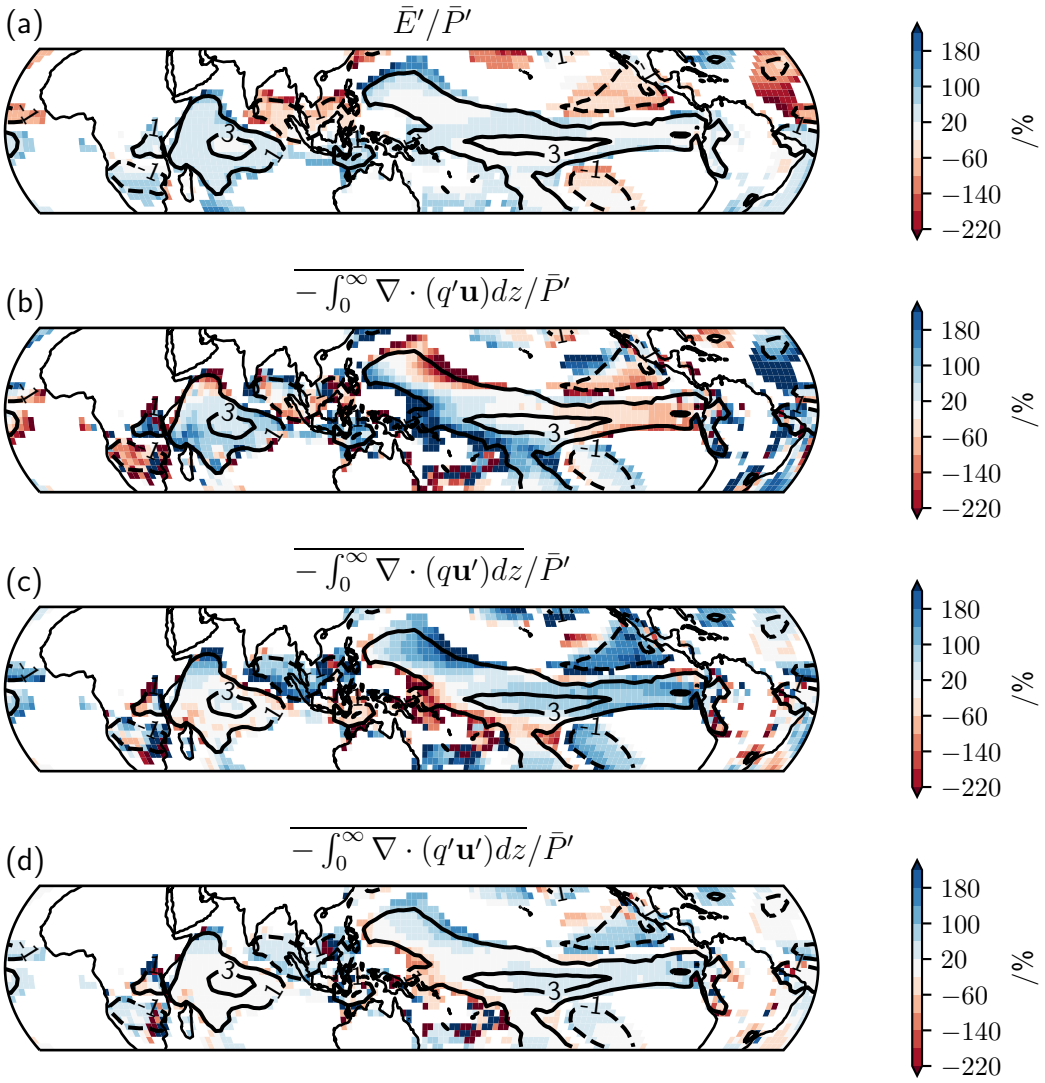

Figure 4.9: As in Figure 4.7, except for the amipTotal minus amip precipitation change.

change, as demonstrated by Figure 4.10. Evaporation increases across the majority of tropical ocean regions, and weakly decreases over subtropical Africa, northern Australia and eastern South America. These evaporation decreases over land are collocated with precipitation decreases, highlighting a relationship between simulated precipitation, soil moisture and evaporation changes (Seneviratne *et al.*, 2010). Consistent with RCP8.5, the thermodynamic contribution from amip4K indicates a strong wet-get-wetter and dry-get-drier precipitation change pattern. This thermodynamic contribution largely dominates the precipitation change over the western equatorial Pacific (Figure 4.11). Interestingly, the dynamic term is also broadly significant, contributing to the substantial precipitation increases (> 1 mm day^{-1}) over the central Indian ocean and the tropical north western, south central and eastern equatorial Pacific. Therefore, in amip4K, circulation change associated with convergence zone shifts contributes significantly to precipitation change. This circulation change occurs without SST gradient changes, the dominant factor over tropical oceans in coupled simulations (Xie *et al.*, 2010). Using a similar experiment, Ma *et al.* (2012) demonstrate how uniform SST warming leads to amplified warming aloft, with tropospheric temperatures following a moist adiabat. Hence in ascent and descent regions, respectively, cooling and warming occurs due to the vertical advection of temperature anomalies, leading to reduced horizontal pressure gradients. In turn, this causes weakening of the Hadley and Walker circulations. In addition, anomalous land warming is linked with shifts regions of convergence and divergence, as explored further in Chapter 5.

In both the amipFuture minus amip4K (Figure 4.12) and amip4xCO2 minus amip (Figure 4.14) mean state precipitation change decompositions, the dynamic term dominates the overall pattern and contributes the majority of the precipitation change, as shown by Figures 4.13 and 4.15, respectively. In the former, anomalous convergence in the central equatorial Pacific, Atlantic and western Indian oceans contributes almost entirely to the strong (> 1.8 mm day^{-1}) precipitation increases. Anomalous divergence over the eastern Indian and subtropical Pacific oceans leads to an equivalent magnitude of precipitation decreases. This pattern of circulation change is linked with the stronger prescribed SST warming in the eastern equatorial Pacific, western Indian and equatorial Atlantic oceans, relative to surrounding regions in amipFuture, leading to enhanced low level convergence over the relatively warmer tropical ocean areas (Xie *et al.*, 2010). In the CO_2 forcing experiment, circulation changes contribute to weaker (~ 1 mm day^{-1}) precipitation increases over southern Africa and northern Australia, and decreases over the tropical Indian, Atlantic and subtropical Pacific oceans. Similarly to amip4K, tropospheric warming and stabilisation, especially over oceans, and near surface changes over land are linked with the circulation changes in amip4xCO2.

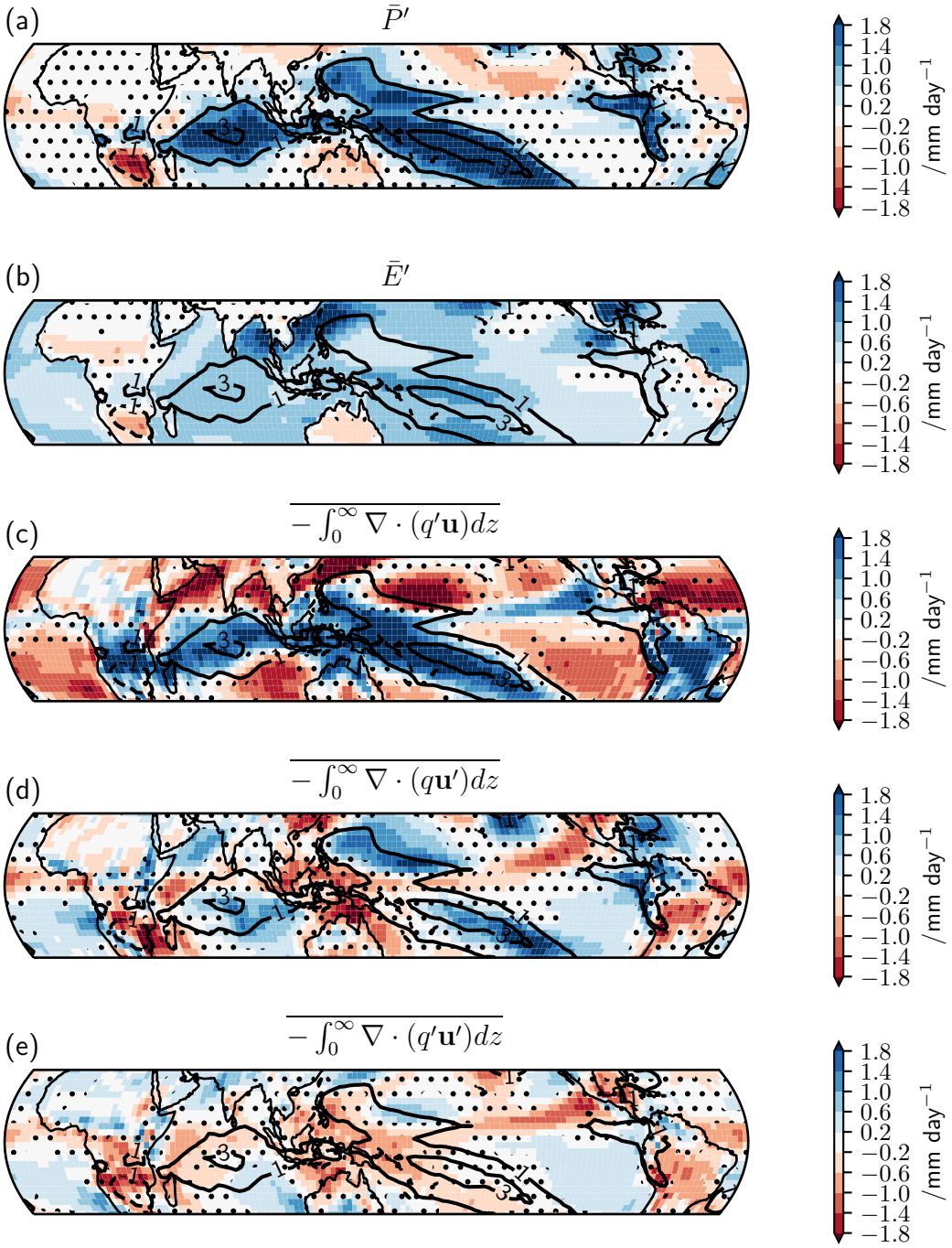

Figure 4.10: As in Figure 4.6, except for the amip4K minus amip precipitation change.

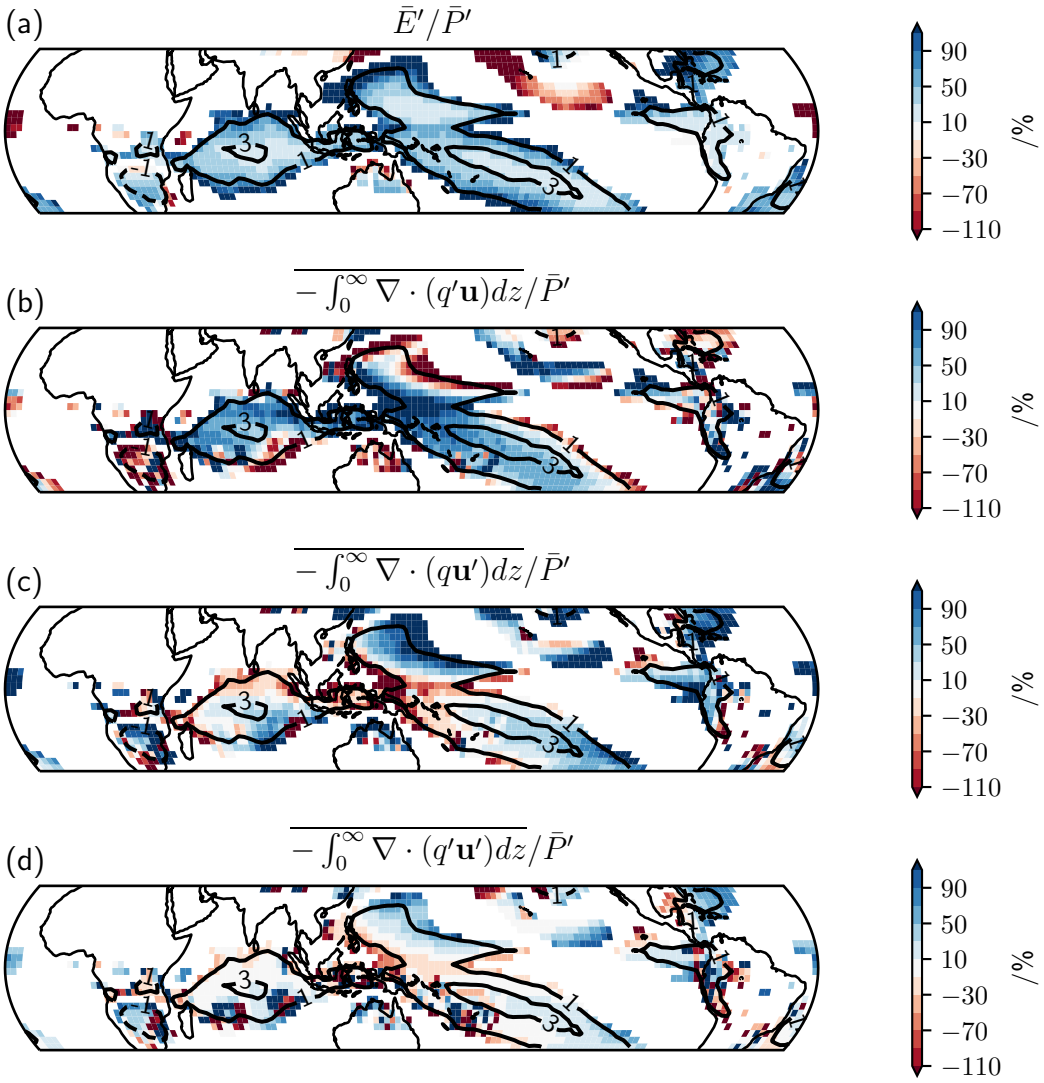

Figure 4.11: As in Figure 4.7, except for the amip4K minus amip precipitation change.

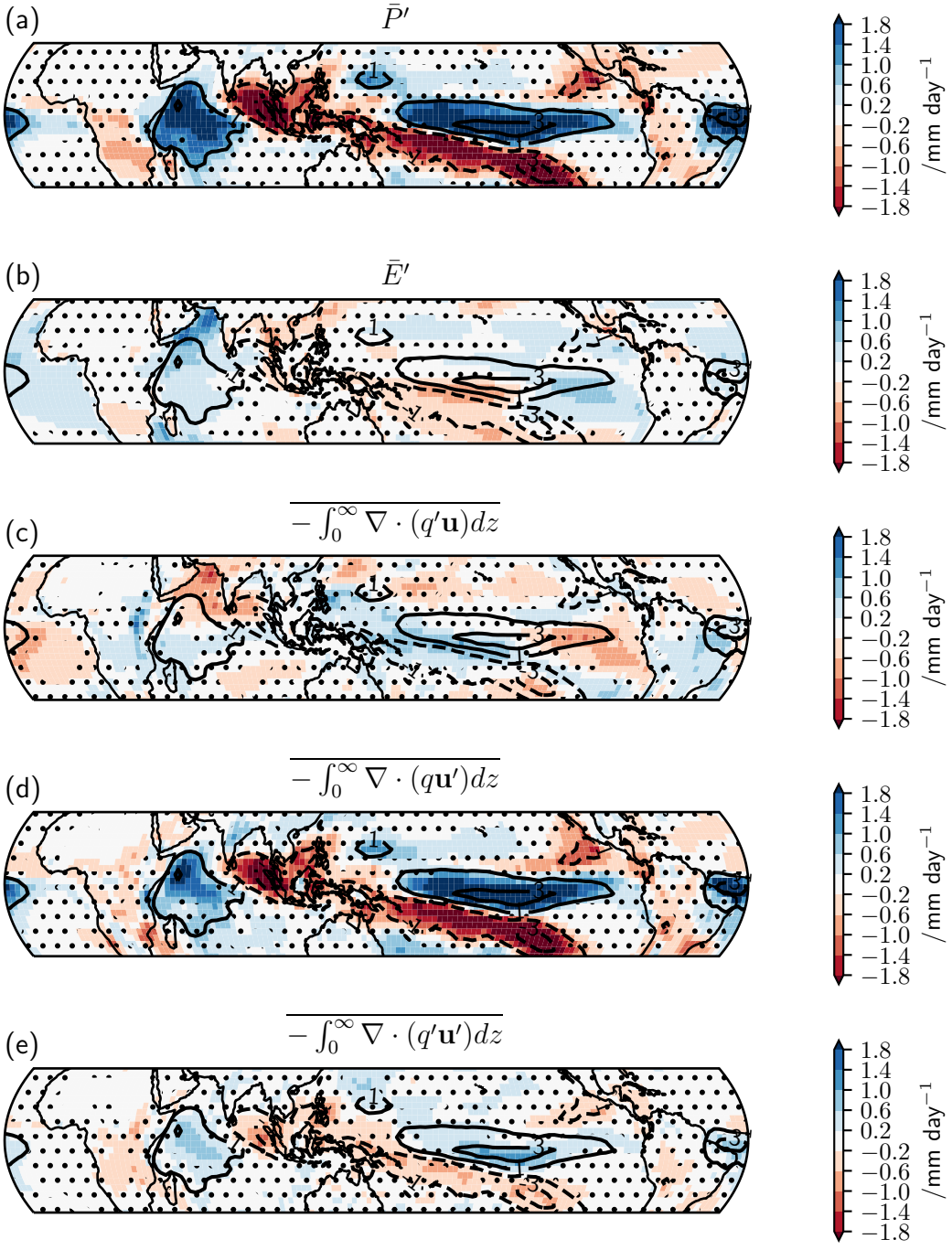

Figure 4.12: As in Figure 4.6, except for the amipFuture minus amip4K precipitation change.

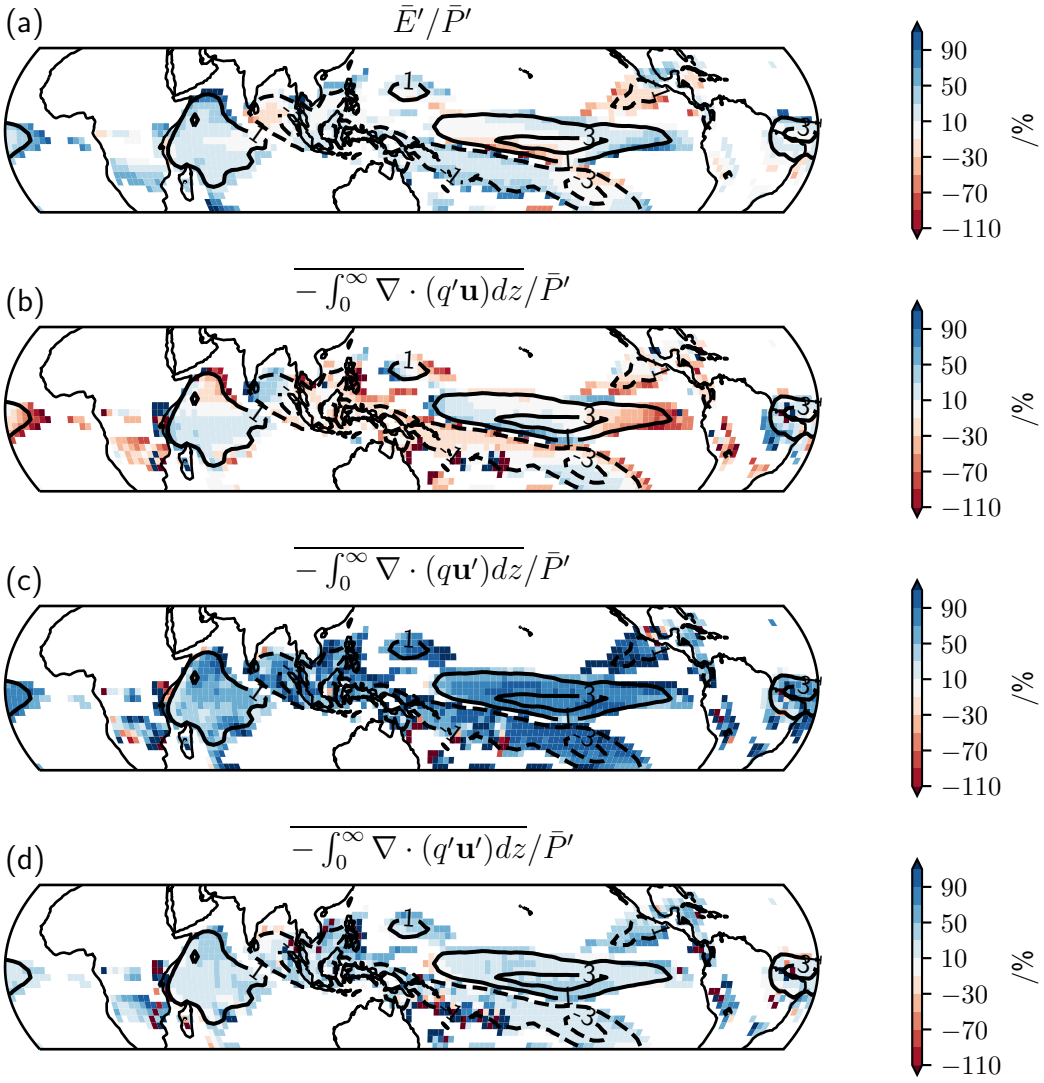

Figure 4.13: As in Figure 4.7, except for the amipFuture minus amip4K precipitation change.

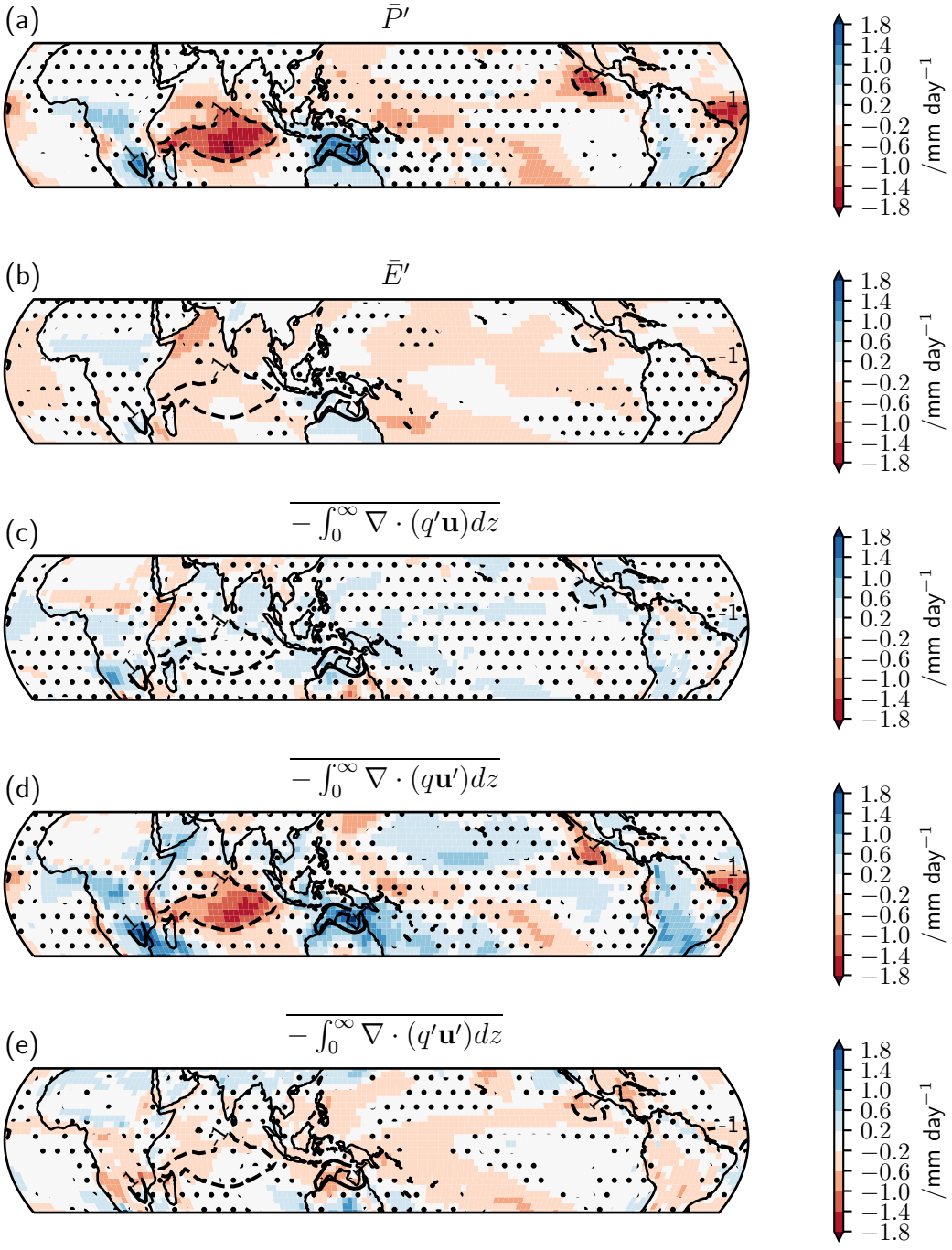

Figure 4.14: As in Figure 4.6, except for the amip4xCO2 minus amip precipitation change.

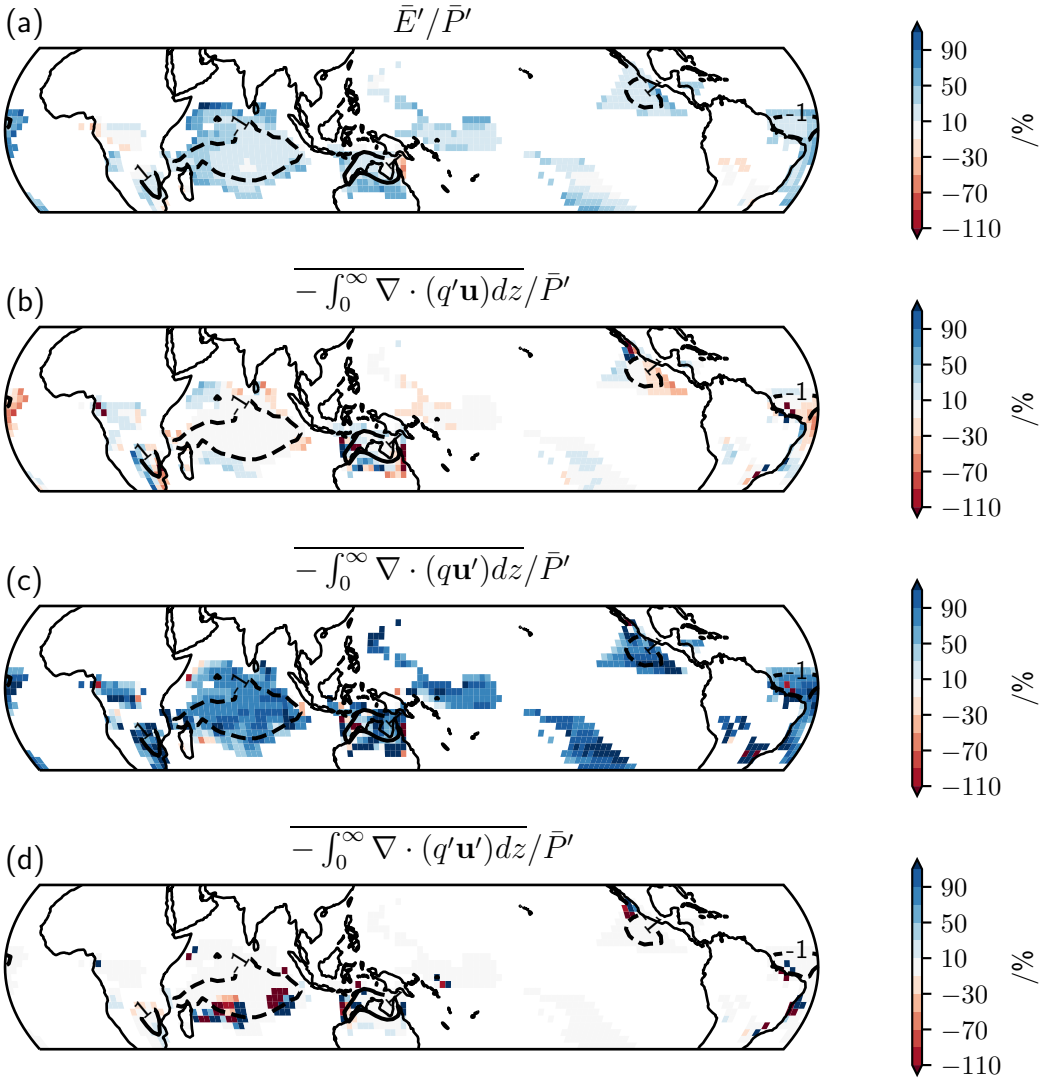

Figure 4.15: As in Figure 4.7, except for the amip4xCO2 minus amip precipitation change.

Decomposing ENSO Anomalous Precipitation Changes

Examining the Seager *et al.* (2010) moisture budget decomposition of the idealised atmosphere-only and coupled climate model El Niño anomalous precipitation, significant changes and contributions are generally confined to the tropical Pacific. This is the region of strongest present day El Niño anomalous precipitation in observations and climate model simulations (Chapters 2, 3 and Section 4.3.1), indicating only minor changes in El Niño teleconnection locations. A common result in each case is that the change in the dynamic component, $\Delta \left[-\int_0^H \nabla \cdot (q\mathbf{u}') \right]_{EN}$, dominates the change in the El Niño anomalous precipitation, $\Delta P'_{EN}$, as shown by Figures 4.16-4.20. Consequently, changes in El Niño anomalous circulation, instead of specific humidity or evaporation, are generally responsible for anomalous precipitation changes.

In the RCP8.5 minus historical (Figure 4.16), and amip4xCO2 minus amip (Figure 4.20) cases, the El Niño anomalous evaporation change is insignificant and negligible ($|\Delta E'_{EN}| < 0.2$ mm day^{-1}) across the tropics. For amipTotal minus amip (Figure 4.17), amipFuture minus amip4K (Figure 4.19) and amip4K minus amip (Figure 4.18), there are minor decreases in anomalous evaporation ($\Delta E'_{EN} \approx -0.4$ mm day^{-1}) near the western coast of Africa and eastern coast of Asia, however these are insignificant with respect to model variability. Since these weak evaporation changes occur in both uniform and patterned SST warming cases, circulation changes linked with land-sea temperature contrast changes, leading to relatively reduced surface wind speeds may contribute.

Consistent with the El Niño anomalous evaporation changes, differences in the thermodynamic component between present day and future El Niño conditions are generally insignificant and negligible across the tropics, in each case. This contrasts the mean state changes, where the thermodynamic term contributes to a large and significant wet-get-wetter and dry-get-drier response due to tropics-wide specific humidity increases, especially over oceans (Held and Soden, 2006). This result implies that specific humidity variability between neutral and El Niño conditions remains relatively constant in present day and atmosphere-only or coupled future simulations.

Except for the amipFuture minus amip4K (Figure 4.19) case, the difference in the nonlinear component is typically small and insignificant, similar to the evaporation change and thermodynamic term difference. In the SST pattern change case, the nonlinear term difference significantly contributes approximately one quarter of the $\Delta P'_{EN}$ increases and decreases in the central and western equatorial Pacific, respectively. In turn, this weakly contributes in amipTotal, however these changes are insignificant relative to inter-model variability in these regions. As discussed in the previous subsection for mean state changes, this small but significant change in the nonlinear component is most substantial when circulation changes are especially large. For amipFuture, where

SST warming is stronger in the eastern relative to the western equatorial Pacific, present day El Niño SST anomalies lead to a reversal of the zonal SST gradient. In contrast, in the uniform warming (amip4K) or CO_2 forcing (amip4xCO2) experiments, El Niño SST anomalies typically only weaken the zonal SST gradient. This leads to an amplification of the circulation anomalies in amipFuture relative to amip4K.

Partitioning Dynamic Contributions to Precipitation Changes

The results of the mean state and El Niño change precipitation decompositions highlight the important role circulation changes play in each of the contributing experiments to amipTotal. By the chain rule, the dynamic component in the Seager *et al.* (2010) moisture budget decomposition can be partitioned into two terms:

$$-\int_0^H \nabla \cdot (q\mathbf{u}')dz = -\int_0^H \mathbf{u}' \cdot \nabla q dz - \int_0^H q\nabla \cdot \mathbf{u}' dz, \tag{4.8}$$

referred to as the advective and divergent terms, respectively. Figure 4.21 demonstrates this partitioning applied to the RCP8.5 minus historical and amipTotal minus amip changes, alongside each component of amipTotal. For amipFuture minus amip4K, amip4xCO2 minus amip and RCP8.5 minus historical, the magnitude of the divergent term is substantially larger than the advective term. In the uniform warming case, both terms are typically a similar magnitude, with the exception of $\int_0^H \nabla \cdot (q\mathbf{u}')dz < 0$ areas, where the divergent term dominates. This implies that circulation changes in each global warming experiment largely affect mean state precipitation on regional scales via pattern changes in convergence and divergence. Changes in moisture advection play a more minor role in affecting mean state precipitation changes.

As discussed previously, the changes in the dynamic term dominates the decomposition of El Niño anomalous precipitation changes in each atmosphere-only and the coupled simulation. The partitioning of each dynamic component into advective and divergent terms is displayed in Figure 4.22. Similar to the mean state changes, the divergent term typically has a larger magnitude than the advective term. Hence, for both the mean climate and climate variability changes, under idealised or more realistic perturbations, convergence and divergence changes contribute substantially to the overall tropical precipitation changes.

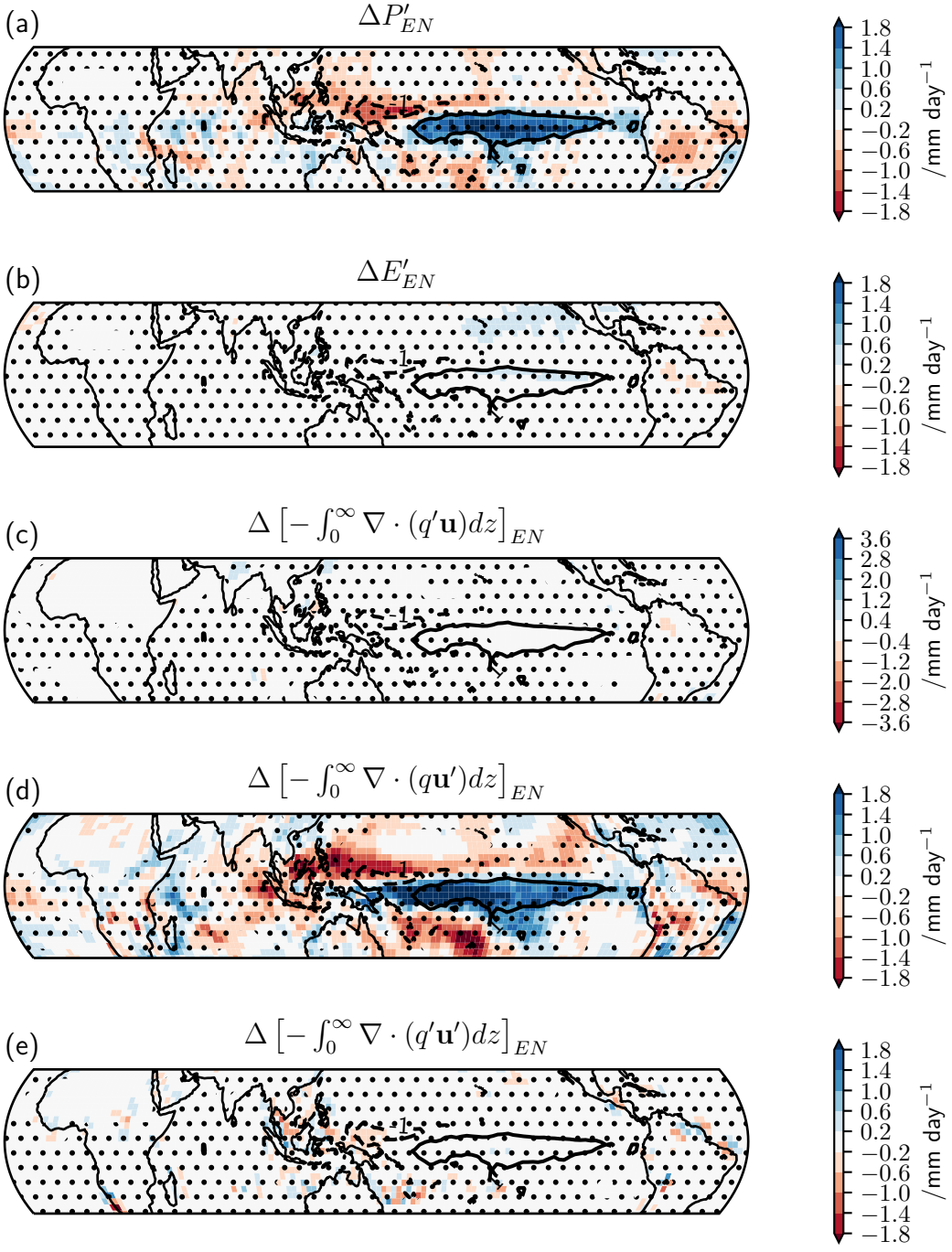

Figure 4.16: As in Figure 4.6, except for the RCP8.5 minus historical El Niño anomalous precipitation change.

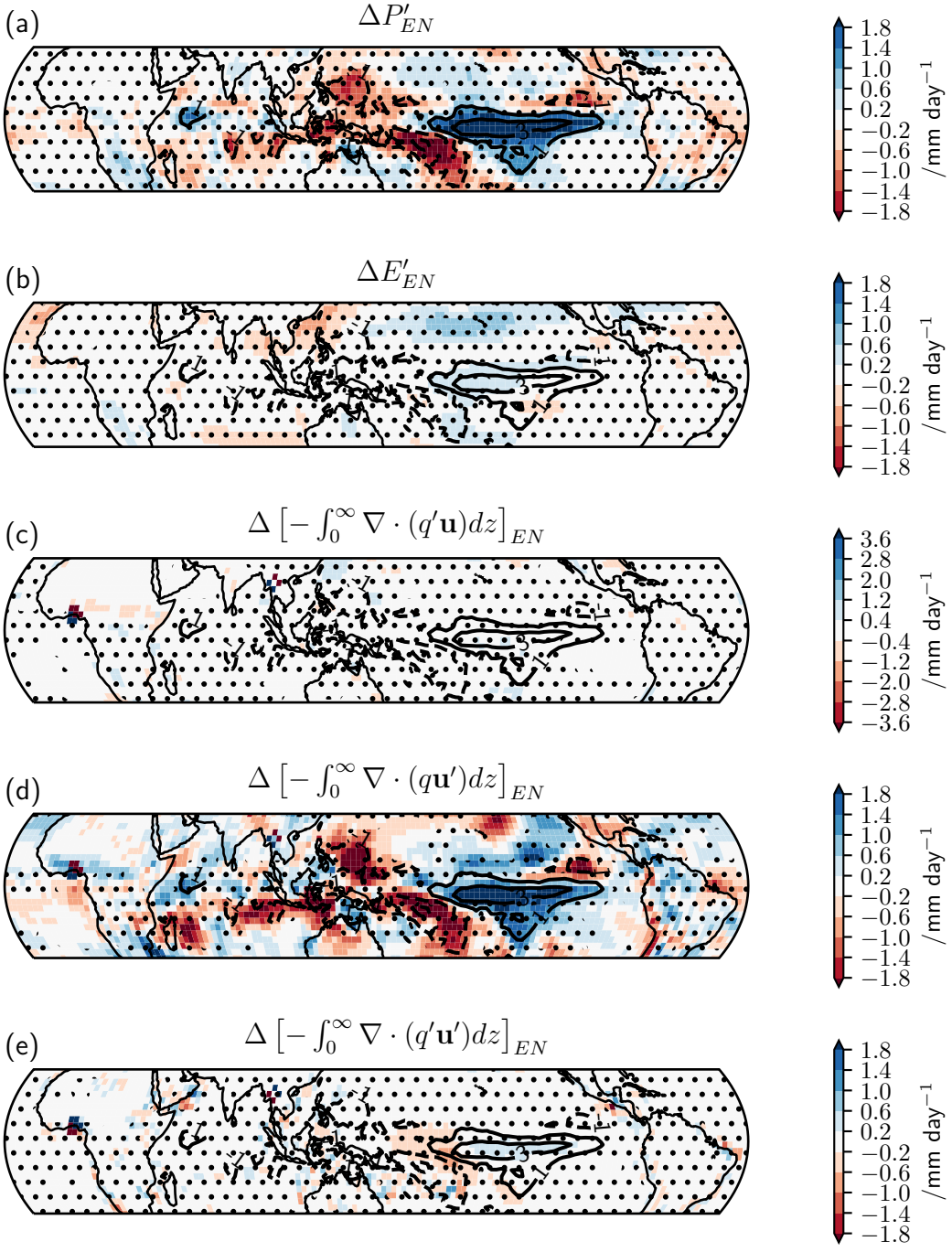

Figure 4.17: As in Figure 4.6, except for the amipTotal minus amip El Niño anomalous precipitation change.

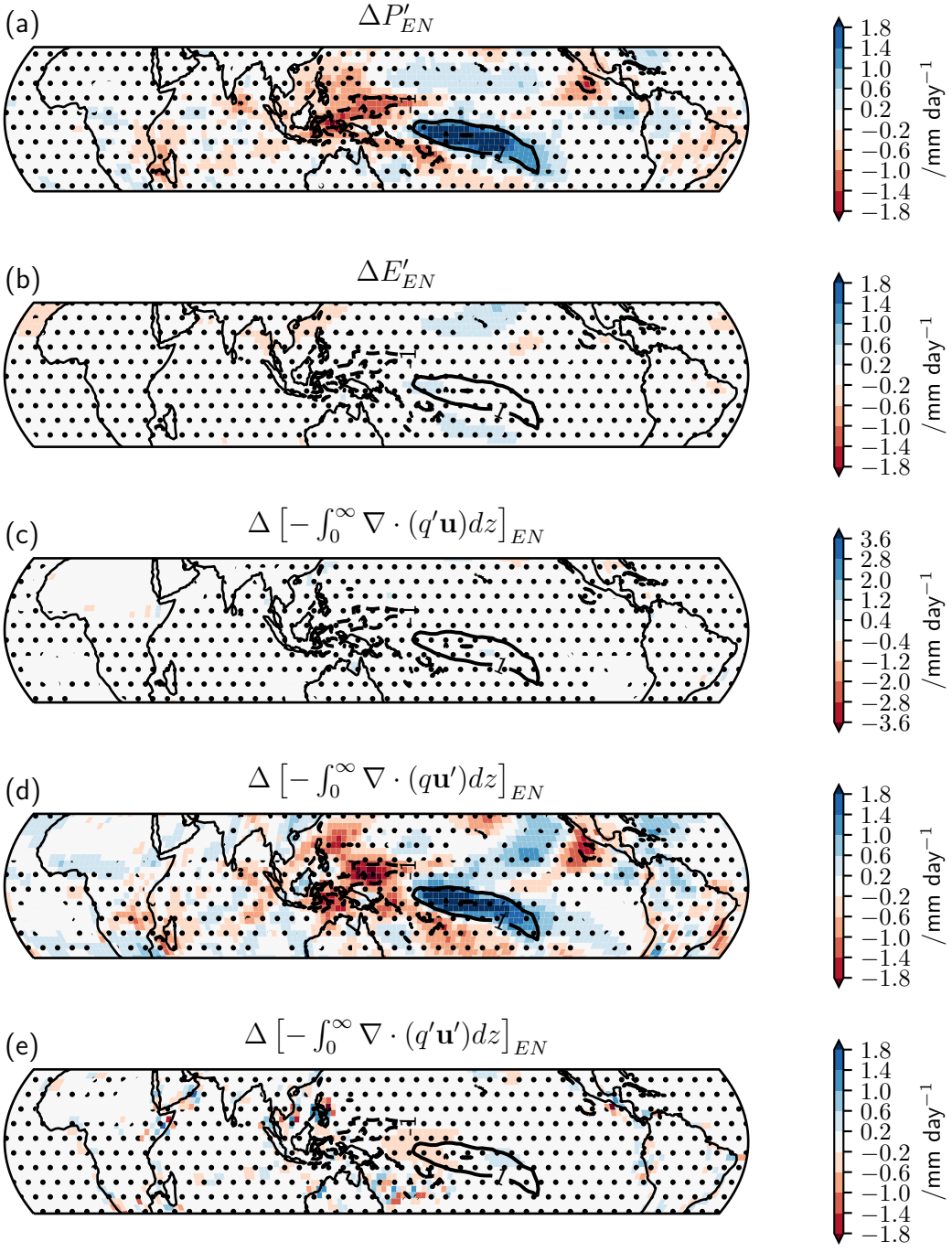

Figure 4.18: As in Figure 4.6, except for the amip4K minus amip El Niño anomalous precipitation change.

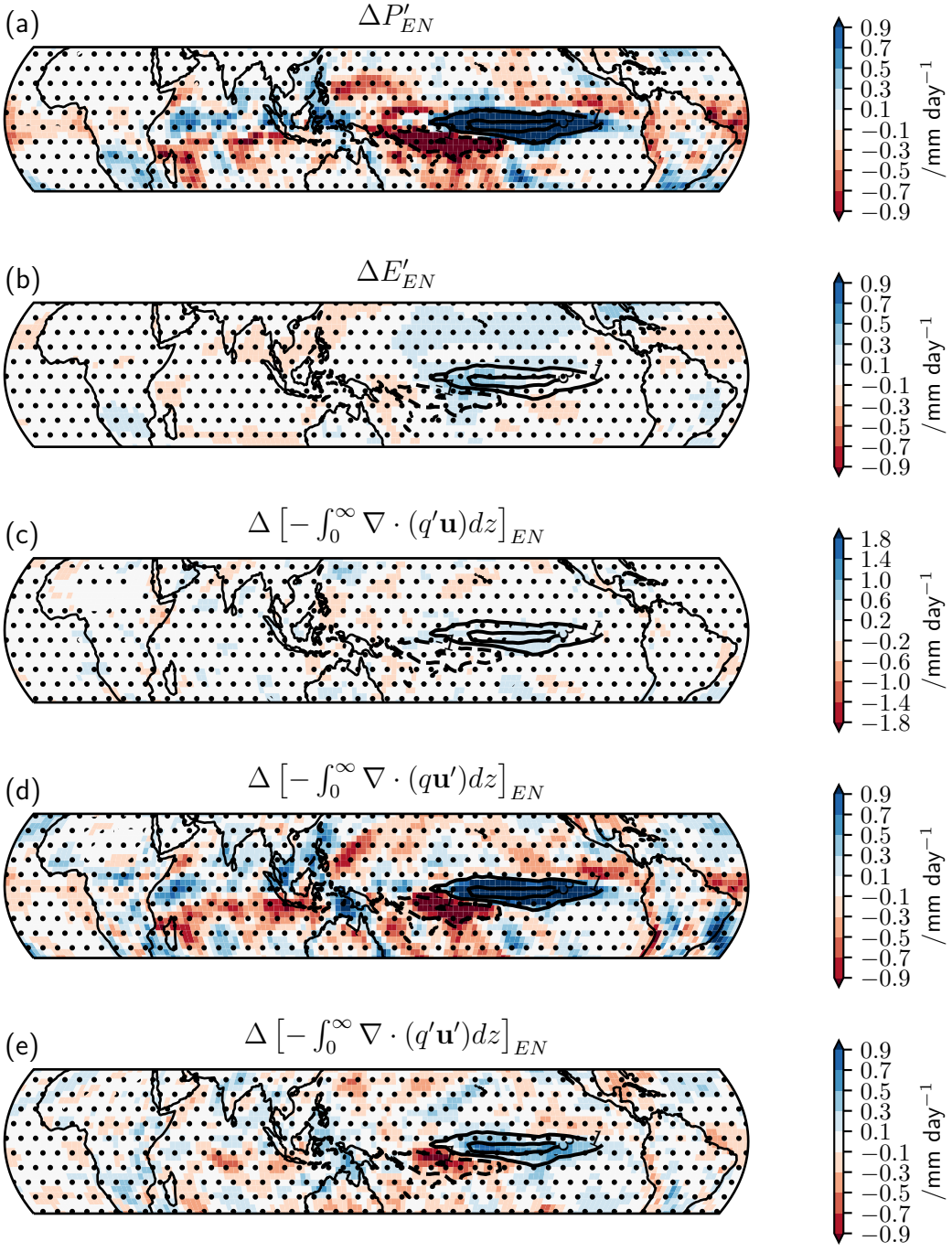

Figure 4.19: As in Figure 4.6, except for the amipFuture minus amip4K El Niño anomalous precipitation change.

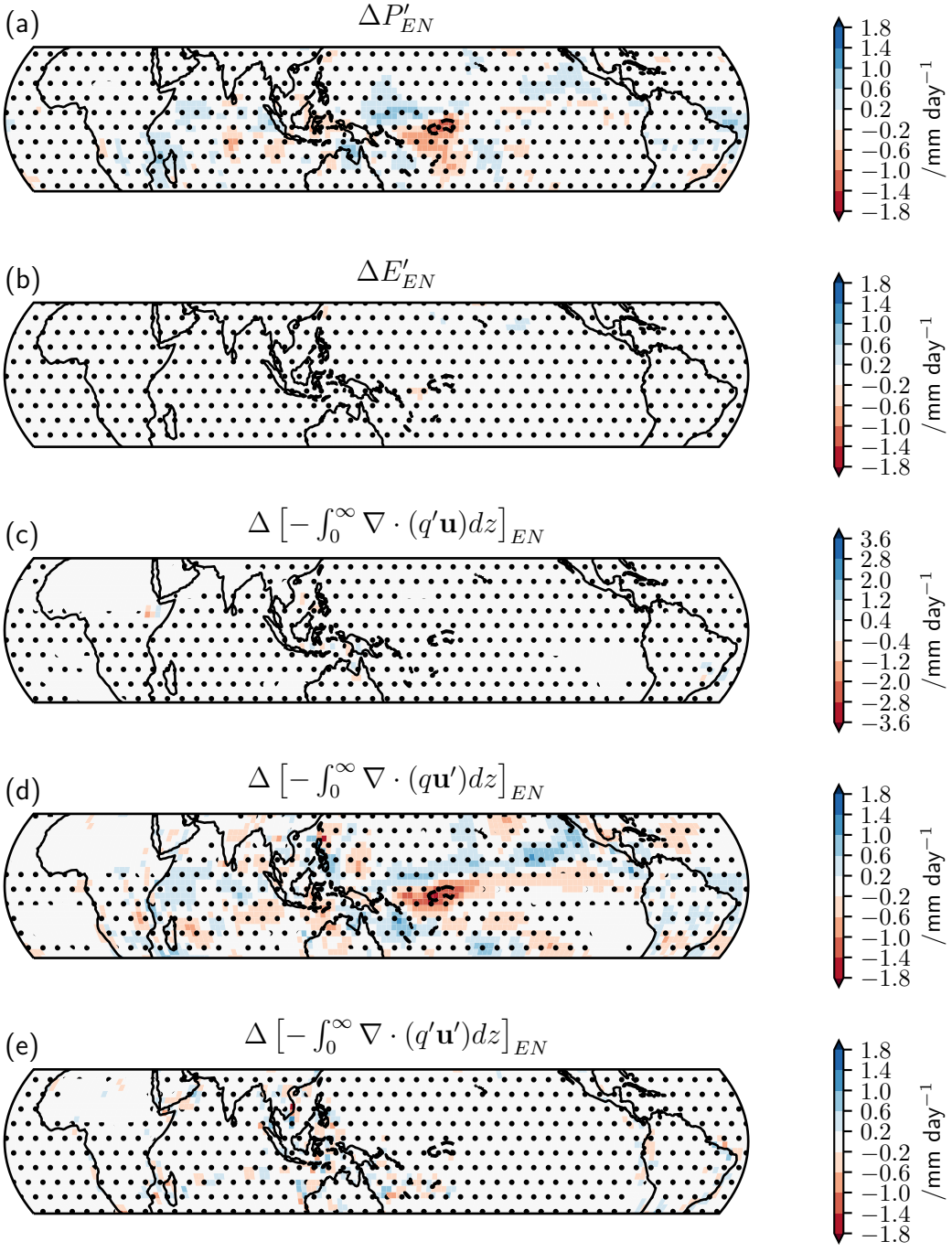

Figure 4.20: As in Figure 4.6, except for the amip4xCO2 minus amip El Niño anomalous precipitation change.

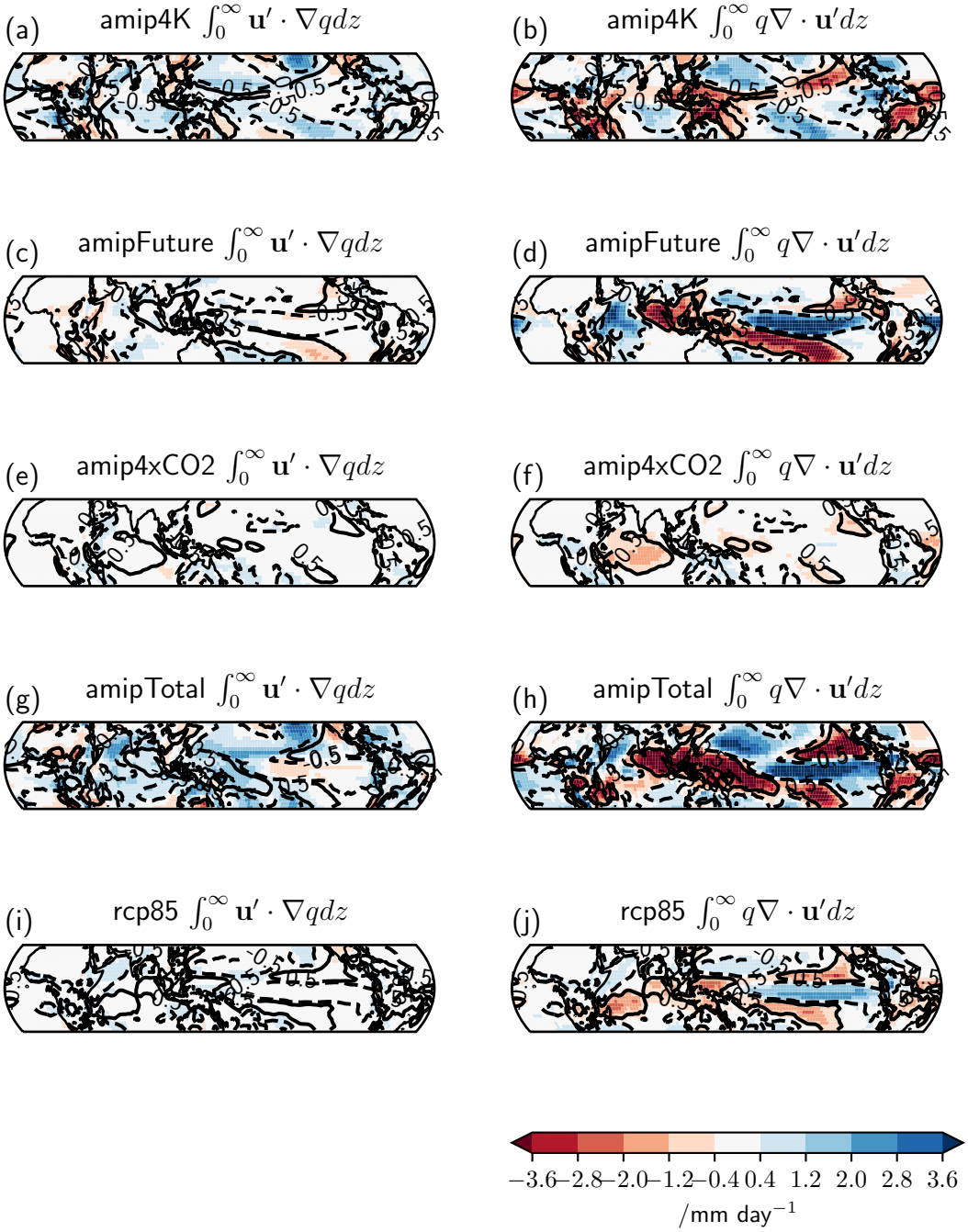

Figure 4.21: Colours show the DJF ensemble mean advective (a, c, e, g, i) and divergent (b, d, f, h, j) components of the dynamic term in the Seager et al. *(2010) moisture budget decomposition, applied to amip4K minus amip (a, b), amipFuture minus amip4K (c, d), amip4xCO2 minus amip (e, f), amipTotal minus amip (g, h) and RCP8.5 minus historical (i, j) mean state changes. Black lines indicate the* ± 1 *mm day*$^{-1}$ *contours of the respective dynamic terms.*

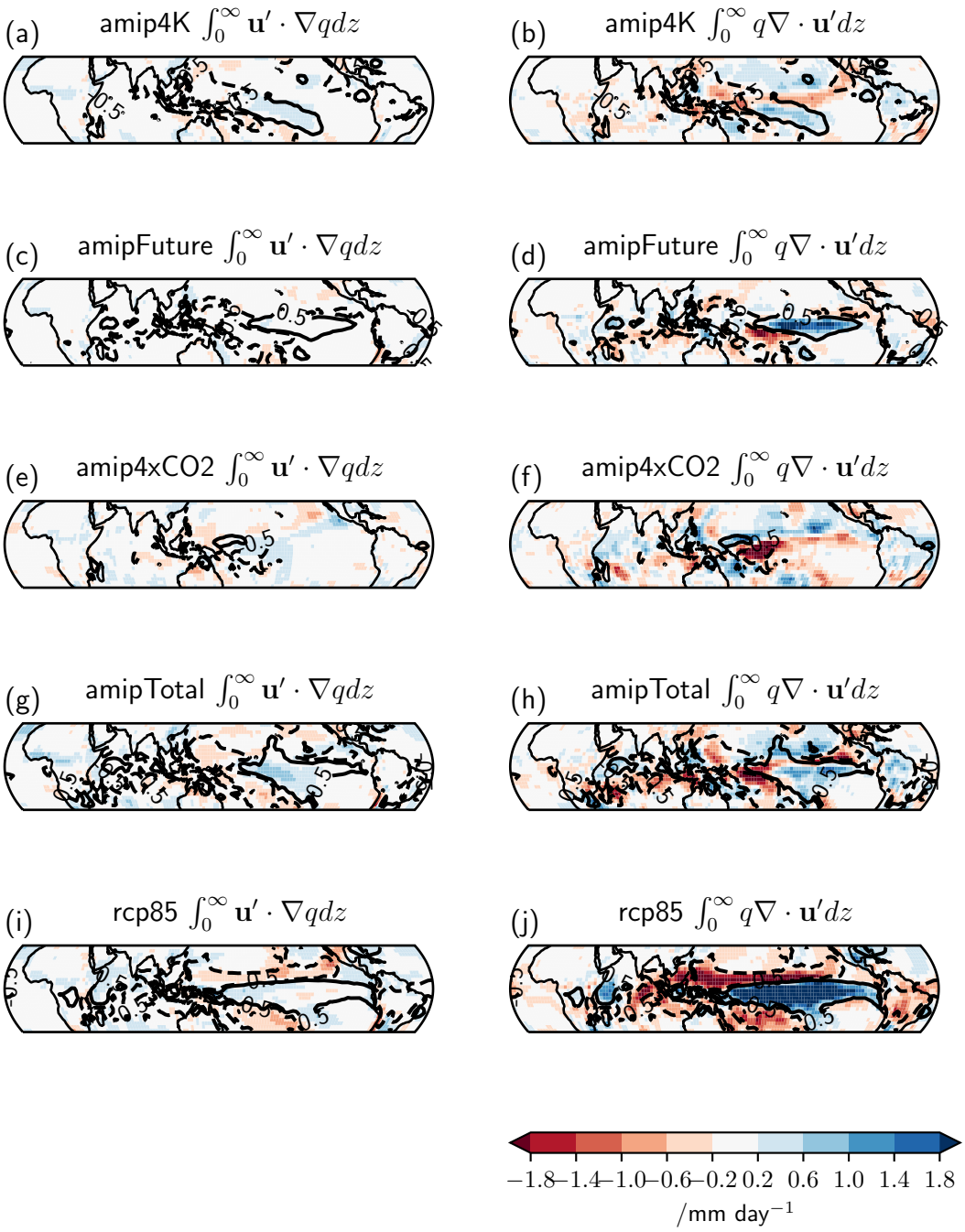

Figure 4.22: As in Figure 4.21, except for the respective El Niño anomaly precipitation changes.

4.4 Discussion and Conclusions

In this chapter, idealised atmosphere-only simulations have been used to provide a mechanistic insight into more realistic coupled global warming experiments. Existing CMIP5 simulations were explored in Section 4.3, with the main result that tropospheric circulation change is strongly linked with both the precipitation mean state and variability change under a variety of future conditions.

An atmosphere-only proxy for the RCP8.5 future coupled experiment, amipTotal, was introduced in Section 4.3.1. This approach yields two benefits: Firstly, present day atmosphere-only simulations exhibit weaker biases relative to coupled simulations, due to issues with atmosphere-ocean feedbacks in the latter, affecting mean state (Li and Xie, 2014; Toh *et al.*, 2018) and variability (Bellenger *et al.*, 2014; Ferrett *et al.*, 2018). Secondly, partitioning amipTotal enables a comparison of the relative contributions of uniform and patterned SST warming, and CO_2 forcing. Moderate to strong correlations are evident between the amipTotal and RCP8.5 anomalies for mean state temperature (0.87) and precipitation (0.64) changes, and El Niño anomaly temperature (0.63) and precipitation (0.57) changes, respectively. Considering mean state changes, enhanced land warming is a robust response to both uniform SST and CO_2 perturbations, consistent with the literature (Joshi *et al.*, 2008). Further changes in regional land-ocean temperature contrasts are evident in simulated El Niño anomaly changes.

In Section 4.3.2, applying the Seager *et al.* (2010) moisture budget decomposition to amipTotal and its constituent components quantifies the relative roles of thermodynamic (specific humidity), dynamic (circulation) and nonlinear (specific humidity and circulation) components to mean state precipitation changes. For RCP8.5, the pattern of precipitation changes are largely a balance of thermodynamic and dynamic contributions, since the nonlinear and evaporation contributions are typically insignificant. Similar results hold for the atmosphere-only response, except for a stronger nonlinear term likely due to the greater tropical mean warming ($+5.1$ K) relative to RCP8.5 ($+3.5$ K). Uniform SST warming in amip4K leads to a thermodynamic component of precipitation increase at large scales (Held and Soden, 2006). Importantly, at regional scales in amip4K a significant dynamic component of precipitation change is present, in the absence of SST gradient changes. In addition to the Ma *et al.* (2012) mechanism of advection of stratification change, a hypothesis that land-ocean temperature contrast changes strongly contribute to the circulation response in amip4K is proposed.

In response to patterned SST warming in amipFuture and CO_2 forcing in amip4xCO2, the dynamic component dominates the mean state precipitation response. In the former, this is due to relatively enhanced convection over the strongest SST anomalies leading to shifts in convergence zones (Xie *et al.*, 2010). In the latter case, Bony *et al.*

(2013) suggest tropospheric warming and relative stabilisation over ocean contributes to an enhanced land-ocean temperature contrast and circulation change. Examining the El Niño anomaly precipitation change, the dynamic component is the major contributor in all experiments. Differences in the evaporation, thermodynamic and nonlinear terms are generally small and insignificant with respect to model variability. Partitioning the dynamic component into advective and convergent terms, the latter is generally largest for both the El Niño anomaly and mean state precipitation changes. This indicates that anomalous convergence or divergence is typically the leading mechanism acting in precipitation changes, with anomalous moisture advection contributing more weakly.

A key result demonstrated in this chapter is the important role of circulation change in modulating both the mean state and variability of tropical precipitation in response to global warming. This is evident in both a realistic, coupled future scenario, RCP8.5, and under idealised SST or CO_2 perturbations in atmosphere-only scenarios. Consequently, the general wet-get-wetter and dry-get-drier paradigm (Held and Soden, 2006) is particularly inadequate at regional scales, especially over tropical land. Consistent with the literature, SST pattern change is a major factor in driving precipitation changes (Xie *et al.*, 2010). However, under uniform SST perturbations, significant circulation changes are simulated, highlighting the important secondary factor of surface condition changes over land.

This chapter has largely reviewed existing results from the literature, applying an established method (Seager *et al.*, 2010) in a framework to partition precipitation mean state and variability changes. The following chapter examines the mechanisms contributing to transient and equilibrium tropical precipitation change in greater detail, using a novel ensemble of HadGEM2-A simulations.

Chapter 5

Future Tropical Precipitation Change Mechanisms in HadGEM2-A

5.1 Introduction

The previous chapter presented an analysis of CMIP5 ensemble mean simulated tropical precipitation change under various global warming perturbations. In particular, the equilibrium atmospheric response to idealised instantaneous SST or CO_2 forcing was found to be a suitable proxy for a more realistic, coupled future scenario. In this chapter, a novel ensemble of atmosphere-only experiments are conducted using a single model to explore how the equilibrium response is reached. Examining the transient response provides a step towards understanding causality in the mechanisms contributing to equilibrium changes. Section 5.2 describes the model used and experimental design. Sections 5.3 and 5.4 discuss the tropical land mean and regional responses, respectively.

5.2 Data and Methods

In order to examine the mechanisms acting to modulate tropical precipitation change in the AMIP experiments, as discussed in Section 4.3, a single model ensemble of HadGEM2-A experiments is used. Simulations are commenced from varying initial conditions, to capture internal variability, and at different ENSO phases in order to evaluate the sensitivity of responses.

5.2.1 The HadGEM2-A Atmosphere-only GCM

HadGEM2-A is the atmosphere-only configuration of HadGEM2, a family of climate models developed at the Met Office, as described by Martin *et al.* (2011). HadGEM2-A consists of the Unified Model (UM) atmosphere general circulation model (GCM), including an aerosol component (Bellouin *et al.*, 2007), and the Met Office Surface Exchanges Scheme (MOSES-II) land surface and hydrology component (Cox *et al.*, 1999; Essery *et*

al., 2003). Specifically, the UM at version 6.6.3 was used for the CMIP5 HadGEM2-A simulations.

The structure of the UM has been developed iteratively since its seminal publication: Cullen (1993). In HadGEM2-A, atmospheric circulation is resolved on 38 vertical levels between 20 m to ∼40 km above the surface, closely following terrain at lower levels and becoming approximately isobaric with height. The atmosphere grid is 1.875° longitude $\times 1.25^\circ$ latitude, and hence HadGEM2-A has a comparable horizontal resolution to the majority of other CMIP5 atmosphere-only models (c.f. Table 4.1). Davies *et al.* (2005) describe the UM dynamical core used in detail, a summary is provided here. The atmosphere is assumed to be non-hydrostatic and compressible. Numerically, Eulerian mass conservation is used, alongside semi-Lagrangian advection and semi-implicit time integration. In climate configuration, a model time step of 30 minutes is used, with 360 days per model year. The Navier-Stokes equations of motion are discretized horizontally on an Arakawa C-grid (Arakawa and Lamb, 1977), where zonal and meridional wind fields are staggered relative to the other prognostic fields, and vertically on a Charney-Phillips grid (Charney and Phillips, 1953).

Consistent with all global climate models contributing to CMIP5, convection is parametrised in HadGEM2-A. The convective mass flux scheme largely follows that of Gregory and Rowntree (1990), with shallow and deep convection diagnosed at each time step from the environmental humidity and temperature profile, following Grant (2001) and Fritsch and Chappell (1980), respectively. If either type convection is diagnosed, vertical mass transport is parametrised above the lifting condensation level and the boundary layer is capped. In HadGEM2-A, a key difference from the Gregory and Rowntree (1990) scheme is the inclusion of adaptive detrainment rates, which improves of the representation of tropical convection and surface wind stress (Derbyshire *et al.*, 2011). Martin *et al.* (2010) detail other minor changes to the convection scheme, relative to that of Gregory and Rowntree (1990), as used in HadGEM2-A. Stratiform precipitation is also parametrised in HadGEM2-A, but these contributions are relatively small in the tropics, as discussed in Chapter 1.

5.2.2 Experiment Design

A schematic of the HadGEM2-A ensemble experiment design is presented in Figure 5.1. Archived start dumps for 1 August 1986, 1988, 1990, 1992, 1994, 1996 and 1998 from the HadGEM2-A amip r1i1p1 contribution to CMIP5 are used to provide initial conditions for seven amip ensemble members. These amip experiments are integrated forward twelve years and five months of model time between 1 August 1986 and 30 December 1998. The start dumps set the initial atmospheric state and soil moisture content in each simulation. Hence, the ensemble is designed to simulate internal variability due to

differences in atmospheric initial conditions but identical prescribed SST, greenhouse gas and aerosol forcing. This seven member amip ensemble represents the control, present day climate. In addition, equivalent seven member ensembles of amip4K, amipFuture and amip4xCO2 simulations are also initialised from these start dumps and integrated forward to 30 December 1998. These experiments follow an identical protocol to CMIP5, except for the time period covered. As discussed in Section 4.2.1, these experiments apply a uniform SST warming (amip4K), patterned SST warming (amipFuture), and CO_2 forcing (amip4xCO2) to the atmosphere. The twenty one climate simulations from these idealised global warming experiments are hereafter referred to as future equilibrium conditions.

In addition to the control and equilibrium ensembles, three further sets of seven amip4K, amipFuture and amip4xCO2 initial condition simulations are performed. These sets branch from the amip control ensemble members on 1 August 1988, 1990 and 1997, and are integrated forward for five model months to 30 December. These simulations will be referred to as the transient conditions, as the atmosphere responds over a timescale of a few days to a few months to these instantaneous perturbations (Dong *et al.*, 2009). The years 1988, 1990 and 1997 are selected since they represent La Niña, neutral and El Niño conditions respectively, via the Oceanic Niño Index (NOAA, 2015). In particular, the magnitude of the Niño3.4 SST anomalies are especially large (~ 2 K) during the La Niña (negative) and El Niño (positive) cases. Subtracting the 1997 simulations from the 1990 simulations provides a proxy for the El Niño anomaly, and similarly for the 1988 minus 1990 simulations for the La Niña anomaly. Simulations are initialised in August since this represents the growth stage for ENSO events (Rasmusson and Carpenter, 1982), and hence equilibrium conditions are reached over the ENSO mature phase when the present day precipitation anomalies are largest.

Daily data is output from these HadGEM2-A simulations and used in this analysis. Three dimensional fields such as zonal and meridional wind, vertical velocity and specific humidity, are saved on twelve pressure levels profiling the troposphere, equivalent to the monthly mean data used in Section 4.3. This improves the vertical resolution in comparison to the daily data in the CMIP5 archive, which is only stored on eight pressure levels between 1000 and 100 hPa. This maintains equivalent accuracy when computing vertical integrals for the daily HadGEM2-A data with the monthly CMIP5 data, as used in Section 4.3.2. For the remainder of this chapter, the HadGEM2-A ensemble mean is assessed in order to reduce internal variability. Significance testing is applied as described in Section 4.2.3, in order to identify robust responses.

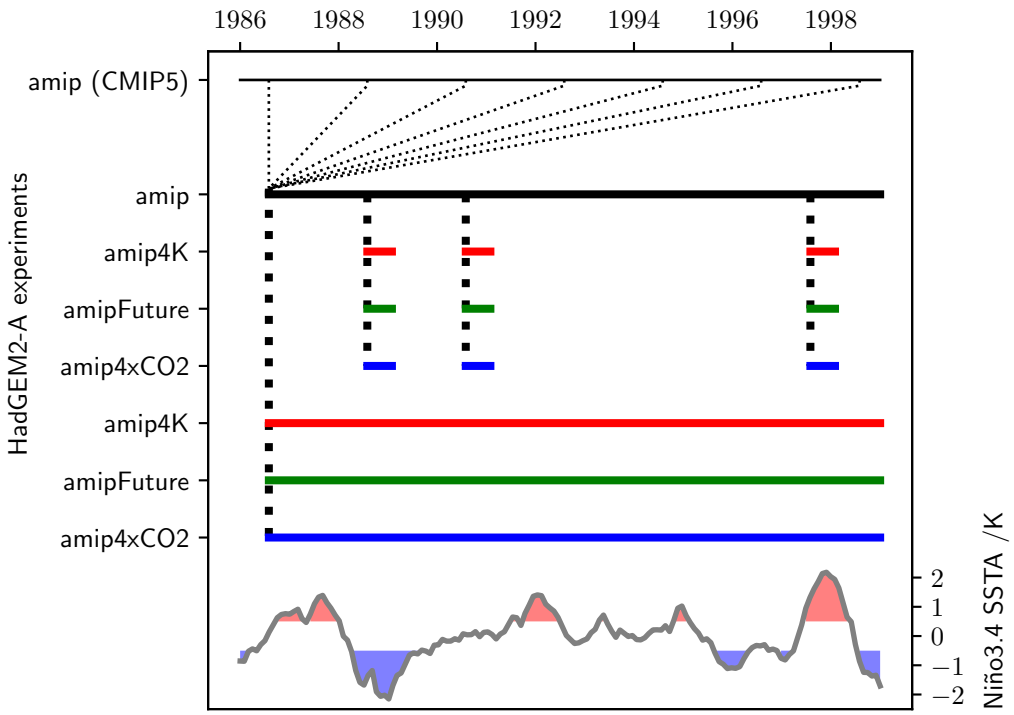

Figure 5.1: Schematic timeline for the HadGEM2-A experiment design (upper panel) and ERSSTv4 (Huang et al.*, 2015) Niño3.4 (5°N-5°S, 120°W-170°W) SST anomalies relative to 1979-2008 (lower panel). In the upper panel, thin lines denote a single ensemble member, thick lines denote seven ensemble members, and dashed lines denote a branch providing initial conditions for a new simulation. Black, red, green and blue lines indicate amip, amip4K, amipFuture and amip4xCO2 experiments, respectively. In the lower panel, red and blue shading denote El Niño and La Niña events, where Niño3.4 SST anomalies are greater than +0.5 K or less than -0.5 K, respectively.*

5.3 Tropical Mean Hydrological Cycle Response

This subsection explores the link between the transient land-ocean temperature contrast response, and changes in the tropical hydrological cycle, under a variety of idealised global warming perturbations. Dong *et al.* (2009) applied a similar framework examining the transient tropospheric response to instantaneous SST perturbations and CO_2 doubling using an earlier version of the UM (HadAM3, Pope *et al.* (2000)). The analysis presented here builds on that of Dong *et al.* (2009), by decomposing the hydrological cycle response to examine the timescales of dynamic and thermodynamic changes.

5.3.1 Tropical Land Response

To explore the tropical hydrological cycle response, firstly temperature and humidity changes over land are examined. Figure 5.2 demonstrates the daily tropical land ensemble mean near surface temperature, relative and specific humidity changes over the first two months of the amip4K, amipFuture and amip4xCO2 experiments. Relatively consistent results are evident for simulations started in 1988, 1990 and 1997, suggesting little sensitivity to the ENSO phase at initialisation. Hereafter, values quoted in this section represent the mean of these three years, unless stated otherwise. Land mean temperature increases rapidly over the first twenty days in both amip4K ($+4$ K) and amipFuture ($+5$ K). This is followed by a slower increase over the next forty days towards the equilibrium levels, at $+5.3$ K and $+7.2$ K, respectively. This highlights how the additional affect of SST pattern change in amipFuture leads to amplified warming, relative to amip4K. This implies that tropical circulation changes, in response to SST gradient changes, are linked with the amplitude of land warming. In amip4xCO2, land warming is considerably weaker, reaching an equilibrium of approximately $+0.5$ K. However, in amip4xCO2 unlike the SST perturbation cases, this level of warming is reached almost immediately.

Dong *et al.* (2009) present a mechanism for how land warming occurs in response to similar SST perturbations. Under instantaneous SST warming, surface air temperature over ocean warms and reaches equilibrium rapidly, since it is closely tied to the local SST. Due to the unrestricted moisture supply over ocean, the tropospheric lapse rate approximately remains on a moist adiabat, hence amplifying warming aloft. Tropospheric warming over land subsequently occurs in part due the advection of warm anomalies inland from coastlines at all levels, as well as wave action. In particular, above the tropical boundary layer, the small Coriolis force ensures horizontal temperature gradients remain weak (Sobel *et al.*, 2001), and hence warm anomalies are rapidly mixed by large scale dynamics. Finally, in the boundary layer over land, moisture limitations lead to a surface warming feedback amplifying land warming relative to the ocean (Joshi *et al.*, 2008).

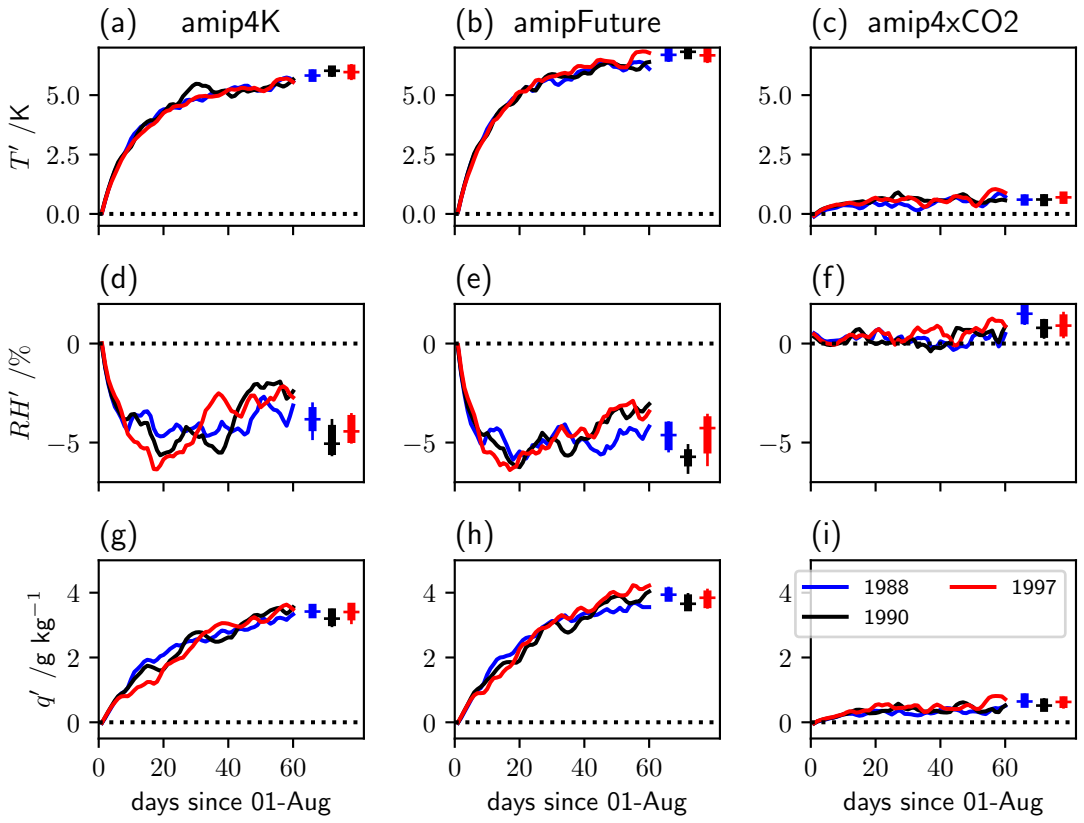

Figure 5.2: Tropical land HadGEM2-A ensemble mean temperature (top row), relative humidity (middle row) and specific humidity (bottom row) anomalies versus time for the first two months of the amip4K (left column), amipFuture (middle column) and amip4xCO2 experiments (right column). Blue, black and red lines indicate experiments started from 1 August 1988, 1990 and 1997, respectively. Boxplots show the interdecile (thin line) and interquartile (thick line) ranges, and median (horizontal line) of daily variability for the corresponding period in the equilibrium simulations. The horizontal black, dotted line denotes zero.

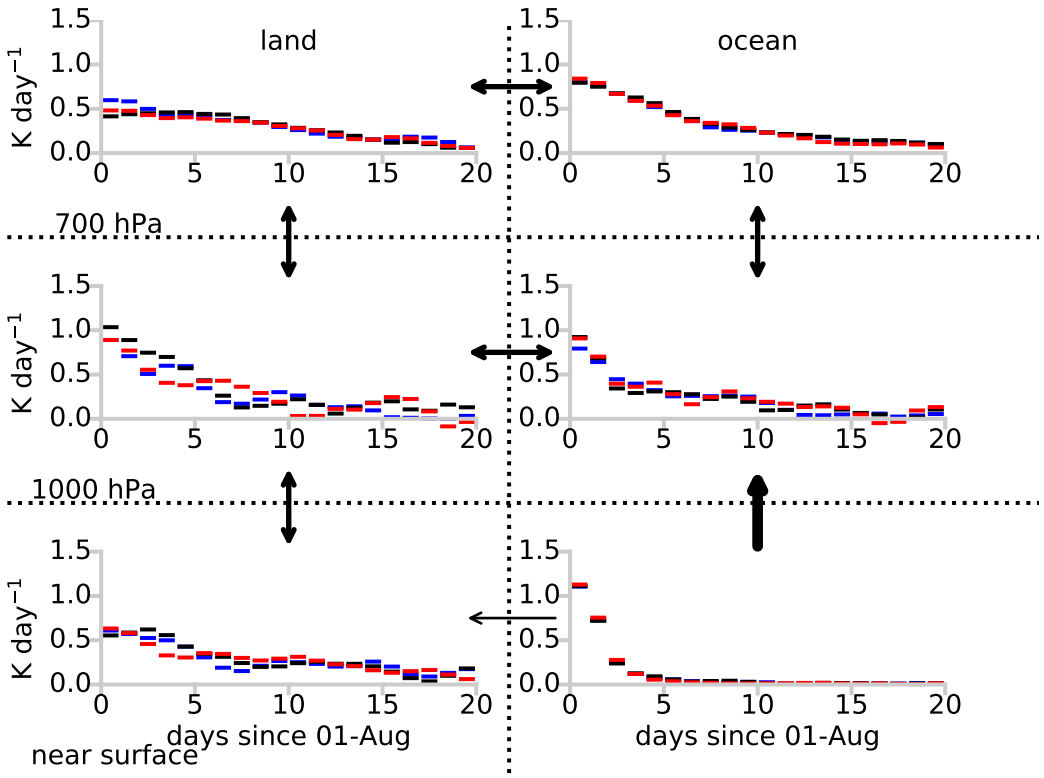

Figure 5.3: Topical land (left) and ocean (right) daily and ensemble mean temperature tendencies in the amipFuture transient simulation, with blue, black and red bars denoting 1988, 1990 and 1997. The top, middle and bottom rows represent the free (700-100 hPa) and lower (1000-700 hPa) tropospheric mass-weighted mean, and near surface (1.5 m) temperatures, respectively. Schematic arrows indicate how warming from the instantaneous SST perturbation propagates vertically and horizontally.

Figure 5.3 presents a schematic demonstrating how tropospheric temperatures respond to the instantaneous SST perturbation in the amipFuture experiment. Similar results are evident for each ENSO phase and also for the amip4K experiment. Consistent with Dong *et al.* (2009), the mean near-surface warming is considerably stronger over tropical ocean (1.2 K day^{-1}) relative to land (0.6 K day^{-1}) on day 1. However, in the lower free troposphere, initial positive temperature tendencies are approximately equal over both land and ocean (1 K day^{-1}). This demonstrates how warming spreads rapidly within the boundary layer due to fast acting waves. Warming is initially weaker in the upper troposphere over both regions, but persist over a longer period due to the slowly adjusting lapse rate, resulting in amplified warming aloft. Additionally, substantial positive temperature tendencies generally persist for longer over land in comparison to ocean. This leads to an amplified land-ocean temperature contrast at equilibrium, similar to the results of (Joshi *et al.*, 2008).

In amip4K and amipFuture, the transient land mean specific humidity, q, response is

more gradual in comparison to the initial rapid land warming. This implies that mixing via waves which spreads warming aloft over land is faster than the inland advection of moisture. Both simulations show a more linear increase over the first two months towards equilibrium values of approximately $+3.5$ g kg^{-1} and $+4$ g kg^{-1}, respectively. Again, the amip4xCO2 equilibrium response is substantially weaker, at $+0.6$ g kg^{-1}, but reached within a shorter time period. In the SST perturbation experiments, q increases over land are partially due to weakly enhanced land evaporation, as shown in Figures 5.4(d-e). In addition, advection from ocean to land of boundary layer moisture increases, due to strongly enhanced ocean evaporation, also contributes to q increases over land.

Notably, there is larger daily variability and ENSO sensitivity to both the transient and equilibrium relative humidity changes, in comparison to temperature and q changes. However, a consistent result is a substantial decrease in tropical land mean relative humidity of -5% in both cases over the first five days. This RH decrease is linked with the rapid increase in temperature and slower increase in q in both experiments. The magnitude of the transient and equilibrium amip4xCO2 RH response is minimal, suggesting relatively constant tropical land mean RH under CO_2 forcing. These humidity results are broadly consistent with those of Dong *et al.* (2009), who argued that moisture limitation over land is again the dominant factor for setting the transient and equilibrium response.

5.3.2 Hydrological Cycle Response

Tropical land mean components of the Seager *et al.* (2010) moisture budget decomposition, applied to the transient experiments, are presented in Figure 5.4. Similar to the temperature and humidity responses, results are relatively consistent in both the SST perturbation experiments, and comparatively weaker under CO_2 forcing. Precipitation initially decreases sharply in the amip4K (-1.2 mm day^{-1}) and amipFuture (-1.5 mm day^{-1}) simulations over the first five days. This decrease is stronger during the La Niña year (1988) relative to the El Niño year (1997). This disparity is likely due to the anomalous precipitation reduction or enhancement over much of the maritime continent and tropical South America, associated with the El Niño or La Niña events, respectively. Over the subsequent 25-45 days, tropical land mean precipitation decreases weaken quite linearly, reaching equilibrium values of approximately -0.3 mm day^{-1} in both experiments. In amip4xCO2, the equilibrium precipitation change, $+0.2$ mm day^{-1}, is established quite steadily without a strong initial response, unlike in amip4K and amipFuture.

As discussed previously, tropical land mean evaporation initially increases in both amip4K and amipFuture, which is linked with rapid near-surface warming and decreased relative humidity. Increasing evaporation and decreasing precipitation over tropical land implies either a weakening of ocean to land moisture advection, increased atmospheric moisture storage over land, or both. Figures 5.4(p) and (q) demonstrate that the transient

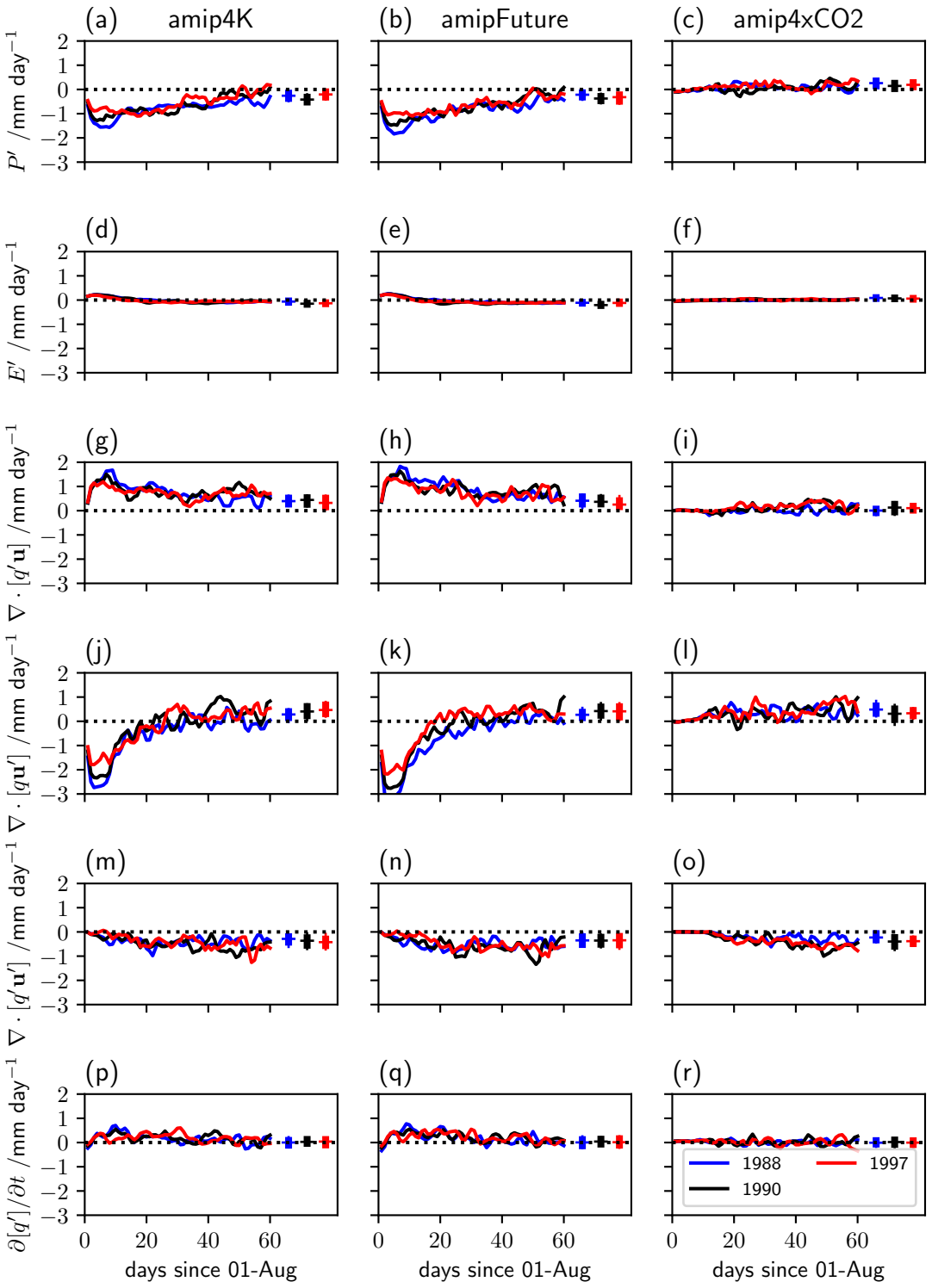

Figure 5.4: As in Figure 5.2, but for components of the Seager et al. *(2010) moisture budget decomposition.*

precipitable water tendency anomaly over tropical land is typically positive over the first 30 days in amip4K and amipFuture. This indicates that in response to these SST perturbations, the troposphere over land gradually stores more moisture. However, the magnitude of this term ($>$0.5 mm day^{-1}) is much smaller than the initial precipitation minus evaporation deficit. Hence, the transient weakening of ocean to land moisture advection dominates the surface moisture budget. At equilibrium, the mean precipitable water tendency anomaly is approximately zero, consistent with the assumption in Chapter 4.

Considering the tropical atmosphere as a closed system, ocean to land moisture advection changes are equivalent to moisture convergence changes over land. This assumption is well supported, since the magnitude of tropical to subtropical land moisture advection is much smaller than the magnitude of ocean to land moisture advection in amip simulations (omitted here for brevity). Examining Figure 5.4, the dynamic term in the Seager *et al.* (2010) decomposition contributes strongly to initially reduced ocean to land moisture advection. For instance, at day 3 the amip4K and amipFuture dynamic contributions are -1.6, -2.3 and -2.9 mm day^{-1} and -2.1, -2.8, -3.2 mm day^{-1}, for 1997, 1990 and 1988 respectively. This reduction is weakly moderated by increased moisture advection due to the thermodynamic term, at approximately $+$1 mm day^{-1} and $+$1.2 mm day^{-1} for each year for amip4K and amipFuture, respectively. Meanwhile, the nonlinear term is initially negligible. This suggests that the short term circulation weakening is only marginally offset by moisture increases, largely contributing to a tropical land mean precipitation decrease since evaporation increases are minimal.

After ten days in both the uniform and patterned SST perturbation experiments, the magnitude of both the thermodynamic and dynamic components weaken, whilst the nonlinear component trends negative. After approximately one month in both simulations, each term reaches equilibrium values, with positive thermodynamic ($+$0.3 mm day^{-1}) and dynamic ($+$0.4 mm day^{-1}) terms offset by a negative nonlinear term (-0.3 mm day^{-1}) and reduced evaporation, resulting in weakened tropical land mean precipitation. Note that the tropical mean moisture budget is not quite closed at equilibrium, as a small fraction of the moisture is anomalously advected from tropical land to subtropical land. These results indicate that for the tropical mean hydrological cycle the dynamic weakening dominates the fast response over 3-5 days, whilst a balance of the thermodynamic and dynamic strengthening and nonlinear weakening set the slower response over 5-30 days.

Vertical profiles for the ocean to land moisture advection components for each experiment are shown by Figure 5.5. For all three years in both SST perturbation experiments, the initial response is dominated by the dynamic component at low levels (> 850 hPa).

For instance, at 925 hPa for day 3-5 in the amip4K simulations, land to ocean $\nabla \cdot (q\mathbf{u}')$ ranges between -8.5 and -11 mm day^{-1}, whilst $\nabla \cdot (q'\mathbf{u})$ and $\nabla \cdot (q'\mathbf{u}')$ are approximately 2.5 mm day^{-1} and -0.5 mm day^{-1}, respectively. Qualitatively similar results hold for amipFuture, suggesting that the strongest initial circulation response in both of these cases is limited to the boundary layer. In contrast to the SST perturbation cases, the initial amip4xCO2 response is negligible throughout the troposphere, consistent with the minimal tropical land mean precipitation change.

As the responses approach equilibrium (day 15-25), the 925 hPa negative dynamic component reduces to a similar magnitude ($\sim$ 2 mm day^{-1}) to the equivalent positive thermodynamic component. Over this period, the dynamic component is mainly negative below 600 hPa, and approximately cancels the thermodynamic component, which is mainly positive, below 500 hPa. Consequently, the nonlinear component sets the overall land mean response. In all three experiments $\nabla \cdot (q'\mathbf{u}')$ is positive beneath 850 hPa, indicating enhanced moisture inflow, and negative between 400-850 hPa, demonstrating enhanced outflow. This is consistent with previous studies examining moisture transport between dry and wet regions (Allan *et al.*, 2014). Therefore, for amip4K and amipFuture where $\nabla \cdot (q'\mathbf{u})$ and $\nabla \cdot (q\mathbf{u}')$ largely cancel, this leads to reduced tropical land mean precipitation. For amip4xCO2, the day 15-25 $\nabla \cdot (q\mathbf{u}')$ response is positive beneath 500 hPa, indicating enhanced low level inflow and reduced upper level outflow. Consequently the nonlinear component in response to CO_2 forcing weakly moderates the positive dynamic component, resulting in a small precipitation increase.

5.3.3 Land-Sea Temperature and Surface Pressure Contrast

Consistent with Dong *et al.* (2009), the immediate dynamic response in amip4K and amipFuture is strongly linked with the initial land-sea temperature contrast due to the instantaneous SST perturbations. Bayr and Dommenget (2013) use the seasonal cycle in present day reanalyses, and decadal trends in climate model simulations of global warming, to demonstrate a relationship between the pattern of tropospheric temperature and sea level pressure, relative to their tropical means. We apply a similar framework considering the transient response in land-ocean temperature and surface pressure contrast. Let $\nabla(\cdot)'$ represent the change in tropical land mean minus tropical ocean mean between present day and idealised global warming. Figure 5.6 demonstrates daily means of tropical land minus ocean tropospheric temperature contrast, $\nabla[T]'$, where:

$$[T] = \left(\frac{g}{p_s - p_T}\right) \int_{p_T}^{p_s} \frac{T}{g} dp$$

is the mass weighted mean temperature, versus the surface pressure contrast, $\nabla p_s'$, for the first month in each transient simulation. For amip4K and amipFuture, there is a significant negative linear association in between $\nabla[T]'$ and $\nabla p_s'$ for each year. However, no

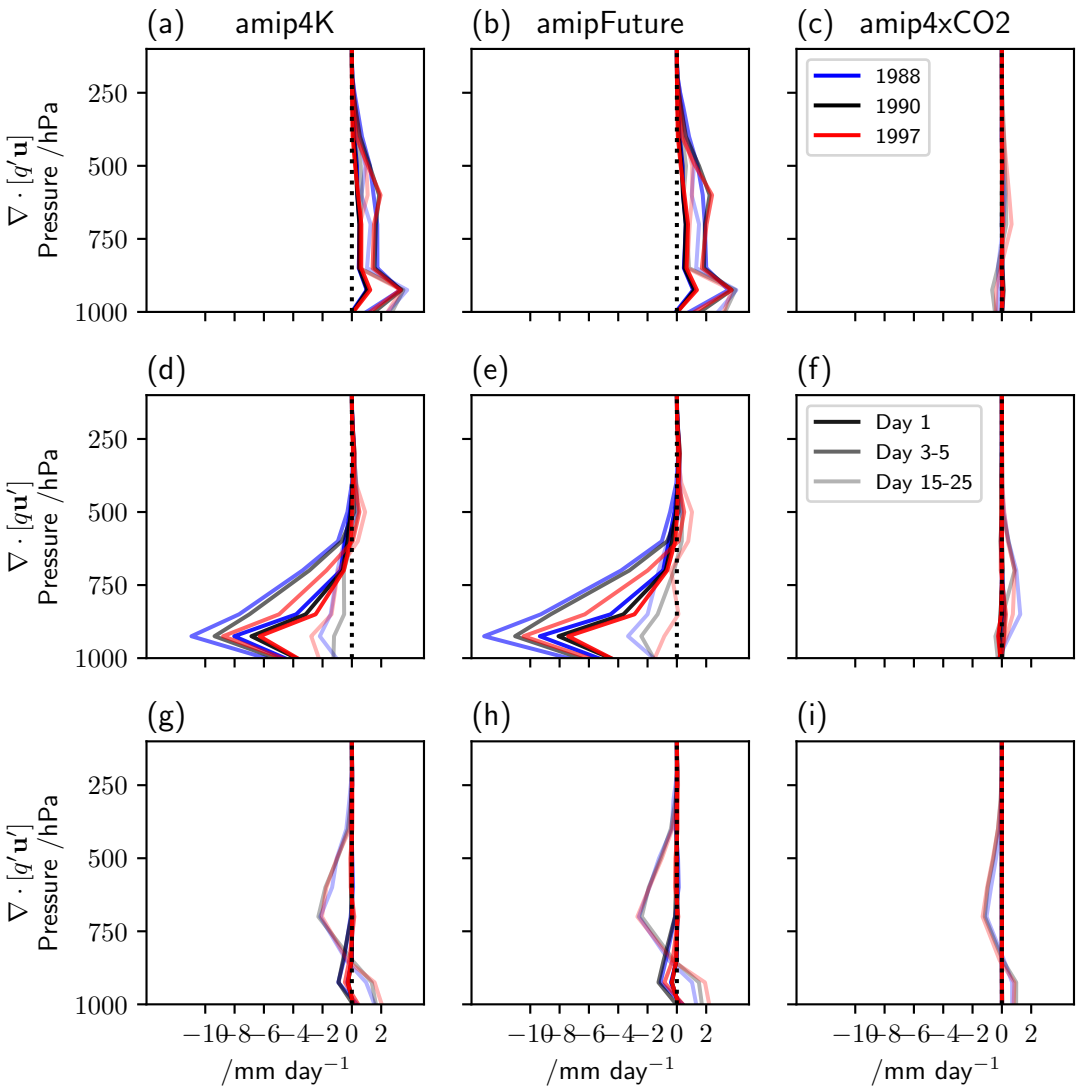

Figure 5.5: Vertical profiles of ensemble mean moisture convergence changes, relative to amip, over tropical land representing the thermodynamic (top), dynamic (middle) and nonlinear (bottom) components of the Seager et al. *(2010) decomposition applied to the transient amip4K (left), amipFuture (middle) and amip4xCO2 (right) experiments. Blue, black and red lines denote simulations started on 1 August 1988, 1990 and 1997, respectively. Low, medium and high transparency indicates the day 1, 3-5 and 15-25 means.*

	amip4K $\hat{\beta}_1$ /hPa K^{-1}		amipFuture $\hat{\beta}_1$ /hPa K^{-1}		amip4xCO2 $\hat{\beta}_1$ /hPa K^{-1}	
	$\nabla p'_s$ versus:		$\nabla p'_s$ versus:		$\nabla p'_s$ versus:	
Year	$\nabla T'_s$	$\nabla [T]'$	$\nabla T'_s$	$\nabla [T]'$	$\nabla T'_s$	$\nabla [T]'$
1988	**-0.97±0.08**	**-4.57±0.97**	**-0.82±0.11**	**-3.52±0.71**	**-1.53±0.57**	-0.90±1.36
1990	**-0.91±0.13**	**-5.75±1.79**	**-1.12±0.14**	**-6.07±1.79**	-0.69±0.72	1.04±1.49
1997	**-0.78±0.18**	**-3.29±1.08**	**-0.93±0.13**	**-3.01±1.15**	**-1.53±1.05**	1.84±1.88

Table 5.1: Regression slope estimates and 95% confidence intervals in Pa K^{-1} for HadGEM2-A ensemble mean tropical land minus ocean surface pressure difference changes, $\nabla p'_s$, versus surface temperature difference changes $\nabla T'_s$ (for days 5-30) and tropospheric temperature difference changes, $\nabla [T]'$, in each AMIP experiment. Corresponding scatter plots are displayed in Figure 5.6. Bold values indicate where the slope estimate is significantly non-zero.

significant linear association is present for the amip4xCO2 simulations. This is perhaps due to the time period chosen, since variability in both $\nabla [T]'$ and $\nabla p'_s$ is substantially higher after 15 days in amip4xCO2. Prior to this, $\nabla p'_s$ steadily decreases to -0.5 hPa whilst $\nabla [T]'$ gradually increases to 0.05 K in this case.

The amip4K and amipFuture results suggest that in response to instantaneous SST warming, as the tropospheric land-ocean temperature contrast immediately decreases before slowly restoring, the land-ocean surface pressure contrast consistently decreases and subsequently increases. Regression slope estimates for each year, as presented in Table 5.1, range between -3.29 to -5.75 hPa K^{-1} and -3.52 to -6.07 hPa K^{-1} for amip4K and amipFuture experiments, respectively. This indicates a weak sensitivity to the ENSO phase for the strength of the relationship between $\nabla [T]'$ and $\nabla p'_s$ under SST perturbations, likely due to spatial differences in the initial surface pressure and temperature patterns.

Scatter plots of surface land-ocean temperature contrast, $\nabla T'_s$, versus $\nabla p'_s$ are also displayed in Figure 5.6. Both amip4K and amipFuture demonstrate a similar pattern, with the immediate negative $\nabla T'_s$ reaching a minimum on day 2, at approximately -3 K, before gradually increasing to reach $+1.5$ K at day 30. The maximum $\nabla p'_s$ is reached more slowly, at approximately $+4$ hPa on day 5-6, and subsequently weakens to $+1$ hPa by day 30. A clear negative association is present during the 5-30 day period, supported by significant negative regression slopes for all years, as demonstrated in Table 5.1. Notably, the relationship between $\nabla p'_s$ and $\nabla T'_s$ (for days 5-30) is weaker in comparison to $\nabla p'_s$ versus $\nabla [T]'$ (for days 1-30), with slope estimates between -0.78 to -0.97 hPa K^{-1} and -0.82 to -1.12 hPa K^{-1} for amip4K and amipFuture respectively. This implies that in the SST perturbation experiments, a larger surface temperature contrast is on average associated with an equivalent pressure contrast as a smaller tropospheric temperature contrast.

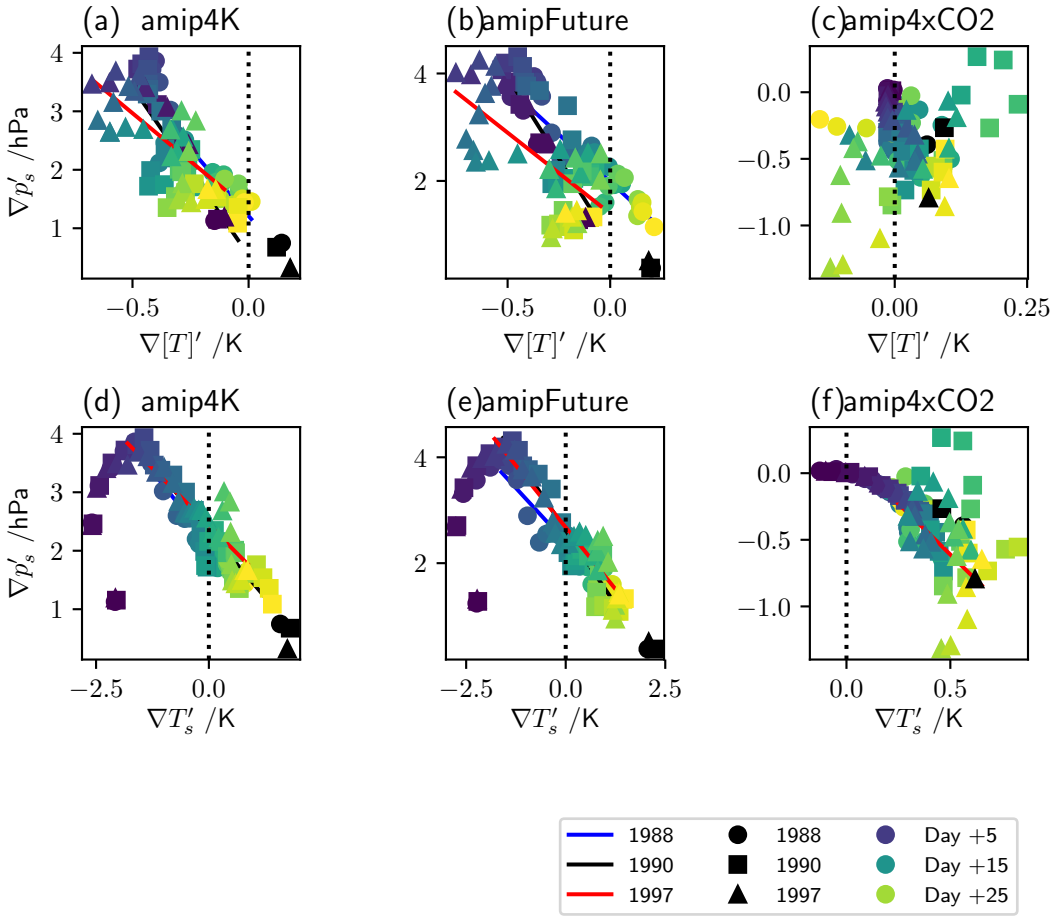

Figure 5.6: Tropical land minus ocean surface pressure contrast, $\nabla p_s'$, versus (a-c) tropospheric temperature contrast, $\nabla[T]'$, and (d-f) surface temperature contrast, $\nabla T_s'$. Points indicate daily means for the first month of each transient experiment, with colours and symbols indicating the day and year, respectively, as in the legend. Blue, black and red lines indicate the linear regression line in each case, for 1988, 1990 and 1997 respectively, by fitting a Gaussian linear model as described in Section 1.2.2. For panels (a-c), this linear model is fitted to all days (1-30). For panels (d-f), the linear model is only fitted to days (5-30), as a qualitatively different association is assumed during days (1-4). Black symbols indicate the respective August equilibrium values.

Unlike the SST perturbation experiments, in amip4xCO2 there is evidence of a negative association between $\nabla p_s'$ and $\nabla T_s'$ (day 1-30), but not $\nabla [T]'$ (day 1-30). Linear regression slope estimates for the former are significantly non-zero for 1988 and 1997, at -1.53 hPa K^{-1} in both years. The 1990 slope estimate, -0.69 hPa K^{-1}, is insignificant at the 5% level, but significantly non-zero at the 10% level. The mean of these amip4xCO2 slope estimates are slightly stronger in comparison to the amip4K and amipFuture cases, but each have a consistent sign. This result suggests that from 5 days after either SST or CO_2 perturbations, the surface land-ocean temperature contrast change is linearly associated with the surface pressure contrast change over the transient period.

These results suggest that the transient response in each experiment can be partitioned into three phases. Immediately (day 1), in amip4K and amipFuture the surface and boundary temperature contrast strongly reverses due to the SST forcing. However, the tropospheric temperature contrast change is negligible since the warming signal propagates more slowly to the free troposphere. Consequently, the immediate surface pressure contrast is relatively weak. Subsequently, over days 2-5, column warming over ocean begins to establish, with warming over land occurring at a slower rate, leading to an increasingly negative land-ocean temperature contrast throughout the troposphere. Correspondingly, the anomalous ocean to land pressure gradient strengthens, leading to strong low level circulation anomalies. Throughout the remainder of the first month (days 5-30), warm anomalies are advected inland and additionally surface moisture limitations act to increase land tropospheric temperatures. This weakens and eventually reverses the transient land-ocean tropospheric temperature contrast, with amplified warming over land. This occurs consistently with a weakening of the land-ocean pressure contrast, reducing and reversing the initial circulation anomalies.

In contrast to the SST perturbation experiments, immediate, transient and equilibrium warming is concentrated over land in amip4xCO2, due to the fixed SST at present day conditions. In coupled simulations, increased CO_2 concentrations leads to reduced net radiative cooling, increased stability due to amplified warming aloft, and circulation weakening (Bony *et al.*, 2013). However, with fixed SST, this effect is restricted over oceans, contributing to relative warming over land. Previous studies have demonstrated that circulation and precipitation changes in amip4xCO2 are jointly a response to the pattern of land warming and direct atmospheric heating (Chadwick *et al.*, 2014, 2019). After a similar initial period to the amip4K and amipFuture cases, the land-ocean surface temperature contrast in amip4xCO2 strengthens. However, the magnitude of this surface temperature contrast is considerably weaker relative to the perturbed SST cases. For instance, at equilibrium, $\nabla T_s'$ is approximately 2, 2.5 and 0.5 K for amip4K, amipFuture and amip4xCO2. Consequently, tropospheric temperature contrasts are much weaker

relative to daily variability for the CO_2 forcing case. Subsequently, at equilibrium, only a small decrease in the surface pressure contrast is evident, at -0.4, -0.3 and -0.7 hPa for 1988, 1990 and 1997, respectively.

5.4 Regional and ENSO-related Hydrological Cycle Response

In Section 5.3, the tropical land mean response to SST perturbations and CO_2 forcing in HadGEM2-A was examined. This subsection explores the regional and ENSO-related precipitation response to these perturbations. This analysis focuses on two tropical rainforest regions: the islands of the maritime continent, and equatorial South America. These regions are selected since both typically experience substantial precipitation changes during present day El Niño or La Niña events (Chang *et al.*, 2004; Trenberth *et al.*, 1988). This analysis identifies a link between regional surface temperature and relative humidity contrasts, the location of the ascending branch of the Walker circulation, and the pattern of precipitation changes.

5.4.1 Precipitation Response

In order to examine the time scale over which tropical precipitation changes occur, Figure 5.7 shows the spatial correlation between five day rolling mean transient and equilibrium ensemble mean precipitation changes for each experiment and year. In amip4K, spatial correlations increase over the first few days, and begin to plateau at approximately 0.5 by day 20-30. In amipFuture the plateau is reached slightly later, around day 35-45, at a slightly higher correlation (0.55). For amip4xCO2, the plateau is reached earlier, near day 20. These correlations do not plateau near 1 due to the relatively high daily variability, and consistent results are obtained for different rolling window lengths. The timescales discussed here are qualitatively similar to those presented by Dong *et al.* (2009). There is a slight sensitivity to year in these results, but the pattern is robust in each case. This suggests that the precipitation response to instantaneous CO_2 forcing and uniform SST perturbations reaches equilibrium over a slightly shorter timescale relative to a patterned SST perturbation in HadGEM2-A. However, by the end of the second month the transient precipitation change is largely consistent with the equilibrium change, in every year and experiment. Consequently, this section focuses on the regional hydrological cycle response over the first two months (August and September) in each experiment.

Exploring tropics-wide precipitation changes in the HadGEM2-A ensemble simulations, the strongest signals are present over the tropical maritime continent, Pacific ocean, South America and western Atlantic. Panels (a) and (b) of Figure 5.8 demonstrates

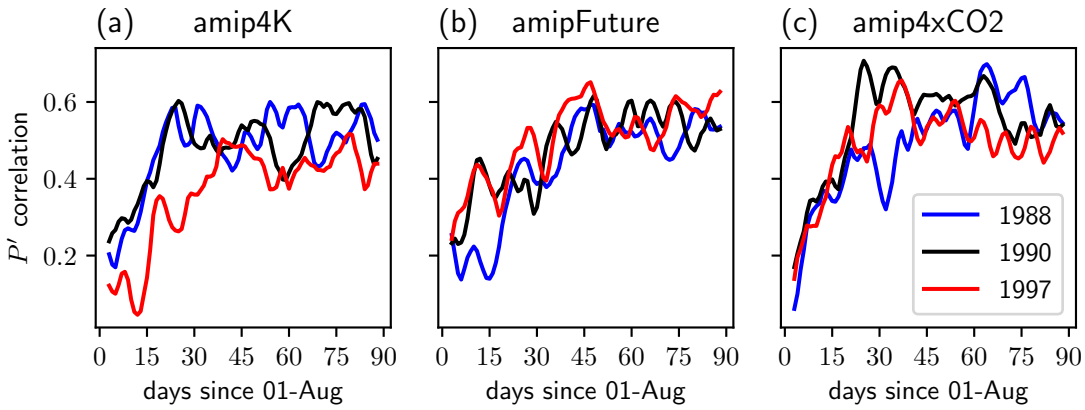

Figure 5.7: Pattern correlation between five day rolling mean transient and equilibrium tropical precipitation anomalies versus time for amip4K (a), amipFuture (b) and amip4xCO2 (c). Blue, black and red lines indicate 1988, 1990 and 1997, respectively.

the HadGEM2-A ensemble mean neutral (1990) and proxy El Niño anomalous (1997 minus 1990) precipitation, respectively. In the neutral case, heavy precipitation (> 12.5 mm day^{-1}) is simulated across the northern off-equatorial Pacific and western Atlantic oceans. Over land, there is substantial precipitation (> 7.5 mm day^{-1}) across much of south east Asia, the islands of Sumatra, northern Borneo and New Guinea, and the Amazon basin. The proxy El Niño anomaly demonstrates a shift in precipitation from the northern off-equatorial Pacific towards the central and eastern Pacific. Additionally, substantial and significant precipitation decreases over New Guinea (< -3 mm day^{-1}), Sumatra, northern Borneo and the Amazon basin (< -1 mm day^{-1}) are simulated.

The August-September HadGEM2-A ensemble mean equilibrium and transient $\bar{P}'$ and $\Delta P'_{EN}$ responses are presented in Figure 5.8 (c-h) and Figure 5.9 (a-f), respectively. The equilibrium and transient $\bar{P}'$ patterns are quite similar for each experiment, with spatial correlations of 0.66, 0.64 and 0.72 for amip4K, amipFuture and amip4xCO2 respectively. Consistently, $\Delta P'_{EN}$ for the equilibrium and transient cases are also similar, with equivalent spatial correlations of 0.54, 0.72 and 0.63. This implies that precipitation response approximately reaches equilibrium well within the first two months in each simulation. Examining $\bar{P}'$, both transient and equilibrium amip4K and amipFuture responses indicate relatively consistent precipitation changes. Simulated neutral precipitation decreases over the Amazon basin, New Guinea and the western equatorial Pacific, and increases over the central-western and northern off-equatorial Pacific, in each case. As with the tropical land mean changes, the amip4xCO2 $\bar{P}'$ pattern is weaker relative to amip4K and amipFuture. Both the transient and equilibrium response indicate precipitation decreases in the north eastern and western tropical Pacific and western tropical Atlantic, and increases ($\sim +1$ mm day^{-1}) in the western equatorial Pacific near New Guinea, with weaker magnitudes in the transient case.

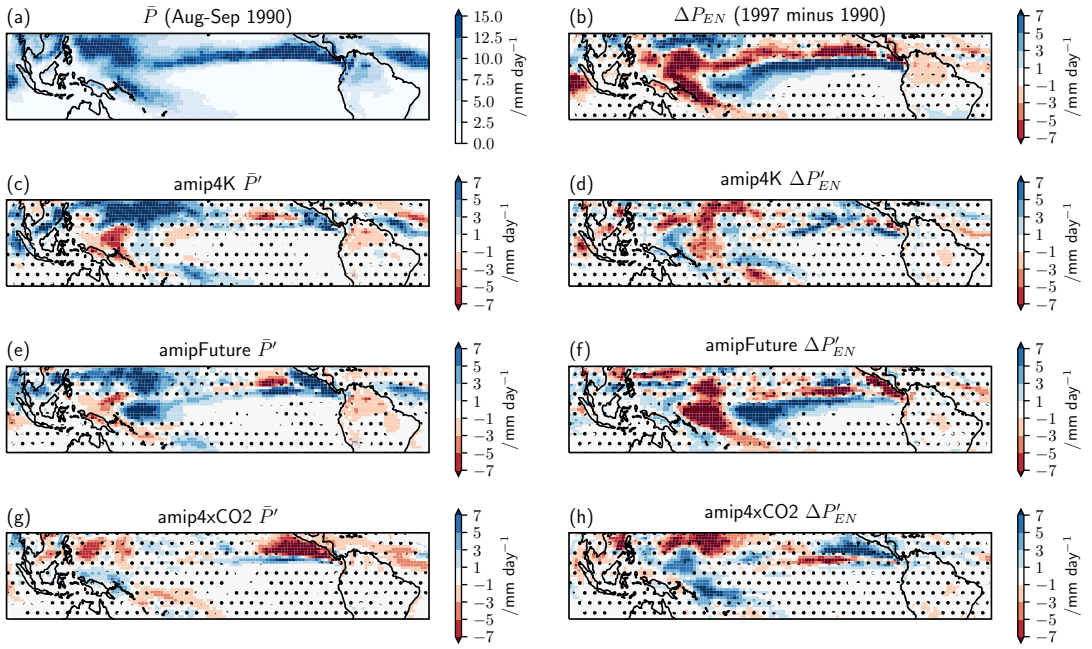

Figure 5.8: Colours indicate present day and equilibrium August-September HadGEM2-A ensemble mean precipitation. (a) amip neutral (1990), $\bar{P}$, and (b) El Niño anomaly (1997 minus 1990), ΔP_{EN}, precipitation. (c, e, g) and (d, f, h) show the neutral precipitation change, $\bar{P}'$, and the El Niño anomaly precipitation change, $\Delta P'_{EN}$, for each equilibrium experiment, respectively. Stippling in (b-h) indicate where the precipitation change is insignificant at the 5% level via a Kolmogorov-Smirnov test.

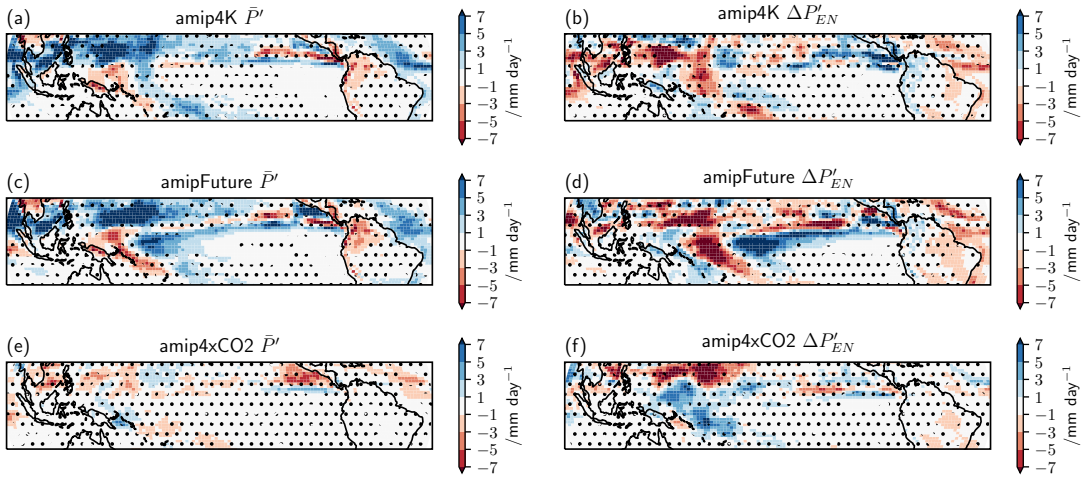

Figure 5.9: As in Figure 5.8 (c-h), except for the HadGEM2-A transient experiments.

The simulated $\Delta P'_{EN}$ indicate substantial changes to anomalous El Niño precipitation for each experiment, equivalent in both the transient and equilibrium responses. Both amip4K and amipFuture simulate a significant weakening and reversal of present day El Niño decreases over New Guinea, where $\Delta P'_{EN}$ is in the range 1-3 mm day^{-1}. Over the Amazon basin, $\Delta P'_{EN}$ is weaker and largely insignificant. The Pacific demonstrates a similar pattern for the amip4K and amipFuture responses, with enhanced decreases in the western Pacific and increases in the central Pacific, but a substantially stronger signal in amipFuture. In amip4xCO2, significant $\Delta P'_{EN}$ changes are simulated in the western north eastern tropical Pacific. However the CO_2 forcing El Niño anomaly response over land is largely insignificant. Generally, these responses to SST and CO_2 perturbations indicate that El Niño dry teleconnections typically weaken, due to climatological drying.

Following Section 5.3, the Seager *et al.* (2010) moisture budget decomposition is used to examine the mechanisms contributing to transient and equilibrium precipitation changes. This is applied to two tropical land areas with significant $\bar{P}'$ changes as shown in Figures 5.8 and 5.9: the island of New Guinea (land grid points within 5°N-5°S, 130°E-150°E) and equatorial South America (land grid points within 5°N-5°S, 35°W-90°W). Figures 5.10 and 5.11 demonstrate the Seager *et al.* (2010) components over August-September in each region, respectively.

Over New Guinea, in amip4K and amipFuture precipitation sharply decreases (-2 mm day^{-1}) during the neutral (1990) and La Niña (1988) cases over the first 2-3 days. In the El Niño year (1997) for these experiments, only very minor precipitation decreases ($<$0.2 mm day^{-1}) are evident. A similar feature is present in these experiments over equatorial South America, with much weaker precipitation decreases during the El Niño case. This is likely due to the negative present day ΔP_{EN} over these regions, as shown by

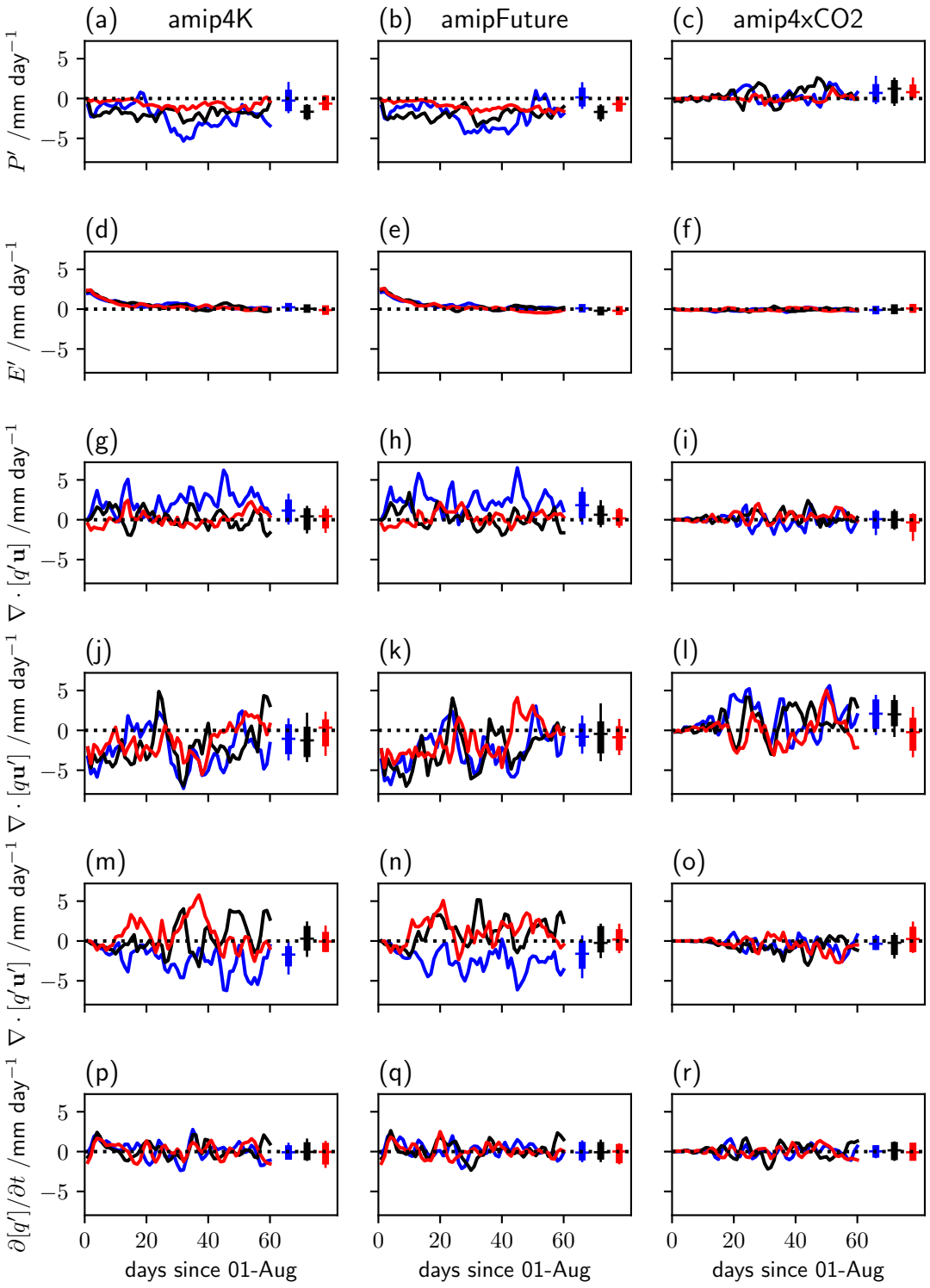

Figure 5.10: As in Figure 5.4, for the island of New Guinea (land within 5°N-5°S, 130°E-150°E) mean hydrological cycle.

Figure 5.8(b), limiting the potential precipitation decreases linked with an initial reversed land-ocean temperature contrast. Consistent with the tropical land mean response, the amip4xCO2 precipitation change is initially negligible over both regions, with only weak equilibrium increases over the maritime continent.

The subsequent transient and equilibrium decreasing precipitation response is quite consistent over both New Guinea and equatorial South America comparing the two SST perturbation experiments. In each region, the neutral and El Niño response over days 3-20 is mainly a balance of increases from the thermodynamic component and decreases from the dynamic component. For New Guinea, the dynamic component is positive in the El Niño case and negative in the neutral case. Each of the other terms in the Seager *et al.* (2010) moisture budget decomposition are approximately equal in the two cases. Hence, circulation change differences affecting low level convergence dominates the positive $\Delta P'_{EN}$ over this region. For equatorial South America, differences between the magnitude of the neutral and El Niño terms are considerably smaller, consistent with the minimal $\Delta P'_{EN}$ changes.

For New Guinea, the precipitation response to SST perturbations in the El Niño case is similar to the La Niña case. However, the Seager *et al.* (2010) moisture budget decompositions indicate different mechanisms. In the latter, a transient and equilibrium positive thermodynamic contribution is negated by a negative nonlinear term. This highlights how regional thermodynamic contributions due to moisture increases are particularly sensitive to the ENSO phase. During present day La Niña conditions, convergence is amplified over New Guinea relative to neutral or El Niño conditions. Therefore, under idealised global warming with increasing moisture, precipitation changes would be amplified during La Niña events without mitigating circulation changes. This case study provides a relatively simplified example, with the following subsection examining the ENSO-related circulation changes in greater detail.

A hypothesis for the differences in the hydrological cycle response to SST perturbations between New Guinea and equatorial South America is based on available moisture supply. New Guinea is an island surrounded by a warm ocean, and hence moisture is relatively unlimited and enhanced convection and convergence over land can be established and maintained once the initial negative land-ocean temperature has reversed. However, since the outflow aloft is also enhanced, the nonlinear term in the Seager *et al.* (2010) moisture budget is negative leading to weak precipitation decreases. In contrast, equatorial South America is continental, with a limited moisture supply, and bordering a cooler ocean to the west. Consequently, after the initial period of precipitation decreases, due to the reversed land-ocean temperature contrast, and weakly enhanced evaporation, surface moisture supply is reduced. In turn, this restricts increases in convection and

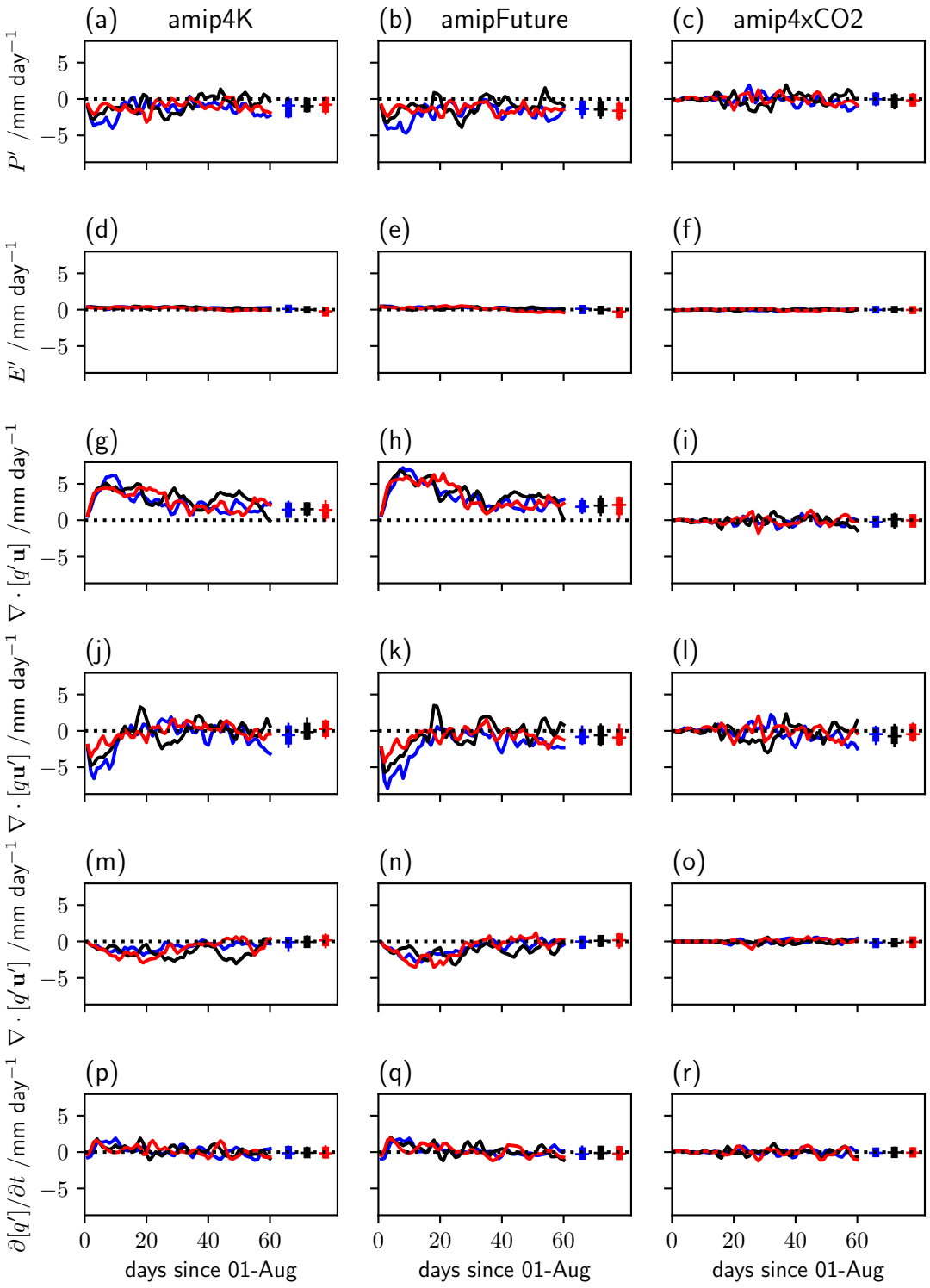

Figure 5.11: As in Figure 5.4, for the equatorial South America (land within 5°N-5°S, 35°W-90°W) mean hydrological cycle.

convergence, leading to a negligible (amip4K) or weakly negative (amipFuture) dynamic component and minimal nonlinear component.

5.4.2 Walker Circulation Shifts

Section 5.3 presented the tropical land mean hydrological cycle response in each of the HadGEM2-A simulations. A robust result is a link between the land-ocean tropospheric or surface (after 5 days) temperature contrast change and the surface pressure contrast change, broadly consistent with Bayr and Dommenget (2013). This pressure contrast anomaly contributes to circulation changes, driving a dynamic component of the tropical precipitation change. The previous subsection explored the regional and ENSO sensitivity of this precipitation change. Zonal shifts in precipitation over the Pacific and surrounding region were identified in both the SST perturbation and CO_2 forcing experiments. These shifts are established quickly and are generally close to equilibrium within two months of the instantaneous perturbations. In this subsection, the Walker circulation response is examined, since this provides a mechanistic framework underpinning the simulated precipitation shifts.

The 5°N-5°S zonal streamfunction, Ψ, describes the equatorial zonal overturning or Walker circulation. This analysis follows Yu and Zwiers (2010) and Yu *et al.* (2012) by defining:

$$\Psi = 2\pi r_E \int_0^p u_D \frac{dp}{g} \tag{5.1}$$

where $r_E \approx 6.371 \times 10^6$ m is the radius of the earth, p is pressure, $g \approx 9.81$ m s^{-2} is acceleration due to gravity and u_D is the meridional mean divergent component of the zonal wind. Here, u_D is calculated from the Helmholtz decomposition of the zonal and meridional wind (Dawson, 2016). Yu and Zwiers (2010) find a weakening of the Walker circulation over the Pacific ocean in recent reanalyses, whilst Yu *et al.* (2012) demonstrate a simulated eastward shift in an ensemble of twenty-first century CMIP3 coupled simulations. Bayr *et al.* (2014) apply an equivalent framework to both CMIP3 and CMIP5 coupled simulations, indicating a similar eastward shift and weakening over the twenty-first century due to tropospheric warming and stabilisation.

The HadGEM2-A AOSND (August-December) neutral (1990) ensemble mean Ψ is presented in Figure 5.12(a), with the proxy El Niño ($\Delta\Psi_{EN}$, 1997 minus 1990) and La Niña ($\Delta\Psi_{LN}$, 1988 minus 1990) anomalies displayed in Figures 5.12(b-c). The main ascent regions in the neutral case, where Ψ changes from positive to negative in the eastward direction, are over the central Indian and western Pacific ocean and equatorial South America. The main feature of the proxy El Niño anomaly is a weakening of the

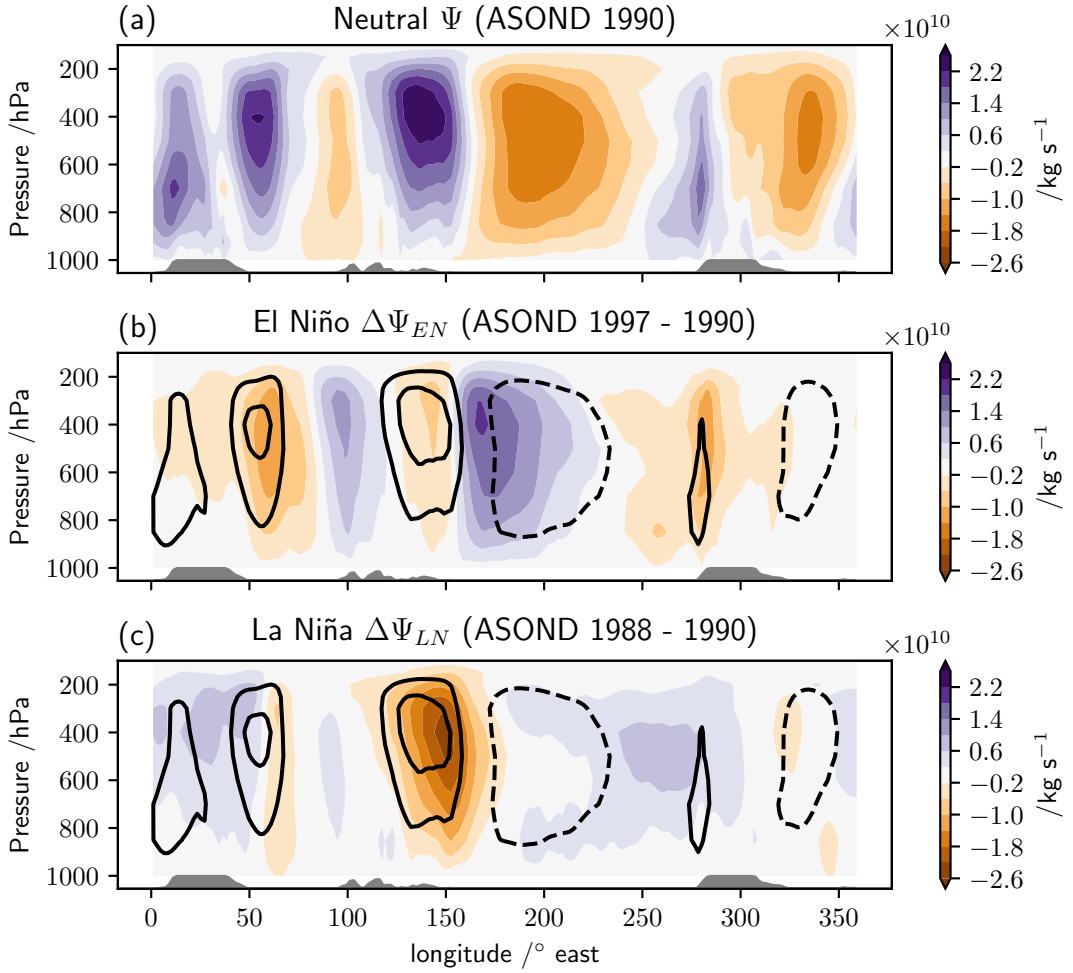

Figure 5.12: Colours show the HadGEM2-A amip August-December 1990 ensemble mean 5°N-5°S zonal streamfunction, Ψ, (a), proxy El Niño (1997 minus 1990), $\Delta\Psi_{EN}$, (b) and La Niña (1988 minus 1990), $\Delta\Psi_{EN}$, (c) anomalies versus pressure. Note the narrower colour bars on panels (b) and (c). Black lines in (b) and (c) denote the Ψ contours at 10^{14} kg s^{-1} intervals. Grey shading indicates the meridional mean land fraction within 5°N-5°S.

neutral circulation over the western Pacific and strengthening over the eastern Pacific. As discussed previously, the proxy El Niño anomalous precipitation indicates decreases over the maritime continent and western Pacific, and increases in the central Pacific, as shown by Figure 5.8(b). This proxy circulation shift is therefore consistent with the eastward shift of the main ascent region, and hence local precipitation maximum, over the Pacific during canonical El Niño events. Conversely, the proxy La Niña anomaly shows a strengthening of the circulation over the maritime continent and weakening over the eastern Pacific. Again, this proxy anomaly typifies the associated westward shift in the Pacific ascent region, and hence local precipitation maximum, during La Niña events (McPhaden *et al.*, 2006).

The mass weighted vertical integral of the zonal streamfunction, $[\Psi] = \int_0^\infty \Psi dz$, defines the net zonal circulation as a function of longitude, λ. Figure 5.13 demonstrates $[\Psi]$ for 1988, 1990 and 1997 in the present day and equilibrium idealised global warming simulations. Generally, in each simulation, $[\Psi]$ is positive over the Indian ocean and South America, and negative over much of the Pacific and Atlantic oceans. (Bayr *et al.*, 2014) recommend the longitude of the zero crossing of $[\Psi]$ from positive to negative, $\lambda_{[\Psi]=0}$, as a metric for the location of ascending branches in the zonal circulation. In this analysis, the value of $\lambda_{[\Psi]=0}$ within the range 130°E-150°W defines the location of the ascending branch of the Pacific Walker circulation. In the HadGEM2-A amip simulation, $\lambda_{[\Psi]=0} = 145.7, 162.3, 180.1$°E for 1988, 1990 and 1997, respectively. This indicates a 17.8° eastward shift for the El Niño proxy, and a 16.6° westward shift for the La Niña proxy.

Both SST perturbation experiments demonstrate eastward shifts in $\lambda_{[\Psi]=0}$ for each year at equilibrium, with the amipFuture response (4.7°, 5.5° and 18.8°) larger than the amip4K response (1.9°, 5.9° and 7.1°, for 1988, 1990 and 1997, respectively). Notably the El Niño shift is amplified in amipFuture relative to amip4K. This is likely due to the relatively enhanced mean state eastern equatorial Pacific SST warming in amipFuture, further weakening the meridional SST gradient during the El Niño year. Contrasting the SST perturbation experiments, in amip4xCO2 a westward shift of $\lambda_{[\Psi]=0}$ is simulated, in addition to an amplification of $[\Psi]$, indicating strengthened circulation. Examining the CMIP5 ensemble mean amip4xCO2 response, He and Soden (2015) suggest that this circulation strengthening is linked with the enhanced land-sea temperature contrast and stabilisation over ocean. Similarly, in HadGEM2-A, the westward shift of the ascending branch is due to the amplified ascent over the relatively warmer maritime continent, and enhanced descent over the western equatorial Pacific.

Hovmöller plots demonstrating the transient $[\Psi]$ response over the first two months in each neutral (1990) experiment are presented in Figure 5.14. Qualitatively consistent results are evident in the La Niña and El Niño experiments, and will be discussed later. Both amip4K and amipFuture simulate a generally consistent initial response over the first five days. Relatively enhanced circulation ($> 10^{14}$ kg s^{-1}) is evident over each equatorial ocean region, contributing to the initial precipitation increase over ocean and decrease over land. The initial amip4xCO2 $[\Psi]$ response is considerably weaker, with circulation anomalies generally less than 2×10^{13} kg s^{-1} prior to ten days after the perturbation. Comparing the zero contour of $[\Psi]$ in transient and control experiments over the western Pacific, an eastward shift of 5-15° and 5-25° is present after twenty days in the amip4K and amipFuture, respectively. The sign of these transient shifts is consistent with the equilibrium response, however daily variability is relatively high in both cases. In contrast, in the CO_2 forcing experiment, any daily shifts are of a considerably smaller

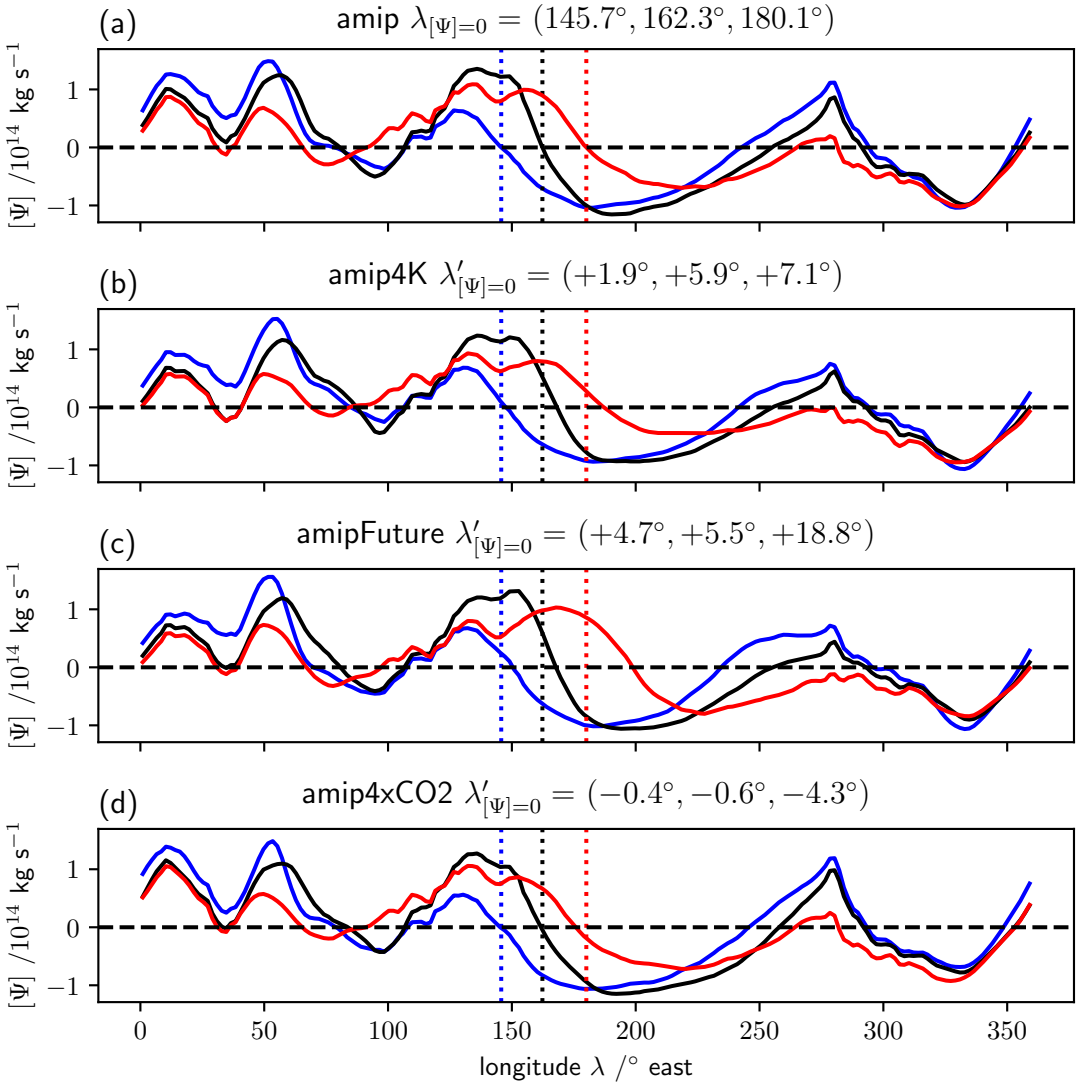

Figure 5.13: Vertically integrated HadGEM2-A ensemble and August-December mean 5°N-5°S zonal streamfunction, $[\Psi]$, versus longitude for the amip (a) and equilibrium amip4K (b), amipFuture (c) and amip4xCO2 (d) experiments. Blue, black and red solid lines denote 1988, 1990 and 1997, respectively. The horizontal black dashed line denotes $[\Psi] = 0$, and the blue, black and red dotted vertical lines indicate the longitude at which $[\Psi] = 0$ for $\lambda \in (130°, 200°)$, representing the ascending branch of the Pacific Walker circulation ($\lambda_{[\Psi]=0}$), in the amip simulation for 1988, 1990 and 1997 respectively. Triplets represent these longitudes in (a), and their changes in (b-d).

magnitude ($< 2^{\circ}$), indicating a weaker circulation response.

Bayr *et al.* (2014) suggest using the mean equatorial Pacific 850 hPa zonal wind, $\overline{u_{850}}$, as a another proxy for the longitude of the ascending branch of the Walker circulation. In global warming simulations, Bayr *et al.* (2014) show that westerly $\overline{u_{850}}$ anomalies are strongly linked to an eastward shift of $\lambda_{[\Psi]=0}$, and vice-versa. The response over the first month of the HadGEM2-A transient simulations is presented in Figure 5.15. Generally, in the SST perturbation experiments, a gradual weakening of the easterly $\overline{u_{850}}$ occurs at the same time as an eastward $\lambda_{[\Psi]=0}$ shift. The largest transient changes are for the neutral and El Niño cases, where the amip $\lambda_{[\Psi]=0}$ is displaced eastward relative to the La Niña case (Figure 5.13). In comparison to amip4K and amipFuture, in amip4xCO2 this general link is not evident, and transient $\overline{u_{850}}$ and $\lambda_{[\Psi]=0}$ changes are typically smaller.

Based on Chapters 2 and 3 and the results of Bayr *et al.* (2014), changes in regional surface air temperature (SAT) and relative humidity (RH) contrasts are hypothesised to modulate zonal shifts of the Walker circulation. Consider two adjacent regions and assume the weak temperature gradient approximation, introduced in Section 1.1.2. If the SAT or RH gradient strengthens then deep convection becomes more favourable over the relatively warmer or more humid region. This would promote a circulation anomaly towards the more favourable region at low levels, sustaining the deep convection, and acting as a positive feedback. The resulting circulation anomaly would be linked with a shift in the low level convergence zone, and hence the location of maximum ascent and precipitation.

From the previous subsection this analysis focusses on four equatorial regions covering the Pacific and surrounding land areas: the maritime continent (MCO, 5°N-5°S, 100°E-150°E), western equatorial Pacific (WPAC, 5°N-5°S, 150°E-150°W), eastern equatorial Pacific (EPAC, 5°N-5°S, 150°W-90°W) and equatorial South America (SAM, 5°N-5°S, 90°W-35°W). Correspondingly, three zonal contrasts are evaluated by differencing area weighted means: MCO minus WPAC, EPAC minus WPAC and SAM minus EPAC. Figures 5.16 and 5.17 demonstrate the regional transient SAT and RH contrasts versus the corresponding regional zonal wind changes, respectively.

Generally, over the first month in the SST perturbation experiments, the weakening and reversal of the initially negative MCO minus WPAC temperature contrast co-occurs with weakening of the local easterly winds. Meanwhile, local easterlies strengthen over the SAM and EPAC region, whilst an equivalent change occurs in the land-ocean temperature contrast. This latter change is clearest in the La Niña experiment, demonstrating some sensitivity to the ENSO phase. These local zonal wind changes contribute to a westerly anomaly across the Pacific, consistent with the transient westward shift of

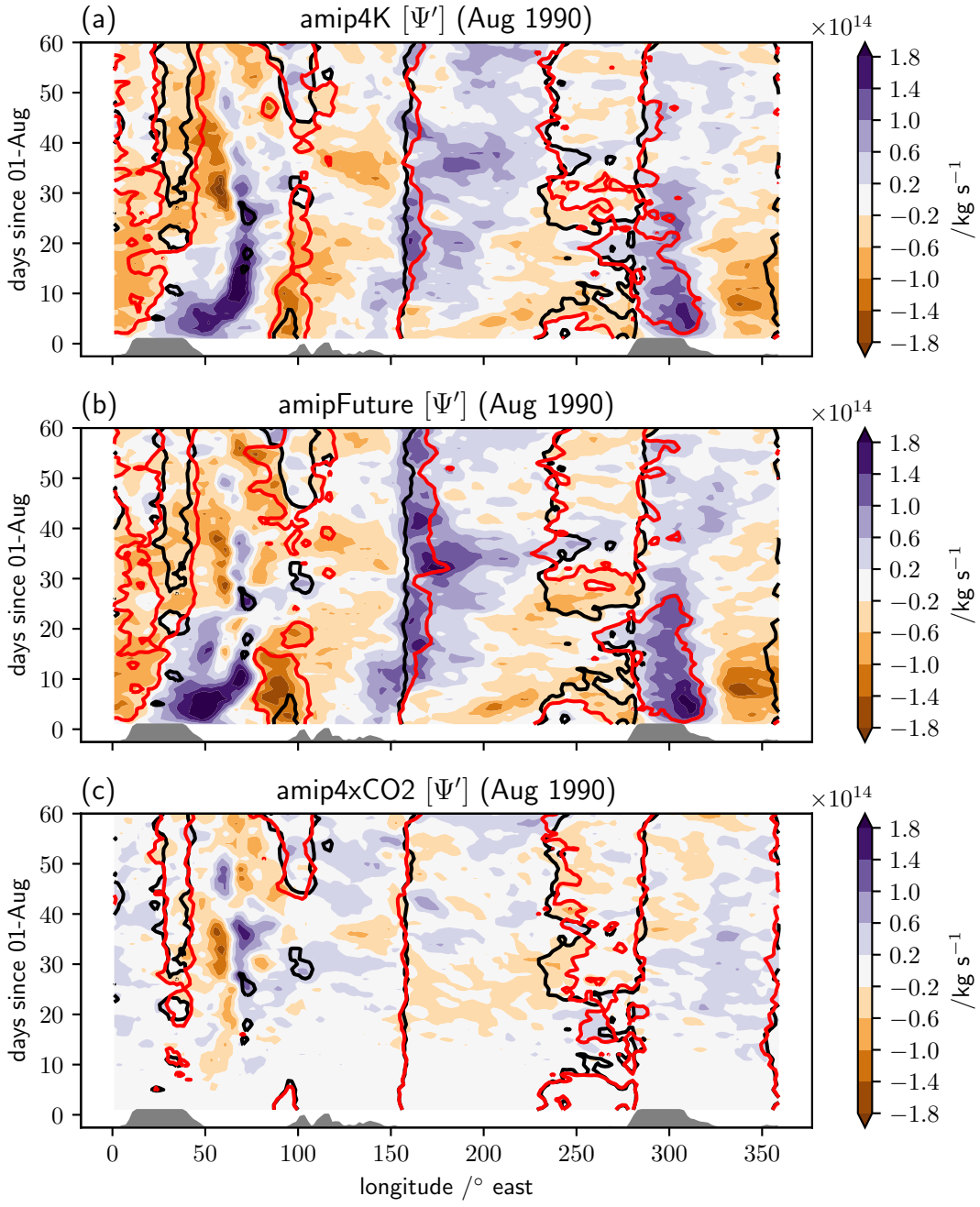

Figure 5.14: Hovmöller plots denoting the transient amip4K (a), amipFuture (b) and amip4xCO2 (c) minus amip changes in the vertically integrated zonal streamfunction, $[\Psi]'$ versus time. Black and red lines represent $[\Psi] = 0$ for the amip and transient experiments, respectively. Grey shading indicates the meridional mean land fraction within 5°N-5°S.

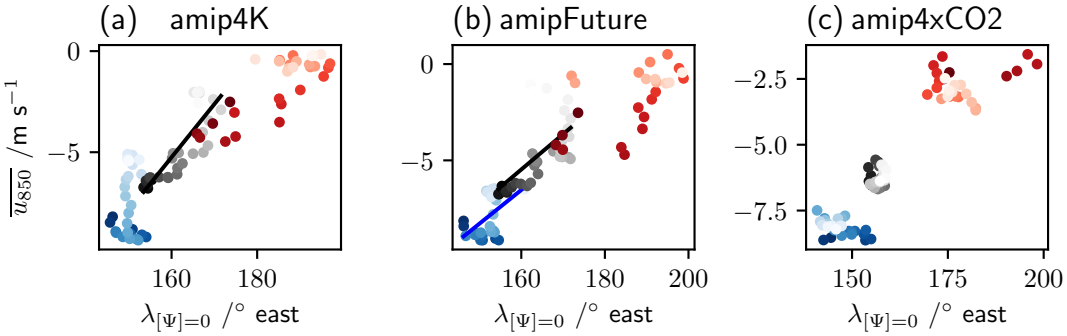

Figure 5.15: Daily mean equatorial Pacific 850 hPa zonal wind, $\overline{u_{850}}$, versus the longitude of the zero-crossing of the vertically integrated equatorial zonal streamfunction for the first month of the amip4K (a), amipFuture (b) and amip4xCO2 (c) transient simulations. Blue, black and red markers and lines denote the 1988 (La Niña), 1990 (neutral) and 1997 (El Niño) experiments, respectively. Lighter marker colours denote the progression for time from day 1 (darkest) to day 30 (lightest). Solid lines indicate where linear regression slopes are significantly different from zero at the 5% level.

$\lambda_{[\Psi]=0}$ (Figure 5.15). This occurs despite the negative EPAC minus WPAC SAT contrast slightly strengthening, highlighting how relative changes over land are dominating the transient circulation response.

Exploring surface RH contrast changes in the transient SST perturbation experiments (Figure 5.17), a greater sensitivity to ENSO phase is present relative to SAT changes. For instance in amip4K and amipFuture, the negative MCO minus WPAC RH contrast weakens as low level winds become more westerly in the El Niño year, and vice-versa in the La Niña year. Over the eastern Pacific and equatorial South America, similarly diverging results are evident, with decreasing land-ocean humidity contrasts linked with increasing westerly and easterly anomalies during the El Niño and La Niña cases, respectively. These differences contribute to the amplified and mitigated $\lambda_{[\Psi]=0}$ westward shifts in the El Niño and La Niña years, relative to the neutral westward shift. In comparison the the SST perturbation cases, simulated changes in amip4xCO2 are relatively weaker. Examining the El Niño year when the eastward $\lambda_{[\Psi]=0}$ shift is largest, a consistent reduction in the MCO minus WPAC temperature and RH gradients occurs with increasing low level easterly anomalies.

These results indicate that for the transient response, changes in regional temperature and relative humidity contrasts typically co-occur with low level circulation anomalies and zonal shifts of the Walker circulation. A schematic summarising the equilibrium changes is presented in Figure 5.18. Generally, in amip4K and amipFuture, the positive land minus ocean surface temperature contrast is negated by a negative relative humidity contrast. The RH contrast wins, and deep convection over the eastern Pa-

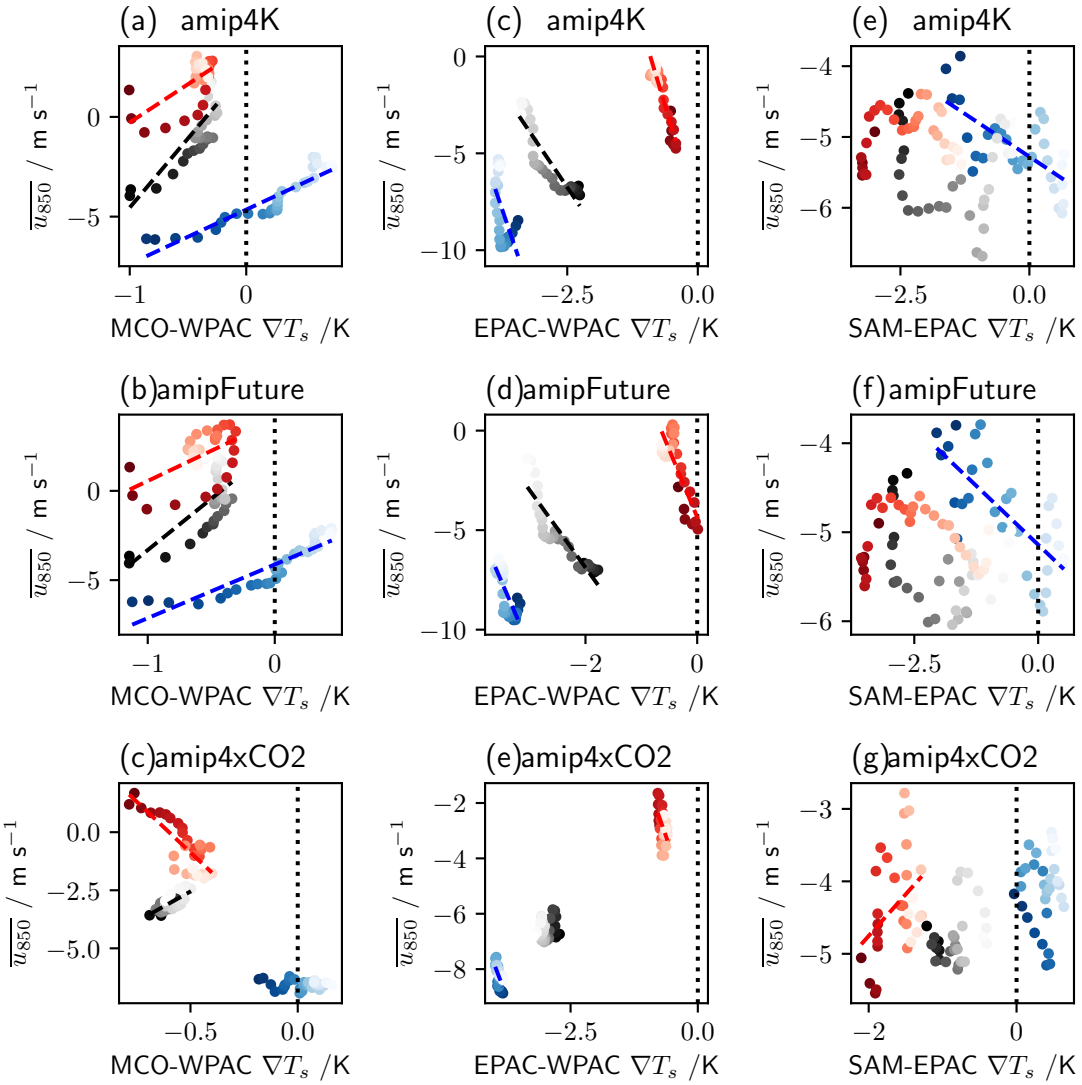

Figure 5.16: Ensemble and regional mean 850 hPa zonal wind, $\overline{u_{850}}$, versus surface air temperature contrasts, ∇T_s, for the first month of each HadGEM2-A transient simulation. The top, middle and bottom rows show the amip4K, amipFuture and amip4xCO2 experiments, respectively. The left, middle and right columns show the MCO minus WPAC, EPAC minus WPAC and SAM minus EPAC gradients and combined mean zonal wind, respectively, with the regional acronyms defined in-text. Marker colours and brightness as in Figure 5.15, denoting the progression of time for each ENSO phase. Corresponding dashed and coloured lines highlight where the regression slopes are significantly non-zero at the 5% level and the dotted, black vertical line shows where $\nabla T_s = 0$.

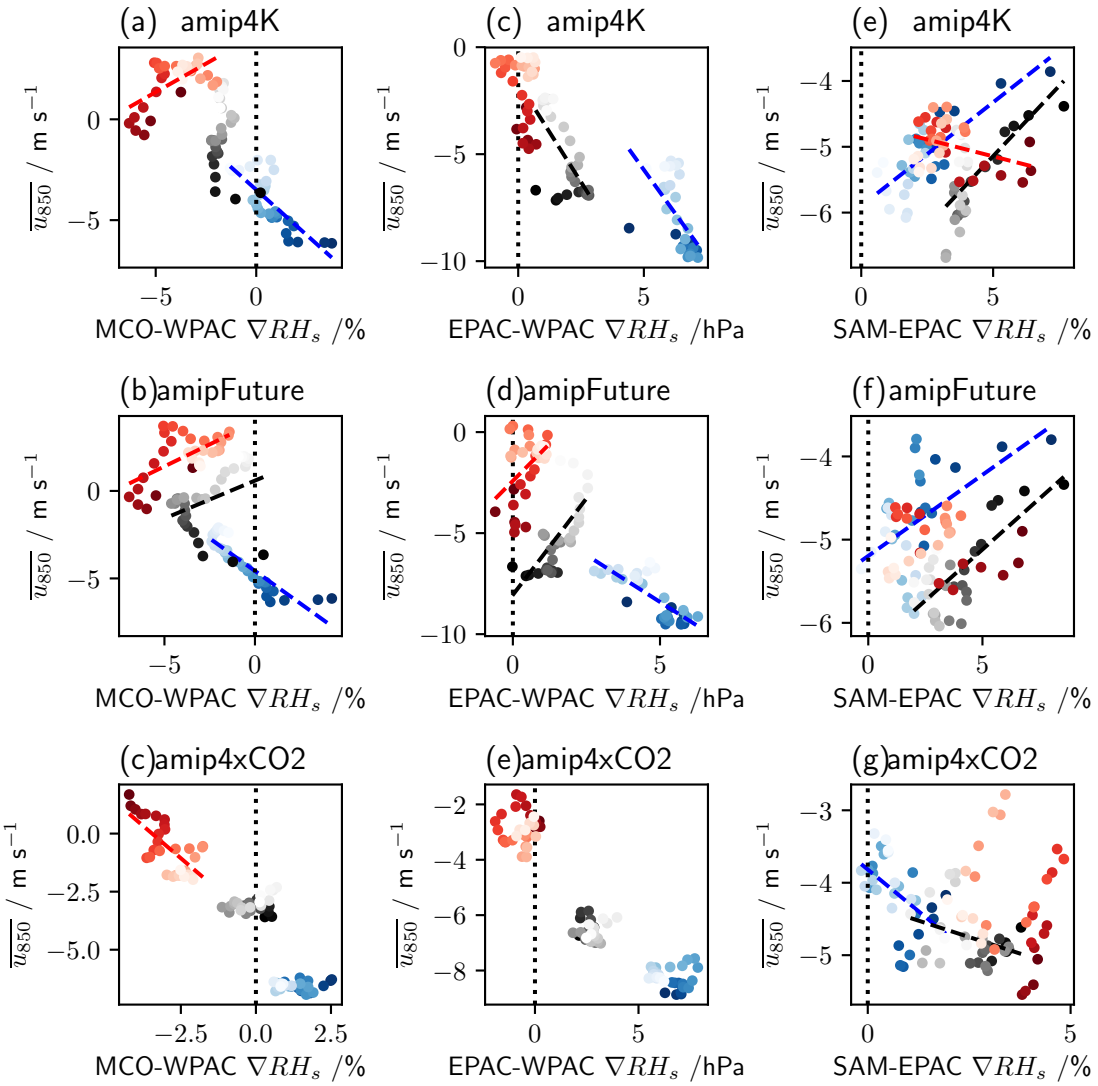

Figure 5.17: Markers, colours and lines as in Figure 5.16, except for the regional surface relative humidity contrasts, ∇RH_s, along the horizontal axis.

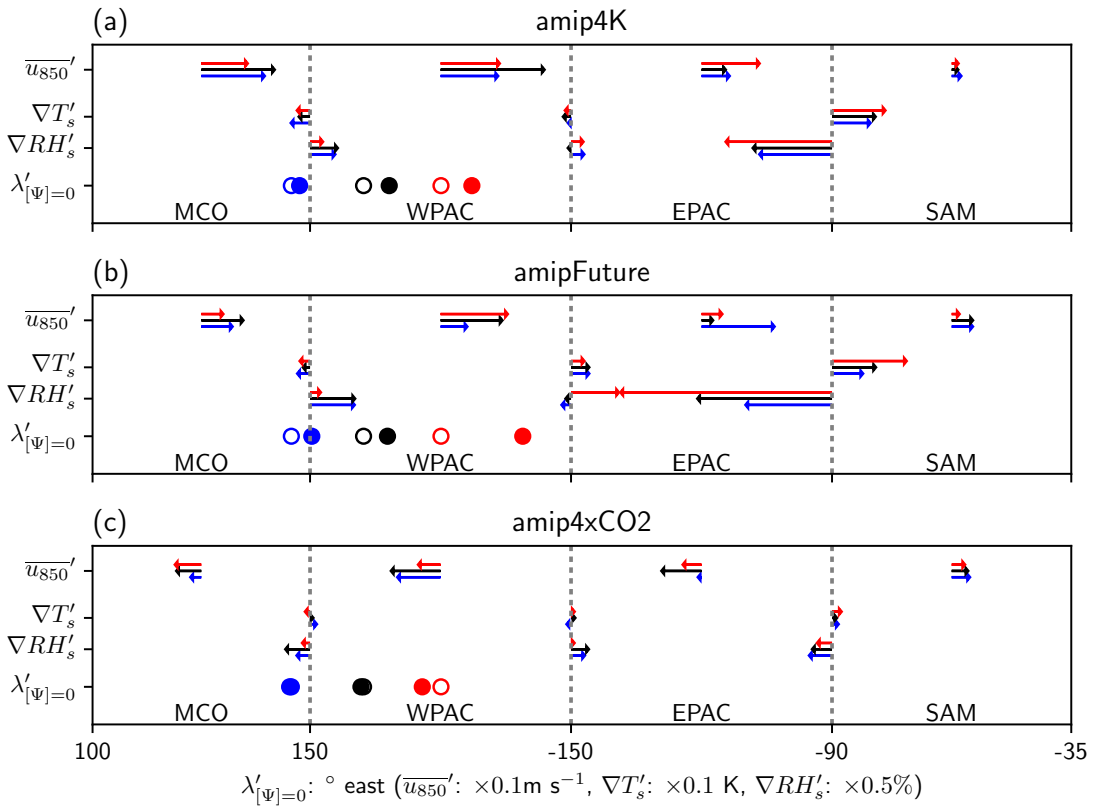

Figure 5.18: Schematic with arrows indicating the equilibrium anomalous ensemble and regional mean 850 hPa zonal wind, $\overline{u_{850}}'$, and inter-regional surface temperature, $\nabla T_s'$, and relative humidity, $\nabla RH_s'$, contrasts. Arrow lengths are scaled relative to the degrees longitude horizontal axis, as defined in the corresponding label. The four equatorial regions: MCO, WPAC, EPAC and SAM represent zonal bands covering 5°N-5°S, as defined in-text. The top, middle and bottom panels represent the amip4K, amipFuture and amip4xCO2 experiments, respectively. Empty and filled circles show the location of the ascending branch of the Walker circulation, $\lambda'_{[\Psi]=0}$, for the control (amip) and perturbation scenarios, respectively. Blue, black and red colours represent the La Niña (1988), neutral (1990) and El Niño (1997) cases, respectively.

cific is enhanced. Associated with these changes, anomalous low level westerlies over the maritime continent and the eastern Pacific are linked with a eastward shift of the ascending branch of the Walker circulation. In contrast, for amip4xCO2 the land minus ocean relative humidity contrast change is positive between the maritime continent and the western equatorial Pacific. This is linked with with anomalous low level easterlies across the Pacific and maritime continent, and a related westward shift of the Walker circulation. Consequently, changes in the position of the ascending branch of the Walker circulation are linked to a careful balance of regional land-ocean contrast changes.

5.5 Discussion and Conclusions

Section 5.1 builds on the results presented by Dong *et al.* (2009). Using a novel ensemble of HadGEM2-A simulations, the transient tropical land mean hydrological cycle response is relatively consistent for experiments initiated during either La Niña, neutral or El Niño phases. A balance of strong dynamic decreases and weaker thermodynamic increases leads to a tropical land mean precipitation decrease over days 1-5 in amip4K (≈ -1 mm day^{-1}) and amipFuture (≈ -1.5 mm day^{-1}), despite weak initial evaporation increases. Towards equilibrium, the dynamic component weakens and the nonlinear component becomes negative and decreases in these SST perturbation cases, contributing to the significant precipitation decrease at equilibrium. In amip4xCO2, a similar balance of dynamic increases and weaker nonlinear decreases contributes to the minor (≈ 0.2 mm day^{-1}) land mean precipitation increases. Examining vertical profiles of ocean to land moisture advection transient responses, changes in the lower troposphere beneath 600 hPa dominate in each experiment and year. At equilibrium in the SST perturbation cases, dynamic decreases are largely balanced by thermodynamic increases, whilst in the CO_2 forcing case the dynamic response is mainly positive with a considerably weaker thermodynamic response. The equilibrium nonlinear response is similar in each experiment, demonstrating enhanced moisture inflow below 850 hPa, but greater outflow above this level.

A mechanism is presented linking these dynamic responses to changes in the land-ocean temperature contrast. Adapting the analysis of Bayr and Dommenget (2013), a significant negative linear association is present between the transient tropospheric land-ocean temperature contrast and the surface pressure contrast in both SST perturbation experiments. From five days after each perturbation, including amip4xCO2, there is also generally a significant negative linear association between the transient surface land-ocean temperature and pressure contrasts. This indicates two stages in the transient circulation and hence hydrological cycle response. Initially, warming over land is muted, especially in the SST perturbation cases. Hence in these cases, a strong negative land-ocean contrast drives a surface pressure contrast and low level circulation anomaly, contributing to the dynamic component of precipitation decreases. Subsequently as the land warms, due to large scale dynamics above the boundary layer and moisture limitation near the surface (Joshi *et al.*, 2008), the temperature contrast weakens and reverses, equivalently weakening and reversing the dynamic component.

Subsequently, Section 5.4 examined the regional and ENSO sensitivity to the hydrological cycle response. Over the extended Pacific region, the August-September precipitation anomalies are relatively consistent in both transient and equilibrium cases. This indicates that the regional precipitation response to SST or CO_2 perturbations approaches equilibrium within two months. Mean precipitation over land generally decreases during

a neutral DJF (1990) in each atmosphere-only experiment. Proxy El Niño anomalous precipitation (1997 minus 1990) demonstrates a stronger regional sensitivity, with significant increases simulated over New Guinea in amip4K and amipFuture. As with the tropical mean response, a balance of thermodynamic and dynamic components is important in modulating the regional response. Moisture supply limitations over equatorial South America, relative to the maritime continent, are hypothesised to contribute to the constrained local equilibrium circulation response over the former.

Finally, motivated by Section 5.3, the sensitivity of the ascending branch of the Walker circulation to competing land-ocean surface contrasts in the eastern and western Pacific is assessed. This follows the methodology of Yu and Zwiers (2010) and Bayr *et al.* (2014). At equilibrium in HadGEM2-A, the SST perturbation experiments lead to an eastward shift, whilst the CO_2 forcing experiment leads to a westward shift, each with a strong dependence on the ENSO phase. In the SST perturbation cases, these shifts become evident within 20 days, and are significantly related to the regional land-ocean temperature contrasts. At equilibrium, the eastern Pacific contrast is stronger than the western Pacific contrast, dragging the Walker circulation eastward in amip4K and amipFuture. However, in the CO_2 forcing experiment no significant relationship is present, suggesting other factors may be responsible for the equilibrium westward shift.

Chapter 6

Discussion and Conclusions

> "Considering that these islands are placed directly under the equator, the climate is far from being excessively hot; this seems chiefly caused by the singularly low temperature of the surrounding water, brought here by the great southern Polar current. Excepting during one short season, very little rain falls, and even then it is irregular; but the clouds generally hang low. Hence, whilst the lower parts of the islands are very sterile, the upper parts, at a height of a thousand feet and upwards, possess a damp climate and a tolerably luxuriant vegetation. This is especially the case on the windward sides of the islands, which first receive and condense the moisture from the atmosphere."
>
> *C. Darwin, The Voyage of the Beagle, 1845*
> (Describing the Galapagos Islands.)

The overarching aim of this thesis has been to improve our understanding of the mechanisms which control tropical precipitation, its variability, and future changes. This is motivated by the relatively high uncertainty in twenty-first century projections of tropical precipitation changes. This stems from disagreement amongst state-of-the-art coupled climate model simulations of anthropogenic global warming (Collins *et al.*, 2013; Christensen *et al.*, 2013). On regional scales, the wet-get-wetter and dry-get-drier paradigm of Held and Soden (2006) is inadequate, as climatological wet and dry regions are expected to shift. Factors such as sea surface temperature (SST) gradients, land surface and atmospheric circulation changes, which exhibit large model diversity in CMIP5, are tightly coupled with the simulated pattern of precipitation change (Xie *et al.*, 2010; Chadwick *et al.*, 2013). Chapters 2 and 3 built upon existing literature to develop a simplified theory for improving our understanding of these regional precipitation change processes.

Substantial interannual variability is evident in present day tropical precipitation observations, much of it linked with the El Niño-Southern Oscillation (ENSO) (Ropelewski

and Halpert, 1987). ENSO representation in coupled climate models has improved over recent generations (Bellenger *et al.*, 2014), and future changes in a handful of ENSO characteristics have been identified (Cai *et al.*, 2015a). Robust tropical Pacific mean state changes, such as a shoaling and flattening of the thermocline, reduced zonal SST gradient and corresponding weakened low level easterly trade winds (Santoso *et al.*, 2013) would lead to an increased frequency of extreme El Niño (Cai *et al.*, 2014) and La Niña (Cai *et al.*, 2015b) events. In addition, a local maximum in SST warming at the equator (Xie *et al.*, 2010) would increasingly lead to equatorward shifts of the SPCZ (Borlace *et al.*, 2014). An eastward shift in the El Niño anomalous SST warming (Huang, 2016) would also contribute to changes in the pattern of teleconnections (Bonfils *et al.*, 2015; Perry *et al.*, 2017).

A complete understanding of how competing mechanisms will affect ENSO anomalous precipitation change is currently lacking in the literature. This motivated an assessment of the relative roles of SST warming and CO_2 forcing to both the mean state and ENSO related precipitation changes, as presented in Chapter 4. Finally, a novel ensemble of atmosphere-only simulations was used in Chapter 5 to further explore how land-ocean warming and humidity contrasts will affect precipitation during future ENSO events.

6.1 Summary and Discussion

In the Introduction (Chapter 1), a review of the recent literature raised four research questions, which have guided the analysis in this thesis. Here, a summary and discussion of each result chapter is presented, highlighting the important and novel contributions to the field.

6.1.1 Can a consistent mechanism explain both present day tropical precipitation variability and simulated future changes?

The first research question posed in the Introduction was "Can a consistent mechanism explain both present day tropical precipitation variability and simulated future changes?" Chapter 2, an extended version of Todd *et al.* (2018), builds upon the study of Lambert *et al.* (2017) who present a simplified method linking tropical precipitation with surface air temperature (SAT) and relative humidity (RH) changes to examine this question. This diagnosis method is based on the weak temperature gradient (WTG) approximation of Sobel *et al.* (2001), which assumes the tropical free tropospheric temperature profile is spatially uniform, due to minimal rotational effects near the equator (Charney, 1963). Consequently, the triggering and maintenance of deep convection, and hence the heaviest precipitation, is favoured over relatively warmer and more humid regions at the surface, where the difference between low and mid level moist static energy is largest

(Xie *et al.*, 2010). Importantly, in observations and ERA-Interim reanalyses, tropical rainforest regions generally have a higher RH compared to the rest of the tropics. Hence, future RH decreases over these areas could plausibly be linked with reduced precipitation.

The simplified Lambert *et al.* (2017) diagnosis method performs reasonably well at diagnosing present day El Niño minus neutral precipitation changes in ERA-Interim and GPCP data. This is supported by good sign agreement and a spatial correlation between observed and diagnosed precipitation anomalies of 0.69. Similar results hold for purely observational (HadCRUT, HadCRUH and GPCP) or reanalysis (ERA-Interim) data sets. However, there is relatively high uncertainty due to systematic errors in each of these data sources. Equivalent good diagnostic performance is found using the CMIP5 multi-model ensemble (MME) of atmosphere-only (amip) and fully coupled (piControl) climate model simulations of El Niño. Spatial correlations, r, for the MME range between 0.51 to 0.8, and 0.5 to 0.87 in each case, respectively. Additionally, a significant positive association in inter-model variability is present between the atmosphere-only and fully coupled diagnosis performance. This indicates that the performance of the Lambert *et al.* (2017) diagnosis method, in the case of natural variability in climate models, is quite independent of how the sea surface conditions are simulated. Hence, causes of diagnosis performance and hence precipitation change mechanism differences amongst the MME are isolated to the atmosphere or land component of each climate model.

Comparing El Niño with simulated global warming (abrupt4xCO2 minus piControl) in the CMIP5 MME, there is generally a weaker and broader spread of precipitation diagnosis performance (r ranging between 0.3 and 0.81) for the latter. In particular, for several models (IPSL-CM5A-LR, IPSL-CM5A-MR, IPSL-CM5B-LR, FGOALS-s2, CCSM4 and inmcm4) sign agreement is especially poor over tropical land areas, with tropical spatial correlations less than 0.5. One feature present in the global warming diagnoses, as well as the atmosphere-only and coupled El Niño diagnoses, is a local performance maximum near the equator. This is consistent with the theoretical basis, since the Coriolis effect increases polewards of the equator, reducing the suitability of the WTG approximation (Sobel *et al.*, 2001). Examining a simplified configuration of the Lambert *et al.* (2017) method, using only RH changes in the diagnosis step, a significant positive association is present between El Niño and global warming performance in inter-model variability. However, no equivalent relationship is present for the full RH-SAT implementation of the Lambert *et al.* (2017) method. This implies that SAT changes affect precipitation change mechanisms differently in CMIP5 simulations of ENSO and global warming.

A major issue with the Lambert *et al.* (2017) diagnosis method for observed and simulated El Niño and simulated global warming, is the underestimation of the magnitude of precipitation changes. For instance, the linear regression slope estimate of diagnoses

versus observations for the El Niño anomalies is 0.41, which is significantly different from unity at the 95% level. This underestimation is linked with the aggregation process in the binning method, which constrains the magnitude of diagnosed changes. This issue motivated a revision of the Lambert *et al.* (2017) method in Chapter 3, to better resolve precipitation as a function of SAT and RH relative to their tropical means. A second issue raised by Chapter 2 is that the Lambert *et al.* (2017) method consistently performs better over tropical oceans relative to tropical land in each test case. For ERA-Interim-GPCP El Niño diagnosed changes, $r = 0.71$ and $r = 0.46$, for ocean and land regions, respectively. This persistent misdiagnosis over land, alongside diagnosis errors over ocean, is also further examined in the latter part of Chapter 3.

Chapter 2 presents three main advances over the Lambert *et al.* (2017) study. Firstly, alternative configurations of the binning method using just RH or SAT changes and the base state SAT or RH demonstrate that ENSO precipitation changes are more strongly linked to local RH changes in comparison SAT changes. Further analysis indicates that this is not simply due to the relative differences in the contributions of RH and SAT changes to low level moist static energy changes. Secondly, by examining ENSO observations and simulations, a consistent mechanism is identified in the link between precipitation and RH changes which bridges present day natural variability and projected global warming. Finally, Chapter 2 presents a novel assessment of the regional suitability of the WTG approximation. This approximation is generally poorer over land relative to ocean across the tropics. Understanding the reasons for this disparity in the WTG approximation is identified as an important area of future work.

In summary, Chapter 2 presents a novel configuration of the Lambert *et al.* (2017) method, which typically performs quite well over tropical oceans at diagnosing both present day ENSO and simulated global warming precipitation anomalies. This method links precipitation and RH changes, relative to the tropical mean RH, based on the background surface air temperature. Consequently, there is some evidence of a consistent mechanism which bridges both present day precipitation interannual variability and future changes. However, this mechanism doesn't apply particularly well over tropical land for a sizeable minority of CMIP5 global warming simulations. Therefore, the simplified binning method of Lambert *et al.* (2017) doesn't completely explain regional patterns of precipitation change. Factors contributing to weak diagnosis performance, such as inhomogeneous changes in RH coupling between the boundary layer and free-troposphere, are explored further in Chapter 3, as discussed below.

6.1.2 Can surface condition changes constrain the uncertainty in present day tropical precipitation variability and simulated future changes?

The second research question was "Can surface condition changes constrain the uncertainty in present day tropical precipitation variability and simulated future changes?'. Together with the issues raised by Chapter 2, this motivated the implementation of the Lambert *et al.* (2017) method in a more sophisticated, Gaussian process (GP) framework in Chapter 3. The logarithm of precipitation is assumed to follow a Gaussian process, where the mean and covariance functions depend on the tropical quantiles of RH, q_H, and SAT, q_T. Notably, for the mean function in (q_H, q_T)-space, GP model uncertainty is typically larger relative to interannual variability. Hence, diagnosed precipitation changes are assessed against the former to determine whether they are significantly non-zero, and if observed or simulated changes are significantly different. Our understanding of tropical precipitation changes is developed by analysing this revised method.

Generally for ERA-Interim-GPCP observations and CMIP5 historical simulations the GP model fit is relatively good. This gives confidence in using the fitted models in the diagnosis framework. A minor issue is that the normality assumption of the logarithm of precipitation is inaccurate in regions where precipitation is close to zero, leading to slightly underestimated variance. However, there is no clear link between goodness of fit to control data and the diagnosis performance for either ENSO or global warming precipitation changes. This suggests weaknesses other assumptions, such as a fixed precipitation function in terms of q_H and q_T or a constant link between surface and lower tropospheric RH, contribute to poor diagnosis performance.

The GP framework leads to a slight diagnostic performance improvement ($r = 0.73$) in comparison to the binning method (Chapter 2) for El Niño minus neutral precipitation changes in ERA-Interim-GPCP. Another improvement is the magnitude of diagnosed precipitation changes, with a slope estimate closer to unity (0.53) in the observed El Niño case. A more comprehensive analysis of present day, observed ENSO is also presented in Chapter 3. For both El Niño and La Niña anomalies, using either the binning or GP framework, diagnosis performance peaks during austral summer, the ENSO mature stage, with better performance for the former ENSO phase. This highlights how the Lambert *et al.* (2017) method and the GP implementation generally perform better at diagnosing precipitation shifts, instead of climatological amplification, when the signal-to-noise ratio of anomalies is greatest.

Extending the global warming analysis presented in Chapter 2, the GP framework is applied to a different simulated late twenty-first century (RCP8.5) minus late twentieth century (historical) change in Chapter 3. Generally consistent results are obtained to

the abrupt4xCO2 and binning case, again with relatively large model diversity. Similar to the observed ENSO changes, slope estimates are typically closer to unity, and spatial correlations increase for 78% of CMIP5 ensemble members. These results demonstrate how the better resolved precipitation function generally improves diagnosis performance in both ENSO and global warming cases. However, the land-ocean performance disparity of the binning method persists for the GP implementation.

In order to understand misdiagnosed precipitation changes, two implicit assumptions of the Lambert *et al.* (2017) method are examined: 1) precipitation as a function of RH and SAT, relative to their tropical means, is invariant under climate perturbations and 2) surface RH changes are strongly coupled to RH changes aloft. To investigate assumption 1), $\hat{P}$ differences between control and perturbation conditions are assessed. For ENSO perturbations, structural changes in $\hat{P}$, mainly due to depopulation or population of (q_H, q_T)-space regions, are small relative to the GP model uncertainty. For example, under El Niño conditions the relatively cool and humid eastern equatorial Pacific warms substantially, and hence the proportion of the tropical oceans where the air is cool and humid above the surface decreases substantially. Consequently, the shape of $\hat{P}$ in this region of (q_H, q_T)-space is less well constrained relative to neutral conditions, with an approximately converse result for the La Niña case. This highlights an unavoidable issue with the Lambert *et al.* (2017) method, as the spread of present day RH and SAT relative to their tropical means also changes under simulated future conditions.

Comparing observed ENSO $\hat{P}$ changes with simulated global warming, assumption 1) is generally less justified for the latter. The coarse scaling of $\hat{P}$ by tropical mean precipitation increases (Lambert *et al.*, 2017), doesn't completely capture the large scale wet-get-wetter and dry-get-drier response. For a subset of representative CMIP5 models, significant $\hat{P}$ changes occur in regions of (q_H, q_T)-space where the land-ocean ratio and the fraction of subtropical contributions changes. As discussed in Chapter 2, the WTG approximation is generally less suitable over land, due to surface orography and vegetation differences, and across the subtropics, where the Coriolis effect is larger. These factors contribute to some of the significant $\hat{P}$ differences between the late twentieth and twenty-first century simulations.

Global warming $\hat{P}$ changes are also found to occur for near-equatorial ocean regions which remain constant in (q_H, q_T)-space, for instance in HadGEM2-ES. This motivates an analysis of vertical RH coupling changes to assess assumption 2). Comparing surface and 850 hPa RH changes for both observed ENSO and simulated global warming, two regimes are typically present. In one regime, RH changes at the surface and aloft are positively associated. In a second regime, the surface RH increases slightly but there is no clear association with RH changes aloft. Generally, surface RH can only change

substantially if RH aloft changes substantially, but RH changes aloft can occur independently of surface changes. This implies assumption 2) is imperfect, and hence RH aloft changes can modulate deep convection and precipitation without corresponding RH changes at the surface.

Typically, 850 hPa RH changes minus surface RH changes are positive and negative in ascent and descent regions, respectively. For observed ENSO and several CMIP5 model global warming simulations where the Lambert *et al.* (2017) diagnosis method performs well, amplified RH increases aloft relative to the surface are co-located with large observed, or simulated, and diagnosed precipitation increases. However, in some CMIP5 models, such as the MIROC family, simulated and diagnosed precipitation decreases in these regions. These results highlight the complex relationships between changes in RH vertical coupling, precipitation and diagnosis performance evident in observations and climate model simulations.

The statistical implementation of the Lambert *et al.* (2017) method presented in Chapter 3 attempts to constrain precipitation changes using surface RH and air temperature changes. This is reasonably successful for ENSO and simulated global warming, with the additional benefit of improved accuracy relative to the Lambert *et al.* (2017) binning method. However, GP model uncertainty is relatively large, so the aim of reducing future precipitation change uncertainty (Chapter 1) is unsatisfied. Instead, the additional affects of structural changes in $\hat{P}$, and the vertical coupling of RH, are identified to play an important role in both present day precipitation variability and simulated future changes. This enhances our understanding of the linked processes which modulate tropical precipitation changes. Further work is necessary to examine additional factors which modulate tropical precipitation changes, discussed later in Section 6.2.

6.1.3 What role does atmosphere-ocean coupling play in precipitation mean state and variability changes?

Chapter 4 addresses the third question posed in the Introduction, "What role does atmosphere-ocean coupling play in precipitation mean state and variability changes?" A multi model ensemble of CMIP5 idealised global warming, atmosphere-only simulations representing uniform SST warming (amip4K), patterned SST warming (amipFuture) and CO_2 forcing (amip4xCO2) are linearly combined to form amipTotal, a proxy for the more realistic, coupled RCP8.5 simulation. This framework follows recent studies (Kent *et al.*, 2015; He and Soden, 2015; Zappa *et al.*, 2018), with the aim of disentangling how tropical precipitation responds to competing forcing processes. One benefit of this method is that the effect of mean state changes on ENSO anomalies, such as uniform or patterned SST warming, can be isolated. A drawback is that atmosphere-ocean feedbacks are not explicitly included, and hence perhaps unrealistically relative future ENSO SST anomalies

remain identical to present day SST anomalies. However, in CMIP5 coupled simulations there is substantial disagreement over how ENSO SST anomalies may change (Cai *et al.*, 2015a), so this method is a parsimonious option. Moreover, there is evidence that prescribing the SST pattern from a coupled experiment to an atmosphere-only model simulates a similar precipitation response (Chadwick *et al.*, 2016), and hence the lack of feedbacks is likely to be a minor issue.

A partitioning framework is introduced in Chapter 4 to evaluate the mean state and El Niño anomaly temperature and precipitation changes in each contribution to amip-Total, which is largely representative of RCP8.5. Consistent with the literature, uniform SST warming and CO_2 forcing causes an enhanced mean state land-ocean temperature contrast, mainly due to moisture limitation over land and hence a steeper adiabatic lapse rate at equilibrium (Joshi *et al.*, 2008). Patterned SST warming also contributes to enhanced land warming via circulation changes. Examining the El Niño temperature changes, uniform SST warming and SST pattern changes each contribute to significant relative warming over northern Africa, eastern Asia and central South America. Meanwhile, relative cooling is present across southern Africa, Australia and subtropical South America in these two experiments. In amip4xCO2, a weaker relative warming signal is also evident over northern Africa and eastern Asia.

The coupled, RCP8.5 mean state precipitation response is largely a balance of thermodynamic and dynamic contributions, representing present day circulation acting upon specific humidity changes, and circulation changes acting on present day specific humidity, respectively. In the zonal mean, changes in the Hadley circulation dominate the precipitation change (Su *et al.*, 2017). A narrowing and intensification of the ITCZ via increased dry air inflow at low levels (termed the upped-ante mechanism (Neelin *et al.*, 2003; Chou *et al.*, 2009)) leads to precipitation increases along the centre of the ITCZ and decreases along its flanks. Corresponding Hadley cell expansion broadens the subtropical descent regions, reducing precipitation in the subtropics. The large scale amip4K response is mainly thermodynamic. However, at regional scales there is also a significant dynamic component, especially over the tropical Indian and Pacific oceans. Importantly, these precipitation changes occur without SST gradient changes, implying a circulation change linked with surface changes over tropical land. Both SST pattern change and CO_2 forcing mean state precipitation responses are dominated by the dynamic component. In the former, deep convection and precipitation increases over the relatively warmest SST (Xie *et al.* (2010), Chapters 2 and 3). This feeds back onto the large scale circulation and leads to precipitation changes over tropical land (explored in Chapter 5). In the latter, CO_2 forcing leads to mean state amplified warming over tropical land, locally enhancing convection and precipitation. Over tropical oceans, upper tropospheric stabilisation dominates and suppresses deep convection, reducing precipi-

tation (Bony *et al.*, 2013).

Similar to the mean state response, in the uniform SST warming case the El Niño anomalous precipitation change is not simply wet-get-wetter and dry-get-drier. Precipitation increases are enhanced along the northern flank of the SPCZ, but not along the central equatorial Pacific. In amipFuture minus amip4K, mean state SST warming relatively enhances precipitation along the central equatorial Pacific and decreases precipitation over off-equatorial regions. Finally, in amip4xCO2, the amplitude of the present day anomaly pattern is slightly mitigated, due to a general weakened circulation over the tropical Pacific. In each contribution to amipTotal, as well as RCP8.5, the dynamic contribution dominates the El Niño anomalous changes. Partitioning the dynamic term into divergence and advection components, the former is responsible for approximately 80% of the changes. This result implies that specific humidity variability remains relatively constant under either uniform SST warming, SST pattern changes or CO_2 forcing, with the circulation response most influential via divergence changes.

Consequently, a number of factors act to modulate the mean state and ENSO precipitation changes in CMIP5 future simulations. For coupled models, in response to CO_2 forcing, SST pattern changes co-occur with circulation changes and enhanced land warming. This leads to a substantial dynamic component of regional precipitation changes. Meanwhile, the background SST warming contributes to increased tropospheric moisture, causing a larger scale thermodynamic wet-get-wetter and dry-get-drier precipitation response. A careful balance of these two components is responsible for the overall pattern of precipitation changes. The results of Chapter 4, supported by recent literature (Power and Delage, 2018), highlight the useful role of idealised atmosphere-only simulations in understanding the competing processes linked to precipitation changes in coupled simulations.

6.1.4 Does tropical land warming relative to ocean warming drive the circulation and precipitation response to global warming?

The final research question is "Does tropical land warming drive the circulation and precipitation response to global warming?" Chapter 5 analyses a novel ensemble of HadGEM2-A atmosphere-only experiments. Building upon Dong *et al.* (2009), the transient and equilibrium precipitation response to the amip4K, amipFuture and amip4xCO2 perturbations are assessed at each ENSO phase. This is motivated by the results of Chapter 4, which identifies a link between equilibrium mean state and ENSO anomaly circulation changes and patterns of land warming.

Chapter 5 presents two major advances over the Dong *et al.* (2009) study. Firstly, the transient and equilibrium precipitation response over land to SST or CO_2 perturbations are shown to be quite sensitive to natural variability. Hence future studies should repeat transient simulations over several different stages of natural variability in order to better understand forced responses. Secondly, the novel HadGEM2-A simulations build our understanding of the mechanisms controlling the pattern of precipitation changes. Regional land-ocean surface air temperature and relative humidity contrasts change over a similar timescale to Walker circulation shifts. This suggests a common link between temperature, RH and precipitation changes, supporting the results presented in Chapters 2 and 3.

Consistent with Dong *et al.* (2009), the transient tropical land mean response to either uniform or patterned SST warming in HadGEM2-A occurs in three main stages. Almost immediately (during day 1), the boundary layer over ocean warms in response to the surface temperature perturbation, and reaches an equilibrium temperature closely tied to the perturbed SST. This generally causes an instant reversal of the land-ocean mean temperature contrast. Subsequently, over days 2-5, the boundary layer and hence surface over land warms, weakening the temporarily reversed land-ocean temperature contrast towards zero. This occurs in part due to inland advection of ocean temperature anomalies, via horizontal mixing, as well as fast acting waves. Simultaneously, the boundary layer and the free troposphere slowly warms as the approximately moist adiabatic lapse rate adjusts to moisture changes. Finally, over days 6-30, warming is amplified in the upper troposphere due to slower lapse rate changes. Meanwhile, surface and boundary layer land temperatures increase further due to moisture limitations, enhancing the land-ocean temperature contrast (Joshi *et al.*, 2008). In contrast to the SST perturbation experiments, in amip4xCO2 the temperature and precipitation response reaches equilibrium over a much shorter timescale, as discussed in more detail in Chapter 5.

Decomposing the hydrological cycle response in amip4K and amipFuture, tropical land mean precipitation sharply decreases over days 1-5, despite concurrent weak evaporation increases. Initially, this is due to a strong negative dynamic contribution, weakly moderated by a positive thermodynamic contribution after day 2. This substantial circulation change is manifested by weakened ocean-to-land winds in the boundary layer. This is driven by an anomalous surface pressure gradient in response to the transient tropospheric temperature contrast, and quantified using the Bayr and Dommenget (2013) framework. Heading towards equilibrium over the first month, the dynamic contribution switches to weakly positive, in part due to the enhanced land-ocean warming contrast, which increases boundary layer inflow, whilst the thermodynamic component remains positive due to increased moisture. These moisture inflow anomalies are negated by the nonlinear term, characterised by enhanced outflow aloft, which is connected to a weak tropical land mean precipitation reduction.

To explore the regional sensitivity of transient and equilibrium responses during different ENSO phases, Chapter 5 focuses on hydrological cycle changes over two important teleconnection regions: New Guinea and equatorial South America. Over New Guinea, significant precipitation decreases are evident in both amip4K and amipFuture for neutral (1990) and La Niña (1998) phases, with no significant changes during the El Niño (1997) phase. In contrast, over equatorial South America, significant decreases are evident during each ENSO phase. Similar to the tropical land mean response, initial precipitation changes over both regions are a balance of negative dynamic contributions and weaker positive thermodynamic contributions. At equilibrium, the nonlinear component dominates, but notably daily variability is quite large. These results, similar to those presented in Chapter 4, highlight the important and linked role of circulation and precipitation changes on a regional scale.

Shifts in the ascending branch of the Walker circulation, defined by the zero crossing of the vertically integrated equatorial zonal streamfunction (Yu and Zwiers, 2010), are explored to understand the regional precipitation response. At equilibrium, a small westward shift is evident in amip4xCO2, with a moderate eastward shift in amip4K and a larger eastward shift in amipFuture. These shifts are amplified during El Niño and suppressed during La Niña in each case, in general agreement with previous studies (Bayr *et al.*, 2014; Huang, 2016). These shifts rapidly occur within the first month of the atmosphere-only simulations, and hence the transient response is examined to develop an understanding of the equilibrium changes.

Consistent with Bayr *et al.* (2014), zonal shifts of the ascending branch of the Walker circulation are positively associated with the low level equatorial Pacific zonal mean wind in the transient evolution. Chapter 5 presents a framework quantifying how these zonal shifts depend on the balance of land-ocean deep convection favourability contrasts (Chapters 2 and 3) in the western and eastern equatorial Pacific with surrounding land regions. For example, during an El Niño case in amip4K, the equatorial South America-eastern Pacific temperature contrast is stronger than the equatorial maritime continent-western Pacific contrast. This is linked with a weakening of the low level Pacific easterlies, shifting the Walker circulation eastwards.

Chapter 5 demonstrates how land warming is one factor strongly linked with tropical circulation changes. More generally, in a novel ensemble of HadGEM2-A simulations, surface condition changes which modulate deep convection (as discussed in Chapters 2 and 3) are coupled to circulation changes, which in turn affects both local and remote precipitation changes.

6.2 Future Work

Several areas of future work are raised from this thesis, as discussed in this section. Two papers are in preparation, one focussing on the main results of Chapter 3 and another motivated by Chapter 4 examining the simulated ENSO precipitation changes identified in Chapter 5.

6.2.1 Improving the Framework for Diagnosing Precipitation Shifts

In evaluating the analysis of the Lambert *et al.* (2017) method presented in Chapters 2 and 3, it is important to note that ENSO and simulated future precipitation changes are not direct analogues. Tropical and global mean warming and radiative balance changes are substantially less during El Niño events, and hence the thermodynamic contribution to precipitation change is of a considerably smaller magnitude. Two further tests could help to bridge between ENSO and global warming precipitation changes. Firstly, seasonal variability could be assessed to examine the effect of changes in incoming shortwave (SW) radiation, for instance by diagnosing summer minus winter changes for each hemisphere. Secondly, diagnoses of amipFuture minus amip4K precipitation changes in CMIP5 could be compared with present day ENSO changes. This latter test would examine if the link between SST and precipitation pattern change remains constant between present day and idealised future conditions. Preliminary results indicate generally good diagnosis performance for these tests, with typically stronger performance relative to either RCP8.5 or abrupt4xCO2 global warming. This provides further evidence of the disparity in precipitation change processes between simulated global warming and natural variability, with further work necessary to improve our understanding.

The analysis of additional factors affecting precipitation changes in Chapter 3 could be extended further by linearising RH changes into specific humidity and temperature change components. Specific humidity changes over land could then be modelled by assuming an equivalent fractional change as over nearby oceans, where the Clausius-Clapeyron relation is approximately followed, building upon the arguments of Rowell and Jones (2006), Chadwick *et al.* (2016) and Byrne and O'Gorman (2016). This framework would diagnose precipitation changes in response to both absolute and relative temperature changes alone. Consequently, the link between the satisfaction of the WTG approximation and diagnosis performance could be more precisely evaluated.

A final area of improvement to explore how precipitation changes are related to surface RH and temperature changes would be to examine tropical land and ocean regions separately. Previous studies indicate contrasting links between precipitation and temperature variability in recent observations over land and ocean. For instance, over land, precipitation and surface air temperatures are typically negatively correlated, as warmer

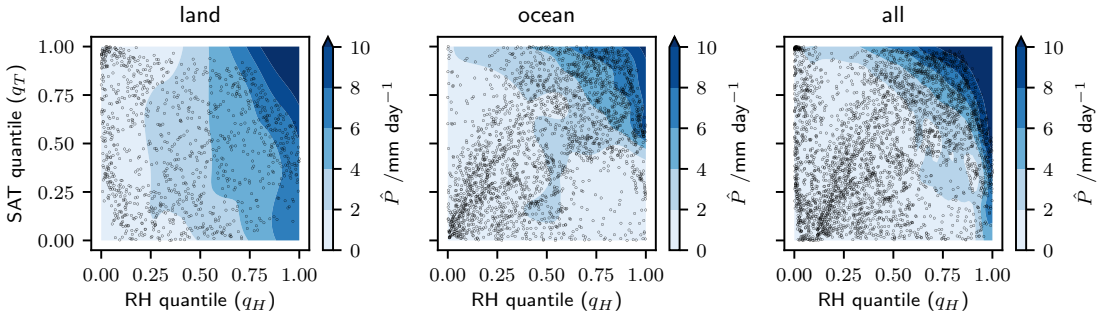

Figure 6.1: GP precipitation mean functions, $\hat{P}$, in (q_H, q_T)-space for ERA-Interim-GPCP 1979-2016 July-June (ENSO) neutral composite means for tropical land (left), ocean (middle) and all (right) grid points. Black circles indicate the respective locations of grid points in (q_H, q_T)-space.

conditions are generally associated with subsidence and reduced cloud cover. In contrast, over ocean a positive correlation is typically found between SST and precipitation, due to favoured convergence and hence ascent over the relatively warmest regions (Trenberth and Shea, 2005; Allan, 2012). Preliminary results for El Niño minus neutral changes in ERA-Interim-GPCP data indicate an improvement in diagnosis performance when precipitation mean functions (in the GP framework, Chapter 3) are evaluated separately over land and ocean. Figure 6.1 indicates the mean function, $\hat{P}$, for the neutral composite mean over land, ocean or all tropical grid points. Notably, $\hat{P}$ demonstrates a stronger dependence on RH over land and SAT over ocean. This suggests that quite different processes modulate precipitation changes over tropical land and ocean, which could explain the persistent land-ocean performance disparity in Chapters 2 and 3. Examining Figure 6.2, merging the separate land and ocean diagnoses results in improved performance over ocean (r increases from 0.67 to 0.78). Over land, spatial correlations indicate little change in tropics-wide performance, however the pattern of diagnosed changes improves over tropical Africa for the split land-ocean case relative to original framework. Note that these values are slightly different from those presented in Chapter 3 since a longer ENSO period (July-June) is examined to maximise teleconnection patterns over land.

6.2.2 Exploring Future Precipitation Mean State and Variability Changes

Chapters 4 and 5 explored precipitation mean state and variability change in CMIP5-class models and simulations. An important test of the hypothesis of a link between patterns of land warming, circulation and hence precipitation change would be to assess alternative models and experiments. For example, the Precipitation Driver Response Model Intercomparison Project (PDRMIP, Myhre *et al.* (2017)) simulations are designed

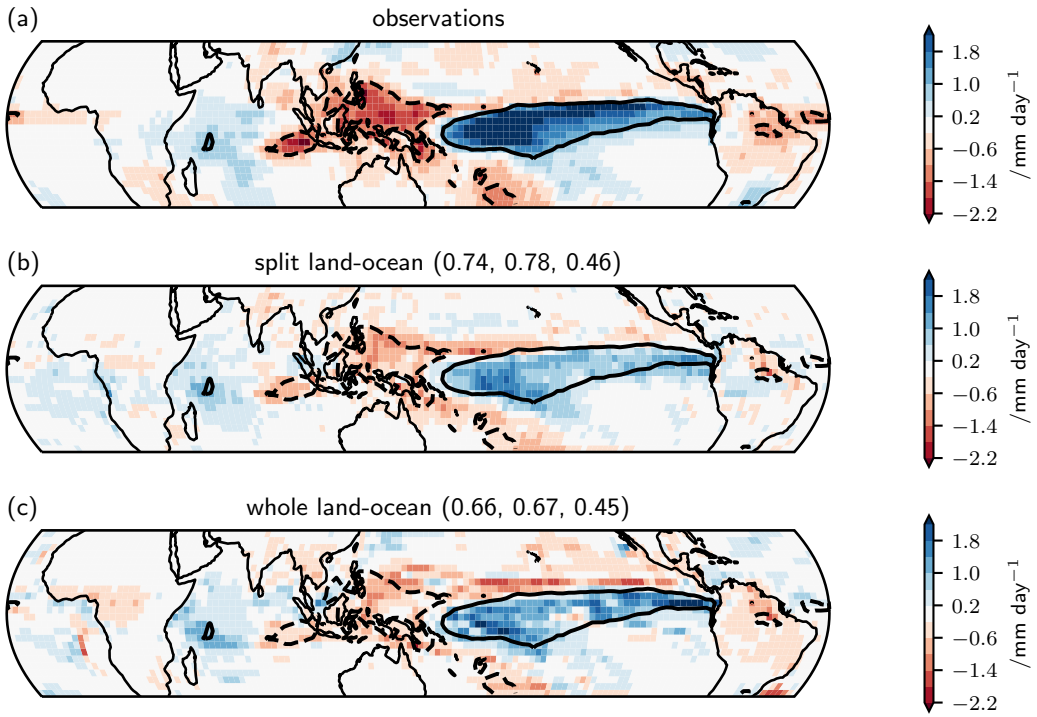

Figure 6.2: ERA-Interim-GPCP 1979-2016 July-June El Niño minus neutral composite mean precipitation changes: (a) GPCP observations. (b) Merged diagnosed changes using the GP method (Chapter 3) for $\hat{P}$ evaluated separately over tropical land and ocean. (c) Diagnosed changes for $\hat{P}$ evaluated over all tropical grid points. In (b,c), triplets in parentheses indicate the spatial correlation versus observations over land, ocean and all tropical grid points.

to examine the precipitation response to a variety of atmospheric forcing processes. The Cloud Feedback Model Intercomparison Project (CFMIP, Webb *et al.* (2017)) is designed to explore the interaction of clouds and regional circulation and precipitation changes. Consequently, repeating the moisture budget decomposition approach (Seager *et al.*, 2010) of Chapter 4 on these alternative experiments would expand the analysis beyond SST and CO_2 forcing. Moreover, comparing CMIP5 with CMIP6 simulations using this framework would assess the effect using a new generation of parametrisations and model components.

Computational and time constraints limited the HadGEM2-A ensemble size available for the analysis in Chapter 5. An important area of future work would be to increase the ensemble size to better capture the uncertainty of simulated changes due to internal variability. In addition, the transient experiments could be repeated with start dates at different points in the seasonal cycle. Examining how quickly equilibrium ENSO-related precipitation responses are reached would help develop our understanding of potential future changes. Two further experiments could be conducted to support the analysis. Firstly the amipFuture and amip4xCO2 perturbations could be combined as a new simulation, in order to assess the linearity assumption of amipTotal. Secondly, the amipFuture transient simulations could be branched directly from the amip4K simulations. This would more precisely improve the assessment of the response due to SST pattern changes alone, and could be compared to the new diagnosis test case as discussed in Section 6.2.1. It would also be interesting to assess the transient response during different ENSO events to examine how sensitive future precipitation changes are to El Niño variability.

The question remains of exactly how to reduce or quantify uncertainty in future precipitation mean state or variability changes. CMIP5 simulations are biased relative to observations, as discussed in Section 4.3.1, and the coupled models often share components, such as the atmosphere model in HadGEM2 and ACCESS families. Hence the ensemble of CMIP5 future projections provides a non-random sample from models which fail to perfectly simulate the observed climate. Perhaps a better approach to probe mechanisms is to use individual idealised simulations based on physical motivations to disentangle the competing processes acting in reality. The use of atmosphere-only perturbed SST and CO_2 experiments in Chapters 4 and 5 and in the literature (for instance Chadwick *et al.* (2014), He and Soden (2015) and Kent *et al.* (2015)) is one example, but these models do not simulate feedbacks and are hence unphysical. Another approach would be to improve our observations of the present day tropical precipitation. Sparsely observed tropical land regions could be targeted in order to help tune coupled climate models, but this is costly and it is impractical to observe precipitation with calibrated rain gauges everywhere.

Since tropical precipitation is typically energetically limited, reducing uncertainty in radiative forcing (Soden *et al.*, 2018) would be another approach to constrain precipitation projections. An additional option would be to further develop our understanding of deep convection. For instance, high resolution simulations using cloud resolving models at regional scales could be used to develop more refined parametrisations (Guichard and Couvreux, 2017). Alternatively, improved computational resources would permit higher resolutions at a global scale (Heinzeller *et al.*, 2016), removing the reliance on convective parametrisation in GCMs.

6.3 Conclusions

The epigraphs to Chapters 1 and 6 highlight the considerable spatial variability of tropical precipitation. Our understanding of the underlying mechanisms, coupled atmosphere-ocean-land processes, has grown substantially since the mid-nineteenth century. Considerable natural tropical precipitation interannual variability is also evident, associated with the El Niño-Southern Oscillation (McPhaden *et al.*, 2006), in both observations and a variety of state-of-the-art climate model simulations. Integrating these climate models forward under idealised or more realistic future scenarios, significant precipitation mean state (Christensen *et al.*, 2013; Collins *et al.*, 2013) and variability (Cai *et al.*, 2015a) changes are simulated. These changes are driven by increased greenhouse gas concentrations, caused by human activity. However, policy-relevant, regional scale precipitation changes remain relatively uncertain (Knutti and Sedlacek, 2012).

This thesis has applied a variety of methods to examine the mechanisms which control tropical precipitation change, with three major results presented. Firstly, a common mechanism has been identified which bridges both present day variability on annual timescales, with simulated centennial changes. The heaviest tropical precipitation typically remains anchored above the relatively warmest and most humid locations, even as these locations move in geographical space. Secondly, tropical circulation and hence precipitation changes are evident in climate model simulations without corresponding SST gradient changes. This extends findings in the literature (for example Xie *et al.* (2010)) by demonstrating the important and linked role of future patterns of land warming and humidity changes with regional hydrological cycle changes. Thirdly, significant ENSO-anomalous precipitation changes over tropical land regions surrounding the Pacific ocean are plausible in response to either uniform or patterned SST warming, or direct CO_2 forcing. Future changes to ENSO-related precipitation are hence likely to be the result of a careful balance of several interacting processes.

Future work is necessary to further develop our understanding of the mechanisms which

control tropical precipitation variability, with the aim to constrain future projected changes. This is important in order to minimise potentially catastrophic environmental damage and socio-economic costs. Building upon this thesis, this could be achieved by identifying and examining further consistent processes which bridge natural present day variability in observations and models, and simulated future changes across a variety of climate models.

Bibliography

Adam, O., Bischoff, T., and Schneider, T., 2016. Seasonal and Interannual Variations of the Energy Flux Equator and ITCZ. Part I: Zonally Averaged ITCZ Position, *J. Climate*, **29**(9), 3219–3230, doi:10.1175/JCLI-D-15-0512.1.

Adler, R. F., Huffman, G. J., Chang, A., Ferraro, R., Xie, P.-P., Janowiak, J., Rudolf, B., Schneider, U., Curtis, S., Bolvin, D., Gruber, A., Susskind, J., Arkin, P., and Nelkin, E., 2003. The Version-2 Global Precipitation Climatology Project (GPCP) Monthly Precipitation Analysis (1979-Present), *J. Hydrometeor.*, **4**(6), 1147–1167, doi:10.1175/1525-7541(2003)004¡1147:TVGPCP¿2.0.CO;2.

Adler, R. F., Gu, G., and Huffman, G. J., 2012. Estimating Climatological Bias Errors for the Global Precipitation Climatology Project (GPCP), *J. Appl. Meteor. Climatol.*, **51**(1), 84–99, doi:10.1175/JAMC-D-11-052.1.

Allan, R. P. and Soden, B. J., 2007. Large discrepancy between observed and simulated precipitation trends in the ascending and descending branches of the tropical circulation, *Geophys. Res. Lett.*, **34**(18), L18705, doi:10.1029/2007GL031460.

Allan, R. P., Soden, B. J., John, V. O., Ingram, W., and Good, P., 2010. Current changes in tropical precipitation, *Environ. Res. Lett.*, **5**(2), 25205, doi:10.1088/1748-9326/5/2/025205.

Allan, R. P., Liu, C., Zahn, M., Lavers, D. A., Koukouvagias, E., and Bodas-Salcedo, A., 2014. Physically Consistent Responses of the Global Atmospheric Hydrological Cycle in Models and Observations, *Surveys in Geophysics*, **35**(3), 533–552, doi:10.1007/s10712-012-9213-z.

Allan, R. P., 2012. Regime dependent changes in global precipitation, *Climate Dyn.*, **39**(3), 827–840, doi:10.1007/s00382-011-1134-x.

Allen, M. R. and Ingram, W. J., 09 2002. Constraints on future changes in climate and the hydrologic cycle, *Nature*, **419**, 224–232, doi:10.1038/nature01092.

Andrews, T. and Webb, M. J., 2018. The Dependence of Global Cloud and Lapse Rate Feedbacks on the Spatial Structure of Tropical Pacific Warming, *J. Climate*, **31**(2), 641–654, doi:10.1175/jcli-d-17-0087.1.

Arakawa, A. and Lamb, V. R. Computational Design of the Basic Dynamical Processes of the UCLA General Circulation Model. volume 17 of *Methods in Computational Physics: Advances in Research and Applications*, pages 173–265. Elsevier, 1977.

Arthur, D. and Vassilvitskii, S., 2007. k-means++: The advantages of careful seeding. In *Proceedings of the eighteenth annual ACM-SIAM symposium on Discrete algorithms*. Society for Industrial and Applied Mathematics.

Atwood, A. R., Battisti, D. S., Wittenberg, A. T., Roberts, W. H. G., and Vimont, D. J., 2016. Characterizing unforced multi-decadal variability of ENSO: a case study with the GFDL CM2.1 coupled GCM, *Climate Dyn.*, **49**(7-8), 2845–2862, doi:10.1007/s00382-016-3477-9.

Bastos, L. S. and O'Hagan, A., 2009. Diagnostics for Gaussian Process Emulators, *Technometrics*, **51**(4), 425–438, doi:10.1198/tech.2009.08019.

Bayr, T. and Dommenget, D., 2013. The Tropospheric Land-Sea Warming Contrast as the Driver of Tropical Sea Level Pressure Changes, *J. Climate*, **26**(4), 1387–1402, doi:10.1175/JCLI-D-11-00731.1.

Bayr, T., Dommenget, D., Martin, T., and Power, S. B., 2014. The eastward shift of the Walker Circulation in response to global warming and its relationship to ENSO variability, *Climate Dyn.*, **43**(9), 2747–2763, doi:10.1007/s00382-014-2091-y.

Bell, G. D., Halpert, M. S., Ropelewski, C. F., Kousky, V. E., Douglas, A. V., Schnell, R. C., and Gelman, M. E., 1999. Climate Assessment for 1998, *Bull. Amer. Meteor. Soc.*, **80**(5), S1–S48, doi:10.1175/1520-0477-80.5s.S1.

Bellenger, H., Guilyardi, E., Leloup, J., Lengaigne, M., and Vialard, J., 2014. ENSO representation in climate models: from CMIP3 to CMIP5, *Climate Dyn.*, **42**(7), 1999–2018, doi:10.1007/s00382-013-1783-z.

Bellouin, N., Boucher, O., Haywood, J., Johnson, C., Jones, A., Rae, J., and Woodward., S. Improved representation of aerosols for HadGEM2. Met Office Hadley Centre, Technical Note 73, 2007.

Berg, W., L'Ecuyer, T., and Haynes, J. M., 2010. The Distribution of Rainfall over Oceans from Spaceborne Radars, *J. Appl. Meteor. Climatol.*, **49**(3), 535–543, doi:10.1175/2009JAMC2330.1.

Biasutti, M., Battisti, D. S., and Sarachik, E. S., 2004. Mechanisms Controlling the Annual Cycle of Precipitation in the Tropical Atlantic Sector in an Atmospheric GCM, *Journal of Climate*, **17**(24), 4708–4723, doi:10.1175/JCLI-3235.1.

Bjerknes, J., 1969. Atmospheric Teleconnections from the Equatorial Pacific, *Mon. Wea. Rev.*, **97**(3), 163–172, doi:10.1175/1520-0493(1969)097¡0163:ATFTEP¿2.3.CO;2.

Bonfils, C. J. W., Santer, B. D., Phillips, T. J., Marvel, K., Leung, L. R., Doutriaux, C., and Capotondi, A., 2015. Relative Contributions of Mean-State Shifts and ENSO-Driven Variability to Precipitation Changes in a Warming Climate, *J. Climate*, **28**(24), 9997–10013, doi:10.1175/JCLI-D-15-0341.1.

Bony, S., Bellon, G., Klocke, D., Sherwood, S., Fermepin, S., and Denvil, S., 2013. Robust direct effect of carbon dioxide on tropical circulation and regional precipitation, *Nat. Geosci.*, **6**, 447–451, doi:10.1038/ngeo1799.

Borlace, S., Santoso, A., Cai, W., and Collins, M., 2014. Extreme swings of the South Pacific Convergence Zone and the different types of El Niño events, *Geophys. Res. Lett.*, **41**(13), 4695–4703, doi:10.1002/2014GL060551.

Boucher, O., Randall, D., Artaxo, P., Bretherton, C., Feingold, G., Forster, P., Kerminen, V.-M., Kondo, Y., Liao, H., Lohmann, U., Rasch, P., Satheesh, S., Sherwood, S., and B. *Climate Change 2013: The Physical Science Basis. Contribution of Working Group I to the Fifth Assessment Report of the Intergovernmental Panel on Climate Change*, chapter Clouds and Aerosols. Cambridge University Press, Cambridge, United Kingdom and New York, NY, USA, 2013.

Bretherton, C. S. and Sobel, A. H., 2002. A Simple Model of a Convectively Coupled Walker Circulation Using the Weak Temperature Gradient Approximation, *J. Climate*, **15**(20), 2907–2920, doi:10.1175/1520-0442(2002)015¡2907:ASMOAC¿2.0.CO;2.

Bretherton, C. S. and Sobel, A. H., 2003. The Gill Model and the Weak Temperature Gradient Approximation, *J. Atmos. Sci.*, **60**(2), 451–460, doi:10.1175/1520-0469(2003)060¡0451:TGMATW¿2.0.CO;2.

Bretherton, C. S., Peters, M. E., and Back, L. E., 2004. Relationships between Water Vapor Path and Precipitation over the Tropical Oceans, *J. Climate*, *J. Climate*, **17**, 1517–1528.

Byrd, R. H., Lu, P., Nocedal, J., and Zhu, C., 1995. A Limited Memory Algorithm for Bound Constrained Optimization, *SIAM Journal on Scientific Computing*, **16**(5), 1190–1208, doi:10.1137/0916069.

Byrne, M. P. and O'Gorman, P. A., 2016. Understanding Decreases in Land Relative Humidity with Global Warming: Conceptual Model and GCM Simulations, *J. Climate*, **29**(24), 9045–9061, doi:10.1175/JCLI-D-16-0351.1.

Byrne, M. P. and Schneider, T., 2016. Energetic Constraints on the Width of the Intertropical Convergence Zone, *J. Climate*, **29**(13), 4709–4721, doi:10.1175/JCLI-D-15-0767.1.

Cai, W., Borlace, S., Lengaigne, M., van Rensch, P., Collins, M., Vecchi, G., Timmermann, A., Santoso, A., McPhaden, M. J., Wu, L., England, M. H., Wang, G., Guilyardi, E., and Jin, F.-F., 2014. Increasing frequency of extreme el niño events due to greenhouse warming, *Nat. Clim. Change*, **4**, 111–116, doi:10.1038/nclimate2100.

Cai, W., Santoso, A., Wang, G., Yeh, S.-W., An, S.-I., Cobb, K. M., Collins, M., Guilyardi, E., Jin, F.-F., Kug, J.-S., Lengaigne, M., McPhaden, M. J., Takahashi, K., Timmermann, A., Vecchi, G., Watanabe, M., and Wu, L., 2015. ENSO and greenhouse warming, *Nat. Clim. Change*, **5**, 849–859, doi:10.1038/nclimate2743.

Cai, W., Wang, G., Santoso, A., McPhaden, M. J., Wu, L., Jin, F.-F., Timmermann, A., Collins, M., Vecchi, G., Lengaigne, M., England, M. H., Dommenget, D., Takahashi, K., and Guilyardi, E., 2015. Increased frequency of extreme la niña events under greenhouse warming, *Nat. Clim. Change*, **5**, 132–137, doi:10.1038/nclimate2492.

Capotondi, A., Wittenberg, A. T., Newman, M., Di Lorenzo, E., Yu, J.-Y., Braconnot, P., Cole, J., Dewitte, B., Giese, B., Guilyardi, E., Jin, F.-F., Karnauskas, K., Kirtman, B., Lee, T., Schneider, N., Xue, Y., and Yeh, S.-W., 2015. Understanding ENSO Diversity, *Bull. Amer. Meteor. Soc.*, **96**(6), 921–938, doi:10.1175/BAMS-D-13-00117.1.

Chadwick, R., Boutle, I., and Martin, G., 2013. Spatial Patterns of Precipitation Change in CMIP5: Why the Rich Do Not Get Richer in the Tropics, *J. Climate*, **26**(11), 3803–3822, doi:10.1175/JCLI-D-12-00543.1.

Chadwick, R., Good, P., Andrews, T., and Martin, G., 2014. Surface warming patterns drive tropical rainfall pattern responses to CO2 forcing on all timescales, *Geophys. Res. Lett.*, **41**(2), 610–615, doi:10.1002/2013GL058504.

Chadwick, R., Good, P., and Willett, K., 2016. A Simple Moisture Advection Model of Specific Humidity Change over Land in Response to SST Warming, *J. Climate*, **29**(21), 7613–7632, doi:10.1175/JCLI-D-16-0241.1.

Chadwick, R., Ackerley, D., Ogura, T., and Dommenget, D., 2019. Separating the influences of land warming, the direct CO 2 effect, the plant physiological effect, and SST warming on regional precipitation changes, *J. Geophys. Res.*, **124**(2), 624–640, doi:10.1029/2018jd029423.

Chadwick, R., 2016. Which Aspects of CO2 Forcing and SST Warming Cause Most Uncertainty in Projections of Tropical Rainfall Change over Land and Ocean?, *J. Climate*, **29**(7), 2493–2509, doi:10.1175/JCLI-D-15-0777.1.

Chang, C.-P., Wang, Z., Ju, J., and Li, T., 2004. On the Relationship between Western Maritime Continent Monsoon Rainfall and ENSO during Northern Winter, *J. Climate*, **17**(3), 665–672, doi:10.1175/1520-0442(2004)017¡0665:OTRBWM¿2.0.CO;2.

Charney, J. G. and Phillips, N. A., 1953. Numerical integration of the quasi-geostrophic equations for barotropic and simple baroclinic flows, *J. Meteor.*, **10**(2), 71–99, doi:10.1175/1520-0469(1953)010¡0071:NIOTQG¿2.0.CO;2.

Charney, J. G., 1963. A Note on Large-Scale Motions in the Tropics, *J. Atmos. Sci.*, **20**(6), 607–609, doi:10.1175/1520-0469(1963)020¡0607:ANOLSM¿2.0.CO;2.

Charney, J. G. *Mathematical Problems of the Geophysical Fluid Dynamics in Lect. Appl. Math. vol. 13*, chapter Tropical cyclogenesis and the formation of the Intertropical Convergence Zone, pages 355–368. Am. Math. Soc., 1971.

Chen, S. S., Houze, R. A., and Mapes, B. E., 1996. Multiscale Variability of Deep Convection In Realation to Large-Scale Circulation in TOGA COARE, *J. Atmos. Sci.*, **53**(10), 1380–1409, doi:10.1175/1520-0469(1996)053¡1380:MVODCI¿2.0.CO;2.

Cho, H.-K., Bowman, K. P., and North, G. R., 2004. A Comparison of Gamma and Lognormal Distributions for Characterizing Satellite Rain Rates from the Tropical Rainfall Measuring Mission, *J. Appl. Meteor.*, **43**(11), 1586–1597, doi:10.1175/JAM2165.1.

Chou, C., Neelin, J. D., Chen, C.-A., and Tu, J.-Y., 2009. Evaluating the "Rich-Get-Richer" Mechanism in Tropical Precipitation Change under Global Warming, *J. Climate*, **22**(8), 1982–2005, doi:10.1175/2008JCLI2471.1.

Christensen, J. H., Kumar, K. K., Aldrian, E., An, S.-I., Cavalcanti, I. F. A., de Castro, M., Dong, W., Goswami, P., Hall, A., Kanyanga, J. K., Kitoh, A., Kossin, J., Lau, N.-C., Renwick, J., Stephenson, D. B., Xie, S.-P., and Zhou, T. *Climate Change 2013: The Physical Science Basis. Contribution of Working Group I to the Fifth Assessment Report of the Intergovernmental Panel on Climate Change*, chapter Climate Phenomena and their Relevance for Future Regional Climate Change. Cambridge University Press, Cambridge, United Kingdom and New York, NY, USA, 2013.

Collins, M., An, S.-I., Cai, W., Ganachaud, A., Guilyardi, E., Jin, F.-F., Jochum, M., Lengaigne, M., Power, S., Timmermann, A., Vecchi, G., and Wittenberg, A., 2010. The impact of global warming on the tropical pacific ocean and el niño, *Nat. Geosci.*, **3**, 391–397, doi:10.1038/ngeo868.

Collins, M., Knutti, R., Arblaster, J., Dufresne, J.-L., Fichefet, T., Friedlingstein, P., Gao, X., Gutowski, W. J., Johns, T., Krinner, G., Shongwe, M., Tebaldi, C., Weaver, A. J., and Wehner, M. *Climate Change 2013: The Physical Science Basis. Contribution of Working Group I to the Fifth Assessment Report of the Intergovernmental Panel on Climate Change*, chapter Long-term Climate Change: Projections, Commitments and Irreversibility. Cambridge University Press, Cambridge, United Kingdom and New York, NY, USA, 2013.

Cowtan, K. and Way, R. G., 2014. Coverage bias in the HadCRUT4 temperature series and its impact on recent temperature trends, *Quart. J. Roy. Meteor. Soc.*, **140**, 1935–1944, doi:10.1002/qj.2297.

Cox, P. M., Betts, R. A., Bunton, C. B., Essery, R. L. H., Rowntree, P. R., and Smith, J., 1999. The impact of new land surface physics on the GCM simulation of climate and climate sensitivity, *Climate Dyn.*, **15**(3), 183–203, doi:10.1007/s003820050276.

Cullen, M. J. P., 1993. The unified forecast/climate model, *Meteorological Magazine*, *Meteorological Magazine*, **122**, 81–94.

Davies, T., Cullen, M. J. P., Malcolm, A. J., Mawson, M. H., Staniforth, A., White, A. A., and Wood, N., 2005. A new dynamical core for the Met Office's global and regional modelling of the atmosphere, *Quart. J. Roy. Meteor. Soc.*, *Quart. J. Roy. Meteor. Soc.*, **131**(608), 1759–1782.

Dawin, C., 1845. *Journal of researches into the natural history and geology of the countries visited during the voyage of H.M.S. Beagle round the world, under the Command of Capt. Fitz Roy, R.N (The Voyage of the Beagle)*. (2 Ed.) John Murray, London, UK.

Dawson, A., 2016. Windspharm: A High-Level Library for Global Wind Field Computations Using Spherical Harmonics, *Journal of Open Research Software*, **4**(1), e31, doi:10.5334/jors.129.

Dee, D. P., Uppala, S. M., Simmons, A. J., Berrisford, P., Poli, P., Kobayashi, S., Andrae, U., Balmaseda, M. A., Balsamo, G., Bauer, P., Bechtold, P., Beljaars, A. C. M., van de Berg, L., Bidlot, J., Bormann, N., Delsol, C., Dragani, R., Fuentes, M., Geer, A. J., Haimberger, L., Healy, S. B., Hersbach, H., Hólm, E. V., Isaksen, L., Kållberg, P., Köhler, M., Matricardi, M., McNally, A. P., Monge-Sanz, B. M., Morcrette, J.-J., Park, B.-K., Peubey, C., de Rosnay, P., Tavolato, C., Thépaut, J.-N., and Vitart, F., 2011. The ERA-Interim reanalysis: configuration and performance of the data assimilation system, *Quart. J. Roy. Meteor. Soc.*, **137**(656), 553–597, doi:10.1002/qj.828.

Derbyshire, S. H., Maidens, A. V., Milton, S. F., Stratton, R. A., and Willett, M. R., 2011. Adaptive detrainment in a convective parametrization, *Quart. J. Roy. Meteor. Soc.*, **137**(660), 1856–1871, doi:10.1002/qj.875.

DiNezio, P. N., Clement, A. C., Vecchi, G. A., Soden, B. J., Kirtman, B. P., and Lee, S.-K., 2009. Climate Response of the Equatorial Pacific to Global Warming, *J. Climate*, **22**(18), 4873–4892, doi:10.1175/2009JCLI2982.1.

Dong, B. and Lu, R., 2013. Interdecadal enhancement of the walker circulation over the Tropical Pacific in the late 1990s, *Adv. Atmos. Sci.*, **30**(2), 247–262, doi:10.1007/s00376-012-2069-9.

Dong, B., Gregory, J. M., and Sutton, R. T., 2009. Understanding Land-Sea Warming Contrast in Response to Increasing Greenhouse Gases. Part I: Transient Adjustment, *J. Climate*, **22**(11), 3079–3097, doi:10.1175/2009JCLI2652.1.

ECMWF. *Part IV: Physical Processes*. IFS Documentation. ECMWF, 2016.

England, M. H., McGregor, S., Spence, P., Meehl, G. A., Timmermann, A., Cai, W., Gupta, A. S., McPhaden, M. J., Purich, A., and Santoso, A., 2014. Recent intensification of wind-driven circulation in the Pacific and the ongoing warming hiatus, *Nat. Clim. Change*, **4**, 222–227, doi:10.1038/nclimate2106.

Essery, R. L. H., Best, M. J., Betts, R. A., Cox, P. M., and Taylor, C. M., 2003. Explicit Representation of Subgrid Heterogeneity in a GCM Land Surface Scheme, *J. Hydrometeor.*, **4**(3), 530–543, doi:10.1175/1525-7541(2003)004¡0530:EROSHI¿2.0.CO;2.

Fasullo, J. T. and Trenberth, K. E., 2008. The Annual Cycle of the Energy Budget. Part I: Global Mean and Land-Ocean Exchanges, *J. Climate*, **21**(10), 2297–2312, doi:10.1175/2007JCLI1935.1.

Feng, X., Haines, K., Liu, C., de Boisséson, E., and Polo, I., 2018. Improved SST-Precipitation Intraseasonal Relationships in the ECMWF Coupled Climate Reanalysis, *Geophys. Res. Lett.*, **45**(8), 3664–3672, doi:10.1029/2018gl077138.

Ferrett, S., Collins, M., and Ren, H.-L., 2018. Diagnosing Relationships between Mean State Biases and El Niño Shortwave Feedback in CMIP5 Models, *J. Climate*, **31**(4), 1315–1335, doi:10.1175/JCLI-D-17-0331.1.

Flato, G., Marotzke, J., Abiodun, B., Braconnot, P., Chou, S. C., Collins, W., Cox, P., Driouech, F., Emori, S., Eyring, V., Forest, C., Gleckler, P., Guilyardi, E., Jakob, C., Kattsov, V., Reason, C., and Rummukainen, M. *Climate Change 2013: The Physical Science Basis. Contribution of Working Group I to the Fifth Assessment Report of the Intergovernmental Panel on Climate Change*, chapter Evaluation of Climate Models. Cambridge University Press, Cambridge, United Kingdom and New York, NY, USA, 2013.

Frierson, D. M. W., Hwang, Y.-T., Fučkar, N. S., Seager, R., Kang, S. M., Donohoe, A., Maroon, E. A., Liu, X., and Battisti, D. S., 2013. Contribution of ocean overturning circulation to tropical rainfall peak in the northern hemisphere, *Nat. Geosci.*, **6**, 940–944, doi:10.1038/ngeo1987.

Fritsch, J. M. and Chappell, C. F., 1980. Numerical Prediction of Convectively Driven Mesoscale Pressure Systems. Part I: Convective Parameterization, *J. Atmos. Sci.*, **37**(8), 1722–1733, doi:10.1175/1520-0469(1980)037¡1722:NPOCDM¿2.0.CO;2.

Fu, Q., Johanson, C. M., Wallace, J. M., and Reichler, T., 2006. Enhanced Mid-Latitude Tropospheric Warming in Satellite Measurements, *Science*, **312**, 1179, doi:10.1126/science.1125566.

Grant, A. L. M., 2001. Cloud-base fluxes in the cumulus-capped boundary layer, *Quart. J. Roy. Meteor. Soc.*, **127**(572), 407–421, doi:10.1002/qj.49712757209.

Gregory, D. and Rowntree, P. R., 1990. A Mass Flux Convection Scheme with Representation of Cloud Ensemble Characteristics and Stability-Dependent Closure, *Mon. Wea. Rev.*, **118**(7), 1483–1506, doi:10.1175/1520-0493(1990)118¡1483:AMFCSW¿2.0.CO;2.

Guichard, F. and Couvreux, F., 2017. A short review of numerical cloud-resolving models, *Tellus A: Dynamic Meteorology and Oceanography*, **69**(1), doi:10.1080/16000870.2017.1373578.

Guilyardi, E., Wittenberg, A., Fedorov, A., Collins, M., Wang, C., Capotondi, A., van Oldenborgh, G. J., and Stockdale, T., 2009. Understanding El Niño in Ocean-Atmosphere General Circulation Models: Progress and Challenges, *Bull. Amer. Meteor. Soc.*, **90**(3), 325–340, doi:10.1175/2008BAMS2387.1.

Guttorp, P. and Gneiting, T., 2006. Studies in the history of probability and statistics XLIX On the Matérn correlation family, *Biometrika*, *Biometrika*, **93**(4), 989–995.

Hadley, G., 1735. Concerning the cause of the general trade-winds, *Philos. Trans. Roy. Soc.*, *Philos. Trans. Roy. Soc.*, **39**, 58–62.

Haffke, C. and Magnusdottir, G., 2013. The South Pacific Convergence Zone in three decades of satellite images, *J. Geophys. Res.*, **118**(19), 10839–10849, doi:10.1002/jgrd.50838.

Hartmann, D. L., Hendon, H. H., and Houze, R. A., 1984. Some Implications of the Mesoscale Circulations in Tropical Cloud Clusters for Large-Scale Dynamics and Climate, *Journal of the Atmospheric Sciences*, **41**(1), 113–121, doi:10.1175/1520-0469(1984)041¡0113:SIOTMC¿2.0.CO;2.

Hartmann, D. L., Tank, A. K., Rusticucci, M., Alexander, L., Brönnimann, S., Charabi, Y., Dentener, F., Dlugokencky, E., Easterling, D., Kaplan, A., Soden, B., Thorne, P., Wild, M., and Zhai, P. *Climate Change 2013: The Physical Science Basis. Contribution of Working Group I to the Fifth Assessment Report of the Intergovernmental Panel on Climate Change*, chapter Observations: Atmosphere and Surface. Cambridge University Press, Cambridge, United Kingdom and New York, NY, USA, 2013.

Hawcroft, M., Haywood, J. M., Collins, M., Jones, A., Jones, A. C., and Stephens, G., 2017. Southern Ocean albedo, inter-hemispheric energy transports and the double ITCZ: global impacts of biases in a coupled model, *Climate Dyn.*, **48**(7), 2279–2295, doi:10.1007/s00382-016-3205-5.

He, J. and Soden, B. J., 2015. Anthropogenic Weakening of the Tropical Circulation: The Relative Roles of Direct CO2 Forcing and Sea Surface Temperature Change, *Journal of Climate*, **28**(22), 8728–8742, doi:10.1175/JCLI-D-15-0205.1.

Heinzeller, D., Duda, M. G., and Kunstmann, H., 2016. Towards convection-resolving, global atmospheric simulations with the Model for Prediction Across Scales (MPAS) v3.1: an extreme scaling experiment, *Geosci. Model Dev.*, **9**(1), 77–110, doi:10.5194/gmd-9-77-2016.

Held, I. M. and Hou, A. Y., 1980. Nonlinear Axially Symmetric Circulations in a Nearly Inviscid Atmosphere, *J. Atmos. Sci.*, **37**(3), 515–533, doi:10.1175/1520-0469(1980)037¡0515:NASCIA¿2.0.CO;2.

Held, I. M. and Soden, B. J., 2006. Robust Responses of the Hydrological Cycle to Global Warming, *J. Climate*, **19**(21), 5686–5699, doi:10.1175/JCLI3990.1.

Holloway, C. E. and Neelin, J. D., 2009. Moisture Vertical Structure, Column Water Vapor, and Tropical Deep Convection, *J. Atmos. Sci.*, **66**(6), 1665–1683, doi:10.1175/2008JAS2806.1.

Holton, J. R., Wallace, J. M., and Young, J. A., 1971. On Boundary Layer Dynamics and the ITCZ, *J. Atmos. Sci.*, *J. Atmos. Sci.*, **28**(2), 275–280.

Houze, R. A., Chen, S. S., Kingsmill, D. E., Serra, Y., and Yuter, S. E., 2000. Convection over the Pacific Warm Pool in relation to the Atmospheric Kelvin-Rossby Wave, *J. Atmos. Sci.*, **57**(18), 3058–3089, doi:10.1175/1520-0469(2000)057¡3058:COTPWP¿2.0.CO;2.

Houze, R. A., 1989. Observed structure of mesoscale convective systems and implications for large-scale heating, *Quart. J. Roy. Meteor. Soc.*, **115**(487), 425–461, doi:10.1002/qj.49711548702.

Houze, R. A., 1993. *Cloud Dynamics*. R. Dmowska (ed.) Academic Press, London, UK.

Houze, R. A., 2004. Mesoscale convective systems, *Rev. Geophys.*, **42**(4), RG4003, doi:10.1029/2004RG000150.

Hu, S. and Fedorov, A. V., 2017. The extreme El Niño of 2015-2016: the role of westerly and easterly wind bursts, and preconditioning by the failed 2014 event, *Climate Dyn.*, *Climate Dyn.*

Hu, Y. and Fu, Q., 2007. Observed poleward expansion of the Hadley circulation since 1979, *Atmos. Chem. Phys.*, **7**, 5229–5236, doi:0.5194/acp-7-5229-2007.

Huang, P. and Chen, D., 2017. Enlarged Asymmetry of Tropical Pacific Rainfall Anomalies Induced by El Niño and La Niña under Global Warming, *J. Climate*, **30**(4), 1327–1343, doi:10.1175/JCLI-D-16-0427.1.

Huang, P. and Xie, S.-P., 2015. Mechanisms of change in ENSO-induced tropical Pacific rainfall variability in a warming climate, *Nat. Geosci.*, *Nat. Geosci.*, **8**, 922–926.

Huang, B., Banzon, V. F., Freeman, E., Lawrimore, J., Liu, W., Peterson, T. C., Smith, T. M., Thorne, P. W., Woodruff, S. D., and Zhang, H.-M., 2015. Extended Reconstructed Sea Surface Temperature Version 4 (ERSST.v4). Part I: Upgrades and Intercomparisons, *J. Climate*, **28**(3), 911–930, doi:10.1175/JCLI-D-14-00006.1.

Huang, P., 2016. Time-Varying Response of ENSO-Induced Tropical Pacific Rainfall to Global Warming in CMIP5 Models. Part I: Multimodel Ensemble Results, *J. Climate*, **29**(16), 5763–5778, doi:10.1175/JCLI-D-16-0058.1.

Hudson, R. D., Andrade, M. F., Follette, M. B., and Frolov, A. D., 2006. The total ozone field separated into meteorological regimes - Part II: Northern Hemisphere mid-latitude total ozone trends, *Atmos. Chem. Phys.*, **6**, 5183–5191, doi:10.5194/acp-6-5183-2006.

Huffman, G. J., Adler, R. F., Bolvin, D. T., Gu, G., Nelkin, E. J., Bowman, K. P., Hong, Y., Stocker, E. F., and Wolff, D. B., 2007. The TRMM Multisatellite Precipitation Analysis (TMPA): Quasi-Global, Multiyear, Combined-Sensor Precipitation Estimates at Fine Scales, *J. Hydrometeor.*, **8**, 38–55, doi:10.1175/JHM560.1.

Hwang, Y.-T. and Frierson, D. M. W., 2013. Link between the double-Intertropical Convergence Zone problem and cloud biases over the Southern Ocean, *Proc. Natl. Acad. Sci. (USA)*, **110**(13), 4935–4940, doi:10.1073/pnas.1213302110.

IPCC, 2000. *Special Report Emissions Scenarios. Prepared by Working Group III of the Intergovernmental Panel on Climate Change*. Cambridge University Press, Cambridge, United Kingdom and New York, NY, USA.

IPCC, 2007. *Contribution of Working Group I to the Fourth Assessment Report of the Intergovernmental Panel on Climate Change*. Cambridge University Press, Cambridge, United Kingdom and New York, NY, USA.

IPCC, 2013. *Climate Change 2013: The Physical Science Basis. Contribution of Working Group I to the Fifth Assessment Report of the Intergovernmental Panel on Climate Change*. Cambridge University Press, Cambridge, United Kingdom and New York, NY, USA.

Jin, F.-F., 1997. An Equatorial Ocean Recharge Paradigm for ENSO. Part I: Conceptual Model, *J. Atmos. Sci.*, **54**(7), 811–829, doi:10.1175/1520-0469(1997)054¡0811:AEORPF¿2.0.CO;2.

Jolliffe, I. T. and Stephenson, D. B., 2012. *Forecast verification: a practitioner's guide in atmospheric science*. John Wiley & Sons, Chichester, United Kingdom.

Joshi, M. M., Gregory, J. M., Webb, M. J., Sexton, D. M. H., and Johns, T. C., 2008. Mechanisms for the land/sea warming contrast exhibited by simulations of climate change, *Climate Dyn.*, **30**(5), 455–465, doi:10.1007/s00382-007-0306-1.

Kent, C., Chadwick, R., and Rowell, D. P., 2015. Understanding uncertainties in future projections of seasonal tropical precipitation, *Journal of Climate*, **28**(11), 4390–4413, doi:10.1175/JCLI-D-14-00613.1.

Knutson, T. R. and Manabe, S., 1995. Time-Mean Response over the Tropical Pacific to Increased CO2 in a Coupled Ocean-Atmosphere Model, *J. Climate*, *J. Climate*, **8**, 2181–2199.

Knutti, R. and Sedlacek, J., 2012. Robustness and uncertainties in the new CMIP5 climate model projections, *Nature Clim. Change*, **3**(4), 369–373, doi:10.1038/nclimate1716.

Knutti, R., Furrer, R., Tebaldi, C., Cermak, J., and Meehl, G. A., 2010. Challenges in Combining Projections from Multiple Climate Models, *J. Climate*, (10), 2739–2758, doi:10.1175/2009JCLI3361.1.

Knutti, R., Masson, D., and Gettelman, A., 2013. Climate model genealogy: Generation CMIP5 and how we got there, *Geophys. Res. Lett.*, **40**(6), 1194–1199, doi:10.1002/grl.50256.

Kuo, Y.-H., Neelin, J. D., and Mechoso, C. R., 2017. Tropical Convective Transition Statistics and Causality in the Water Vapor-Precipitation Relation, *J. Atmos. Sci.*, **74**(3), 915–931, doi:10.1175/JAS-D-16-0182.1.

Lambert, F. H., Ferraro, A. J., and Chadwick, R., 2017. Land-Ocean Shifts in Tropical Precipitation Linked to Surface Temperature and Humidity Change, *J. Climate*, **30**(12), 4527–4545, doi:10.1175/JCLI-D-16-0649.1.

Lau, W. K. M. and Kim, K.-M., 2015. Robust Hadley Circulation changes and increasing global dryness due to CO2 warming from CMIP5 model projections, *Proc. Natl. Acad. Sci. (USA)*, **112**(12), 3630–3635, doi:10.1073/pnas.1418682112.

L'Heureux, M. L., Lee, S., and Lyon, B., 2013. Recent multidecadal strengthening of the Walker circulation across the tropical Pacific, *Nat. Clim. Change*, **3**, 571–576, doi:10.1038/nclimate1840.

Li, G. and Xie, S.-P., 2014. Tropical Biases in CMIP5 Multimodel Ensemble: The Excessive Equatorial Pacific Cold Tongue and Double ITCZ Problems, *J. Climate*, **27**(4), 1765–1780, doi:10.1175/JCLI-D-13-00337.1.

Lin, J.-L., 2007. The Double-ITCZ Problem in IPCC AR4 Coupled GCMs: Ocean-Atmosphere Feedback Analysis, *J. Climate*, **20**(18), 4497–4525, doi:10.1175/JCLI4272.1.

Lindzen, R. S. and Nigam, S., 1987. On the Role of Sea Surface Temperature Gradients in Forcing Low-Level Winds and Convergence in the Tropics, *Journal of the Atmospheric Sciences*, **44**(17), 2418–2436, doi:10.1175/1520-0469(1987)044¡2418:OTROSS¿2.0.CO;2.

Liu, C. and Allan, R. P., 2013. Observed and simulated precipitation responses in wet and dry regions 1850-2100, *Environ. Res. Lett.*, **8**(3), 34002, doi:10.1088/1748-9326/8/3/034002.

Loeb, N. G., Wang, H., Cheng, A., Kato, S., Fasullo, J. T., Xu, K.-M., and Allan, R. P., 2016. Observational constraints on atmospheric and oceanic cross-equatorial heat transports: revisiting the precipitation asymmetry problem in climate models, *Climate Dyn.*, **46**(9), 3239–3257, doi:10.1007/s00382-015-2766-z.

Lu, J., Vecchi, G. A., and Reichler, T., 3 2007. Expansion of the Hadley cell under global warming, *Geophys. Res. Lett.*, **34**(6), doi:10.1029/2006GL028443.

Lu, J., Chen, G., and Frierson, D. M. W., 2008. Response of the Zonal Mean Atmospheric Circulation to El Niño versus Global Warming, *J. Climate*, **21**(22), 5835–5851, doi:10.1175/2008JCLI2200.1.

Ma, J. and Xie, S.-P., 2013. Regional Patterns of Sea Surface Temperature Change: A Source of Uncertainty in Future Projections of Precipitation and Atmospheric Circulation, *J. Climate*, **26**(8), 2482–2501, doi:10.1175/JCLI-D-12-00283.1.

Ma, J., Xie, S.-P., and Kosaka, Y., 2012. Mechanisms for Tropical Tropospheric Circulation Change in Response to Global Warming, *J. Climate*, **25**(8), 2979–2994, doi:10.1175/JCLI-D-11-00048.1.

MacQueen, J., 1967. Some methods for classification and analysis of multivariate observations. In *Proceedings of the Fifth Berkeley Symposium on Mathematical Statistics and Probability, Volume 1: Statistics*, pages 281–297, Berkeley, CA, USA. University of California Press.

Martin, G. M., Milton, S. F., Senior, C. A., Brooks, M. E., Ineson, S., Reichler, T., and Kim, J., 2010. Analysis and reduction of systematic errors through a seamless approach to modeling weather and climate, *J. Climate*, **23**(22), 5933–5957, doi:10.1175/2010JCLI3541.1.

Martin, G. M., Bellouin, N., Collins, W. J., Culverwell, I. D., Halloran, P. R., Hardiman, S. C., Hinton, T. J., Jones, C. D., McDonald, R. E., McLaren, A. J., O'Connor, F. M.,

Roberts, M. J., Rodriguez, J. M., Woodward, S., Best, M. J., Brooks, M. E., Brown, A. R., Butchart, N., Dearden, C., Derbyshire, S. H., Dharssi, I., Doutriaux-Boucher, M., Edwards, J. M., Falloon, P. D., Gedney, N., Gray, L. J., Hewitt, H. T., Hobson, M., Huddleston, M. R., Hughes, J., Ineson, S., Ingram, W. J., James, P. M., Johns, T. C., Johnson, C. E., Jones, A., Jones, C. P., Joshi, M. M., Keen, A. B., Liddicoat, S., Lock, A. P., Maidens, A. V., Manners, J. C., Milton, S. F., Rae, J. G. L., Ridley, J. K., Sellar, A., Senior, C. A., Totterdell, I. J., Verhoef, A., Vidale, P. L., and Wiltshire, A., 2011. The HadGEM2 family of Met Office Unified Model climate configurations, *Geosci. Model Dev.*, **4**(3), 723–757, doi:10.5194/gmd-4-723-2011.

McPhaden, M. J., Zebiak, S. E., and Glantz, M. H., 2006. ENSO as an Integrating Concept in Earth Science, *Science*, **314**(5806), 1740–1745, doi:10.1126/science.1132588.

Misra, V., Marx, L., Brunke, M., and Zeng, X., 2008. The Equatorial Pacific Cold Tongue Bias in a Coupled Climate Model, *J. Climate*, **21**(22), 5852–5869, doi:10.1175/2008JCLI2205.1.

Mitchell, J. F. B., Wilson, C. A., and Cunnington, W. M., 1987. On CO2 climate sensitivity and model dependence of results, *Quarterly Journal of the Royal Meteorological Society*, **113**(475), 293–322, doi:10.1002/qj.49711347517.

Möbis, B. and Stevens, B., 2012. Factors controlling the position of the Intertropical Convergence Zone on an aquaplanet, *J. Adv. in Model. Earth Syst.*, **4**(4), M00A04, doi:10.1029/2012MS000199.

Morice, C. P., Kennedy, J. J., Rayner, N. A., and Jones, P. D., 2012. Quantifying uncertainties in global and regional temperature change using an ensemble of observational estimates: The HadCRUT4 data set, *J. Geophys. Res.*, **117**(D8), D08101, doi:10.1029/2011JD017187.

Moss, R. H., Edmonds, J. A., Hibbard, K. A., Manning, M. R., Rose, S. K., van Vuuren, D. P., Carter, T. R., Emori, S., Kainuma, M., Kram, T., Meehl, G. A., Mitchell, J. F. B., Nakicenovic, N., Riahi, K., Smith, S. J., Stouffer, R. J., Thomson, A. M., Weyant, J. P., and Wilbanks, T. J., 2010. The next generation of scenarios for climate change research and assessment, *Nature*, **463**, 747–756, doi:0.1038/nature08823.

Myhre, G., Forster, P. M., Samset, B. H., Hodnebrog, O., Sillmann, J., Aalbergs, S. G., Andrews, T., Boucher, O., Faluvegi, G., Fleschner, D., Iversen, T., Kasoar, M., Kharin, V., Kirkeveg, A., Lamarque, J.-F., Olivia, D., Richardson, T. B., Shindell, D., Shine, K. P., Stjern, C. W., Takemura, T., Voulgarakis, A., and Zwiers, F., 2017. PDRMIP: A Precipitation Driver and Response Model Intercomparison Project: Protocol and Preliminary Results, *Bull. Amer. Meteor. Soc.*, **98**(6), 1185–1198, doi:10.1175/BAMS-D-16-0019.1.

Neelin, J. D. and Held, I. M., 1987. Modeling Tropical Convergence Based on the Moist Static Energy Budget, *Mon. Wea. Rev.*, *Mon. Wea. Rev.*, **115**(1), 3–12.

Neelin, J. D., Battisti, D. S., Hirst, A. C., Jin, F.-F., Wakata, Y., Yamagata, T., and Zebiak, S. E., 1998. ENSO theory, *J. Geophys. Res.*, **103**(C7), 14261–14290, doi:10.1029/97JC03424.

Neelin, J. D., Chou, C., and Su, H., 2003. Tropical drought regions in global warming and El Niño teleconnections, *Geophys. Res. Lett.*, **30**(24), 2275, doi:10.1029/2003GL018625.

Nesbitt, S. W. and Zipser, E. J., 2003. The Diurnal Cycle of Rainfall and Convective Intensity according to Three Years of TRMM Measurements, *J. Climate*, **16**(10), 1456–1475, doi:10.1175/1520-0442-16.10.1456.

NOAA. Historical El Niño/ La Niña episodes (1950-present), 2015. Accessed 13 January 2017. [Available online at `http://www.cpc.ncep.noaa.gov/products/analysis_monitoring/ensostuff/ensoyears.shtml`].

NOAA/ESRL. Trends in Atmospheric Carbon Dioxide, 2019. Accessed 14 April 2019. [Available online at `https://www.esrl.noaa.gov/gmd/ccgg/trends/gl_data.html`].

Perry, S. J., McGregor, S., Gupta, A. S., and England, M. H., 2017. Future Changes to El Niño-Southern Oscillation Temperature and Precipitation Teleconnections, *Geophys. Res. Lett.*, **44**(20), 10608–10616, doi:10.1002/2017GL074509.

Pfhal, S. and Neidermann, N., 2011. Daily covariations in near-surface relative humidity and temperature over the ocean, *J. Geophys. Res.*, **116**, D19104, doi:10.1029/2011JD015792.

Philander, G., 1990. *El Niño, La Niña, and the Southern Oscillation*. Academic Press, London, UK.

Pope, V. D., Gallani, M. L., Rowntree, P. R., and Stratton, R. A., 2000. The impact of new physical parametrizations in the Hadley Centre climate model: HadAM3, *Climate Dyn.*, **16**(2), 123–146, doi:10.1007/s003820050009.

Power, S. B. and Delage, F. P. D., 2018. El Niño-Southern Oscillation and Associated Climatic Conditions around the World during the Latter Half of the Twenty-First Century, *J. Climate*, **31**(15), 6189–6207, doi:10.1175/JCLI-D-18-0138.1.

Power, S., Delage, F., Chung, C., Kociuba, G., and Keay, K., 2013. Robust twenty-first-century projections of El Niño and related precipitation variability, *Nature*, **502**, 541–545, doi:10.1038/nature12580.

Rasmussen, C. E. and Williams, C. K. I., 2006. *Gaussian Processes for Machine Learning*. the MIT press, Cambridge, Massachusetts and London, England.

Rasmusson, E. M. and Carpenter, T. H., 1982. Variations in Tropical Sea Surface Temperature and Surface Wind Fields Associated with the Southern Oscillation/El Niño, *Mon. Wea. Rev.*, **110**(5), 354–384, doi:10.1175/1520-0493(1982)110¡0354:VITSST¿2.0.CO;2.

Riahi, K., Grübler, A., and Nakicenovic, N., 2007. Scenarios of long-term socio-economic and environmental development under climate stabilization, *Technological Forecasting and Social Change*, **74**(7), 887–935, doi:10.1016/j.techfore.2006.05.026.

Richter, I. and Xie, S.-P., 2008. Muted precipitation increase in global warming simulations: A surface evaporation perspective, *J. Geophys. Res.*, **113**(D24), doi:10.1029/2008JD010561. D24118.

Roca, R., Aublanc, J., Chambon, P., Fiolleau, T., and Viltard, N., 2014. Robust observational quantification of the contribution of mesoscale convective systems to rainfall in the tropics, *J. Climate*, **27**(13), 4952–4958, doi:10.1175/JCLI-D-13-00628.1.

Ropelewski, C. F. and Halpert, M. S., 1987. Global and Regional Scale Precipitation Patterns Associated with the El Niño/Southern Oscillation, *Mon. Wea. Rev.*, **115**(8), 1606–1626, doi:10.1175/1520-0493(1987)115¡1606:GARSPP¿2.0.CO;2.

Rosenfeld, D., Lohmann, U., Raga, G. B., O'Dowd, C. D., Kulmala, M., Fuzzi, S., Reissell, A., and Andreae, M. O., 2008. Flood or Drought: How Do Aerosols Affect Precipitation?, *Science*, **321**(5894), 1309–1313, doi:10.1126/science.1160606.

Rowell, D. P. and Jones, R. G., 2006. Causes and uncertainty of future summer drying over Europe, *Climate Dyn.*, **27**(2), 281–299, doi:10.1007/s00382-006-0125-9.

Santoso, A., McGregor, S., Jin, F.-F., Cai, W., England, M. H., An, S.-I., McPhaden, M. J., and Guilyardi, E., 2013. Late-twentieth-century emergence of the el niño propagation asymmetry and future projections, *Nature*, **504**, 126–130, doi:10.1038/nature12683.

Schiro, K. A., Neelin, J. D., Adams, D. K., and Lintner, B. R., 2016. Deep Convection and Column Water Vapor over Tropical Land versus Tropical Ocean: A Comparison between the Amazon and the Tropical Western Pacific, *J. Atmos. Sci.*, **73**(10), 4043–4063, doi:10.1175/JAS-D-16-0119.1.

Schumacher, C. and Houze, R. A., 2003. Stratiform Rain in the Tropics as Seen by the TRMM Precipitation Radar, *J. Climate*, **16**(11), 1739–1756, doi:10.1175/1520-0442(2003)016¡1739:SRITTA¿2.0.CO;2.

Seager, R. and Henderson, N., 2013. Diagnostic Computation of Moisture Budgets in the ERA-Interim Reanalysis with Reference to Analysis of CMIP-Archived Atmospheric Model Data, *J. Climate*, **26**(20), 7876–7901, doi:10.1175/JCLI-D-13-00018.1.

Seager, R., Naik, N., and Vecchi, G. A., 2010. Thermodynamic and Dynamic Mechanisms for Large-Scale Changes in the Hydrological Cycle in Response to Global Warming, *J. Climate*, **23**(17), 4651–4668, doi:10.1175/2010JCLI3655.1.

Seidel, D. J. and Randel, W. J., 2006. Variability and trends in the global tropopause estimated from radiosonde data, *J. Geophys. Res.*, **111**, D21101, doi:10.1029/2006JD007363.

Seidel, D. J., Fu, Q., Randel, W. J., and Reichler, T. J., 2008. Widening of the tropical belt in a changing climate, *Nature Geoscience*, **1**, 21–24, doi:10.1038/ngeo.2007.38.

Seneviratne, S. I., Corti, T., Davin, E. L., Hirschi, M., Jaeger, E. B., Lehner, I., Orlowsky, B., and Teuling, A. J., 2010. Investigating soil moisture-climate interactions in a changing climate: A review, *Earth-Science Reviews*, **99**(3), 125–161, doi:10.1016/j.earscirev.2010.02.004.

Sherwood, S. C., Ingram, W., Tsushima, Y., Satoh, M., Roberts, M., Vidale, P. L., and O'Gorman, P. A., 2010. Relative humidity changes in a warmer climate, *J. Geophys. Res.*, **115**(D9), D09104, doi:10.1029/2009JD012585.

Smith, T. M. and Reynolds, R. W., 2005. A Global Merged Land-Air-Sea Surface Temperature Reconstruction Based on Historical Observations (1880-1997), *J. Climate*, **18**(12), 2021–2036, doi:10.1175/JCLI3362.1.

Sobel, A. H. and Bretherton, C. S., 2000. Modeling Tropical Precipitation in a Single Column, *J. Climate*, **13**(24), 4378–4392, doi:10.1175/1520-0442(2000)013¡4378:MTPIAS¿2.0.CO;2.

Sobel, A. H., Nilsson, J., and Polvani, L. M., 2001. The Weak Temperature Gradient Approximation and Balanced Tropical Moisture Waves, *J. Atmos. Sci.*, **58**(23), 3650–3665, doi:10.1175/1520-0469(2001)058¡3650:TWTGAA¿2.0.CO;2.

Soden, B. J., Collins, W. D., and Feldman, D. R., 2018. Reducing uncertainties in climate models, *Science*, **361**(6400), 326–327, doi:10.1126/science.aau1864.

Solomon, A. and Newman, M., 2012. Reconciling disparate twentieth-century Indo-Pacific ocean temperature trends in the instrumental record, *Nat. Clim. Change*, **2**, 691–699, doi:10.1038/nclimate1591.

Stephens, G. L., Li, J., Wild, M., Clayson, C. A., Loeb, N., Kato, S., L'Ecuyer, T., Stackhouse Jr, P. W., Lebsock, M., and Andrews, T., 2012. An update on Earth's energy balance in light of the latest global observations, *Nat. Geosci.*, **5**, 691–696, doi:0.1038/ngeo1580.

Stephens, G. L., Hakuba, M. Z., Webb, M. J., Lebsock, M., Yue, Q., Kahn, B. H., Hristova-Veleva, S., Rapp, A. D., Stubenrauch, C. J., Elsaesser, G. S., and Slingo, J.,

2018. Regional Intensification of the Tropical Hydrological Cycle During ENSO, *Geophys. Res. Lett.*, **45**(9), 4361–4370, doi:10.1029/2018gl077598.

Su, H., Jiang, J. H., Neelin, J. D., Shen, T. J., Zhai, C., Yue, Q., Wang, Z., Huang, L., Choi, Y.-S., Stephens, G. L., and Yung, Y. L., 2017. Tightening of tropical ascent and high clouds key to precipitation change in a warmer climate, *Nature Communications*, **8**, 15771, doi:10.1038/ncomms15771.

Takahashi, K. and Battisti, D. S., 2007. Processes Controlling the Mean Tropical Pacific Precipitation Pattern. Part I: The Andes and the Eastern Pacific ITCZ, *Journal of Climate*, **20**(14), 3434–3451, doi:10.1175/JCLI4198.1.

Taylor, K. E., Williamson, D., and Zwiers, F. The Sea Surface Temperature and Sea-Ice Concentration Boundary Conditions for AMIP II Simulations. PCMDI Report No. 60, 2000.

Taylor, K. E., Stouffer, R. J., and Meehl, G. A., 2012. An Overview of CMIP5 and the Experiment Design, *Bull. Amer. Meteor. Soc.*, **93**(4), 485–498, doi:10.1175/BAMS-D-11-00094.1.

Timmermann, A., An, S.-I., Kug, J.-S., Jin, F.-F., Cai, W., Capotondi, A., Cobb, K., Lengaigne, M., McPhaden, M. J., Stuecker, M. F., Stein, K., Wittenberg, A. T., Yun, K.-S., Bayr, T., Chen, H.-C., Chikamoto, Y., Dewitte, B., Dommenget, D., Grothe, P., Guilyardi, E., Ham, Y.-G., Hayashi, M., Ineson, S., Kang, D., Kim, S., Kim, W., Lee, J.-Y., Li, T., Luo, J.-J., McGregor, S., Planton, Y., Power, S., Rashid, H., Ren, H.-L., Santoso, A., Takahashi, K., Todd, A., Wang, G., Wang, G., Xie, R., Yang, W.-H., Yeh, S.-W., Yoon, J., Zeller, E., and Zhang, X., 2018. El niño–southern oscillation complexity, *Nature*, *Nature*, **559**, 535–545.

Todd, A., Collins, M., Lambert, F. H., and Chadwick, R., 2018. Diagnosing ENSO and global warming tropical precipitation shifts using surface relative humidity and temperature., *J. Climate*, **31**(4), 1413–1433, doi:10.1175/JCLI-D-17-0354.1.

Toh, Y. Y., Turner, A. G., Johnson, S. J., and Holloway, C. E., 2018. Maritime Continent seasonal climate biases in AMIP experiments of the CMIP5 multimodel ensemble, *Climate Dyn.*, **50**(3), 777–800, doi:10.1007/s00382-017-3641-x.

Trenberth, K. E. and Guillemot, C. J., 1995. Evaluation of the Global Atmospheric Moisture Budget as Seen from Analyses, *J. Climate*, **8**(9), 2255–2272, doi:10.1175/1520-0442(1995)008¡2255:EOTGAM¿2.0.CO;2.

Trenberth, K. E. and Shea, D. J., 2005. Relationships between precipitation and surface temperature, *Geophys. Res. Lett.*, **32**(14), L14703, doi:10.1029/2005gl022760.

Trenberth, K. E. and Stepaniak, D. P., 2001. Indices of El Niño evolution, *J. Climate*, **14**(8), 1697–1701, doi:10.1175/1520-0442(2001)014¡1697:LIOENO¿2.0.CO;2.

Trenberth, K. E., Branstator, G. W., Karoly, D., Kumar, A., Lau, N.-C., and Ropelewski, C., 1988. Progress during TOGA in understanding and modeling global teleconnections associated with tropical sea surface temperatures, *J. Geophys. Res.*, **103**(C7), 14291–14324, doi:10.1029/97JC01444.

Trenberth, K. E., Branstator, G. W., Karoly, D., Kumar, A., Lau, N.-C., and Ropelewski, C., 1998. Progress during TOGA in understanding and modeling global teleconnections associated with tropical sea surface temperatures, *Journal of Geophysical Research: Oceans*, **103**(C7), 14291–14324, doi:10.1029/97JC01444.

Trenberth, K. E., Smith, L., Qian, T., Dai, A., and Fasullo, J., 2007. Estimates of the Global Water Budget and Its Annual Cycle Using Observational and Model Data, *J. Hydrometeor.*, **8**(4), 758–769, doi:10.1175/JHM600.1.

Trenberth, K. E., Fasullo, J. T., and Kiehl, J., 2009. Earth's Global Energy Budget, *Bull. Amer. Meteor. Soc.*, **90**(3), 311–324, doi:10.1175/2008BAMS2634.1.

Vecchi, G. A. and Soden, B. J., 2007. Global Warming and the Weakening of the Tropical Circulation, *J. Climate*, **20**(17), 4316–4340, doi:10.1175/JCLI4258.1.

Walker, G. T., 1923. Correlation in Seasonal Variations of Weather, VIII: A Preliminary Study of World Weather, *Memoirs of the Indian Meteorological Department*, *Memoirs of the Indian Meteorological Department*, **24**(4), 75–131.

Wallace, A. R., 1869. *The Malay Archipelago: The land of the orang–utan, and the bird of paradise. A narrative of travel, with sketches of man and nature*. (1 Ed.) Macmillan, London, UK.

Webb, M. J. and Lock, A. P., 2012. Coupling between subtropical cloud feedback and the local hydrological cycle in a climate model, *Climate Dyn.*, **41**(7-8), 1923–1939, doi:10.1007/s00382-012-1608-5.

Webb, M. J., Andrews, T., Bodas-Salcedo, A., Bony, S., Bretherton, C. S., Chadwick, R., Chepfer, H., Douville, H., Good, P., Kay, J. E., Klein, S. A., Marchand, R., Medeiros, B., Siebesma, A. P., Skinner, C. B., Stevens, B., Tselioudis, G., Tsushima, Y., and Watanabe, M., 2017. The Cloud Feedback Model Intercomparison Project (CFMIP) contribution to CMIP6, *Geosci. Model Dev.*, **10**(1), 359–384, doi:10.5194/gmd-10-359-2017.

Webster, P. J., 2004. *The Hadley Circulation: Present, Past and Future*. (H. F. Diaz and R. Bradley eds.) Springer Netherlands.

Wentz, F. J., Ricciardulli, L., Hilburn, K., and Mears, C., 2007. How Much More Rain Will Global Warming Bring?, *Science*, **317**(5835), 233–235, doi:10.1126/science.1140746.

Widlansky, M. J., Timmermann, A., Stein, K., McGregor, S., Schneider, N., England, M. H., Lengaigne, M., and Cai, W., 2012. Changes in south pacific rainfall bands in a warming climate, *Nat. Clim. Change*, **3**, 417–423, doi:10.1038/nclimate1726.

Wilks, D. S., 2016. "The Stippling Shows Statistically Significant Grid Points": How Research Results are Routinely Overstated and Overinterpreted, and What to Do about It, *Bull. Amer. Meteor. Soc.*, **97**(12), 2263–2273, doi:10.1175/BAMS-D-15-00267.1.

Willett, K. M., Jones, P. D., Gillett, N. P., and Thorne, P. W., 2008. Recent Changes in Surface Humidity: Development of the HadCRUH Dataset, *J. Climate*, **21**(20), 5364–5383, doi:10.1175/2008JCLI2274.1.

Xie, P. and Arkin, P. A., 1997. Global Precipitation: A 17-Year Monthly Analysis Based on Gauge Observations, Satellite Estimates, and Numerical Model Outputs, *Bull. Amer. Meteor. Soc.*, **78**(11), 2539–2558, doi:10.1175/1520-0477(1997)078¡2539:GPAYMA¿2.0.CO;2.

Xie, P. and Arkin, P. A., 1998. Global Monthly Precipitation Estimates from Satellite-Observed Outgoing Longwave Radiation, *J. Climate*, **11**(2), 137–164, doi:10.1175/1520-0442(1998)011¡0137:GMPEFS¿2.0.CO;2.

Xie, S.-P. and Philander, G., 1994. A coupled ocean-atmosphere model of relevance to the ITCZ in the eastern Pacific, *Tellus A*, **46**(4), 340–350, doi:10.1034/j.1600-0870.1994.t01-1-00001.x.

Xie, S.-P., Deser, C., Vecchi, G. A., Ma, J., Teng, H., and Wittenberg, A. T., 2010. Global Warming Pattern Formation: Sea Surface Temperature and Rainfall, *J. Climate*, **23**(4), 966–986, doi:10.1175/2009JCLI3329.1.

Yeh, S.-W., Kug, J.-S., Dewitte, B., Kwon, M.-H., Kirtman, B. P., and Jin, F.-F., 2009. El niño in a changing climate, *Nature*, **461**, 511–514, doi:10.1038/nature08316.

Yu, B. and Zwiers, F. W., 2010. Changes in equatorial atmospheric zonal circulations in recent decades, *Geophys. Res. Lett.*, **37**(5), L05701, doi:10.1029/2009GL042071.

Yu, B., Zwiers, F. W., Boer, G. J., and Ting, M. F., 2012. Structure and variances of equatorial zonal circulation in a multimodel ensemble, *Climate Dyn.*, **39**(9), 2403–2419, doi:10.1007/s00382-012-1372-6.

Zappa, G., Pithan, F., and Shepherd, T. G., 2018. Multimodel Evidence for an Atmospheric Circulation Response to Arctic Sea Ice Loss in the CMIP5 Future Projections, *Geophys. Res. Lett.*, **45**(2), 1011–1019, doi:10.1002/2017GL076096.